University of Dundee

DOCTOR OF PHILOSOPHY

Energy cascade of internal gravity waves in oceans

Gururaj, Saranraj

Award date:
2023

Energy cascade of internal gravity waves in oceans

by
Saranraj Gururaj

This thesis is submitted for the degree of

Doctor of Philosophy

awarded by

School of Science and Engineering,

University of Dundee

October 2023

Contents

Declaration

This thesis is the result of my own work and includes nothing which is the outcome of work done in collaboration except as declared in the Preface and specified in the text. It is not substantially the same as any that I have submitted, or, is being concurrently submitted for a degree or diploma or other qualification at the University of Dundee or any other University or similar institution except as declared in the Preface and specified in the text. I further state that no substantial part of my thesis has already been submitted, or, is being concurrently submitted for any such degree, diploma or other qualification at the University of Dundee or any other University or similar institution except as declared in the Preface and specified in the text.

Saranraj Gururaj
March 2023

Energy cascade of internal gravity waves in oceans

Saranraj Gururaj

Internal gravity waves are large length scale waves that exist in the bulk of the ocean, and they play a crucial role in the ocean's energy budget. Various mechanisms cause the energy in internal gravity waves to cascade to small length scales. At small length scales, internal waves cause turbulence and mixing of waters with different densities. Mixing plays a prominent role in sustaining climate-influencing flows such as Meridional Overturning Circulation. This thesis is dedicated to understanding the mechanisms that cascade internal waves' energy to small length scales. First, using multiple scale analysis, we study triad interactions of low mode internal gravity waves that occur in the presence of slowly varying bathymetry. The waves' group speed and horizontal wavenumber vary with fluid depth, and the variation influences the energy transfer between the waves. Moreover, if the stratification is non-constant, detuning can be induced in wave-wave interactions that occur in a region of non-constant fluid depth. Detuning can affect the energy transfer between the waves. Nonlinear coupling coefficients and growth rates are observed to be sensitive to changes in fluid depth. Higher order self-interactions, where the bathymetry acts as a zero-frequency wave, are also studied. Secondly, we study 5-wave systems that consist of two parent waves (waves with large amounts of energy) and three daughter waves (waves with infinitesimal energy). The five waves form two different triads, where each of these triads consists of one parent wave and two daughter waves, with one daughter wave shared between the two triads. The growth rate of 5-wave systems for different combinations of parent wavevectors is studied. Scenarios where the 5-wave system instability is more dominant than triads are analysed in detail. Apart from influencing wave-wave interactions, topographies can directly scatter a low mode internal wave and cause a cascade of the wave's energy. In the final chapter, internal wave topography interaction in the presence of a steady surface confined current is studied by conducting numerical simulations. The dependence of mode-1 wave scattering on the height and slope of the topography is studied. In the presence of a current, the mode-1 wave with positive phase speed has different properties compared to the mode-1 wave with negative phase speed, and we study the scattering of both mode-1 waves.

Acknowledgements

First of all, I have to thank my supervisor, Dr. Anirban Guha, for providing me with knowledge and training in many things related to life and career. This thesis would not have been possible without him. He has always been ready to discuss research, and I was able to meet him whenever needed, and this was crucial in progressing the thesis. I realise that I have a long way to go to become a well-established researcher, but I like to think I have also come a long way from where I started, and Dr. Guha is the main reason for my progress.

PhD is always a very tough journey, and I have had the good fortune of having friends to whom I could talk and vent when things are not going well. I like to thank Benjamin, Bala, Arun, and Akanksha with whom I could talk whenever needed. The conversations about chess, computer games, and movies were always relaxing and funny. My thanks also go to Subhajit Kar for helping me to run several open-source codes.

In this journey, I have also met wonderful 'pod' mates Raheem, Alessio, Jinhui, and Tom, who always made the workplace enjoyable. Working with them was a welcome change after the solitude we all had to endure because of the coronavirus. The visits to Pub also were fun. A special thanks to my roommate Ross as well for many enjoyable conversations about football. I believe that I gained some wonderful friends during my stay at Dundee.

I would also like to thank my cousin Babukumar, my cousin-in-law Vidhya Babukumar, and my two wonderful nieces Laya and Rhea for supporting me massively in Scotland. They helped me to settle in Scotland. Moreover, they were always very welcoming, invited me to every family function (and gave me lots of food). I did not feel isolated in a different country because of them.

Last but not least, my gratitude goes to my Mother, Father, Grandfather, and grandmother (on my mum's side) for supporting me throughout my life. My parents have worked hard to support me through all stages of my life and studies, and I cannot thank them enough.

List of Figures

List of Tables

List of Variables

Common for all chapters

(u, v, w) - (Zonal, meridional, vertical) velocity

ψ - streamfunction in (x, z) plane

T - Temperature

κ - Diffusivity

ρ' - Density of the fluid.

κ - Density Perturbation

$\rho_{base}(z)$ - Base density Profile

ρ_0 - Reference Density (1000 kg/m^3)

Ω - Frequency of Earth's rotation $(\approx 7 \times 10^{-5}\mathrm{s}^{-1})$.

p' - Perturbation pressure

$\bar{p}$ - Hydrostatic pressure

Re - Reynolds Number

b - Buoyancy perturbation

ω - Frequency

$\mathbf{k}$ - Wavevector

(k, l, m) - (Zonal, meridional, vertical) wavenumbers

N - Buoyancy frequency

θ_{lat} - Latitude

f - Local coriolis frequency ($2\Omega \sin \theta_{\text{lat}}$)

$\tilde{f}$ - Non-traditional vertical coriolis frequency ($2\Omega \cos \theta_{\text{lat}}$)

ν - Kinematic viscosity

μ - Dynamic viscosity

$\mathcal{G}_T$ - Thermal expansion coefficient

(c_x^p,c_z^p) - (Horizontal, vertical) phase speed

(c_x^g,c_z^g) - (Horizontal, vertical) group speed

S$^{(P)}$ - Wave steepness

ϕ - Modal shape of the internal wave in $z-$direction

ω_d - Semi-diurnal frequency

$f_{28.9^\circ}$ - f at $\theta_{\text{lat}} = 28.9^\circ$

H - Mean depth

Len$_x$ - Horizontal domain length

$h(x)$ - Topography function

$H_b(x)$ - Deviation from the mean depth

k_b - Topography's wavenumber

Ψ - Streamfunction in $(x-\eta)$ coordinates

$\mathbb{B}$ - Buoyancy perturbation in $(x-\eta)$ coordinates

$\mathbb{P}$ - Pressure in $(x-\eta)$ coordinates

$(\mathbb{U}, \mathbb{V}, \mathbb{W})$ - (Zonal, meridional, vertical) velocity in $(x-\eta)$ coordinates

σ - Growth rate

σ_{ref} - Reference growth rate

ϵ_a - Small parameter used for scaling amplitude of the wave.

ϵ_t - Small parameter used for scaling amplitude's time scale.

$A^{(R)}$ - Denotes the control area chosen

Chapter 2

$\mathcal{U}$ - Defined in page 26

N.R.T - Defined in page 28

(C_{21}, C_{12}) - Defined in page 28

$\mathcal{J}\{,\}$ - Defined in page 30

$(L_x, L_\eta, L_{xx}, L_{\eta\eta})$ - Defined in page 30

ϵ_x - Defined in page 30.

(ϵ_h, ϵ_k) - Defined in page 31.

$(\Xi_j, \widehat{\Xi}_j)$ - Defined in page 30 & 32

$\mathcal{L}$ - Defined in page 33

χ_j - Defined in page 33

$\mathcal{M}$ - Defined in page 34

P_j - Defined in page 34

$\mathfrak{P}_j$ - Defined in page 35

OE$^{(2)}$ - Defined in page 35

NL - Defined in page 35

$\gamma_{j,i}$ - Defined in page 36

β - Defined in page 36

$(\mathrm{NL}_{(\mathbb{B},j)}, \mathrm{NL}_{(\mathbb{V},j)}, \mathrm{NL}_{(\Psi,j)})$ - Defined in page 37

Γ - Defined in page 38

$(\mathfrak{N}, \mathfrak{D}, \mathcal{D})$ - Defined in page 39

$\Delta\omega$ - Defined in page 39

$\Delta\omega_s$ - Defined in page 41

$a_{(*,s)}$ - Defined in page 41

$\mathcal{N}$ - Defined in page 41

ζ - Defined in page 42

$(\langle \mathrm{TE}_j \rangle, \widehat{\mathrm{TE}}_j)$ - Defined in page 42 & 43

Δk - Defined in page 44

(N_b, N_{max}, z_c, W_p) - Defined in page 44

α - Defined in page 46

$\Delta\mathcal{K}$ - Defined in page 47

$(\mathcal{K}_{\min}, \widehat{\mathcal{K}})$ - Defined in page 47

$\mathbf{INV}(x)$ - Defined in page 50

Δm - Defined in page 50

$\Delta\mathcal{K}_s$ - Defined in page 53

$\mathcal{A}$ - Defined in page 65

$(\mathrm{LIN}_3, \mathrm{NonL}_3)$ - Defined in page 66

W_T - Defined in page 68

ν_{12x} - Defined in page 70

Dif() - Defined in page 70

$F(x)$ - Defined in page 72

Eu - Defined in page 73

(ν_{6x}, ν_{6z}) - Defined in page 74

$(x_{\mathrm{PCK}}, W_{\mathrm{PCK}})$ - Defined in page 74

Chapter 3

$\mathcal{D}^{(3)}$ - Defined in page 84

VT - Defined in page 84

$(\mathscr{U}_j, \mathscr{V}_j, \mathscr{B}_j, \mathscr{P}_j)$ - Polarisation relations - Defined in page 85

$\mathcal{V}$ - Defined in page 85

NLT - Defined in page 86

$(\mathcal{E},\mathcal{S})$ - Defined in page 86

$(\mathfrak{E}_{(j,p,d)},\mathfrak{D}_{(j,b,c)})$ - Defined in page 86

$\widehat{\sigma}$ - Defined in page 87

θ - Defined in page 93

$(\mathcal{R}_{\text{noise}}, \mathcal{A}_{\text{noise}})$ - Defined in page 95

$\text{Phase}_{\text{noise}}$ - Defined in page 95

$(k_{\text{noise}}, m_{\text{noise}}, k_{\text{lowest}})$ - Defined in page 95

$(\widehat{E}, E_{\text{ref}})$ - Defined in page 96

$(\hat{u}_{\text{FR}}, \hat{w}_{\text{FR}}, \hat{v}_{\text{FR}}, \hat{b}_{\text{FR}})$ - Defined in page 96

σ_{cl} - Defined in page 97

ν_H - Defined in page 100

$\mathcal{Q}$ - Defined in page 103

Chapter 4

Υ - Defined in page 108

Θ - Defined in page 108

z_{WKB} - Defined in page 111

N_{mean} - Defined in page 111

$(u_{\text{base}}, u_{\text{total}})$ - Defined in page 112

Δ_{2D} - Defined in page 112

SP(x) - Defined in page 112

$(x_{s1}, x_{s2}, W_s, \vartheta_S)$ - Defined in page 112

$\mathcal{H}$ - Defined in page 112

Δ_{2D} - Defined in page 112

(h_t, W_T, x_T) - Defined in page 113

Φ - Defined in page 113

(U_c, W_{crt}, z_{crt}) - Defined in page 114

Ri - Defined in page 114

$(\mathcal{F}_u, \mathcal{F}_w, \mathcal{F}_b)$ - Defined in page 115

(x_F, W_F, ϑ_F) - Defined in page 115

$(E_{pe}, E_{ke}, E^{(\text{vis})}, {E^{(\text{vis})}}_H)$ - Defined in page 116

TF - Defined in page 116

K_D - Defined in page 117

$(\mathcal{T}, \mathcal{T}_{inc})$ - Defined in page 117&118

(u_R, u_{ω_d}) - Defined in page 118

$A_n(x,t)$ - Defined in page 118
$(p_{\omega_d}, w_{\omega_d}, b_{\omega_d})$ - Defined in page 119
$(p_R, P_{f2}^{(N)}, P_{f2})$ - Defined in page 120
$(\mathrm{Er}_{\mathrm{max}}, \mathrm{Er}_{\mathrm{avg}})$ - Defined in page 120
$\Delta\langle\mathcal{T}_1\rangle$ - Defined in page 124
$\Delta\langle\mathcal{T}_1\rangle^{(4)}$ - Defined in page 127
$\langle\mathcal{T}_{4-\infty}\rangle$ - Defined in page 127
$(u_{\mathrm{ref}}, u_{\mathrm{inc}})$ - Defined in page 129

Chapter 5

$(\mathrm{AS}_k, \mathcal{Z}_k)$ - Defined in page 146

Appendices

$\widehat{c}_g$ - Defined in page 150
$\widehat{\mathfrak{N}}$ - Defined in page 150
$(\mathcal{W}, \mathcal{W}_u)$ - Defined in page 151
$(\widehat{\mathcal{H}}_{12}, \widehat{\mathcal{H}}_{16})$ - Defined in page 158
$(\widehat{D}/\widehat{D}t, \widehat{\Delta}_{2D})$ - Defined in page 158
Rsd - Defined in page 158

Chapter 1

Introduction

1.1 Motivation: Internal gravity waves' part in oceans and the Earth's climate

Meridional Overturning Circulation (MOC) is a system of ocean currents spanning thousands of kilometers transporting heat, salt, carbon, and nutrients to different parts of the ocean. A highly simplified schematic of MOC is given in figure 1.1. MOC is composed of surface currents, deepwater currents in the depths of the ocean, downwelling near the poles where the surface currents sink to form deepwater, and upwelling that brings the waters in the depths of the ocean back to the surface. Unlike the deepwater formation that is confined to the poles mostly, upwelling is spread throughout the ocean and is the most challenging part of MOC to model and quantify. The deepwater current that originates in the Nordic seas is known as the North Atlantic deep water, while the deepwater current that originates in the Southern Ocean is known as Antarctic bottom water. Interestingly, the deep water formation in the North-Pacific ocean is not as significant as in the Atlantic ocean (Talley, 2013). In the poles, the salinity of the water is lower in the pacific ocean compared to their counterparts in the north Atlantic ocean. As a result, even if the water is cooled significantly near the poles in the pacific ocean, it cannot sink to the depths of the ocean.

MOC influences the Earth's climate in many ways. In the North Atlantic Ocean, MOC transports approximately $18-20$ Sverdrups (1 Sverdrup is $10^6\,\mathrm{m}^3\mathrm{s}^{-1}$) of water (LeBel *et al.*, 2008; Frajka-Williams *et al.*, 2019) and 1.5 petawatts of heat towards the North pole

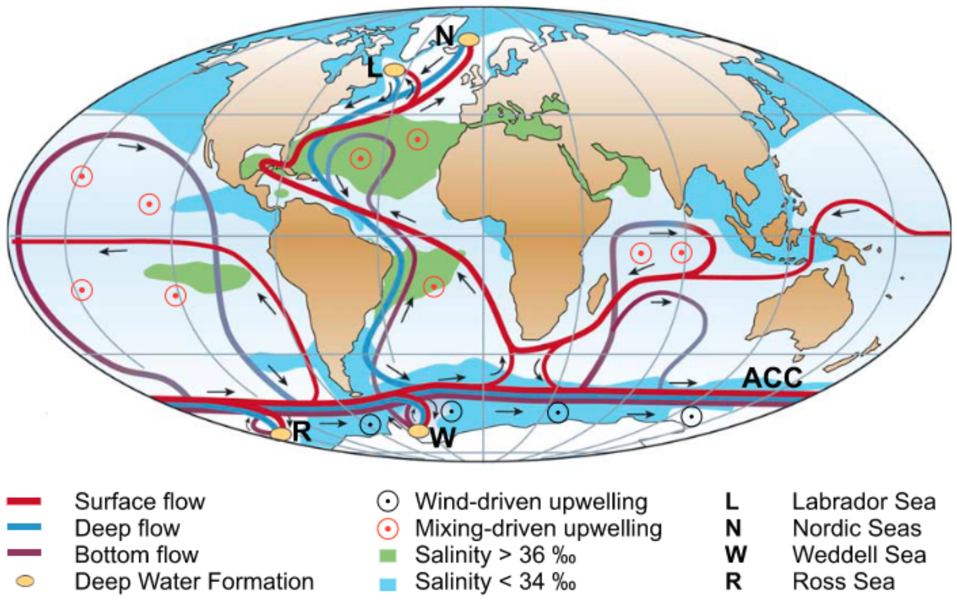

Figure 1.1: A simplified picture of MOC showing various surface currents, deepwater currents, and the locations of deep water formation (Kuhlbrodt *et al.*, 2007).

(Johns *et al.*, 2011). The heat transported by the MOC is a primary reason why Northwestern Europe is warmer than the zonal mean temperature of its latitude (Palter, 2015). Many global climate models show that MOC may weaken over the next few decades (Gregory *et al.*, 2005; Schmittner *et al.*, 2005). The weakening of MOC can instigate a change in rainfall patterns over the North Atlantic and tropics (Liu *et al.*, 2020). The slow down of the Atlantic branch of MOC can result in cooling of the Northern Hemisphere and can lead to an increase of sea ice in the Arctic because of the reduced heat advection (Vellinga & Wood, 2002; Liu *et al.*, 2020). A rise in the sea level can also occur with the weakening of MOC (Levermann *et al.*, 2005). The sea level is heavily linked to the Deep water formation in the Atlantic ocean. If the deep water formation in the North Atlantic is affected, then the ocean slowly warms up: this is because the deep water formation is a source of very cold water. Because of the increase in the temperature, water expands and hence sea level rises with it. Moreover, MOC also influences many currents in the oceans. Currents can play a huge role in increasing the local/regional sea level in some regions. Considering the crucial role MOC plays in the Earth's climate, modeling it accurately is necessary to reliably predict the climate of the Earth.

To properly model MOC, we need to understand what are the factors that drive MOC. Like all flows, MOC requires some external source of energy to counter the viscous effects/dissipation. Munk & Wunsch (1998) in their pioneering paper provide a rough estimate that approximately 0.4TWs is required to maintain MOC in its current state. There are multiple factors that drive MOC, and the three main contested factors are (1) temperature gradient in the sea surface because of the latitude-dependent heating of the sun, (2) mixing waters of different densities (diapycnal mixing), and (3) the wind stress acting on the sea surface. First, we begin with the temperature gradient. The surface water in the poles is colder than the surface waters near the equator, and horizontal temperature gradients are capable of creating fluid motion. However, it has been well established now that the temperature gradient alone cannot drive the MOC (Munk & Wunsch, 1998; Paparella & Young, 2002; Wang & Huang, 2005). The mechanical energy obtained from the sea surface temperature gradient is approximately 1.5GW, hence 1000 times lower than the value required (Wang & Huang, 2005). MOC transports 1-2 PWs of heat energy, however, the efficiency in converting this heat energy to mechanical energy is too low ($\sim 10^{-7}$). The efficiency is estimated by calculating the mechanical energy that is generated as a result of the temperature gradient on the surface. For oceanic parameters, Wang & Huang (2005) provide an estimate of around $1.5 \times 10^9 W$ generated due to surface temperature gradient by using the idealised horizontal convection model of (Paparella & Young, 2002). The heat energy carried by the currents in the ocean is approximately $2 \times 10^{15} W$. Hence the ratio of mechanical energy generated to the heat flux advected is $\approx 10^{-7}$. As a result, other factors (mixing and wind stress) are required for the sustenance of MOC.

Munk (1966) proposed internal waves (which can cause mixing) can be a potential source of the mechanical energy required to sustain the MOC. In most regions of the ocean, the density of the water increases with depth, and this variation is mainly because of salinity and temperature. Internal gravity waves are basically perturbations in a stably stratified fluid that can transport momentum and energy. Buoyancy acts as the restoring force for the internal waves. There are some similarities between surface gravity waves (which we readily observe in the ocean) and internal gravity waves. The surface waves exist in the air-water interface because of the sharp density difference between air and water. Similarly, internal waves exist in the bulk of the ocean due to a small but continuous density stratification. A huge portion of internal gravity waves in the ocean are generated by the tides (solar and lunar), pushing the density stratified water up and down the rough seafloor (Baines, 1973; Bell Jr., 1975; Balmforth *et al.*, 2002; Llewellyn Smith & Young, 2003), and a large part of these waves have very large length scales (O(10-100)km). As a result, the solar and lunar tides play a major role in sustaining MOC by generating internal waves. In general, in the thesis, by large length scales, we usually mean the waves' wavelength is in the order of kilometers. It is very difficult for a low amplitude internal wave to break and create turbulence when its wavelength is in the order of kilometers. As a result, the energy has to cascade to small length scales. A mode-1 internal wave typically has a vertical wavelength of 2 to 5kms and a horizontal wavelength of 20 to 50 km. Unlike the mode-1 internal wave, internal wave beams can have a width of only 0.5 kilometers which is much lower than what we see in a mode-1 wave. However, the length scales are still in the order of hundreds of meters to kilometers and the energy needs to cascade. However, care should be taken when classifying the internal wave beam length scale and a low mode's length scale. Energy in the large length scale internal waves eventually cascades to small length scales and causes turbulence that results in the mixing of warm water (less dense) with the cold water (denser) (Munk & Wunsch, 1998; Wunsch & Ferrari, 2004; Kuhlbrodt *et al.*, 2007). Such mixing causes a downward diffusion of heat which is balanced by the upwelling of the heavier water. Basically, mixing acts as an external source of potential energy. Note that the water that sinks at the poles (deepwater formation) has to be returned to the surface for an overturning circulation to exist. As a result, even though MOC is a flow that spans thousands of kilometers, it is still influenced/sustained by turbulent mixing that occurs at centimeter–meter length scale. Assuming a linear relationship between temperature and density of the water, to estimate the diffusivity value required to upwell the deep waters formed at the poles, Munk (1966) proposed a simplified model where, under steady state, the vertical turbulent diffusion of temperature is balanced by the advection of buoyancy. The simplified equation proposed was

$$w\frac{dT}{dz} = \frac{d}{dz}\left(\kappa\frac{dT}{dz}\right), \tag{1.1}$$

where w is the vertical velocity (or velocity in the direction of gravity), T is the temperature, and κ is the diffusivity. Using observed density profiles in the central Pacific Ocean and assuming uniform upwelling (constant w) throughout the ocean, it was estimated that $\kappa \approx 10^{-4}\mathrm{m}^2\mathrm{s}^{-1}$ is required to upwell 25 Sverdrups of water. Similar values for κ were obtained by Munk & Wunsch (1998) using zonally averaged density profiles. Note that $\kappa \approx 10^{-4}\mathrm{m}^2\mathrm{s}^{-1}$ is several orders of magnitude higher than the molecular diffusivity of heat which is $\approx 1.4 \times 10^{-7}\mathrm{m}^2\mathrm{s}^{-1}$. As a result, molecular diffusion on its own cannot upwell enough water to match the downwelling at the poles. Without increased diffusivity caused by turbulence, MOC in its current state cannot exist (Samelson & Vallis, 1997; Munk & Wunsch, 1998). Internal waves can contribute 0.6-0.9TW for mixing in the ocean (Munk & Wunsch, 1998). Internal waves forced by the semidiurnal tide are estimated to contain around 0.7TW (Vic *et al.*, 2019). As a result, considering the amount of energy internal waves possess, ocean mixing caused by them can heavily influence the large scale flows.

By now, we have established mixing plays an important role in sustaining MOC by providing potential energy. However, complexities arise in modeling MOC or any large length scale flow in the ocean with the effects of mixing. Large scale ocean models which are used to simulate and study MOC cannot resolve small scale turbulence without a tremendous increase in computational resources, which is not practical currently. As a result, the effects of turbulent mixing have to be parameterised and provided as an input to the ocean circulation models. Since turbulent mixing effectively results in the diffusion of heat into the ocean, the small scale turbulent motions are modeled as a local increase in the diffusivity of temperature/salt. Several studies and models show the state of MOC is sensitive to different parameterisations of diffusivity profiles. Meridional heat transport in the north Atlantic, sea ice in the Antarctic, and the strength of the overturning flow are sensitive to the background diffusivity value (Hieronymus *et al.*, 2019). Modeling MOC using a constant diffusivity value (higher than the molecular diffusivity) resulted in different circulation strength compared to the results obtained using an exponentially decaying diffusivity profile (Mashayek *et al.*, 2015). The ocean stratification predicted by the models varies as the diffusivity profiles are changed (Melet *et al.*, 2013). Simulations of the climate using an ocean–ice–atmosphere–land–biogeochemistry coupled model showed that the ocean state can be sensitive to the lateral (and vertical) mixing profiles (Melet *et al.*, 2016). Oka & Niwa (2013) show that the volume transport by the MOC in the pacific ocean is sensitive to far-field internal wave mixing parameterisations.

Considering the fact that internal waves are one of the most dominant factors that cause mixing in the ocean (St. Laurent *et al.*, 2002; Wunsch & Ferrari, 2004), we need to understand/know how much internal wave energy dissipates in which part of the ocean. Interestingly, a large portion of the internal waves does not get dissipated near the location where they are generated. St. Laurent *et al.* (2002) assume that $60 - 70\%$ of the internal waves generated by the tide-topography interactions propagate away from the topography. $75\% - 92\%$ of internal waves generated at Hawaiian Ridge radiates away (Klymak *et al.*, 2006). Observational studies using satellite altimetry show that internal waves with large length scales can travel for a long distance - $O(1000)$kms (Zhao *et al.*, 2016). Moreover, mode-1 waves near Hawaii have been observed to travel more than 1000 km (Ray & Mitchum, 1997). Mode-3 waves have been observed to travel up to 300 km in the Bay of Biscay (Pingree & New, 1995). Note that the percentage of internal waves' energy dissipated locally can vary by a wide margin depending on the specific topography. A numerical study on the internal wave generation in Luzon Strait shows that about 50% of the energy is lost locally (Jan *et al.*, 2008). To find the locations where the internal wave dissipates, the mechanisms that can cause energy cascade in the internal waves have to be understood so that we can 'track' the decay of the waves. The equations of motion used to model internal waves are presented in the next section. Moreover, the properties of internal waves and the most important mechanisms by which the energy in internal waves cascade to small length scales are explained.

1.2 Modeling internal gravity waves

To model internal waves and their related processes in the ocean, Navier-Stokes equations, along with the mass conservation equation are used. Note that we want to model waves whose time scales are similar to the tidal time scales (tides generate the waves). As a result, the effects of the Earth's rotation are considered, and the terms modeling the Coriolis effects are added to the Navier-Stokes equation. However, the sphericity of the Earth is not considered since the waves' length scale is not as large as the radius of the Earth. To this end, we study the governing equations in a Cartesian form on a plane tangent to the Earth's surface considering its simplicity. If we incorporate the above-mentioned conditions and simplifications, the governing equations in 3D would be

$$\rho\left(\frac{\partial u}{\partial t}+u\frac{\partial u}{\partial x}+v\frac{\partial u}{\partial y}+w\frac{\partial u}{\partial z}-fv+\tilde{f}w\right)=-\frac{\partial p}{\partial x}+\mu\Delta u \tag{1.2}$$

$$\rho\left(\frac{\partial v}{\partial t}+u\frac{\partial v}{\partial x}+v\frac{\partial v}{\partial y}+w\frac{\partial v}{\partial z}+fu\right)=-\frac{\partial p}{\partial y}+\mu\Delta v \tag{1.3}$$

$$\rho\left(\frac{\partial w}{\partial t}+u\frac{\partial w}{\partial x}+v\frac{\partial w}{\partial y}+w\frac{\partial w}{\partial z}-\tilde{f}u\right)=-\frac{\partial p}{\partial z}-\rho g+\mu\Delta w \tag{1.4}$$

$$\frac{\partial \rho}{\partial t}+u\frac{\partial \rho}{\partial x}+v\frac{\partial \rho}{\partial y}+w\frac{\partial \rho}{\partial z}+\rho\left(\frac{\partial u}{\partial x}+\frac{\partial v}{\partial y}+\frac{\partial w}{\partial z}\right)=0 \tag{1.5}$$

where x, y and z are the spatial coordinates in the zonal direction (along a constant latitude), meridional direction (along a constant longitude) and the direction normal to the earth's surface, respectively. (u, v, w) are the zonal (from east to west), meridional (from south to north) and vertical velocity, respectively. ρ is the total density, p is the pressure field, and μ is the dynamic viscosity of water. $f = 2\Omega\sin\theta_{\text{lat}}$ and $\tilde{f} = 2\Omega\cos\theta_{\text{lat}}$, where $\Omega \approx 7\times10^{-5}\text{s}^{-1}$ is the frequency of the Earth's rotation and θ_{lat} is the latitude at which the tangent plane is located. The operator Δ is defined as $\Delta \equiv \partial^2/\partial x^2 + \partial^2/\partial y^2 + \partial^2/\partial z^2$. In the oceans, the variation in density is only about 2.5% of the mean density (Mellor &

Ezer, 1995). As a result, the total density field can be split as

$$\rho = \rho_0 + \rho_{\text{base}}(z) + \rho'(x, y, z, t), \quad \text{where} \quad \rho_0 \gg \rho_{\text{base}} + \rho'. \tag{1.6}$$

ρ_0 is the mean density value ($\rho_0 \approx 1000\text{kgm}^{-3}$), $\rho_{\text{base}}(z)$ is the base density profile, and $\rho'(x, y, z, t)$ is the perturbation density. The small variation in the density allows us to use the Boussinesq approximation in the momentum equations. This approximation leads to a considerable simplification – density variations are only important in the gravity term. Moreover, using equation (1.6), the mass conservation equation at leading order reduces to (Vallis, 2017)

$$\frac{\partial u}{\partial x} + \frac{\partial v}{\partial y} + \frac{\partial w}{\partial z} = 0. \tag{1.7}$$

The traditional approximation for the rotational effects is used (Gerkema & J. Zimmerman, 2008), which basically assumes that $\tilde{f} = 0$. The approximation is reliant on the fluid flow (the internal waves) being nearly horizontal with large length scales (assuming the vertical motions are very small because of the suppression by the gravity/buoyancy effects). Note that traditional approximation depends on the length scale of the waves and not simply the domain height. This is because the domain height can be quite different from the scale of internal waves sometimes (for example, localised internal wave beams). Moreover, the traditional assumption also relies on the fact that in the vertical direction, hydrostatic balance is nearly satisfied. In this thesis, parameters are chosen such that the waves are nearly in hydrostatic balance. From here on, f is assumed to be constant, and this approximation is known as f-plane approximation. The simplified equations are then given by

$$\frac{\partial u}{\partial t} + u\frac{\partial u}{\partial x} + v\frac{\partial u}{\partial y} + w\frac{\partial u}{\partial z} - fv = -\frac{1}{\rho_0}\frac{\partial p'}{\partial x} + \nu\Delta u \tag{1.8}$$

$$\frac{\partial v}{\partial t} + u\frac{\partial v}{\partial x} + v\frac{\partial v}{\partial y} + w\frac{\partial v}{\partial z} + fu = -\frac{1}{\rho_0}\frac{\partial p'}{\partial y} + \nu\Delta v \tag{1.9}$$

$$\frac{\partial w}{\partial t} + u\frac{\partial w}{\partial x} + v\frac{\partial w}{\partial y} + w\frac{\partial w}{\partial z} = -\frac{1}{\rho_0}\frac{\partial p'}{\partial z} - \frac{\rho'}{\rho_0}g + \nu\Delta w \tag{1.10}$$

where $\nu \equiv \mu/\rho_0 \approx 10^{-6}\text{m}^2\text{s}^{-1}$ is the kinematic viscosity of water and p' is the perturbation pressure. $\bar{p}$ is the hydrostatic pressure, given by

$$\bar{p} = \int g(\rho_0 + \rho_{\text{base}})dz. \tag{1.11}$$

It balances the base density term in the vertical momentum equation. Note that we still need one more equation for closure. For simplicity, we assume that density of the water is only influenced by temperature, and a linear equation of state is used to relate density and temperature (T). Moreover, temperature is assumed to satisfy the advection-diffusion equation given by

$$\frac{\partial T}{\partial t} + u\frac{\partial T}{\partial x} + v\frac{\partial T}{\partial y} + w\frac{\partial T}{\partial z} = \kappa \Delta T. \tag{1.12}$$

Using a linear equation of state $\rho = \rho_0 + \mathcal{G}_T T$, where $\mathcal{G}_T$ is the thermal expansion coefficient, the evolution equation for the perturbation density is written as

$$\frac{\partial \rho'}{\partial t} + u\frac{\partial \rho'}{\partial x} + v\frac{\partial \rho'}{\partial y} + w\frac{\partial \rho'}{\partial z} + w\frac{d\rho_{\text{base}}}{dz} = \kappa \Delta \rho' + \kappa \frac{d^2\rho_{\text{base}}}{dz^2} \tag{1.13}$$

The final set of equations are (1.7)–(1.10) along with (1.13).

To understand the properties of internal waves, the dispersion relation for linear internal waves is derived. We assume a 2D case ($\partial/\partial y = 0$) from here on for simplicity. Even though $\partial/\partial y = 0$, the $y-$momentum equation is still strongly linked with the other equations through the Coriolis term. To derive the dispersion relation, the nonlinear advection terms are assumed to be very small compared to the linear terms, and they are neglected. In oceans, the waves usually have a length scale in the order of kilometers with a typical amplitude of 0.1ms^{-1}. The Reynolds number ($Re \equiv UL/\nu$) for large length scale waves would typically be greater than 10^8. Hence, the viscous terms are also not considered. Finally, we define buoyancy b as $b \equiv -g/\rho_0 \rho'$ to simplify the governing equations. Note that positive (negative) buoyancy means the water parcel experiences an upward (downward) force. After the simplification, the linearised equations read as

$$\frac{\partial u}{\partial t} - fv = -\frac{1}{\rho_0}\frac{\partial p'}{\partial x} \tag{1.14}$$

$$\frac{\partial v}{\partial t} + fu = 0 \tag{1.15}$$

$$\frac{\partial w}{\partial t} = -\frac{1}{\rho_0}\frac{\partial p'}{\partial z} + b \tag{1.16}$$

$$\frac{\partial b}{\partial t} + N^2 w = 0 \tag{1.17}$$

$$\frac{\partial u}{\partial x} + \frac{\partial w}{\partial z} = 0 \tag{1.18}$$

Where N^2 is the square of the Brunt–Väisälä frequency, and is given by

$$N^2(z) \equiv -\frac{g}{\rho_0}\frac{d\rho_{\text{base}}}{dz}. \tag{1.19}$$

N^2 provides a measure of how rapidly the base density varies with the depth. For a stably stratified fluid, N^2 is always positive. If N^2 is negative, it means heavier fluid is on top of a lighter fluid which usually leads to Rayleigh-Taylor instability. In this thesis, N^2 is always taken to be a positive quantity. Moreover, base density is assumed to vary only in the direction of gravity (ρ_{base} is strictly a function of z). However, in nature, density can vary in the horizontal directions as well (for example, density fronts), but that is not the focus of this thesis.

Now assuming $(d\psi/dz, -d\psi/dx) = (u, w)$, equations (1.14)–(1.18) can be reduced to a single equation in terms of ψ. The linear streamfunction evolution equation is given by

$$\frac{\partial^2}{\partial t^2}\left(\frac{\partial^2\psi}{\partial x^2} + \frac{\partial^2\psi}{\partial z^2}\right) + N^2(z)\frac{\partial^2\psi}{\partial x^2} + f^2\frac{\partial^2\psi}{\partial z^2} = 0 \tag{1.20}$$

N is taken as a constant for simplicity, and an unbounded fluid domain is taken. Under such conditions, we consider ψ to be of the normal mode form:

$$\psi = \psi_0 \exp\left[\mathrm{i}(kx + mz - \omega t)\right], \tag{1.21}$$

where ψ_0 is simply a constant. (ω, k, m) are the frequency, horizontal wavenumber, and the vertical wavenumber of the wave, respectively. Substituting (1.21) in (1.20) leads to the dispersion relation of 2D internal waves

$$\omega^2 = \frac{N^2k^2 + f^2m^2}{k^2 + m^2} = \frac{N^2(k/m)^2 + f^2}{(k/m)^2 + 1} \tag{1.22}$$

Hence for propagating internal waves, the condition $f < \omega < N$ has to be satisfied. Note that propagating internal wave solutions are also possible if $f > \omega > N$ is satisfied. However, in this thesis, we mainly focus on the parameter regime: $f < \omega < N$. A very interesting property of internal waves is that a single frequency can have an infinite number of wavevectors as solutions of equation (1.22). Only the direction of the wavevector is decided by the frequency. Moreover, for a given $|k|$ and $|m|$, the wave can propagate in four different directions. This is shown in figure 1.2.

The phase speed for a 2D internal wave is given by

$$c_x^p = \frac{\omega k}{k^2 + m^2} \qquad c_z^p = \frac{\omega m}{k^2 + m^2} \tag{1.23}$$

where c_x^p and c_z^p denote the horizontal and vertical phase speed, respectively. The horizontal and vertical group speed (denoted by c_x^g and c_z^g, respectively) for an internal wave are given by

$$c_x^g = \frac{\partial \omega}{\partial k} = \frac{k\,(N^2 - \omega^2)}{\omega(k^2 + m^2)} \qquad c_z^g = \frac{\partial \omega}{\partial m} = -\frac{m(\omega^2 - f^2)}{\omega(k^2 + m^2)} \tag{1.24}$$

Another interesting property for internal waves is that if the phase speed vector points upward (downward), then the group speed vector points downward (upward) as shown in figure 1.2.

A plane internal wave's steepness is defined as the ratio of vertical gradient of buoyancy perturbation ($\partial b/\partial z$) to the square of buoyancy frequency (N^2). Mathematically, this can be expressed as (for $f = 0$) (Koudella & Staquet, 2006),

$$\mathrm{S}^{(P)} = \frac{\psi_0 m k}{\omega} = \frac{\psi_0 m \sqrt{(k^2 + m^2)}}{N} \tag{1.25}$$

Note that ψ_0 is the stream function amplitude. For $\mathrm{S}^{(P)} = 1$, the isopycnals in the fluid medium become vertical at some locations. This means that the wave can cause convective overturning because it essentially brings a heavier fluid parcel on top of a lighter fluid parcel. $\mathrm{S}^{(P)}$ is often used as a measure of nonlinearity of the wave.

Before we learn more about internal waves, a brief detour is taken to introduce the other most predominant wave in the oceans: near-inertial waves. Near-inertial waves are basically internal waves whose frequency is very close to the inertial frequency f. Note that as $\omega \to f$, $k \to 0$ in equation (1.22) thus implying that the horizontal length scales of near-inertial waves is several orders of magnitude higher than the vertical length scales. Near-inertial waves also play a major role in the ocean's energy budget and are predominantly generated by the wind stress acting on the sea surface (Alford *et al.*, 2016).

The Internal waves we intend to study in this thesis are of low amplitude/steepness, and their nonlinear effects are not very high. However, the ocean contains nonlinear internal waves that exist within the fluid. Here we also provide a brief introduction to the internal solitary waves (also known as solitons) which are nonlinear internal waves that exist because of the balance between the steepening and the dispersion effect. Solitary

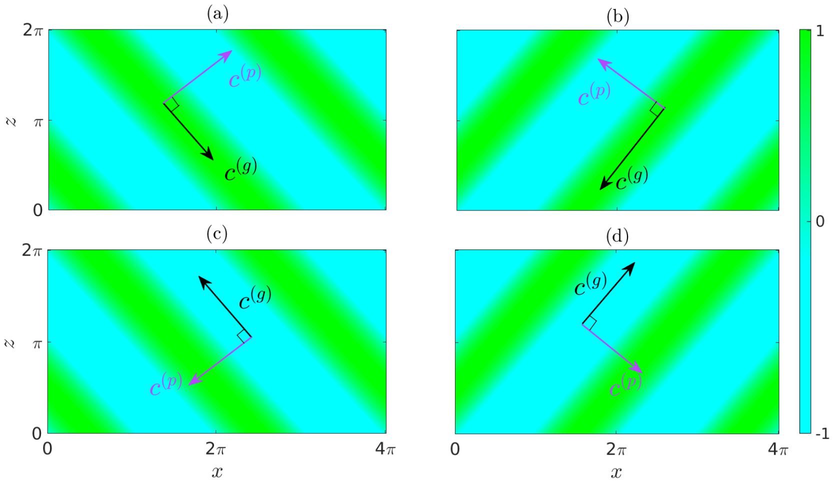

Figure 1.2: Streamfunction contours of an internal wave, where the green and blue regions respectively show the crest and trough. For a given $|k|$ and $|m|$, the four different phase speed directions and the corresponding group speed directions are shown. The wavevector of the internal waves are as follows: (a) $(|k|, |m|)$, (b) $(-|k|, |m|)$, (c) $(-|k|, -|m|)$ and (d) $(|k|, -|m|)$.

waves are quite common in the ocean, and are usually found in coastal areas/continental shelves. For example, solitary waves have been observed in the North China Sea (Duda *et al.*, 2004) and the Australian North West Shelf (Van Gastel *et al.*, 2009). These waves typically exist within the fluid as a large dip/elevation of isopycnals. Solitary waves can generate strong shear as they propagate, which in turn can cause instabilities (like Kelvin-Helmholtz) thus producing elevated turbulent dissipation and mixing (Carr *et al.*, 2015; Fructus *et al.*, 2009).

1.2.1 Vertically Bounded Domain

The water in the ocean is bounded in the vertical direction by the ocean floor at the bottom and the air-sea surface at the top. Hence it would be insightful to understand how the dispersion relation changes for a vertically bounded domain. For simplicity, we assume that the ocean's bottom surface is flat. Moreover, we also assume that the air-water interface can be modeled as a rigid, free-slip boundary (Gerkema & J. Zimmerman, 2008). Typically, the internal waves inside the bulk of the ocean can easily have large amplitudes (>10 meters) because the density stratification is very small. However, the same wave does not possess enough energy to displace the air-water surface where the density difference is several orders of magnitude higher. As a result, internal waves that are generated inside the ocean have a very weak surface presence and are approximated well using the rigid-lid approximation. The assumptions would mean that $\psi = 0$ at the top and bottom surface thus enforcing the impenetrability condition. The coordinate system is chosen such that the top and bottom surfaces are located at $z = 0$ and $z = -H$, respectively, where H is the depth of the ocean. Here, the analysis is not limited to a constant N. Assuming $\psi = \phi(z) \exp\left[\mathrm{i}(kx - \omega t)\right]$ and substituting it in (1.20) results in

$$\frac{d^2\phi}{dz^2} + k^2 \frac{N^2(z) - \omega^2}{\omega^2 - f^2}\phi = 0. \tag{1.26}$$

Equation (1.26) with boundary conditions $\phi = 0$ at $z = 0$ and $-H$ is actually a Sturm-Liouville eigenvalue problem. Equation (1.26) admits countably infinite solutions (unlike the unbounded domain, where the solution set is uncountably infinite) or 'modes' for a single frequency ω. The eigenvalues are $\pm k_n$, where n is a positive integer. The word 'mode' is used because, in a bounded domain, the vertical structure of the streamfunction (ϕ_n) can be seen as different modes of vibration similar to a taut string held at both ends. Moreover, the pair $\pm k_n$ has a unique eigenfunction ϕ_n which satisfies (1.26). Physically, the positive and negative eigenvalues model waves that propagate towards x and $-x$, respectively. For uniform stratification (N being constant), the solution of equation (1.26) is analytically derivable. The solution is given by:

$$\phi_n = \sin\left(m_n z\right), \qquad m_n = \pm\frac{n\pi}{H}, \qquad k_n = \pm\frac{n\pi}{H}\sqrt{\frac{\omega^2 - f^2}{N^2 - \omega^2}} \tag{1.27}$$

where ϕ_n is the $n-$th mode, and (k_n, m_n) are the $n-$th mode's horizontal and vertical wavenumber, respectively. Note that m_n is independent of (ω, f, N). In general, the solution for (1.26) has to be obtained numerically for non-uniform stratifications. For a non-constant N, some examples of mode shapes are given in figure 1.3(a), and the stratification profile used in constructing those mode shapes is given in 1.3(b). This profile of buoyancy frequency is commonly used in literature as a substitute for realistic N profiles. Wentzel–Kramers–Brillouin method (WKB method) can be used to solve equation (1.26) for a vertically varying stratification (Smith & Young, 2002; Echeverri *et al.*, 2009). However, the method has a high accuracy only when the vertical wavelength of the wave is much smaller than the length scale of buoyancy frequency variation (Mathur *et al.*, 2016).

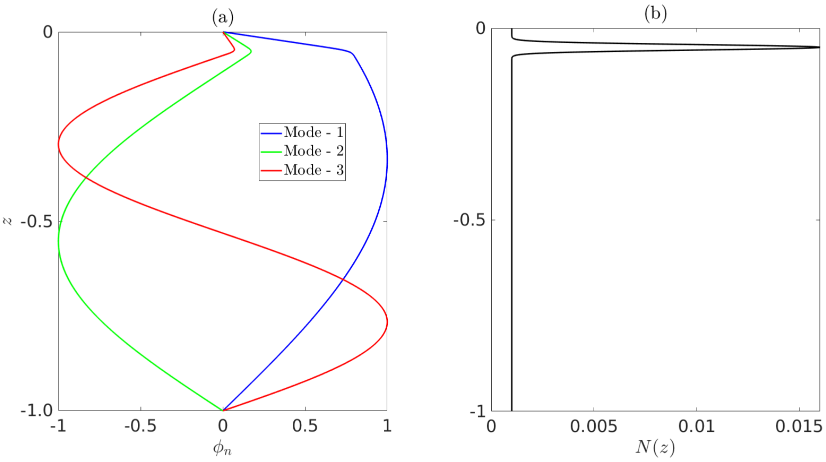

Figure 1.3: (a) The vertical mode shape (ϕ) of modes 1,2 and 3. (b) The corresponding background stratification profile used in constructing the modes given in (a).

1.2.2 Orthogonality

Equation (1.26), being a Sturm-Liouville boundary value problem, has eigenfunctions that form an orthogonal basis. The orthogonality property is as follows:

$$\int_{-H}^{0} \frac{N^2-\omega^2}{\omega^2-f^2}\phi_m\phi_n dz = \delta_{m,n} \tag{1.28}$$

The proof for the above condition is not given here, however, it is easily derivable (Gerkema & J. Zimmerman, 2008). The above property is often used in identifying the spectrum of internal waves.

1.3 Mechanisms that cause the energy cascade in internal waves

The primary mechanisms that cause the energy in internal gravity waves to cascade to small length scales are wave-wave interactions, wave-topography interactions, and wave-mean flow interactions. A simplified schematic of the three mechanisms is shown in figure 1.4. Once small length scale waves are formed because of these interactions, wave-breaking will occur due to convective overturning or shear instabilities (Koudella & Staquet, 2006; Sutherland, 2010). Convective overturning and shear instabilities are highly

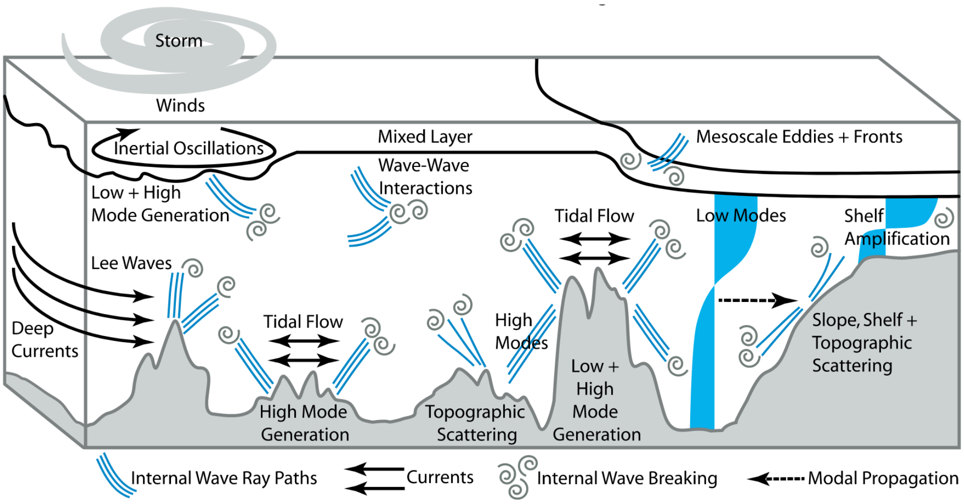

Figure 1.4: Various processes that can cause internal wave energy cascade: wave-wave interactions, wave-topography interactions, and wave-mean interactions (MacKinnon *et al.*, 2017).

nonlinear processes that cause mixing. A brief explanation of the wave-wave interactions, wave-topography interactions, and wave-mean flow interactions are given below.

1.3.1 Wave-wave interactions

In wave-wave interactions, a wave with a large amount of energy (often referred to as the parent wave) ‘slowly’ transfers its energy to secondary (daughter) waves with different frequencies and/or wavelengths. By ‘slowly’, it is meant that the rate of energy transfer occurs at a much slower rate compared to the frequency of the waves. The daughter waves often have infinitesimal energy at the beginning of the process. Moreover, the process is ‘weakly’ nonlinear. This means that the nonlinear terms are necessary for the energy transfer, however, the magnitude of the nonlinear terms is not as large as the linear terms given in equations (1.14)–(1.17). Note that since the process is reliant on nonlinear terms, the rate of energy transfer depends on the amplitude of the waves. A wave with large length scale can provide its energy to a wave with small length scales. A simple image of wave-wave interactions distorting a mode-1 internal wave is shown in figure 1.5. At $t = 0$, a mode-1 internal wave structure can be seen. At $t = t_{end}$, the structure is clearly different because there are multiple waves present in the system and all of them were forced by the mode-1 wave. More details on wave-wave interactions are provided in chapters 2 and 3.

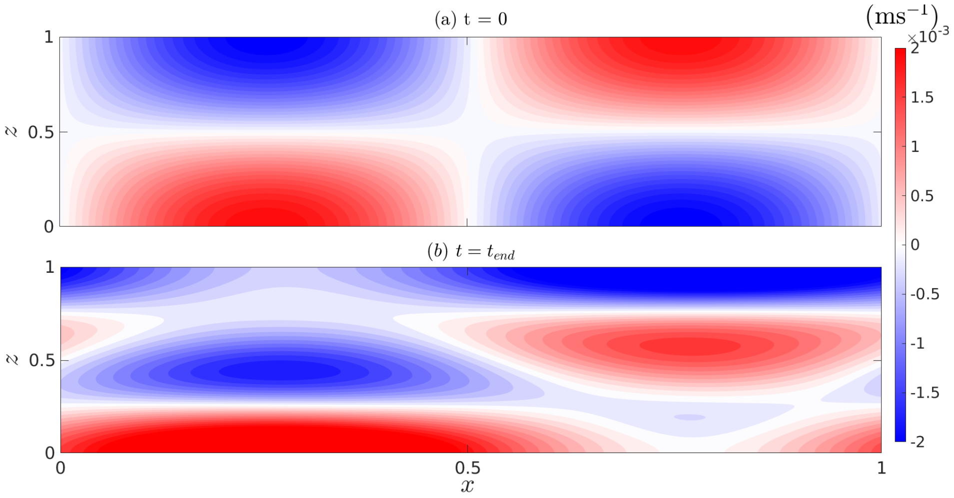

Figure 1.5: (a) Horizontal velocity field of a mode-1 internal gravity wave at $t = 0$. (b) Horizontal velocity field consisting of multiple waves. The waves, other than mode-1, were resonantly forced via wave-wave interactions.

1.3.2 Wave-topography interactions

When an internal wave encounters a solid obstacle in its path, the ensuing refraction and/or reflection of the wave may result in energy cascade. An internal wave mode encountering a topography (which is a solid obstacle) in its path can lead to wave ‘scattering’, where a mode-1 wave gives its energy to mode-2,3 and so on. A simple schematic of the mechanism is shown in figure B.4. A mode-1 internal wave comes from the left side of the domain, encounters a topography, and gets scattered. The scattering results in the generation of multiple modes that have smaller wavelengths than the incoming mode-1. The resulting wave field often manifests in the form of a beam-like structure. An internal wave beam is basically a superposition of multiple internal modes (Gerkema & J. Zimmerman, 2008). Unlike wave-wave interactions, the mechanism here is linear and can occur without the nonlinear advection terms in the Navier-Stokes equation. Note that just because wave-topography interactions can occur without the advection terms does not mean the advection terms may not be important. For incoming waves with large amplitude, advection terms are crucial to model the physics accurately. In the oceans, low mode internal waves are attenuated by wave-wave interactions more compared to wave-topography interactions (de Lavergne *et al.*, 2019, 2020). More details on wave-topography interactions are provided in chapter 4.

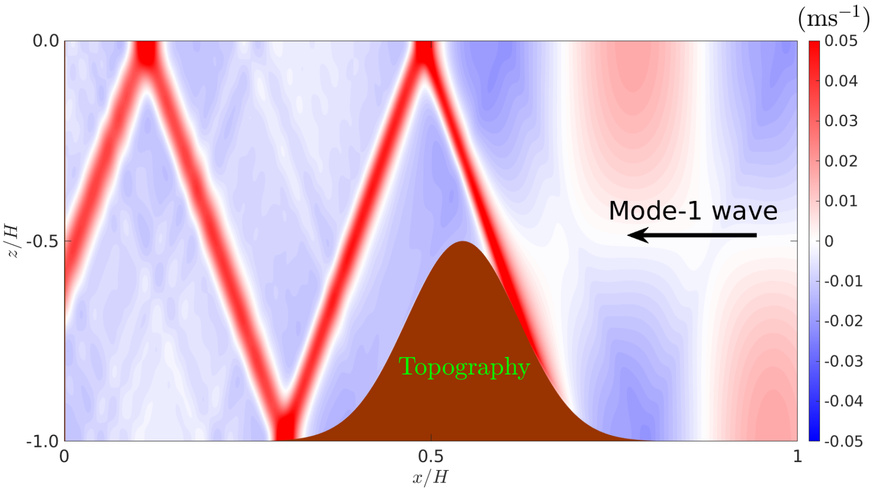

Figure 1.6: Mode-1 scattering by a topography. A mode-1 wave enters the domain from the right side and impacts the topography resulting in a beam like structure.

1.3.3 Wave-mean flow interactions

Wave-mean interactions play a crucial role in the waves' energy cascade. However, this physics is not studied in detail in this thesis. Nevertheless, a brief introduction to wave-mean interactions is provided here. Wave-mean interaction is a process where the wave interacts with a flow that does not change much with time (the time scale of the mean flow is much larger than the time scale of the wave itself). Some examples of mean flows in the ocean are mesoscale eddies (horizontal length scales around ≈ 100km) and currents. The ocean has an abundance of mesoscale eddies that are in geostrophic balance. Interaction of an internal wave with barotropic balanced motions (eddies that do not vary in the vertical direction) can cause horizontal isotropisation of the internal wave (Wagner *et al.*, 2017; Savva & Vanneste, 2018). If the balanced motions vary in the vertical direction, they can cause an energy cascade in the internal waves. The higher wavenumbers generated by the interaction will also have the same frequency (Dunphy & Lamb, 2014; Dunphy *et al.*, 2017; Kafiabad *et al.*, 2019; Savva *et al.*, 2021). The physics is similar to wave-topography interactions. However, scattering by time-varying mean flows will lead to the scattered waves having different frequencies (Dong *et al.*, 2020). Mesoscale eddies are one of the main reasons for energy cascade in the near-inertial waves (Perkins, 1976; Kunze, 1985; Whalen *et al.*, 2018) as well. The eddies reduce the horizontal length scales of the near-inertial waves and channel them to the depths of the ocean where the waves can cause mixing. Interestingly, the near-inertial waves can also drain the eddies' energy and transport it to the depths of the ocean (Barkan *et al.*, 2021). Jets/currents can create horizontal variations in the background density field, which are referred to as geostrophic fronts. An internal wave interacting with geostrophic fronts may get scattered (Kelly & Lermusiaux, 2016; Li *et al.*, 2019).

1.4 Problems addressed in this thesis

The rest of the thesis is dedicated to understanding the mechanisms that cause the energy in internal waves to cascade to small length scales. As mentioned previously, many processes lead to internal waves' energy cascade, and the thesis primarily focuses on wave-wave interactions and wave-topography interactions, which are two of the most important mechanisms. A brief summary of the different problems addressed in this thesis is provided below.

1.4.1 Resonant and near-resonant internal wave triads in a vertically bounded domain with mild-slope bathymetry

The mode-1 internal wave can travel a very long distance (O(1000)km) in the ocean. Moreover, the ocean depth may not be constant for the entire journey of the mode-1 wave. In chapter 2, the effect of slowly varying fluid depth on wave-wave interactions of the mode-1 wave is studied. The non-constant fluid depth changes the properties of the internal waves, specifically, the wavenumber and the modal shape. Higher order self-interaction of a mode-1 internal wave in the presence of a monochromatic, small-amplitude topography is also investigated.

1.4.2 5-wave interactions in internal gravity waves

In this chapter, we focus on the stability of two parent waves that coexist in a region without directly interacting with each other. The motivation for this study stems from the fact that in the oceans, multiple parent waves travel in the midst of each other. The specific focus is on 5-wave interactions that consist of two parent waves and three daughter waves. Assuming both parent waves have the same frequency and wavevector norm, for different parent wave vector orientations/directions, the growth rates of the 5-wave system are calculated. Moreover, the conditions in which the 5-wave system instability is faster than the 3-wave system instability are identified.

1.4.3 Topographic scattering of internal waves in the presence of a steady surface current

Surface currents are ubiquitous in the ocean, and internal waves frequently travel in the presence of a current. In this chapter, the effect of a steady, stable surface current on the scattering of a mode-1 internal wave by topography is studied. The current is assumed to have a non-zero velocity only near the surface, and its amplitude in the depths of the oceans is taken to be zero. Hence, the current is a vertically varying stable shear flow (Richardson number $(N^2/(\partial u/\partial z)^2)$ is always greater than 1/4.) In the presence of a current, the mode-1 wave with a positive phase speed has different properties compared to the mode-1 wave that has a negative phase speed. The scattering of both mode-1 waves (positive and negative phase speeds) is explored. The amplitude of the incoming waves is chosen to be low so that the physics is almost in a linear regime. The influence of the current on scattering of internal waves by topographies with different heights and widths is analysed in detail.

Chapter 2

Resonant and near-resonant internal wave triads in a vertically bounded domain with mild-slope bathymetry

This chapter is a modified version of the work published in Gururaj & Guha (2022), ”Resonant and near-resonant internal wave triads for non-uniform stratifications. part 2. vertically bounded domain with mild-slope bathymetry. J. Fluid Mech. 943, A33.”

This chapter also consists of a very small portion of the work published in Gururaj & Guha (2020), ”Energy transfer in resonant and near-resonant internal wave triads for weakly non-uniform stratifications. Part 1. Unbounded domain. J. Fluid Mech. 899, A6.”

2.1 Introduction

An internal gravity wave can become unstable via resonant triadic wave-wave interactions if it has the largest frequency in a triad (Hasselmann, 1967); through this mechanism, energy is irreversibly transferred from a high frequency primary (parent) wave to lower frequency secondary (daughter) waves. In a triad, a wave of angular frequency ω_3 and wavevector $\mathbf{k}_3$ (parent wave) can resonantly transfer its energy to two ‘daughter’ waves when both specific wavevector and frequency conditions are met between the parent waves and the daughter waves (Davis & Acrivos, 1967; Thorpe, 1966; Hasselmann, 1967; Phillips, 1977). The ‘triad’ conditions are given by

$$\mathbf{k}_3 = \mathbf{k}_1 + \mathbf{k}_2, \quad \text{and} \quad \omega_3 = \omega_1 + \omega_2. \tag{2.1}$$

where $\mathbf{k}_j = (k_j, l_j, m_j)$ is the wavevector of the $j-$th wave. Daughter waves are denoted by subscripts 1,2. The conditions are a consequence of the quadratic nonlinearity of the Navier-Stokes equations. Moreover, for resonance, all three waves in a triad should satisfy the dispersion relation. In the triad instability, amplitudes of the daughter waves’ grow exponentially with time, while the total energy is conserved between the three waves. Compared to the parent wave’s wavevector norm/magnitude, the daughter waves can have a higher or a lower wavevector norm. We would like to make a small explanation on the difference between ‘Triadic Resonant Instability’ and ‘Triadic Resonant Interaction’. Triadic Resonant Instability is often used for cases where we study the stability of a single parent internal gravity wave. In this case, the daughter waves’ energy at the initial times is often negligible compared to the parent waves’ energy. Triadic Resonant Interaction is a broader name that is used to denote the interaction of 3 internal waves that satisfy the triad conditions. Unlike Triadic Resonant Instability where two daughter waves’ energy at the initial times is negligible, there is no restriction on the amplitude of waves involved in the interaction. Triadic Resonant Instability can be seen as a subset of Triadic Resonant Interaction.

As a consequence of different conditions (triad conditions and dispersion relation) that need to be satisfied by the daughter waves, not all waves can be a part of a triad involving given parent wave. Using the constraints imposed by equations (1.22) and (2.1), for a given (ω_3, k_3, m_3) (hence a particular parent wave), all possible triads can be found by solving (Richet *et al.*, 2018)

$$s_3 \underbrace{\sqrt{\frac{N^2k_3^2 + f^2m_3^2}{(k_3^2 + m_3^2)}}}_{\omega_3} = s_1 \underbrace{\sqrt{\frac{N^2k_1^2 + f^2m_1^2}{(k_1^2 + m_1^2)}}}_{\omega_1} + s_2 \underbrace{\sqrt{\frac{N^2(k_3 - k_1)^2 + f^2(m_3 - m_1)^2}{(k_3 - k_1)^2 + (m_3 - m_1)^2}}}_{\omega_2}. \tag{2.2}$$

where s_j can be 1 or -1, and is used to represent the signs of each term. Note that in equation (2.1), either $|\omega_1| = |\omega_2| + |\omega_3|$, or $|\omega_3| = |\omega_2| + |\omega_1|$, or $|\omega_3| = |\omega_2| + |\omega_1|$ can be satisfied. However, in equation (2.2) we need the s_j terms to allow that same freedom because the square root terms are always strictly positive. Without the s_j term, $|\omega_3| = |\omega_2| + |\omega_1|$ would be strictly enforced in equation (2.2). We have to find (k_1, m_1) which satisfy equation (2.2). The equation is solved for different values of ω_1 such that

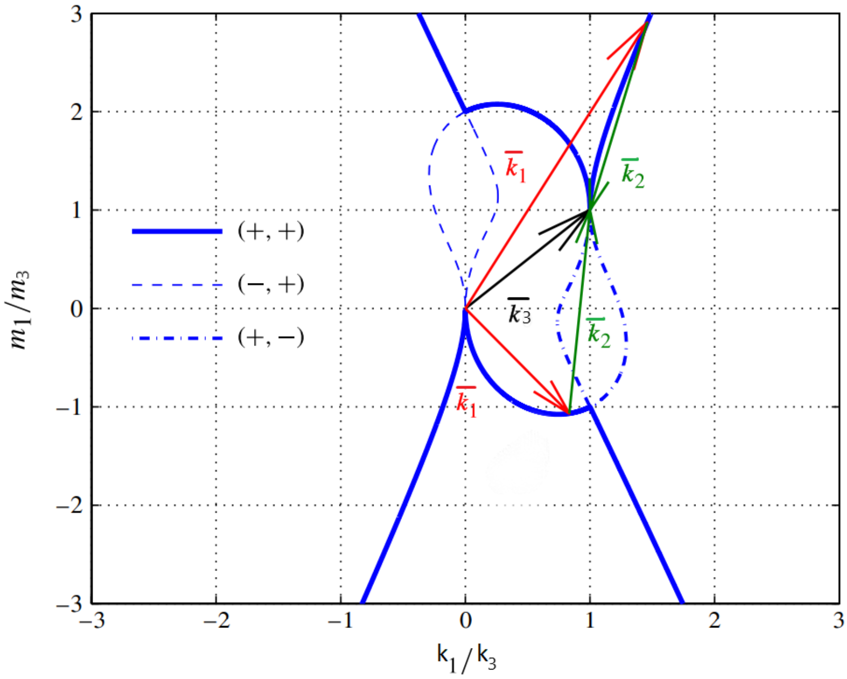

Figure 2.1: The possible triad solutions (Bourget *et al.*, 2013). $f = 0$ was taken. Wave indices have been edited to match the notations used in this thesis. The bar variables are used to denote vectors.

$\omega_1 \in (f, \omega_3 - f)$. By fixing ω_1, the relationship between k_1 and m_1 is fixed because of the internal waves' dispersion relation. As a result, there are two different parameters (ω_1 and k_1) that have to spanned to get all possible solutions of the equation. $s_3 = 1$ is assumed without losing any generality. The solutions for equation (2.2) is given in figure 2.1 for different s_1, s_2 values. The figure uses $k_3 = m_3 = 1$ for the parent wave. Moreover, the two green and red arrows show two specific example of daughter waves combinations that are possible for the given parent wave. The primary focus is generally given to the $(+,+)$ curve in the figure which is obtained by setting $s_1 = 1$ and $s_2 = 1$. Note that if $s_1 = s_2 = 1$, both terms on the RHS of equation (2.2) are positive quantities. Hence, every point on this curve satisfy the Hasselmann (1967) instability condition (both daughter waves' frequencies should be lower than the parent wave's frequency). The growth rate of the daughter waves depends on their frequencies and wavevectors.

Stability of a single internal gravity plane wave has been studied extensively in the past few decades. 2D instability analysis is sufficient for parent/primary waves with small amplitude or 'steepness', (Klostermeyer, 1991), where a plane internal wave's steepness is defined as the ratio of horizontal velocity amplitude to the horizontal phase speed. Mathematically, this can be expressed as (for $f = 0$) (Koudella & Staquet, 2006),

$$\mathrm{S}^{(P)} = \frac{\psi_0 mk}{\omega} = \frac{\psi_0 m\sqrt{(k^2 + m^2)}}{N} \tag{2.3}$$

where ψ_0 is the stream function amplitude. $\mathrm{S}^{(P)}$ is often used as a measure of nonlinearity of the wave. The most unstable daughter wave combination for a small amplitude parent wave varies with ω_3/N (Sonmor & Klaassen, 1997), kinematic viscosity (ν) (Bourget *et al.*, 2013, 2014) and Coriolis frequency (f) (Young *et al.*, 2008; Maurer *et al.*, 2016). Without rotational effects and under inviscid conditions, for $\omega_3/N < 0.68$, the most unstable subharmonic daughter wave combination satisfies $|\mathbf{k}_1| < |\mathbf{k}_3| < |\mathbf{k}_2|$(Sonmor & Klaassen, 1997). However, for $\omega_3/N > 0.68$, the most dominant instability satisfies $|\mathbf{k}_3| \ll |\mathbf{k}_2| \approx |\mathbf{k}_1|$. This instability is called as Parametric Subharmonic Instability (PSI) (MacKinnon & Winters, 2005; Young *et al.*, 2008). PSI is a specific type of triad interaction where $\omega_2 \approx \omega_1 \approx \omega_3/2$. In the oceans, viscosity has very little effect on large length scale waves. However, in laboratory conditions, viscosity can play a major role in deciding the type of triad because viscosity hinders daughter waves with larger wavenumbers more compared to waves with smaller wavenumbers (Bourget *et al.*, 2013). Viscosity can affect PSI significantly because the daughter waves can have very high wavenumbers in PSI. Instability of finite amplitude parent internal waves ($\mathrm{S}^{(P)} > 1$) is a 3 dimensional process (Klostermeyer, 1991; Lombard & Riley, 1996; Ghaemsaidi & Mathur, 2019). Throughout this thesis, the focus is on weakly nonlinear interactions, that is interactions where the wave almost behaves as a linear wave while its amplitude is slowly modified.

Rotational effects can be very important for triadic interactions. MacKinnon & Winters (2005) conducted numerical simulations where a semidiurnal mode-1 internal wave, starting near the equator, was forced to propagate towards the North pole. The internal wave lost a significant amount of energy near the 'critical' latitude (28.9°), where the near-inertial waves' frequency (f) is exactly half of the semidiurnal internal tide's frequency. Mathematically this is given by:

$$f_{28.9^\circ} \approx 0.7 \times 10^{-4}\mathrm{s}^{-1} = \omega_d/2 \tag{2.4}$$

Here $\omega_d = 1.4 \times 10^{-4}\mathrm{s}^{-1}$ is the semidiurnal frequency. The energy flux of the mode-1 wave dropped by 60% in the vicinity of the critical latitude, and the reason for the energy loss was concluded to be Parametric Subharmonic Instability (PSI). The significant decay of the internal wave observed by MacKinnon & Winters (2005) was not noticed in an observational study conducted by Alford *et al.* (2007). Rather a dissipation of around $10 - 20\%$ of the internal wave energy was estimated. Numerical simulations conducted by Hazewinkel & Winters (2011) agree broadly with Alford *et al.* (2007) (the dissipation of the mode-1 tide was reduced to $\approx 15\%$). Using multiple scale analysis, Young *et al.* (2008) provides an e-folding time of approximately nine days for a mode-1 internal wave near the critical latitude. A similar e-folding time was also observed in a numerical simulation of Hazewinkel & Winters (2011). Near the critical latitude, the inertial daughter waves have very small vertical length scales which can lead to increased kinetic energy dissipation (Yi *et al.*, 2017; Richet *et al.*, 2017, 2018). Moreover, when semidiurnal internal wave modes interact with an ambient wave field that follows Garrett-Munk spectrum, their decay is fastest near the critical latitude (Hibiya *et al.*, 1998; Onuki & Hibiya, 2018; Olbers *et al.*, 2020).

Poleward of the critical latitude, the decay of the parent wave cannot be instigated by small amplitude daughter waves. The reason is, for propagating internal waves, $\omega_j > f$ is needed. However, when $f > \omega_d/2$, the conditions $\omega_1, \omega_2 > f$ and $\omega_1 + \omega_2 = \omega_d$ cannot be satisfied simultaneously. Note that for a semidiurnal parent internal wave with frequency $\omega_3 = \omega_d$, equation (2.1) and $\omega_1 > f$ and $\omega_2 > f$ cannot be simultaneously satisfied. For example, assume $f = 0.6\omega_d$. Then both ω_1 and ω_2 should be greater than $0.6\omega_d$ so that waves-1 and 2 are propagating waves. However, if both ω_1 and ω_2 are greater than $0.6\omega_d$ then $\omega_1 + \omega_2 \neq \omega_d$. Hence triad condition is violated. Interestingly, a little poleward of the critical latitude the resonant triads can still exist and the parent wave can decay by those triads (Young *et al.*, 2008). For example, the growth rates at $f = 0.75 \times 10^{-4}\text{s}^{-1}$ are comparable to the growth rates at critical latitude. This was observed in numerical simulations conducted by Richet *et al.* (2018) as well. This is because even though resonant triads cannot be formed poleward of the critical latitude, near-resonant triads can still be formed. Provided the detuning is not significant, energy transfer will still occur. Note that detuning monotonically increases as f is increased from $\omega_d/2$. Hence energy transfer is also reduced monotonically as f is increased and at one point becomes the transfer becomes very weak.

For constant N, triads in a vertically bounded domain are qualitatively similar to the plane wave triads. One important distinction comes in the possible triad solutions. In a bounded domain, the wavenumber-spectrum is discrete as a consequence of the constraint posed by equation (1.26). As a result, the lower limit for vertical wavenumber of daughter waves is π/H for any ω, f, N. Hence for a mode-1 primary wave, triad solutions in figure 2.1

that have $|m_1/m_3| < 1$ are not possible (Sutherland & Jefferson, 2020). In Varma & Mathur (2017), the conditions for the existence of resonant weakly nonlinear wave-wave interactions in a non-uniform vertically varying stratification were studied. They proved that resonant triads and self-interactions can exist if (i) they satisfy the frequency and the horizontal wavenumber condition, and (ii) each wave's functional form in $z-$direction is non-orthogonal to the nonlinear forcing terms.

Triad interactions are not the only form of weakly nonlinear wave-wave interaction. In the presence of a non-constant N, a wave with frequency (ω) and horizontal wavenumber (k) can 'self-interact' and give its energy to a wave with twice the frequency and horizontal wavenumber $(2\omega, 2k)$. This process is commonly known as self-interaction, and only two waves are involved in a self-interactions unlike triads. The self-interaction process would be resonant if both (ω, k) and $(2\omega, 2k)$ satisfy the dispersion relation. Interestingly, a plane internal wave in a constant stratification cannot self-interact. The nonlinear terms identically goes to zero for any (ω, k, m) (Tabaei & Akylas, 2003). A mode-1 internal wave can only self-interact with another mode-1 internal wave. Moreover, the interaction is resonant only when $\omega \gg f$ and $N \gg \omega$ (Wunsch, 2017). Numerical simulations performed by Sutherland (2016) show that self interaction of a mode-1 internal wave is faster than triad interactions when $f \approx 0$. Moreover, the wave with frequency 2ω can self interact and pass its energy to the 4ω wave (Sutherland & Dhaliwal, 2022) as well. In realistic ocean scenarios, such resonant cascade for mode-1 is only possible near the equator where $\omega \gg f$. A small detuning in frequency can make the energy transfer between the two waves periodic in time(Baker & Sutherland, 2020). It was also observed that as detuning was increased, the energy transfer was reduced. Liang *et al.* (2017) showed that self-interaction also occurs in the presence of uniform stratification, provided the nonlinear terms in the free surface boundary condition are taken into account.

Triad interactions involving internal wave beams can be very different from the wave-wave interactions of internal wave modes. Internal wave beams are localised in space, hence the daughter waves' group speed can play a major role as well. Because of the finite nature of the internal wave beams, daughter waves with low group speeds can extract more energy compared to daughter waves with higher group speeds. However, for internal wave modes that span hundreds of kilometers, the group speed of the daughter waves does not matter. Internal wave beams contain a spectrum of waves hence the resonant triad conditions are less stringent. In the presence of uniform stratification, an internal wave mode often contains only one or two wavevectors hence the triad conditions are more strict. Note that the decay of both internal wave beams and modes has to be studied to

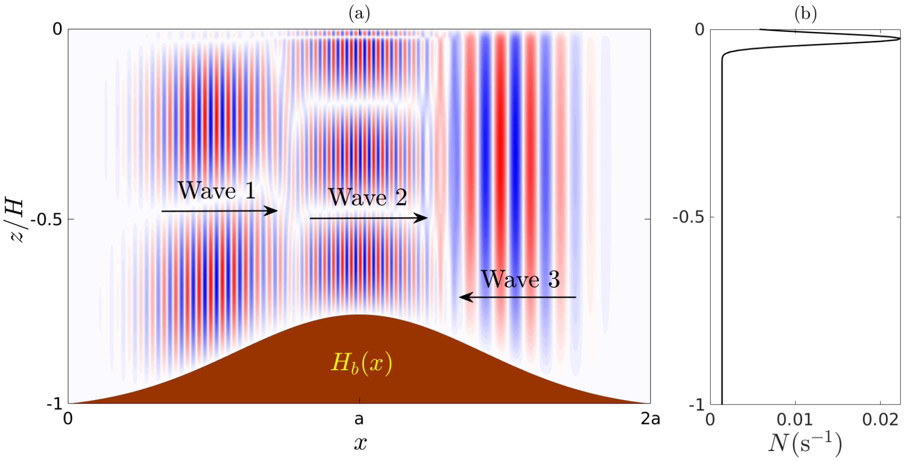

Figure 2.2: A general schematic of the problem to be studied. The figure shows the streamfunction field of three wave packets interacting in the presence of a varying bathymetry $h(x)$. H is the mean depth (equivalent to the depth in flat bathymetry situation), while $H_b(x)$ denotes the submarine topography shape. (b) The stratification profile used in constructing the modes. The same non-uniform stratification model is used throughout the chapter.

properly estimate the decay of internal waves in the ocean as both modes and beams are ubiquitous in the ocean.

The effect of variation of the ocean depth on internal wave triads involving low modes is studied on this chapter. A simplified schematic of the setup is given in figure 2.2. The motivation behind this study stems from the simple fact that ocean depth varies spatially, hence waves can move from one depth to another while they are interacting in a medium of varying stratification. Note that mode-mode coupling can occur due to the depth changes and/or density gradient changes. To understand the effects of the depth change, we have also considered the case of constant stratification. However, since the buoyancy frequency in the ocean varies in the $z-$ direction in most regions. As a result, we have also considered the variation of N and h. As a result, consideration of constant depth that has been used in the studies before might be an over-simplification in some scenarios. The effect of change in fluid depth on resonant and near-resonant interactions between three distinct waves is our primary focus.

The remaining sections are organised as follows. In §2.2, a toy model that captures the essence of wave-amplitude derivation process used in the subsequent chapters is presented. In §2.3, we derive the amplitude evolution equations of the constituent waves of a triad in the presence of a slowly varying bathymetry using the Boussinesq Navier-Stokes equations in the $f-$plane. To derive these equations, the streamfunction, buoyancy perturbation, and meridional velocity due to each wave are assumed to be a product of a slowly varying amplitude and a rapidly varying phase that are functions of space and time. In §2.4 and §2.5, the effect on the horizontal wavenumber condition when waves interact in a region of varying ocean depth in the presence of uniform and non-uniform stratification are respectively studied. In §2.6, we have studied the effect of ocean depth variation on the rate of energy transfer in triadic interactions and self-interactions in the presence of a non-uniform stratification. In §2.7, we analyze higher order self-interactions of a wave in the presence of small-amplitude monochromatic topography. In §2.8, the reduced order equations derived in this chapter are validated by solving the full Boussinesq equations using an open source code Dedalus (Burns *et al.*, 2020). The chapter has been summarized in §2.9.

2.2 Toy Model

We will first look at a toy model that captures the essence of the derivation process that is used to derive the wave amplitude equations from the Navier-Stokes Equations. To this end, let us assume a partial differential equation given by

$$\frac{\partial \mathcal{U}}{\partial t} + c_k \frac{\partial \mathcal{U}}{\partial x} + c_m \frac{\partial \mathcal{U}}{\partial z} = \epsilon_s \left\{ \mathcal{U}, \frac{\partial \mathcal{U}}{\partial x} + \frac{\partial \mathcal{U}}{\partial z} \right\}, \tag{2.5}$$

where $\mathcal{U}$ is some variable that depends on time (t) and spatial coordinates (x, z). c_k and c_m are some constants. The operator $\{G_1, G_2\} \equiv (\partial G_1/\partial x)(\partial G_2/\partial z) - (\partial G_1/\partial z)(\partial G_2/\partial x)$ denotes the Poisson bracket. ϵ_s is a small parameter which is used to denote the fact that nonlinear terms are much smaller than the linear terms. We are interested in modeling the stability of the base flow $\mathcal{U}_3 = \exp \mathrm{i}(\mathbf{k}_3.\mathbf{x} - \omega_3 t) + c.c$ to some small perturbation $\mathcal{U}_p$, where $c.c.$ denotes the complex conjugate. Substituting $\mathcal{U}_3$ in equation (2.5) would lead to

$$(k_3 c_k + m_3 c_m - \omega_3) = 0, \tag{2.6}$$

$$\left\{ \mathcal{U}_3, \frac{\partial \mathcal{U}_3}{\partial x} + \frac{\partial \mathcal{U}_3}{\partial z} \right\} = 0 \tag{2.7}$$

Equation (2.6) is basically the dispersion relation satisfied by wave-3. Moreover, for the wavevector $\mathbf{k}_3$ (or any single wavevector) the nonlinear terms are zero, hence the wave is a complete solution of equation (2.5). Now, let us assume the perturbation $\mathcal{U}_p$ takes the form given by

$$\mathcal{U}_p = \epsilon_s(\tilde{\mathcal{U}}_2(\epsilon_s t) \exp \mathrm{i}(\mathbf{k}_2.\mathbf{x} - \omega_2 t) + \tilde{\mathcal{U}}_1(\epsilon_s t) \exp \mathrm{i}(\mathbf{k}_1.\mathbf{x} - \omega_1 t) + c.c) \tag{2.8}$$

where $\tilde{\mathcal{U}}_j$ is the amplitude of the $j-$th wave-like perturbation, and it is assumed to vary in time slowly ($d\tilde{\mathcal{U}}_j/dt \ll \omega_j$). We assume $\tilde{\mathcal{U}}_j$ is a slow function of time anticipating the perturbation waves' amplitude would change because of the nonlinear interactions. The small parameter ϵ_s is once again used to denote the fact that the perturbation is much smaller than the base flow. Substituting (2.8) in (2.5), at order $O(\epsilon_s)$, the perturbation will also satisfy the dispersion relation. As a result

$$(k_1 c_k + m_1 c_m - \omega_1) = 0, \quad \text{and} \quad (k_2 c_k + m_2 c_m - \omega_2) = 0. \tag{2.9}$$

Note that this means the perturbation also consists of linear waves (like the parent wave) whose amplitudes ($\tilde{\mathcal{U}}_j$) are slow functions of time. Now we expand the nonlinear term

$$\left\{\mathcal{U}, \frac{\partial \mathcal{U}}{\partial x} + \frac{\partial \mathcal{U}}{\partial z}\right\} = \underbrace{\left\{\mathcal{U}_3, \frac{\partial \mathcal{U}_p}{\partial x} + \frac{\partial \mathcal{U}_p}{\partial z}\right\}}_{\mathcal{O}(\epsilon_s)} + \underbrace{\left\{\mathcal{U}_p, \frac{\partial \mathcal{U}_3}{\partial x} + \frac{\partial \mathcal{U}_3}{\partial z}\right\}}_{\mathcal{O}(\epsilon_s)} + \underbrace{\left\{\mathcal{U}_p, \frac{\partial \mathcal{U}_p}{\partial x} + \frac{\partial \mathcal{U}_p}{\partial z}\right\}}_{\mathcal{O}(\epsilon_s^2)}. \tag{2.10}$$

The final term in the RHS of (2.10) models the interaction among the different waves of the perturbation. The final term would be much smaller than the other two terms in the RHS, hence it is not considered. We now focus on the term $\partial \mathcal{U}_3/\partial x(\partial^2 \mathcal{U}_p/\partial x \partial z + \partial^2 \mathcal{U}_p/\partial z^2)$. The subsequent analysis can be easily used for the other $\mathcal{O}(\epsilon_s)$ term as well. To this end, $\partial \mathcal{U}_3/\partial x(\partial^2 \mathcal{U}_p/\partial x \partial z + \partial^2 \mathcal{U}_p/\partial z^2)$ can be expanded as

$$\begin{aligned}
\frac{\partial \mathcal{U}_3}{\partial x}\left(\frac{\partial^2 \mathcal{U}_p}{\partial x \partial z} + \frac{\partial^2 \mathcal{U}_p}{\partial z^2}\right) = & - \mathrm{i} k_3 \tilde{\mathcal{U}}_2 (m_2^2 + m_2 k_2) \exp \mathrm{i}(k_3 x - \omega_3 t) \exp \mathrm{i}(k_2 x - \omega_2 t) \\
& - \mathrm{i} k_3 \tilde{\mathcal{U}}_1 (m_1^2 + m_1 k_1) \exp \mathrm{i}(k_3 x - \omega_3 t) \exp \mathrm{i}(k_1 x - \omega_1 t) \\
& - \mathrm{i} k_3 \bar{\bar{\tilde{\mathcal{U}}}}_2 (m_2^2 + m_2 k_2) \underbrace{\exp \mathrm{i}(k_3 x - \omega_3 t) \exp \mathrm{i}(\omega_2 t - k_2 x)}_{\text{wave-1 phase}} \\
& - \mathrm{i} k_3 \bar{\bar{\tilde{\mathcal{U}}}}_1 (m_1^2 + m_1 k_1) \underbrace{\exp \mathrm{i}(k_3 x - \omega_3 t) \exp \mathrm{i}(\omega_1 t - k_1 x)}_{\text{wave-2 phase}} + c.c.
\end{aligned} \tag{2.11}$$

where $\bar{\bar{\tilde{\mathcal{U}}}}_j$ denotes the complex conjugate of $\tilde{\mathcal{U}}_j$. Let us now make a crucial assumption that $(\mathbf{k}_j, \omega_j)$ satisfy $\mathbf{k}_3 = \mathbf{k}_2 + \mathbf{k}_1$ and $\omega_3 = \omega_2 + \omega_1$, which are same as the triad conditions mentioned earlier. As a result of this assumption, combination of wave-3 term with certain wave-1 terms would have the same phase as wave-2, and this is shown in equation (2.11). Similarly, combination of some wave-3 and wave-2 terms would have the same phase as wave-1. Note how the parent wave term has to combine with the 'conjugate part' of the perturbation flow. As a result, we have two nonlinear terms that are resonant because they have the same phase as the perturbation waves. Considering this, the evolution equation for $\tilde{\mathcal{U}}_j$ at $\mathcal{O}(\epsilon_s^2)$ can be written as

$$\frac{\partial \tilde{\mathcal{U}}_1}{\partial t} = C_{12}\bar{\tilde{\mathcal{U}}}_2 + (\text{N.R.T}) \exp \mathbf{i}(\omega_1 t - k_1 x) \tag{2.12a}$$

$$\frac{\partial \tilde{\mathcal{U}}_2}{\partial t} = C_{21}\bar{\tilde{\mathcal{U}}}_1 + (\text{N.R.T}) \exp \mathbf{i}(\omega_2 t - k_2 x) \tag{2.12b}$$

where C_{12} and C_{21} are constants that have to determined by considering all nonlinear terms that have the phase of wave-1 and wave-2, respectively. N.R.T denotes the non-resonant terms: terms that do not have the phase of wave-1 or wave-2. For example, in equation (2.11), there are nonlinear terms that are proportional to $\exp \mathbf{i}((\mathbf{k}_3 + \mathbf{k}_2)x - (\omega_3 + \omega_2)t)$. On a much longer time scale, these terms would not impact the system significantly, hence they are neglected. This would further reduce equations (2.12a) and (2.12b) to

$$\frac{\partial \tilde{\mathcal{U}}_2}{\partial t} = C_{21}\bar{\tilde{\mathcal{U}}}_1 \quad \text{and} \quad \frac{\partial \tilde{\mathcal{U}}_1}{\partial t} = C_{12}\bar{\tilde{\mathcal{U}}}_2 \tag{2.13}$$

The system of equations given in (2.13) can admit exponentially growing solutions, and this shows that the perturbations' amplitude can grow indefinitely. They can grow exponentially when $\bar{C}_{12}C_{21}$ or $\bar{C}_{21}C_{12}$ is a positive quantity. Note that we needed equation (2.9) (dispersion relation) to be satisfied along with the triad conditions to arrive at this point. The perturbations are 'almost' linear waves whose amplitude is slowly modulated because of the nonlinear interactions. Wave-wave interactions of internal gravity waves can be modeled using similar mathematical techniques/procedures (multiple scale analysis).

2.3 Derivation of the governing equations in terrain-following coordinates

The incompressible, inviscid, 2D (in the x–z plane) Navier-Stokes equations on the f–plane under the Boussinesq approximation can be expressed in terms of the perturbation streamfunction ψ, meridional velocity v, and the perturbation buoyancy b as follows:

$$\frac{\partial}{\partial t}\left(\nabla^2\psi\right)+\frac{\partial b}{\partial x}-f\frac{\partial v}{\partial z}=-\{\nabla^2\psi,\psi\}, \tag{2.14a}$$

$$\frac{\partial v}{\partial t}+f\frac{\partial \psi}{\partial z}=-\{v,\psi\}, \tag{2.14b}$$

$$\frac{\partial b}{\partial t}-N^2\frac{\partial \psi}{\partial x}=-\{b,\psi\}. \tag{2.14c}$$

Horizontal velocity (x-direction), u, and the vertical velocity, w, are given by $u=\partial\psi/\partial z$, and $w=-\partial\psi/\partial x$. The operator $\{G_1,G_2\}\equiv(\partial G_1/\partial x)(\partial G_2/\partial z)-(\partial G_1/\partial z)(\partial G_2/\partial x)$ denotes the Poisson bracket. Viscous effects have been neglected owing to the fact that we consider waves with long wavelengths. The fluid domain is bounded at the top ($z=0$) by a rigid-lid (i.e., zero vertical velocity, leading to the boundary condition $\psi(x,0)=0$). The bottom boundary at $z=h(x)$ satisfies the impenetrable boundary condition $\psi(x,h(x))=0$.

Instead of solving the fully nonlinear equations (2.14a)–(2.14c) numerically, we combine (2.14a)–(2.14c) into a single equation and employ a multiple-scale analysis. To this end, we perform ∂(2.14a)/∂t+ $f\partial$(2.14b)/∂z $-\partial$(2.14c)/∂x, which results in

$$\frac{\partial^2}{\partial t^2}\left(\nabla^2\psi\right)+N^2\frac{\partial^2\psi}{\partial x^2}+f^2\frac{\partial^2\psi}{\partial z^2}=-\frac{\partial}{\partial t}\left(\{\nabla^2\psi,\psi\}\right)+\frac{\partial}{\partial x}\left(\{b,\psi\}\right)-f\frac{\partial}{\partial z}\left(\{v,\psi\}\right). \tag{2.15}$$

Following the approach of Maugé & Gerkema (2008), we now change the governing equations to terrain following coordinates, where a new variable (η) is defined as:

$$\eta\equiv-\frac{z}{h(x)}. \tag{2.16}$$

η serves as a spatial coordinate instead of z. According to the definition (2.16), the bottom boundary condition at $z=h(x)$ would now be enforced at $\eta=-1$, while the surface boundary condition at $z=0$ remains unaltered, except that it is now at $\eta=0$. The governing equations, which are in the x–z coordinates, need to be transformed into the x–η coordinates. The correspondence between the variables in the x–z and x–η coordinate systems are as follows:

$$\psi(x,z,t)\Rightarrow\Psi(x,\eta,t),\qquad b(x,z,t)\Rightarrow\mathbb{B}(x,\eta,t),\qquad v(x,z,t)\Rightarrow\mathbb{V}(x,\eta,t). \tag{2.17}$$

On transforming the differential operators from x–z coordinates to x–η coordinates and substituting the transformed variables in (2.15), we arrive at

$$\left[\frac{\partial^2}{\partial t^2}(L_{xx}+L_{\eta\eta})+N^2(-h(x)\eta)L_{xx}+f^2L_{\eta\eta}\right]\Psi=-\frac{\partial}{\partial t}\left[\mathcal{J}\{(L_{xx}+L_{\eta\eta})\Psi,\Psi\}\right] \\ +L_x\left(\mathcal{J}\{\mathbb{B},\Psi\}\right)-fL_\eta\left(\mathcal{J}\{\mathbb{V},\Psi\}\right), \tag{2.18}$$

where the operators $L_x, L_\eta, L_{xx}, L_{\eta\eta}$, and $\mathcal{J}\{G_1,G_2\}$ have the following definitions:

$$L_x\equiv\frac{\partial}{\partial x}+\frac{\partial\eta}{\partial x}\frac{\partial}{\partial\eta},\qquad L_\eta\equiv-\frac{1}{h}\frac{\partial}{\partial\eta},\qquad L_{\eta\eta}\equiv\frac{1}{h^2}\frac{\partial^2}{\partial\eta^2}, \tag{2.19a}$$

$$L_{xx}\equiv\frac{\partial^2}{\partial x^2}+\frac{\eta^2}{h^2}\left(\frac{\partial h}{\partial x}\right)^2\frac{\partial^2}{\partial\eta^2}-2\frac{\eta}{h}\left(\frac{\partial h}{\partial x}\right)\frac{\partial^2}{\partial\eta\partial x}+\frac{\eta}{h}\left[\frac{2}{h}\left(\frac{\partial h}{\partial x}\right)^2-\frac{\partial^2 h}{\partial x^2}\right]\frac{\partial}{\partial\eta}, \tag{2.19b}$$

$$\mathcal{J}\{G_1,G_2\}\equiv L_x(G_1)L_\eta(G_2)-L_\eta(G_1)L_x(G_2). \tag{2.19c}$$

For performing multiple-scale analysis, we assume wavelike perturbations, and the streamfunction due to the j-th wave ($j=1,2,3$) is given according to the following ansatz:

$$\Psi_j=a_j(\epsilon_x x,\epsilon_t t)\Xi_j(x,\eta,t)+\text{c.c.}, \tag{2.20}$$

where a_j is the slowly varying complex amplitude, and $\Xi_j(x,\eta,t)$ is the rapidly varying phase part of the j-th wave. The small parameters ϵ_t and ϵ_x are respectively used to denote the weak variation of the amplitude function with time and streamwise (x) direction. The amplitude is assumed to be an $\mathcal{O}(\epsilon_a)$ quantity, where ϵ_a is a small parameter. We choose ϵ_a so that the low modes' steepness or Froude number is small (Legg, 2014). The bathymetry (h), which is simply the negative of the fluid depth, is assumed to be of the form:

$$h=-H+\epsilon_h H_b(k_b x), \tag{2.21}$$

where H represents the mean depth of the fluid domain, H_b denotes the submarine topography shape, ϵ_h is its amplitude, and k_b^{-1} represents the length scale of the bathymetry. We always assume the bathymetry to have a 'mild slope'; for this we use an analog condition of that used for surface gravity waves (Meyer, 1979; Kirby, 1986):

$$\frac{1}{\mathcal{K}_j}\frac{\partial h}{\partial x}=\mathcal{O}(\epsilon_h\epsilon_k)\ll\mathcal{O}(1), \tag{2.22}$$

where $\mathcal{K}_j \equiv k_j h$ is the nondimensional horizontal wavenumber (k_j being the horizontal wavenumber) of the $j-$th internal wave. Moreover, the relation $k_j^{-1} = \epsilon_k k_b^{-1}$ is used in (2.22), which implies that either of the parameters, ϵ_h or ϵ_k, could be a small quantity while the other could potentially be an $\mathcal{O}(1)$ quantity. We use mild-slope assumption in this chapter because we want to focus *only* on the wave-wave interactions. Without the mild slope assumption, the topography itself can scatter the low mode and cause energy cascade. This can be seen in the later results of chapter 4 where most of the topographies cannot be classified as mild slope. The topographies are chosen to be smooth enough so that the scattering of the internal waves is negligible. The primary assumption in this chapter is that the scattering of internal waves by the topography is always negligible because of the mild slope assumption. Internal wave scattering is largely dependent on the slope of the wave, which is almost constant (wave's slope is dependent on N, which is nearly constant away from the pycnocline) even for higher modes whose horizontal wavenumber is much larger. The main condition that should be satisfied for a mild slope topography is that the criticality (Υ) of the topography should be less 0.1. The criticality is defined as:

$$\Upsilon \equiv \max\left(\frac{1}{\tan\Theta}\frac{dh}{dx}\right) \tag{2.23}$$

As long $\Upsilon \leq 0.1$, the scattering of the low mode internal wave would be very low. Note that the mild slope condition in this case can *still* lead to internal gravity wave scattering. Scaling analysis to find the relations between these small parameters is given in the end of this chapter in appendix A. The choice of mild-slope bathymetry is also realistically relevant. We took GEBCO Bathymetry data to verify that in certain regions topographies vary smoothly and we believe in these cases the approach used should be valid. This is shown in the figure below. The figure uses bathymetry data from GEBCO. The curves plotted in figure 2.3(b) are horizontal transects of the bathymetry taken from the small region enclosed by the blue and red lines of 2.3(a). We can see that the bathymetry changes slowly but steadily over hundreds of kilometers in two of the 3 transects.

2.3.1 Leading order analysis

Next, equation (2.20) is substituted in (2.18). At the leading order ($\mathcal{O}(\epsilon_a)$), the governing equation (2.18) reduces to:

$$\left(\frac{\partial^2}{\partial x^2} + \frac{1}{h^2}\frac{\partial^2}{\partial \eta^2}\right)\frac{\partial^2 \Xi_j}{\partial t^2} + N^2(-h(x)\eta)\frac{\partial^2 \Xi_j}{\partial x^2} + \frac{f^2}{h^2}\frac{\partial^2 \Xi_j}{\partial \eta^2} = 0. \tag{2.24}$$

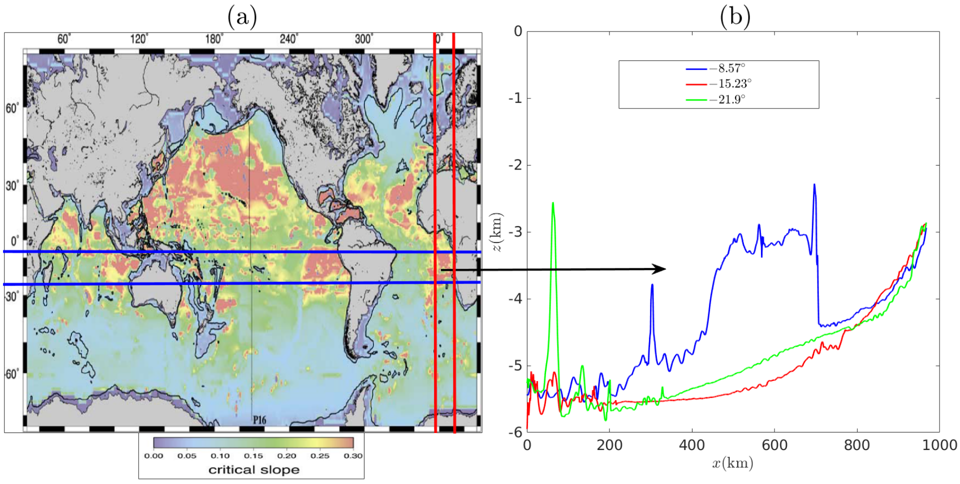

Figure 2.3: (a) Critical slope from Becker & Sandwell (JGR Oceans, 2008). (b) 3 longitudinal transects of bathymetry from the highlighted area. Bathymetry data is obtained from GEBCO.

The conversion of equation (2.15) (which is in $x-z$ coordinates) to equation (2.18) (which is in $x-\eta$ coordinates) does not involve any assumptions. The procedure outlined in Maugé & Gerkema (2008) is simply followed. However, the 'mild slope' assumption is used to study weakly nonlinear wave-wave interactions in the presence of slowly varying topography. As a result, equation (2.24) is significantly more simplified compared to the linear terms given in equation (2.18). Hereafter we drop the argument of N^2, assuming it is implied. Furthermore assuming $\Xi_j = \widehat{\Xi}_j(x,\eta)\mathrm{e}^{-\mathrm{i}\omega_j t}$, where ω_j is the angular frequency of the j-th internal wave, (2.24) simplifies to

$$\left[(N^2-\omega_j^2)\frac{\partial^2}{\partial x^2} - \frac{\omega_j^2-f^2}{h^2}\frac{\partial^2}{\partial \eta^2}\right]\widehat{\Xi}_j = 0. \tag{2.25}$$

For a mild slope bathymetry, we can use variable separation to solve (2.25) at the leading order. To this end we assume $\widehat{\Xi}_j = \phi_j(\eta;x)P_j(x)$, which leads to

$$\frac{h^2}{P_j}\frac{\partial^2 P_j}{\partial x^2} = \frac{\omega_j^2-f^2}{N^2-\omega_j^2}\frac{1}{\phi_j}\frac{\partial^2\phi_j}{\partial \eta^2} = -\mathcal{K}_j^2, \tag{2.26}$$

where ϕ_j parametrically depends on x via h. The specific notation $\phi_j(\eta;x)$ is used to denote that ϕ_j varies parametrically with $h(x)$, and therefore with x. The primary assumption is that the variation of ϕ_j with respect to the horizontal direction is very small. This is because the fluid depth varies very slowly in the $x-$direction, which is the primary assumption made in this chapter. We emphasize that in the x–η coordinates, the presence of bathymetry makes N also be a function of x; see figure 2.4 for clarity. In general for weakly varying media, dispersion relation has to be evaluated locally (for example, Refs.

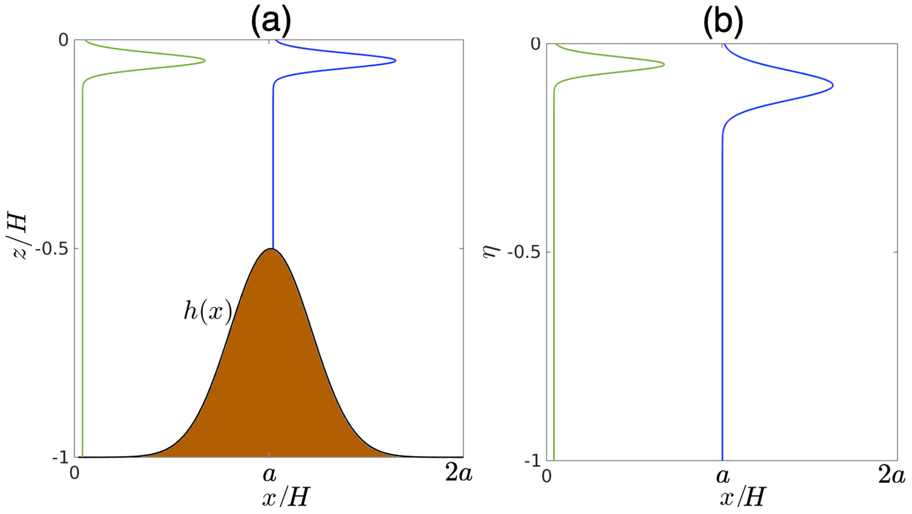

Figure 2.4: The effective change in the stratification profile $N(z)$ when the coordinates are changed from (a) x–z to (b) x–η in the presence of bathymetry. For the latter case, if N is a function of z in x–z, it becomes a function of both η and x in x–η. N profiles corresponding to the top of a seamount and an abyssal plain region have been respectively denoted by blue and green colors.

Grimshaw (1988, 1994) also use a similar procedure to study triads in weakly varying shear flows).

Two separate equations, one for P_j and the other for ϕ_j, can be formed from (2.26):

$$\left[\frac{\partial^2}{\partial x^2}+\frac{\mathcal{K}_j^2}{h^2}\right]P_j=0, \tag{2.27a}$$

$$\mathcal{L}_j\phi_j\equiv\left[\frac{\partial^2}{\partial\eta^2}+\mathcal{K}_j^2\chi_j^2\right]\phi_j=0, \tag{2.27b}$$

where $\chi_j\equiv\sqrt{(N^2-\omega_j^2)/(\omega_j^2-f^2)}$ is defined for convenience.

The boundary conditions for (2.27b) are $\phi_j=0$ at $\eta=0,-1$. The nondimensional horizontal wavenumber of the $j-$th wave, i.e. $\mathcal{K}_j$, is the set of eigenvalues obtained from (2.27b), which can vary in x when N is a function of x in x–η coordinates. Equation (2.27b) is evaluated at each x to obtain ϕ_j for that x. However, $\phi_j's$ dependence on x is slow (since h is assumed to be slowly varying); as a result, the phase part behaves as a separate entity in the leading order. An important point to note is the convention used in this study. While positive (negative) k_j implies waves propagating along $+x$ $(-x)$, owing to the fact that h is negative, $\mathcal{K}_j$ follows the exactly opposite convention. This means that a negative (positive) $\mathcal{K}_j$ implies that the wave is traveling along $+x$ $(-x)$ direction. Moreover we notice that (2.27b) does not explicitly depend on h. The only way

(2.27b) can be influenced by h is through N when the latter varies in the $z-$direction (in x–z coordinates). However, for a uniform stratification (N = constant), eigenvalues of (2.27b) are independent of h. In this case the eigenvalues are given by

$$\mathcal{M}_j \equiv \mathcal{K}_j \chi_j = n\pi, \tag{2.28}$$

where n is a positive integer. We also observe that the quantity $\mathcal{M}_j$ behaves like the vertical wavenumber of the wave that is nondimensionalised by the local bathymetry h.

Meanwhile, P_j at the leading order of the WKB approximation is given by

$$P_j = \exp\left[\mathrm{i}\int_0^x \frac{\mathcal{K}_j(x')}{h(x')}\,dx'\right]. \tag{2.29}$$

Note that we do not use the WKB method in the vertical $z-$direction. The method would not give accurate results if $N(z)$ varies rapidly in the vertical direction. The WKB method is used only for the horizontal direction where it is justified because of the slow variation of the fluid depth. A function $\beta_j(\epsilon_k x)$ is introduced such that P_j is corrected to P_j/β_j. This slow varying function $\beta_j(\epsilon_k x)$, which acts as a correction to the first order WKB solution (2.29), is given in (2.37). Note that P_j/β_j is still a solution of (2.27a) in the leading order even after the above-mentioned correction. To normalize the eigenfunction of the waves obtained from (2.27b), every wave's ϕ_j is constrained to satisfy:

$$\frac{1}{2}\int_{-1}^{0}\frac{1}{h^2}\left[\mathcal{K}_j^2\phi_j^2 + \left(\frac{\partial \phi_j}{\partial \eta}\right)^2\right]\partial\eta = 1. \tag{2.30}$$

After this normalisation, waves having the same amplitude (a_j) will also have the same energy density at a given h, provided $\beta_j = 1$.

The meridional velocity and the buoyancy perturbation at the leading order can be obtained by respectively converting (2.14b) and (2.14c) into the x–η coordinates and then substituting the streamfunction ansatz (2.20):

$$\mathbb{V}_j = \mathrm{i}\frac{f}{h\omega_j}\frac{a_j}{\beta_j}\frac{\partial \phi_j}{\partial \eta}P_j \mathrm{e}^{-\mathrm{i}\omega_j t} + \text{c.c.}, \tag{2.31}$$

$$\mathbb{B}_j = \mathrm{i}\frac{N^2}{\omega_j}\frac{a_j}{\beta_j}\frac{\partial P_j}{\partial x}\phi_j \mathrm{e}^{-\mathrm{i}\omega_j t} + \text{c.c.} \tag{2.32}$$

2.3.2 Second order analysis

2.3.2.1 Amplitude evolution equations for a resonant triad in the presence of a non-uniform stratification

Triad interaction between three internal waves occurs at $\mathcal{O}(\epsilon^2)$. Below we describe the detailed derivation that finally leads to the amplitude evolution equations (2.45a)–(2.45c) of the waves constituting a triad.

After substituting the streamfunction (2.20), meridional velocity (2.31), and buoyancy perturbation (2.32) in (2.18), the equation for the j-th wave can be written as:

$$a_j \frac{\mathfrak{P}_j}{\beta_j} \mathcal{L}_j \phi_j = -\mathrm{OE}_j^{(2)}, \tag{2.33}$$

where $\mathfrak{P}_j \equiv P_j \mathrm{e}^{-\mathrm{i}\omega_j t}$, $\mathcal{L}_j$ has been defined in (2.27b), and

$$\begin{aligned}\mathrm{OE}_j^{(2)} \equiv\ & \underbrace{\mathrm{i}\frac{\partial a_j}{\partial t}\left(\phi_j \mathcal{K}_j^2 - \frac{\partial^2 \phi_j}{\partial \eta^2}\right)\frac{2\omega_j}{h^2}\left(\frac{\mathfrak{P}_j}{\beta_j}\right) + 2\mathrm{i}(N^2-\omega_j^2)\left(\frac{\mathcal{K}_j}{h}\phi_j \frac{\partial a_j}{\partial x}\right)\left(\frac{\mathfrak{P}_j}{\beta_j}\right)}_{\text{Linear term-1}} \\ & \underbrace{+\,\mathrm{i}(N^2-\omega_j^2)\frac{\mathcal{K}_j}{h}\left[2\frac{\partial \phi_j}{\partial x} + \frac{\phi_j h}{\mathcal{K}_j}\frac{\partial}{\partial x}\left(\frac{\mathcal{K}_j}{h}\right) - \frac{2\eta}{h}\frac{\partial h}{\partial x}\frac{\partial \phi_j}{\partial \eta} - 2\frac{\phi_j}{\beta_j}\frac{d(\beta_j)}{dx}\right]\left(a_j \frac{\mathfrak{P}_j}{\beta_j}\right)}_{\text{Linear term-2}} - \mathrm{NL}_j.\end{aligned} \tag{2.34}$$

$\mathrm{OE}_j^{(2)}$ is the collection of all the linear and nonlinear (NL_j) terms at $\mathcal{O}(\epsilon^2)$ which have the phase of the $j-$th wave. Equation (2.33) can have a non-trivial solution when $\mathrm{OE}_j^{(2)}$ is orthogonal to the adjoint solutions of the linear operator $\mathcal{L}_j$, and this procedure is outlined in Craik (1971). The complete mathematical proof for using such condition is given in detail in Ince (1956, §9.34). Following Craik (1971), $\mathrm{OE}_j^{(2)}$ is multiplied by ϕ_j (since $\mathcal{L}_j$ is a self-adjoint operator, ϕ_j is also the solution of the adjoint of $\mathcal{L}_j$) and then integrated in the η direction inside the boundary limits. This would result in:

$$\begin{aligned} & 2\left[\mathrm{i}\omega_j \frac{\partial a_j}{\partial t}\left(\gamma_j^{(1)}\mathcal{K}_j^2 - \gamma_j^{(2)}\right)\frac{1}{h^2} + \mathrm{i}\gamma_j^{(3)}\left(\frac{\mathcal{K}_j}{h}\frac{\partial a_j}{\partial x}\right)\right]\frac{\mathfrak{P}_j}{\beta_j} \\ & + \mathrm{i}\frac{\mathcal{K}_j}{h}\left[2\gamma_j^{(4)} + \frac{h\gamma_j^{(3)}}{\mathcal{K}_j}\frac{\partial}{\partial x}\left(\frac{\mathcal{K}_j}{h}\right) - \gamma_j^{(5)}\frac{2}{h}\frac{\partial h}{\partial x} - \frac{2\gamma_j^{(3)}}{\beta_j}\frac{d\beta_j}{dx}\right] a_j \frac{\mathfrak{P}_j}{\beta_j} = \int_{-1}^{0} \mathrm{NL}_j \phi_j d\eta, \end{aligned} \tag{2.35}$$

where $\gamma_j^{(n)}$ are functions that vary in the x-direction, and are obtained after integration in the η direction. The expressions for $\gamma_{(j,i)}^{(n)}$, which are used in §2.3.2.1 and §2.7, are provided below:

$$\begin{aligned}
\gamma_{(j,i)}^{(1)} &= \int_{-1}^{0} [\phi_j]\, \phi_i d\eta, & \gamma_{(j,i)}^{(2)} &= \int_{-1}^{0} \left[\frac{\partial^2 \phi_j}{\partial \eta^2}\right] \phi_i d\eta, \\
\gamma_{(j,i)}^{(3)} &= \int_{-1}^{0} \left[(N^2-\omega_j^2)\phi_j\right] \phi_i d\eta, & \gamma_{(j,i)}^{(4)} &= \int_{-1}^{0} \left[(N^2-\omega_j^2)\frac{\partial \phi_j}{\partial x}\right] \phi_i d\eta, \\
\gamma_{(j,i)}^{(5)} &= \int_{-1}^{0} \left[\eta(N^2-\omega_j^2)\frac{\partial \phi_j}{\partial \eta}\right] \phi_i d\eta, & \gamma_{(j,i)}^{(6)} &= \int_{-1}^{0} \left[\eta^2(N^2-\omega_j^2)\frac{\partial^2 \phi_j}{\partial \eta^2}\right] \phi_i d\eta, \\
\gamma_{(j,i)}^{(7)} &= \int_{-1}^{0} \left[\eta(N^2-\omega_j^2)\frac{\partial^2 \phi_j}{\partial x \partial \eta}\right] \phi_i d\eta, & \gamma_{(j,i)}^{(8)} &= \int_{-1}^{0} \left[(N^2-\omega_j^2)\frac{\partial^2 \phi_j}{\partial x^2}\right] \phi_i d\eta.
\end{aligned} \tag{2.36}$$

Throughout this chapter, $\gamma_{(j,j)}$ is simply denoted by γ_j for convenience. Up to this point, β_j is an arbitrary function, and for convenience, β_j is defined such that the second square-bracketed term in the LHS of (2.35) vanishes identically. It also implies that 'Linear term-2' in (2.34) also vanishes identically. In mathematical terms this means,

$$\beta_j = \exp\left\{\int_0^x \frac{h}{2\mathcal{K}_j}\frac{1}{\gamma_j^{(3)}}\left[\left(2\gamma_j^{(4)} - \gamma_j^{(5)}\frac{2}{h}\frac{\partial h}{\partial x}\right)\left(\frac{\mathcal{K}_j}{h}\right) + \gamma_j^{(3)}\frac{\partial}{\partial x}\left(\frac{\mathcal{K}_j}{h}\right)\right] dx\right\}. \tag{2.37}$$

For constant N, β_j can be analytically simplified to $\beta_j = h(x)/h(0) = -h(x)/H$, where it is assumed that $h(0) = -H$. Equivalent β_j functions were derived in Lahaye & Smith (2020) using a different approach. For this particular choice of β_j, if the amplitudes a_j are $x-$invariant, the energy flux will be $x-$invariant as well, regardless of the modal shape, or depth. More importantly, a wave packet's maximum amplitude does not change when β_j, given by (2.37), is used in (2.35). For example, let us assume that the wave packet travels from a depth H_1 to H_2. Moreover, let us assume that the packet at H_1 is given by $a_j = A_j \exp(-x^2)$, where A_j is some constant. Then a_j, after the packet propagates to a depth H_2 would be $a_j = A_j \exp(-(c_j x)^2)$, where c_j is a function which depends on the wave properties, H_1 and H_2. Notice that the maximum wave-amplitude A_j is still unchanged. Hence growth rates, under pump wave approximation, can be calculated using A_j. This invariance of the maximum value of the a_j with varying h is very useful in estimating wave growth rates in this study, in which a major focus is on wave interactions in a region of varying h.

Next we outline the procedure to obtain $\int_{-1}^{0} \mathrm{NL}_j \phi_j d\eta$ in (2.35) to complete the amplitude evolution equations. The streamfunction, meridional velocity and buoyancy frequency ansatz are substituted in the nonlinear terms of (2.18), and all the terms with the phase of the $j-$th wave are collected. In terrain following coordinates, There would be a significant number of nonlinear terms but the quantity can be reduced by using some assumptions. The operator $\partial/\partial x$ is assumed to operate only on the phase of the wave. This is because amplitude (a_j) and the eigenfunction (ϕ_j) are slow functions of x, and the length scale of their variation would be an order of magnitude higher than wavelength of the waves as per our initial assumption. Moreover, differential operators in equations (2.19a)–(2.19c) having coefficients $dh/dx, d^2h/dx^2$ are also neglected. Hence, the following relations are used while evaluating nonlinear terms:

$$L_x\left(\frac{a_j\phi_j}{\beta_j}P_j\right) \approx \frac{a_j\phi_j}{\beta_j}\left(\frac{\partial P_j}{\partial x}\right) \approx \frac{a_j\phi_j}{\beta_j}\left(k_jP_j\right), \tag{2.38}$$

$$L_{xx}\left(\frac{a_j\phi_j}{\beta_j}P_j\right) \approx \frac{a_j\phi_j}{\beta_j}\left(\frac{\partial^2 P_j}{\partial x^2}\right) \approx \frac{a_j\phi_j}{\beta_j}\left(-k_j^2P_j\right) \tag{2.39}$$

Note that using (2.38) and (2.39), the Poisson bracket ($\mathcal{J}\{\}$) can also be simplified easily. Considering the above simplifications, the resultant resonant nonlinear terms, after omitting non-resonant terms, can be written in a compact form as given below:

$$\int_{-1}^{0}\mathrm{NL}_1\phi_1 d\eta = \left[\int_{-1}^{0}\left(\widehat{\mathrm{NL}}_{(\Psi,1)}+\widehat{\mathrm{NL}}_{(\mathbb{B},1)}+\widehat{\mathrm{NL}}_{(\mathbb{V},1)}\right)\phi_1 d\eta\right]\frac{a_3\bar{a}_2}{\beta_2\beta_3}\mathfrak{P}_3\bar{\mathfrak{P}}_2 \tag{2.40a}$$

$$\int_{-1}^{0}\mathrm{NL}_2\phi_2 d\eta = \left[\int_{-1}^{0}\left(\widehat{\mathrm{NL}}_{(\Psi,2)}+\widehat{\mathrm{NL}}_{(\mathbb{B},2)}+\widehat{\mathrm{NL}}_{(\mathbb{V},2)}\right)\phi_2 d\eta\right]\frac{a_3\bar{a}_1}{\beta_1\beta_3}\mathfrak{P}_3\bar{\mathfrak{P}}_1 \tag{2.40b}$$

$$\int_{-1}^{0}\mathrm{NL}_3\phi_3 d\eta = \left[\int_{-1}^{0}\left(\widehat{\mathrm{NL}}_{(\Psi,3)}+\widehat{\mathrm{NL}}_{(\mathbb{B},3)}+\widehat{\mathrm{NL}}_{(\mathbb{V},3)}\right)\phi_3 d\eta\right]\frac{a_1a_2}{\beta_1\beta_2}\mathfrak{P}_1\mathfrak{P}_2 \tag{2.40c}$$

$\mathrm{NL}_{(*,j)} \equiv \int_{-1}^{0}\widehat{\mathrm{NL}}_{(*,j)}\phi_j d\eta$ is defined for convenience and their expressions are given by

$$\begin{aligned}
\mathrm{NL}_{(\Psi,1)} &= \frac{\omega_1}{h^4}\left[\mathcal{K}_3\left(\zeta_3\omega_3^2\Gamma_2^{(1)}-\zeta_3\Gamma_2^{(2)}-\Gamma_3^{(3)}\right)-\mathcal{K}_2\left(\zeta_2\omega_2^2\Gamma_3^{(1)}-\zeta_2\Gamma_3^{(2)}-\Gamma_2^{(3)}\right)\right]\\
&+\frac{\omega_1}{h^4}\left[\left(\mathcal{K}_2^2-\mathcal{K}_3^2\right)\left(\mathcal{K}_2\Gamma_3^{(1)}+\mathcal{K}_3\Gamma_2^{(1)}\right)\right],\\
\mathrm{NL}_{(\Psi,2)} &= \frac{\omega_2}{h^4}\left[\mathcal{K}_3\left(\zeta_3\omega_3^2\Gamma_1^{(1)}-\zeta_3\Gamma_1^{(2)}-\Gamma_3^{(3)}\right)-\mathcal{K}_1\left(\zeta_1\omega_1^2\Gamma_3^{(1)}-\zeta_1\Gamma_3^{(2)}-\Gamma_1^{(3)}\right)\right]\\
&+\frac{\omega_2}{h^4}\left[\left(\mathcal{K}_1^2-\mathcal{K}_3^2\right)\left(\mathcal{K}_1\Gamma_3^{(1)}+\mathcal{K}_3\Gamma_1^{(1)}\right)\right],\\
\mathrm{NL}_{(\Psi,3)} &= \frac{\omega_3}{h^4}\left[\mathcal{K}_1\left(\zeta_2\omega_2^2\Gamma_1^{(1)}-\zeta_2\Gamma_1^{(2)}-\Gamma_2^{(3)}\right)+\mathcal{K}_2\left(\zeta_1\omega_1^2\Gamma_2^{(1)}-\zeta_1\Gamma_2^{(2)}-\Gamma_1^{(3)}\right)\right]\\
&+\frac{\omega_3}{h^4}\left[\left(\mathcal{K}_2^2-\mathcal{K}_1^2\right)\left(\mathcal{K}_1\Gamma_2^{(1)}-\mathcal{K}_2\Gamma_1^{(1)}\right)\right].
\end{aligned} \tag{2.41}$$

$$\begin{aligned}
\mathrm{NL}_{(\mathbb{B},1)} &= \frac{(\mathcal{K}_3-\mathcal{K}_2)}{h^4}\left[\mathcal{K}_2\mathcal{K}_3\left(\frac{1}{\omega_2}-\frac{1}{\omega_3}\right)\Gamma^{(4)}+\left(\frac{\mathcal{K}_3}{\omega_3}-\frac{\mathcal{K}_2}{\omega_2}\right)\left(\mathcal{K}_3\Gamma_2^{(2)}-\mathcal{K}_2\Gamma_3^{(2)}\right)\right],\\
\mathrm{NL}_{(\mathbb{B},2)} &= \frac{(\mathcal{K}_3-\mathcal{K}_1)}{h^4}\left[\mathcal{K}_1\mathcal{K}_3\left(\frac{1}{\omega_1}-\frac{1}{\omega_3}\right)\Gamma^{(4)}+\left(\frac{\mathcal{K}_3}{\omega_3}-\frac{\mathcal{K}_1}{\omega_1}\right)\left(\mathcal{K}_3\Gamma_1^{(2)}-\mathcal{K}_1\Gamma_3^{(2)}\right)\right],\\
\mathrm{NL}_{(\mathbb{B},3)} &= \frac{(\mathcal{K}_1+\mathcal{K}_2)}{h^4}\left[\mathcal{K}_1\mathcal{K}_2\left(\frac{1}{\omega_1}+\frac{1}{\omega_2}\right)\Gamma^{(4)}+\left(\frac{\mathcal{K}_2}{\omega_2}-\frac{\mathcal{K}_1}{\omega_1}\right)\left(\mathcal{K}_1\Gamma_2^{(2)}-\mathcal{K}_2\Gamma_1^{(2)}\right)\right]
\end{aligned} \tag{2.42}$$

$$\begin{aligned}
\mathrm{NL}_{(\mathbb{V},1)} &= \frac{f^2}{h^4}\left[\left(\frac{1}{\omega_3}+\frac{1}{\omega_2}\right)(\mathcal{K}_2+\mathcal{K}_3)\left(\zeta_3\omega_3^2\Gamma_2^{(1)}-\zeta_3\Gamma_2^{(2)}+\zeta_2\omega_2^2\Gamma_3^{(1)}-\zeta_2\Gamma_3^{(2)}\right)\right]\\
&\quad+\frac{f^2}{h^4}\left[\left(\frac{\mathcal{K}_2}{\omega_3}+\frac{\mathcal{K}_3}{\omega_2}\right)\left(\Gamma_2^{(3)}+\Gamma_3^{(3)}\right)\right],\\
\mathrm{NL}_{(\mathbb{V},2)} &= \frac{f^2}{h^4}\left[\left(\frac{1}{\omega_3}+\frac{1}{\omega_1}\right)(\mathcal{K}_1+\mathcal{K}_3)\left(\zeta_3\omega_3^2\Gamma_1^{(1)}-\zeta_3\Gamma_1^{(2)}+\zeta_1\omega_1^2\Gamma_3^{(1)}-\zeta_1\Gamma_3^{(2)}\right)\right]\\
&\quad+\frac{f^2}{h^4}\left[\left(\frac{\mathcal{K}_1}{\omega_3}+\frac{\mathcal{K}_3}{\omega_1}\right)\left(\Gamma_1^{(3)}+\Gamma_3^{(3)}\right)\right],\\
\mathrm{NL}_{(\mathbb{V},3)} &= \frac{f^2}{h^4}\left[\left(\frac{1}{\omega_1}-\frac{1}{\omega_2}\right)(\mathcal{K}_1-\mathcal{K}_2)\left(\zeta_1\omega_1^2\Gamma_2^{(1)}-\zeta_1\Gamma_2^{(2)}+\zeta_2\omega_2^2\Gamma_1^{(1)}-\zeta_2\Gamma_1^{(2)}\right)\right]\\
&\quad-\frac{f^2}{h^4}\left[\left(\frac{\mathcal{K}_2}{\omega_1}+\frac{\mathcal{K}_1}{\omega_2}\right)\left(\Gamma_2^{(3)}+\Gamma_1^{(3)}\right)\right].
\end{aligned} \tag{2.43}$$

Moreover, $\Gamma_j^{(n)}$ are defined as follows:

$$\begin{aligned}
\Gamma_1^{(1)} &= \int_{-1}^{0}\phi_2\phi_3\frac{\partial\phi_1}{\partial\eta}d\eta, & \Gamma_2^{(1)} &= \int_{-1}^{0}\phi_1\phi_3\frac{\partial\phi_2}{\partial\eta}d\eta, & \Gamma_3^{(1)} &= \int_{-1}^{0}\phi_2\phi_1\frac{\partial\phi_3}{\partial\eta}d\eta,\\
\Gamma_1^{(2)} &= \int_{-1}^{0}N^2\phi_2\phi_3\frac{\partial\phi_1}{\partial\eta}d\eta, & \Gamma_2^{(2)} &= \int_{-1}^{0}N^2\phi_1\phi_3\frac{\partial\phi_2}{\partial\eta}d\eta, & \Gamma_3^{(2)} &= \int_{-1}^{0}N^2\phi_2\phi_1\frac{\partial\phi_3}{\partial\eta}d\eta,\\
\Gamma_1^{(3)} &= \int_{-1}^{0}\phi_2\phi_3\frac{\partial^3\phi_1}{\partial\eta^3}d\eta, & \Gamma_2^{(3)} &= \int_{-1}^{0}\phi_1\phi_3\frac{\partial^3\phi_2}{\partial\eta^3}d\eta, & \Gamma_3^{(3)} &= \int_{-1}^{0}\phi_2\phi_1\frac{\partial^3\phi_3}{\partial\eta^3}d\eta,\\
\Gamma^{(4)} &= \int_{-1}^{0}\frac{\partial N^2}{\partial\eta}\phi_1\phi_2\phi_3 d\eta.
\end{aligned} \tag{2.44}$$

Note that $\mathrm{NL}_{(*,j)}$ is directly used in amplitude evolution equations as given just below in equations (2.45a)–(2.45c) and (2.46b).

The amplitude evolution equations for the three internal gravity waves are finally obtained after equating the LHS of (2.35) with its RHS; where the latter has been expressed in terms of (2.41)–(2.43):

$$\frac{\partial a_1}{\partial t} + c^{(g)}_{(x,1)}\frac{\partial a_1}{\partial x} = \mathfrak{N}_1 a_3 \bar{a}_2 \exp\left[\int_0^x \mathrm{i}(\mathcal{K}_3 - \mathcal{K}_1 - \mathcal{K}_2)/h \, dx' + \mathrm{i}\Delta\omega t\right], \tag{2.45a}$$

$$\frac{\partial a_2}{\partial t} + c^{(g)}_{(x,2)}\frac{\partial a_2}{\partial x} = \mathfrak{N}_2 a_3 \bar{a}_1 \exp\left[\int_0^x \mathrm{i}(\mathcal{K}_3 - \mathcal{K}_1 - \mathcal{K}_2)/h \, dx' + \mathrm{i}\Delta\omega t\right], \tag{2.45b}$$

$$\frac{\partial a_3}{\partial t} + c^{(g)}_{(x,3)}\frac{\partial a_3}{\partial x} = \mathfrak{N}_3 a_1 a_2 \exp\left[\int_0^x \mathrm{i}(\mathcal{K}_1 + \mathcal{K}_2 - \mathcal{K}_3)/h \, dx' - \mathrm{i}\Delta\omega t\right], \tag{2.45c}$$

where

$$c^{(g)}_{(x,j)} = \left[\frac{2\mathrm{i}\mathcal{K}_j\gamma_j^{(3)}}{h\mathfrak{D}_j}\right], \quad \text{in which} \quad \mathfrak{D}_j = 2\mathrm{i}\omega_j\left(\gamma_j^{(1)}\mathcal{K}_j^2 - \gamma_j^{(2)}\right)/h^2, \tag{2.46a}$$

$$\mathfrak{N}_j = \frac{1}{\mathcal{D}_j}\left[\mathrm{NL}_{(\mathbb{V},j)} + \mathrm{NL}_{(\mathbb{B},j)} + \mathrm{NL}_{(\Psi,j)}\right]. \tag{2.46b}$$

In the above equation

$$\mathcal{D}_1 = \mathfrak{D}_1\frac{\beta_2\beta_3}{\beta_1}, \quad \mathcal{D}_2 = \mathfrak{D}_2\frac{\beta_1\beta_3}{\beta_2}, \quad \mathcal{D}_3 = \mathfrak{D}_3\frac{\beta_1\beta_2}{\beta_3}. \tag{2.47}$$

The coefficient $c^{(g)}_{(x,j)}$ denotes the (weakly varying) horizontal group speed and $\mathfrak{N}_j$ denotes the nonlinear coupling coefficient of the j-th wave; $\mathfrak{N}_j$ determines the rate of energy transfer between the waves. $\Delta\omega \equiv \omega_1 + \omega_2 - \omega_3$ denotes the detuning in the frequency. The argument of the exponential terms in (2.45a)–(2.45c) denote both the detuning in the horizontal wavenumber condition and the frequency condition. For a pure resonant triad, $\mathcal{K}_3 - \mathcal{K}_1 - \mathcal{K}_2 = 0$ and $\Delta\omega = 0$. When $\mathcal{K}_3 - \mathcal{K}_1 - \mathcal{K}_2 \neq 0$ or $\Delta\omega \neq 0$, the triad is said to be *detuned*. The equations are only valid when both $\Delta\omega/\omega_j \ll 1$ and $\Delta\mathcal{K}/\mathcal{K}_j \ll 1$ are satisfied, that is, the equations are valid only near the vicinity of resonance. Analytical methods have also been developed for studying wave-wave interactions in non-resonant regimes in the presence of a slowly varying background shear flow (for example: Voelker *et al.* (2021); Grimshaw (1988, 1994)), where the wave train can pass through non-resonant regimes and resonant regimes. However, this is not in the scope of this study. To summarize, amplitude (a_j) in the wave amplitude equations can vary because of the group speed term, or the nonlinear term. The group speed term is responsible for the advection of a wave packet, while the nonlinear term is responsible for energy transfer among the waves. Moreover, waves' energy density changes because of its motion through a region of varying h. ϕ_j and β_j are heavily involved in the change in energy density that occur in a wave due to its motion through a region of varying h. Note that the evolution of a_j does not provide complete information of the changes in a wave's quantities. This is because $\Psi_j = a_j\phi_j/\beta_j P_j \mathrm{e}^{-\mathrm{i}\omega_j t}$, where ϕ_j and β_j themselves are functions of x.

For a triad, the parent wave is always the wave-3, while the daughter waves (subharmonic waves) are wave-1 and wave-2. To determine how fast the daughter waves grow, a growth rate parameter (σ) is defined as follows:

$$\sigma \equiv \sqrt{\mathfrak{N}_1\mathfrak{N}_2 A_3^2}, \tag{2.48}$$

where A_3 is the parent wave's amplitude, which is held constant. To obtain this expression, the pump wave approximation of Craik *et al.* (1978) is used. Pump wave approximation is a strong assumption which is only valid at initial times where the parent wave has much more energy than the daughter waves. Equation (2.48) reveals that growth rate is directly dependent on the nonlinear coupling coefficients. If we ignore the nonlinear terms, equations (2.45a)–(2.45c) model the movements of internal wavepackets over a mild-slope bathymetry. We emphasize here that wave scattering is not included in these equations. The amplitude variation of internal waves was recently analyzed by Lahaye & Smith (2020) (the authors focused on internal wave scattering, which is essentially a linear mechanism). While we have restricted our study to mild-slope conditions, we have extended the previous works by including the physics of (i) finite width wave packets, (ii) nonlinearity, and (iii) detuning in the horizontal wavenumber condition and hence investigation of both resonant (zero detuning) and near-resonant conditions. In this paper, we mainly focus on the variation of detuning, and growth rates (using pump wave approximation) with h/H for wave-wave interactions. Even though equations (2.45a)–(2.45c) allows finite width wave packets, we do not discuss it significantly since these have been studied in Gururaj & Guha (2020). The combined effect of nonlinear coupling coefficients, group speed and detuning have been discussed in Gururaj & Guha (2020).

The main results of scaling analysis, detailed in appendix A, is summarized here. There can be three different relations/combinations between the small parameters and they are given by:

$$\epsilon_t \sim \frac{\mathfrak{N}}{\omega}\epsilon_a \tag{2.49a}$$

$$\epsilon_t \sim \widehat{c}_g\epsilon_x \tag{2.49b}$$

$$\epsilon_t \sim \frac{\mathfrak{N}}{\omega}\epsilon_a, \widehat{c}_g\epsilon_x \tag{2.49c}$$

where $\widehat{c}_g$ is a non-dimensional term that gives a scale of the group speed. Equations (2.49a)–(2.49c) provides the scaling for 'Linear term-1' and NL_j given in (2.34). These are also the final terms which are present in wave amplitude equations (2.45a)–(2.45c). The wave amplitude (a_j) can evolve due to the group speed term or the nonlinear term. Note that if $\mathfrak{N}$ or ϵ_a is reduced (implying that nonlinear coupling coefficients or amplitude is reduced), then we can expect nonlinear effects to decrease. In such cases, equation (2.49b) would be satisfied. However, if ϵ_x is reduced (which means packet width is increased), then the effect of group speed, which advects the packets, is reduced. In these cases, equation (2.49a) would be satisfied.

2.3.2.2 Amplitude evolution equations for self-interaction in non-uniform stratification

Self-interactions can be considered as a special case of triad interactions. The evolution equations for the self-interaction of a mode can be obtained from the set of equations (2.45a)–(2.45c) after some straightforward modifications. The complete set of governing equations for the self-interaction of a mode in the presence of a mild-slope bathymetry h is given below:

$$\frac{\partial a_{(3,s)}}{\partial t} + c^{(g)}_{(x,3)} \frac{\partial a_{(3,s)}}{\partial x} = \mathcal{N}_3 a^2_{(1,s)} \exp\left[\int_0^x \mathrm{i}(2\mathcal{K}_1 - \mathcal{K}_3)/h \, dx' + \mathrm{i}\Delta\omega_s t\right], \tag{2.50a}$$

$$\frac{\partial a_{(1,s)}}{\partial t} + c^{(g)}_{(x,1)} \frac{\partial a_{(1,s)}}{\partial x} = \mathcal{N}_1 a_{(3,s)} \bar{a}_{(1,s)} \exp\left[\int_0^x \mathrm{i}(\mathcal{K}_3 - 2\mathcal{K}_1)/h \, dx' - \mathrm{i}\Delta\omega_s t\right], \tag{2.50b}$$

where the subscript 's' denotes self-interaction. Moreover, $\Delta\omega_s = 2\omega_1 - \omega_3$. Unlike the triad case, the parent wave for self-interaction is wave-1 while the daughter (superharmonic) wave is wave-3. The notation throughout this chapter follows the convention that wave-3 always has the highest frequency (hence for triads, wave-3 becomes the parent wave). The functions $c^{(g)}_{(x,j)}$ are the same as the expressions given in (2.46a). The functions $\mathcal{N}_j$, which are the nonlinear coupling coefficients for the self-interaction process, are given by:

$$\mathcal{N}_1 = \mathfrak{N}_2, \tag{2.51a}$$

$$\mathcal{N}_3 = \frac{2\mathcal{K}_1^3}{h^4\mathcal{D}_3}\left(\frac{\Gamma^{(4)}}{\omega_1}\right) - \frac{2f^2}{h^4\mathcal{D}_3}\left(\frac{\Gamma^{(3)}_1\mathcal{K}_1}{\omega_1}\right) + \frac{\mathcal{K}_1\omega_3}{h^4\mathcal{D}_3}\left(\zeta_1\omega_1^2\Gamma^{(1)}_1 - \zeta_1\Gamma^{(2)}_1 - \Gamma^{(3)}_1\right). \tag{2.51b}$$

where $\zeta_j \equiv \mathcal{K}_j^2/(\omega_j^2 - f^2)$ is defined for convenience. Here all $\Gamma, \mathcal{D}_j$ terms in equations (2.51a) and (2.51b) are evaluated using (2.44) and (2.47) by simply considering all '2' subscripts as '1'. For example, substituting β_1 for β_2 in $\mathcal{D}_j$ and similarly substituting ϕ_1 for ϕ_2 in Γ expressions. This is because in self-interaction, wave-2 is the same as wave-1.

The equations (2.50a)–(2.50b) can predict the growth of the daughter wave and the consequent decay of the parent wave. For obtaining the growth rate of the daughter waves, the pump wave approximation is used again and hence the parent wave's amplitude $a_{(1,s)}$ is treated as constant. This yields (assuming plane waves in the $x-$direction):

$$a_{(3,s)} = \left[\mathcal{N}_3 a_{(1,s)}^2\right] t, \tag{2.52}$$

where the term in square brackets denote the growth rate. To evaluate the growth rates, the maximum amplitude is assumed to not vary in the $x-$direction. This is possible because of the β_j functions. Note that while solving the wave-amplitude equations, the exponential term and the group speed can influence the evolution of the wave. However, growth rates are mainly evaluated for cases where the detuning is very low or zero (hence the exponential term does not any effect). In addition, by assuming the wave packets are very long in the $x-$direction, the group speed term's influence can also be minimised. Note that the main purpose of evaluating the growth rates is to get a measure/estimate of the strength of the nonlinear term. From the above equation it is evident that $\mathcal{N}_3$ acts as a proxy to the growth rate. Note that PSI can also simultaneously occur for the same parent wave. The most dominant instability will depend on the stratification, amplitude, and wavevector of the parent wave.

2.3.3 Energy evaluation

The time average energy density for an internal gravity wave over its time period is given by:

$$\langle \mathrm{TE}_j \rangle = \frac{\omega_j}{2\pi} \int_0^{2\pi/\omega_j} \frac{\rho_0}{2} \left[\left(\frac{\partial \psi_j}{\partial z} \right)^2 + \left(\frac{\partial \psi_j}{\partial x} \right)^2 + v_j^2 + \frac{b_j^2}{N^2} \right] dt. \tag{2.53}$$

The domain integrated total energy per unit length in y-direction is given by:

$$\widehat{\mathrm{TE}}_j = \int_0^D \int_h^0 \langle \mathrm{TE}_j \rangle dz dx = \int_0^D \int_{-1}^0 \langle \mathrm{TE}_j \rangle (-h(x)) d\eta dx. \tag{2.54}$$

After some simplification, we arrive at:

$$\widehat{\mathrm{TE}}_j = \int_0^{\mathrm{Len}_x} \int_{-1}^{0} -\frac{2}{h} \left[\mathcal{K}_j^2 \phi_j^2 + \left(\frac{\partial \phi_j}{\partial \eta} \right)^2 \right] |a_j|^2 \frac{\rho_0}{\beta_j^2} d\eta dx, \tag{2.55}$$

where Len_x is the length of the domain in the x-direction. $\widehat{\mathrm{TE}}_j$ is non-dimensionalized with the initial energy of parent wave (abbreviated as 'Pw'): $E_j = \widehat{\mathrm{TE}}_j / \widehat{\mathrm{TE}}_{Pw}|_{t=0}$. Note that $Pw = 3$ (i.e. wave-3) for triads and $Pw = 1$ (i.e. wave-1) for self-interactions.

2.4 Triad interactions in a uniform stratification in the presence of a mild-slope bathymetry

2.4.1 Effect of bathymetry on the triad resonance conditions

A key question to address here is – are the resonant triad conditions met when three waves interact in a region of varying domain height (which inherently means that the waves are travelling over a varying bottom bathymetry). It is shown that there is no violation of the resonant triad conditions (both horizontal and vertical wavenumbers) anywhere in the domain, provided the conditions are perfectly satisfied for any given domain height. Without any loss of generality, the condition for the horizontal wavenumber is:

$$k_3 = k_1 + k_2, \quad \text{or in nondimensional terms} \quad \mathcal{K}_3 = \mathcal{K}_1 + \mathcal{K}_2, \tag{2.56}$$

where $k_j = \mathcal{M}_j/(\chi_j h)$, and χ_j is defined below (2.27b). The dimensional horizontal wavenumber condition provides more insight into this situation, and yields:

$$\frac{1}{h} \left(\frac{\mathcal{M}_1}{\chi_1} + \frac{\mathcal{M}_2}{\chi_2} - \frac{\mathcal{M}_3}{\chi_3} \right) = 0. \tag{2.57}$$

Since χ_j and $\mathcal{M}_j$ are constants for uniform stratification, the triad conditions will still be satisfied everywhere in the domain (provided it is satisfied for any given h), even though the bathymetry varies. For near resonant triads, the non-dimensionalized detuning between the horizontal wavenumbers is constant, as is shown below. Let us consider three waves which have a mismatch of Δk in the horizontal wavenumber condition when

$h = -H_1$. This can be written as:

$$-\frac{1}{H_1}\left(\frac{\mathcal{M}_1}{\chi_1}+\frac{\mathcal{M}_2}{\chi_2}-\frac{\mathcal{M}_3}{\chi_3}\right) = \Delta k. \tag{2.58}$$

Now, if the same waves or modes interact at a different location for which $h = -H_2$, then the detuning at that location is $(\Delta k H_1)/H_2$. However, the dimensional wavenumbers also change by the factor H_1/H_2. Thus the ratio $\Delta k/k_j$ is maintained.

2.4.2 Effect of bathymetry on the nonlinear coupling coefficients of resonant triads

Here we focus on the nonlinear coupling coefficients in resonant triad interactions (i.e. no detuning) in the presence of a uniform stratification and a weakly varying bathymetry. Equation (2.48) revealed that the growth rate of the daughter waves is dependent on the nonlinear coupling coefficients. For constant N, the nonlinear coupling coefficients ($\mathfrak{N}_j$) in (2.46b) can be further simplified:

$$\begin{aligned}\mathfrak{N}_1 = \frac{\mathrm{i}H}{2h^2\omega_1\kappa_1\kappa_2\kappa_3}&\Bigg[N^2(\mathcal{K}_3-\mathcal{K}_2)\left\{\left(\frac{\mathcal{K}_3}{\omega_3}-\frac{\mathcal{K}_2}{\omega_2}\right)(\mathcal{K}_2\mathcal{M}_3-\mathcal{K}_3\mathcal{M}_2)\right\}\\ &+\omega_1\left\{(\mathcal{K}_2\mathcal{M}_3-\mathcal{K}_3\mathcal{M}_2)\left(\mathcal{M}_2^2+\mathcal{K}_2^2-\mathcal{K}_3^2-\mathcal{M}_3^2\right)\right\},\\ &+f^2\left(\mathcal{M}_3-\mathcal{M}_2\right)\left\{\left(\frac{\mathcal{K}_3}{\omega_3}+\frac{\mathcal{K}_2}{\omega_2}\right)(\mathcal{M}_3\mathcal{M}_2)-\left(\frac{\mathcal{K}_2}{\omega_3}+\frac{\mathcal{K}_3}{\omega_2}\right)\left(\mathcal{M}_2^2+\mathcal{M}_3^2\right)\right\}\Bigg],\end{aligned} \tag{2.59a}$$

$$\begin{aligned}\mathfrak{N}_2 = \frac{\mathrm{i}H}{2h^2\omega_2\kappa_1\kappa_2\kappa_3}&\Bigg[N^2(\mathcal{K}_3-\mathcal{K}_1)\left\{\left(\frac{\mathcal{K}_3}{\omega_3}-\frac{\mathcal{K}_1}{\omega_1}\right)(\mathcal{K}_1\mathcal{M}_3-\mathcal{K}_3\mathcal{M}_1)\right\}\\ &+\omega_2\left\{(\mathcal{K}_1\mathcal{M}_3-\mathcal{K}_3\mathcal{M}_1)\left(\mathcal{M}_1^2+\mathcal{K}_1^2-\mathcal{K}_3^2-\mathcal{M}_3^2\right)\right\},\\ &+f^2\left(\mathcal{M}_3-\mathcal{M}_1\right)\left\{\left(\frac{\mathcal{K}_1}{\omega_1}+\frac{\mathcal{K}_3}{\omega_3}\right)(\mathcal{M}_1\mathcal{M}_3)-\left(\frac{\mathcal{K}_1}{\omega_3}+\frac{\mathcal{K}_3}{\omega_1}\right)\left(\mathcal{M}_1^2+\mathcal{M}_3^2\right)\right\}\Bigg],\end{aligned} \tag{2.59b}$$

$$
\begin{aligned}
\mathfrak{N}_3 = \frac{\mathrm{i}H}{2h^2\omega_3\kappa_1\kappa_2\kappa_3}\Bigg[& N^2(\mathcal{K}_1+\mathcal{K}_2)\left\{\left(\frac{\mathcal{K}_1}{\omega_1}-\frac{\mathcal{K}_2}{\omega_2}\right)(\mathcal{K}_2\mathcal{M}_1-\mathcal{K}_1\mathcal{M}_2)\right\} \\
& +\omega_3\left\{(\mathcal{K}_2\mathcal{M}_1-\mathcal{K}_1\mathcal{M}_2)\left(\mathcal{M}_1^2+\mathcal{K}_1^2-\mathcal{K}_2^2-\mathcal{M}_2^2\right)\right\} \\
& +f^2\left(\mathcal{M}_1+\mathcal{M}_2\right)\left\{\left(\frac{\mathcal{K}_1}{\omega_2}+\frac{\mathcal{K}_2}{\omega_1}\right)(\mathcal{M}_1^2+\mathcal{M}_2^2)-\left(\frac{\mathcal{K}_1}{\omega_1}+\frac{\mathcal{K}_2}{\omega_2}\right)(\mathcal{M}_1\mathcal{M}_2)\right\}\Bigg],
\end{aligned}
\tag{2.59c}
$$

where $\kappa_j = \sqrt{\mathcal{M}_j^2+\mathcal{K}_j^2}$. Note that the above expressions are obtained only when the vertical wavenumber condition is satisfied. The terms inside the square brackets are constant and hence do not vary with the bathymetry h (the fact that $\mathcal{K}_j$ and $\mathcal{M}_j$ are constants for a constant N is given in (2.28)). For constant N, $\beta_j = -h(x)/H$, which has been used in (2.59a)–(2.59c), and this finally results in $\mathfrak{N}_j \propto 1/h^2$. Hence for waves traveling from a given fluid depth to a lesser depth (i.e. as the waves climb up a seamount), the nonlinear coupling coefficients, and hence the growth rates, increase following the inverse square rule.

In summary, for a uniform stratification, if three modes satisfy the resonant triad condition at a particular domain height, then they would satisfy the resonant triad condition for any domain height. Moreover, we also showed that the nonlinear coupling coefficients increase (decrease) as the fluid depth decreases (increases) following an inverse square law.

2.5 Triad and self interactions in a non-uniform stratification in the presence of a mild-slope bathymetry: detuning effects

In §2.4, it was shown that in the presence of a uniform stratification, if the triad condition is satisfied between three modes at a particular h, then they are satisfied for all h. However in non-uniform stratification, such a simple outcome is not possible. In certain types of triads, there can be a heavy mismatch in the horizontal wavenumber condition as the waves involved in the triad interact in a region of varying domain height. This may affect the energy transfer between the waves.

In this section we study the factors that decide the detuning (or mismatch) between the horizontal wavenumber of the waves as h is varied in the presence of non-uniform stratification. Here as well as in the rest of this paper, we will consider a Gaussian function to represent the buoyancy frequency:

$$N(z) = N_b + N_{\text{max}} \exp[-\left\{(z - z_c)/W_p\right\}^2], \tag{2.60}$$

where the parameters N_b, N_{max}, W_p, and z_c are varied. This kind of profile (see figure 2.2(b)) is a simplified representation of oceanic stratification and is widely used in the literature; see Grisouard *et al.* (2011), Mathur *et al.* (2014), and Varma & Mathur (2017). The peak in the buoyancy frequency near the surface is used to model the typical thermocline/pycnocline observed in the oceans. In oceans, the thermocline is usually very close to the surface. Moreover, near the thermocline the density of the water varies rapidly as depth increases because of the drop in temperature (heat does not penetrate significantly into depth of the oceans). Because of the rapid variation in the density, buoyancy frequency has a spike near the surface. The stratification profiles are chosen such that the pycnocline is above the topography. If the topography cuts the pycnocline, internal wave scattering may be significant as shown in Hall *et al.* (2013).

2.5.1 Effect of varying h on the horizontal wavenumber condition for waves satisfying $f \ll \omega_j \ll N_b$

First we study the class of triads for which the angular frequencies of the constituent waves obey the condition $f \ll \omega_j \ll N_b$. It is assumed that the parent wave (angular frequency ω_3) gives its energy to two subharmonic daughter waves of angular frequencies ω_1 and ω_2 respectively, that is, the condition $\omega_1 < \omega_3$ and $\omega_2 < \omega_3$ is always assumed. A parameter $\alpha \in (0, 1)$ is defined such that $\omega_1 = \alpha\omega_3$ and $\omega_2 = (1 - \alpha)\omega_3$. Two different types of interactions, Class-1 and Class-2, are defined for which a parent wave can form a triad with the subharmonic daughter waves.

2.5.1.1 Class-1 interactions

Three waves with angular frequencies $(\omega_3, \omega_1, \omega_2)$ such that $\omega_3 = \omega_1 + \omega_2$ is assumed. Furthermore we assume that at a particular h, the horizontal wavenumber condition is satisfied between mode i of wave-1, mode j of wave-2, mode k of wave-3, i.e.

$$\mathcal{K}_{3(k)} = \mathcal{K}_{1(i)} + \mathcal{K}_{2(j)}, \tag{2.61}$$

where i, j and k are not all equal. This constitutes a Class-1 interaction. Now if the stratification profile changes (the stratification profile will change in x–η coordinates provided h is varying), then the wavenumbers $\mathcal{K}_{1(i)}, \mathcal{K}_{2(j)}, \mathcal{K}_{3(k)}$ will also change. However, for a given change in h, all the wavenumbers need not change in a way such that the condition (2.61) is satisfied. For example, if $\mathcal{K}_{1(i)} = \text{func}(h)$, then it is possible that $\mathcal{K}_{2(j)} \neq c\,\text{func}(h)$, where c and func( ) denote an arbitrary constant and function respectively. Therefore, even though the triad condition may be satisfied at a particular h, it may not be satisfied for all h. Hence Class-1 triads might get detuned as they interact in a region of varying h.

To measure the detuning (or mismatch) in the horizontal wavenumber, we define a new variable $\Delta\mathcal{K}$:

$$\Delta\mathcal{K} \equiv \frac{\mathcal{K}_{3(k)} - \mathcal{K}_{1(i)} - \mathcal{K}_{2(j)}}{\mathcal{K}_{\text{min}}}, \tag{2.62}$$

where $\mathcal{K}_{\text{min}}$ is the minimum wavenumber of the three wavenumbers at a particular x-coordinate. $\Delta\mathcal{K}$ basically acts as a non-dimensional measure of the detuning between the waves, and for a resonant triad, $\Delta\mathcal{K} = 0$.

We now study how different (nondimensional) wavenumbers $\mathcal{K}_{3(n)}$ of frequency ω_3 change as h is varied in the presence of a non-uniform stratification. To obtain $\mathcal{K}_{3(n)}$ for a given stratification profile, we solve (2.27b) for $h/H \in [-1, -0.2]$. The functional form of h, as long it is mildly varying, does not influence the wavenumbers or detuning at a particular h. The non-uniform stratification profile given by (2.60) is used throughout this chapter. The stratification profiles are chosen such that $N_{\text{max}} = (2N_b, 4N_b, ...12N_b)$, $W_p = (H/200, 2H/200...5H/200)$, and $z_c = (H/80, H/40, H/20, H/10)$; and we consider all possible (120) combinations. Moreover, $\omega_3 = 0.1N_b$ and $f = 0$ is used consistently for all combinations. Figure 2.5 show the variation of $\widehat{\mathcal{K}}_{3(n)} \equiv \mathcal{K}_{3(n)}(h)/\mathcal{K}_{3(n)}(H)$ with h/H for different modes n. Figures 2.5(a)–2.5(c) uses the stratification profile $N^{(1)}$ with the following parameters: $N_{\text{max}} = 2N_b$, $W_p = H/200$, and $z_c = H/80$. Moreover, figures 2.5(d)–2.5(f) uses the profile $N^{(2)}$ given by: $N_{\text{max}} = 10N_b$, $W_p = H/50$, and $z_c = H/10$. Note that $N^{(1)}$ has a sharp pycnocline, while $N^{(2)}$ has a larger W_p resulting in a wider pycnocline. For profiles where all three parameters are low (e.g. $N^{(1)}$), $\widehat{\mathcal{K}}_{3(1)}$ is nearly constant for some range of h/H and then starts decreasing. This can be seen

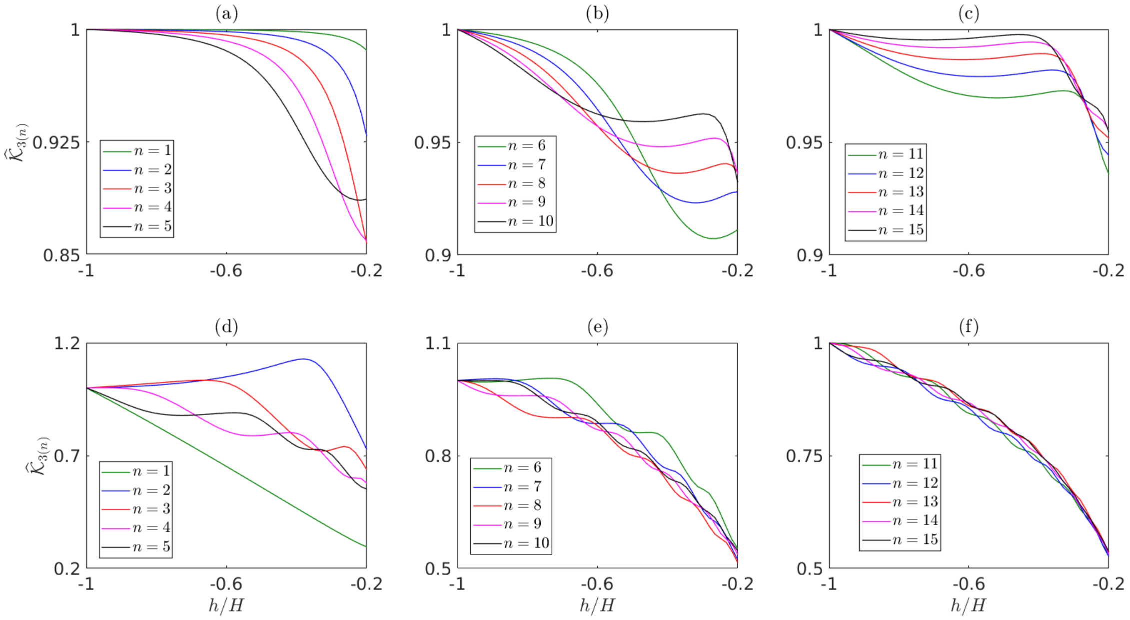

Figure 2.5: Variation of $\widehat{\mathcal{K}}_{3(n)}$ with h/H for two different stratification profiles. For stratification profile $N^{(1)}$: (a) modes 1-5, (b) modes 6-10 and (c) modes 11-15. For stratification profile $N^{(2)}$: (d) modes 1-5, (e) modes 6-10 and (f) modes 11-15.

in figure 2.5(a), where the first five modes exhibit this behaviour. Moreover, for profiles where all z_c, W_p, N_{max} are high (e.g. $N^{(2)}$), $\widehat{\mathcal{K}}_{3(1)}$ decreases almost linearly with h/H, as can be clearly seen in figure 2.5(d). For any profile, $\widehat{\mathcal{K}}_{3(1)}$ always decreases as the fluid depth is reduced for $h/H \in [-1, -0.2]$. However this behaviour does not hold for any mode other than mode 1. For example, for $z_c = H/10$ (regardless of W_p, N_{max}), $\widehat{\mathcal{K}}_{3(2)}$ increases for some h/H as fluid depth is reduced, see figure 2.5(d) (blue curve). Similar behaviour is also observed for modes 3,4 and 5 when W_p is low. In summary, the variation of $\widehat{\mathcal{K}}_{3(1)}$ with h/H can be different from that of the higher modes' wavenumber, which can result in detuning.

For profiles with high W_p, $\widehat{\mathcal{K}}_{3(n)}$ for $n > 10$ starts to collapse on each other, see figure 2.5(f). In such kind of scenarios, since $\widehat{\mathcal{K}}_{3(n)}$ remains nearly the same, $\Delta\mathcal{K}$ will not be induced by the difference in higher modes' $\widehat{\mathcal{K}}_{3(n)}$. In general it was observed that as W_p is reduced, n has to be higher for the modes to collapse on each other.

The interaction of mode-1 internal wave (wave-3) with different modes in the presence of two different non-uniform stratification profiles is considered next. These profiles are a part of the 120 profiles that was already mentioned. Sample results are shown in figure 2.6 in which the frequencies and stratification profile parameters are as follows:

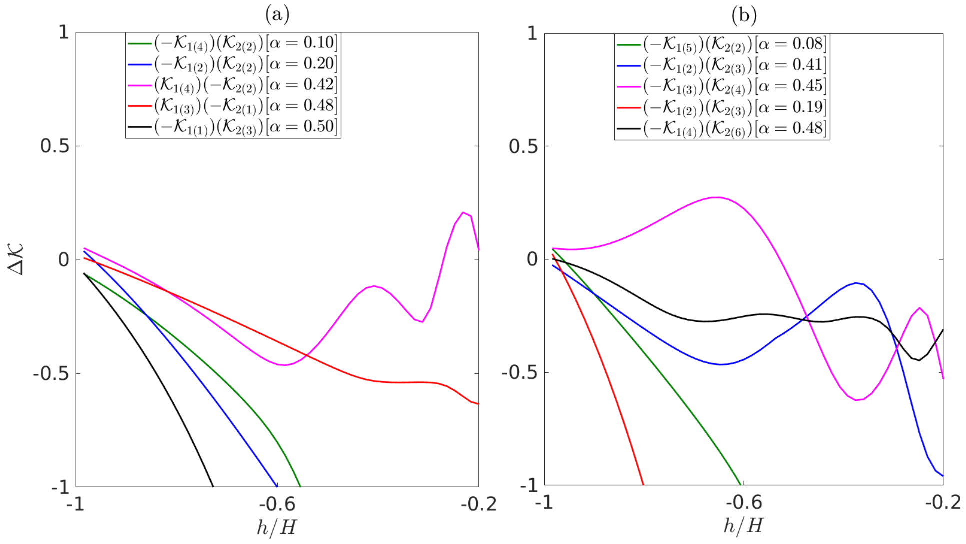

Figure 2.6: Variation of detuning ($\Delta\mathcal{K}$) with h/H for various modal interactions pertaining to the stratification profiles (a) $N^{(3)}$, and (b) $N^{(4)}$. The legends indicate what daughter waves were involved in the triad interactions. $\alpha \equiv \omega_1/\omega_3$.

- $N^{(3)}$: $\omega_3 = 0.1N_b$, $f = 0$,$N_{\text{max}} = 10N_b$, $W_p = H/100$ and $z_c = H/10$.
- $N^{(4)}$: $\omega_3 = 0.1N_b$, $f = 0$,$N_{\text{max}} = 10N_b$, $W_p = H/50$ and $z_c = H/20$.

For each profile, 5 different modal interactions are shown. Figure 2.6 clearly reveals that the detuning can be quite sensitive to the changes in the domain height. The triad interactions whose detuning is minimal as h is varied will be favored provided they also have comparable growth rates to the interactions that are heavily detuned during the free evolution.

2.5.1.2 Class-2 interactions: A special case of triad interactions

The interaction in Class-2 is between the n-th modes (where $n \in \mathbb{Z}^+$) of different waves constituting a triad. For example, if mode 1 with frequency ω_1, mode 1 with frequency ω_2 and mode 1 with frequency ω_3 form a triad, it is classified as a Class-2 interaction. This kind of triad is possible when $f \ll \omega_j \ll N_b$. To show how this interaction is possible, we consider the eigen-problem concerning the $n-$th mode of the $j-$th wave:

$$\frac{\partial^2 \phi_{j(n)}}{\partial \eta^2} + \mathcal{K}_{j(n)}^2 \chi_j^2 \phi_{j(n)} \approx \frac{\partial^2 \phi_{j(n)}}{\partial \eta^2} + \left(\frac{\mathcal{K}_{j(n)}}{\omega_j}\right)^2 N^2 \phi_{j(n)} = 0, \tag{2.63}$$

where $\chi_j \approx N/\omega_j$ is used (under the approximation $f \ll \omega_j \ll N_b$), and the system is solved using the boundary conditions: $\phi_{j(n)} = 0$ at $\eta = 0$ and $\eta = -1$. However, by Sturm Liouville theory, for a given operator (here $\partial^2/\partial\eta^2$) and weight function (here $N(z)^2$), the $n-$th eigenvalue (here $\mathcal{K}_{j(n)}/\omega_j$) is unique, i.e., $\mathcal{K}_{j(n)}/\omega_j = \mathbf{INV}(x)\ \forall j$. Note that the $\mathbf{INV}(x)$ does not vary with j, however, the $\mathbf{INV}(x)$ can vary in the $x-$direction. Therefore, if the triad condition for frequency: $\omega_3 = \omega_2 + \omega_1$ is valid, this automatically implies validity of the wavenumber condition $\mathcal{K}_{3(n)} = \mathcal{K}_{1(n)} + \mathcal{K}_{2(n)}$.

The situation mentioned above is true for all stratification profiles satisfying $f \ll \omega_j \ll N(z)$ (at all z locations). This is especially important because in the presence of a bathymetry, the stratification profile changes in the x direction in $x-\eta$ coordinates. However, for Class-2 interaction, all three non-dimensional wavenumbers (eigenvalues) are the same functions of h since they are the same eigenvalues divided by their frequency. Thus the resonant triad condition will be still be satisfied even if h is varied significantly (i.e. variation of h will not cause detuning). Note that, in the parameter regime of $f \ll \omega_j \ll N(z)$, only class-2 self interactions were observed in numerical experiments of Sutherland (2016), hence class-2 triads may always be dominated by self interactions, resulting in parent wave's energy transfer to the superharmonics instead of subharmonics. As a result, class-2 triads may not be practically as relevant as class-2 self interactions.

2.5.1.3 Mismatch in the vertical wavenumber condition for vertically propagating waves in a weakly varying stratification

Until now, we focused on the detuning induced in triads that contain low mode internal waves. However, small scale internal waves that propagate vertically can get dissipated before they get projected as modes. For example, internal wave beams generated by a topography often encounter a pycnocline where they can engage in wave-wave interactions and get dissipated (Diamessis *et al.*, 2014; Gayen & Sarkar, 2013, 2014). For these vertically propagating waves, change in the background stratification can induce detuning. This is because when a wave propagates vertically in a region of varying stratification, its vertical wavenumber changes while frequency and horizontal wavenumber remain constant. Therefore, if three waves form a resonant triad on a particular background stratification, they will fail to do so once they move to another region with a different background stratification – there will be a detuning (Δm) of the vertical wavenumbers, which is given by

$$\Delta m = m_3 - (m_1 + m_2) = k_3\sqrt{\frac{N^2-\omega_3^2}{\omega_3^2-f^2}} - \left(k_1\sqrt{\frac{N^2-\omega_1^2}{\omega_1^2-f^2}} + k_2\sqrt{\frac{N^2-\omega_2^2}{\omega_2^2-f^2}}\right). \quad (2.64)$$

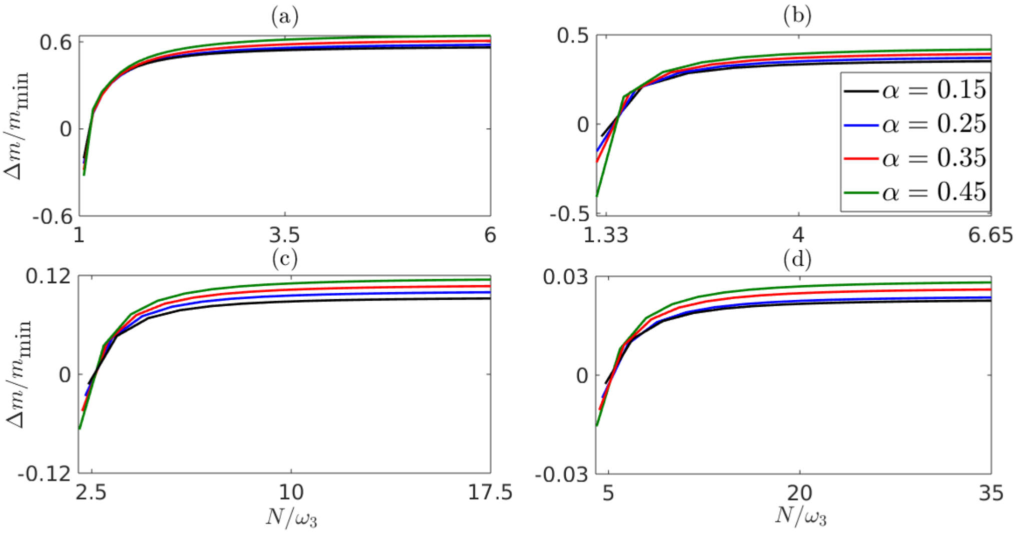

Figure 2.7: Variation of detuning in vertical wavenumber for different values of ω_3/N_b. (a) $\omega_3/N_b = 0.9$, (b) $\omega_3/N_b = 0.75$, (c) $\omega_3/N_b = 0.4$ and (d) $\omega_3/N_b = 0.2$. Here m_{min} represents the lowest vertical wavenumber among the three waves at that particular stratification. Rotational effects are neglected ($f = 0$).

Here N is assumed to slowly vary in the $z-$direction. The main factors which influence detuning are the waves' frequencies, wavenumbers and the background stratification, whose effect is elaborated in figures 2.7 and 2.8.

To study the variation of Δm, four different values of ω_3/N_b are chosen. At $N = N_b$, the vertical wavenumber condition is assumed to be satisfied without any detuning and N_b is referred as base stratification. For each value of ω_3/N_b, we consider four different α values. For each α, there are four unique wavevectors for the daughter waves which encompass the $(+,+)$ curve in figure 2.1. The four unique triad combinations (for a particular α and ω_3/N_b) can be characterized as:

- $(k_2/k_3, |m_2/m_1|) \in (1,\infty) \times (0,1)$,
- $(k_2/k_3, |m_2/m_1|) \in (0,1) \times (1,\infty)$,
- $(k_2/k_3, |m_2/m_1|) \in (0,1) \times (0,1)$,
- $(k_2/k_3, |m_2/m_1|) \in (1,\infty) \times (1,\infty)$.

Initially we study the effect of the variation of ω_3/N_b and α on detuning. To this end, we focus on those triads whose daughter waves have wavenumbers satisfying $(k_2/k_3, |m_2/m_1|) \in (0,1) \times (1,\infty)$. The results are given in figure 2.7. It can be observed that, for a given α,

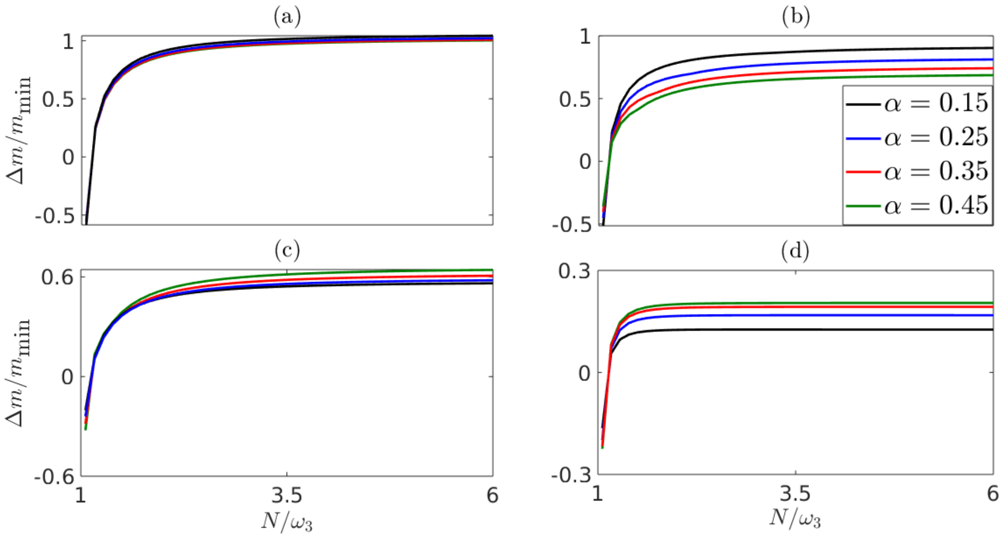

Figure 2.8: Variation of detuning for $\omega_3/N_b = 0.9$ and various daughter wave combinations. (a) $(k_2/k_3, |m_2/m_1|) \in (1, \infty) \times (0, 1)$, (b) $(k_2/k_3, |m_2/m_1|) \in (0, 1) \times (0, 1)$, (c) $(k_2/k_3, |m_2/m_1|) \in (0, 1) \times (1, \infty)$, and (d) $(k_2/k_3, |m_2/m_1|) \in (1, \infty) \times (1, \infty)$. Rotational effects are neglected.

detuning significantly increases as ω_3/N_b is increased for the same increase in the background stratification. Detuning asymptotes to a constant value as N is increased, hence the difference in detuning caused by moderate and strong stratifications would be minimal. We observe that detuning has a strong sensitivity to stratification for higher values of ω_3/N_b. For example, figure 2.7(a) shows that a small variation in stratification causes significant detuning for $\omega_3/N_b = 0.9$ near N_b.

In figure 2.8, we focus on the detuning for different wavevector (of daughter waves) combinations with ω_3/N_b fixed at 0.9. We observe that out of all combinations, the triads satisfying $(k_2/k_3, |m_2/m_1|) \in (1, \infty) \times (1, \infty)$ undergo the least amount of detuning with changes in the background stratification. Therefore, such triads may be the pathway through which the parent wave decomposes for high values of ω_3/N_b. The triads shown in figure 2.8(a) have values of non-dimensional detuning close to 1, which would mean that such triads are not possible in varying stratifications. Moreover, for a particular ω_3/N_b value, detuning can increase or decrease with an increase in α depending on the wavevector of the daughter waves. For example, figures 2.8(a) and 2.8(b) show that detuning increases with decrease in α. However, for the triads in figures 2.8(c) and 2.8(d) detuning increases with an increase in α.

2.5.2 Effect of bathymetry on horizontal wavenumber condition for Class-1 self-interaction

Detuning can also be introduced during a self-interaction process as h is varied. Following the same terminology as before, we classify self-interactions as Class-1 and Class-2. As shown by Wunsch (2017), Class-2 self-interactions will always be slightly detuned, where the detuning increases as f increases. This is due to the fact that in a non-uniform stratification, if the $n-$th mode of (ω) satisfies the dispersion relation, then the n-th mode of (2ω) will be able to satisfy it only approximately.

Following (2.62), the detuning for a self-interaction process is defined as

$$\Delta\mathcal{K}_s = \frac{\mathcal{K}_{3(k)} - 2\mathcal{K}_{1(i)}}{\mathcal{K}_{1(i)}}, \tag{2.65}$$

where wave-3 is the superharmonic (daughter) wave, while wave-1 is the parent wave, i.e. $\omega_1 = \omega_3/2$ (following the convention used throughout this chapter that wave-3 has the highest frequency). The amplitude evolution equations for a self-interaction process is discussed in §2.3.2.2.

For the range $f \ll \omega_j \ll N(z)$, Class-2 self-interaction process will follow similar principles outlined in §2.5.1.2. As mentioned in §2.5.1.2, significant variations in h for this frequency range will not introduce detuning in Class-2 self-interactions. The other end of the parameter space where $(N^2 - \omega_j^2) \approx N^2$ is no longer valid is studied. Hence, out of Class-1 and Class-2 self-interactions, only the latter is possible. This would mean that as the domain height changes, the detuning introduced could be significant. Interestingly though, if the wavenumbers involved in the self-interaction change with h/H in a similar way, the detuning is insignificant, see figure 2.9. The frequencies and the stratification profile parameters used here are:

- $N^{(6)}$: $N_{\text{max}} = 10N_b$, $W_p = H/100$ and $z_c = H/10$.
- $N^{(7)}$: $N_{\text{max}} = 10N_b$, $W_p = H/100$ and $z_c = H/20$,

and $f = 0$ always. Figure 2.9(a) uses the set $N^{(6)}$, and shows the variation of the horizontal wavenumber of mode-2 (of $\omega_3 = 0.89N_b$) and mode-3 (of $\omega_1 = \omega_3/2$). These modes satisfy the condition for resonant self-interaction. We observe that these two wavenumbers behave quite similarly for a wide range of h/H, and hence the detuning, shown in figure

2.9(b), is small (and constant for an appreciable range), in spite of the fact that it is a Class-1 interaction. The same phenomenon is also shown for several other self-interaction combinations in figure 2.9(c), where the parameter set $N^{(7)}$ is used.

The detuning for all the combinations shown stays constant for a certain range of h/H. Class-1 *triad* interactions may also give rise to a small detuning for a range of h/H, provided all the modes involved behave in a similar way. However, this is a more stringent condition than a self-interaction process, where only two waves are involved. Note that the reduced order equations are valid only when $\Delta\mathcal{K}_s \ll 1$ or $\Delta\mathcal{K} \ll 1$. However, the above statement does not necessarily mean that the wavenumbers themselves cannot change significantly. The only requirement is detuning should be a small quantity in a self-interaction, or a triad interaction. This occurs when all the wavenumbers in a weakly nonlinear interaction nearly have the same functional dependence on h. For example, the detuning will not vary significantly with h if:

$$k_1(h) \approx C_1\mathcal{Y}(h), \quad k_2(h) \approx C_2\mathcal{Y}(h), \quad k_3(h) \approx C_3\mathcal{Y}(h), \tag{2.66}$$

where C_1, C_2, C_3 are some constants, and $\mathcal{Y}$ is some function that depends on h. As long as the wavenumbers follow equation (2.66), then $\Delta k = k_1+k_2-k_3$ (and hence $\Delta\mathcal{K}$) does not vary significantly with h. For example, this is shown for some self-interactions in figure 2.10, where $\Delta\mathcal{K}_s$ is a small quantity even as the depth change significantly. For the same parameters used in figure 2.9 of the chapter, the horizontal wavenumber of the two modes involved in a self-interaction is plotted in figure 2.10. Note that the normalised, non-dimensionalised horizontal wavenumber ($\widehat{\mathcal{K}}$) is plotted. It can be seen that the horizontal wavenumbers at $h/H = -0.5$ is nearly twice as much as their value at $h/H = -1$. However, $\Delta\mathcal{K}_s$ still follows $\Delta\mathcal{K}_s \ll 1$. As a result, for this specific interaction, the reduced order equation is at least valid for $h/H \in [-1, -0.5]$.

For any class-2 self-interaction (same $n-$th mode interaction) in the presence of non-uniform stratification, detuning is expected to be a small quantity for the $\mathcal{O}(1)$ changes in depth and wavenumber. Baker & Sutherland (2020) and Sutherland (2016) focus on such Class-2 self interactions. Detuning would satisfy $\Delta\mathcal{K}_s \ll 1$ even for $\mathcal{O}(1)$ changes in depth and horizontal wavenumber.

To summarize, in the presence of a non-uniform stratification, we divide triad and self-interactions into two classes: Class-1 and Class-2. Class-1 interactions contain waves whose mode numbers are all not the same, while Class-2 interactions contain waves which

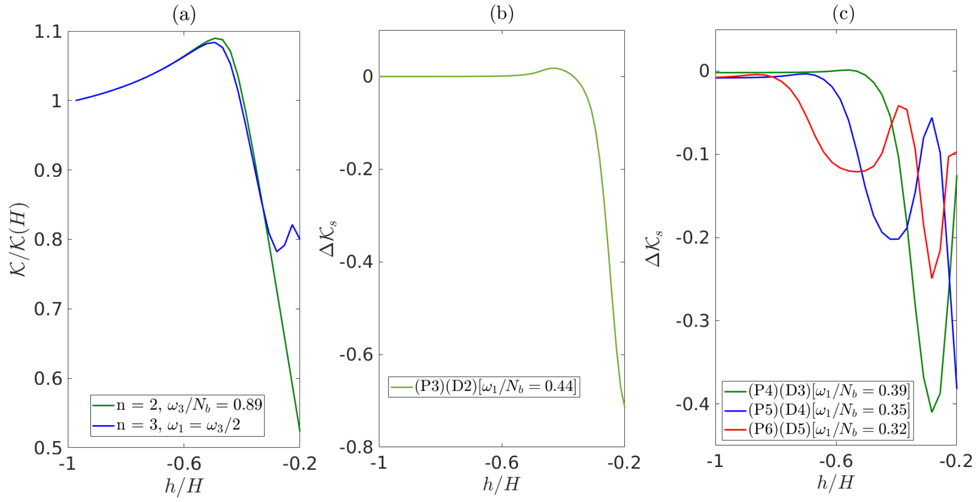

Figure 2.9: (a) Variations of $\mathcal{K}_{3(2)}$ and $\mathcal{K}_{1(3)}$ with h/H for the parameter set $N^{(6)}$. (b) Variation of detuning with h/H for the same case. (c) The detuning for three different self-interaction combinations for the parameter set $N^{(7)}$. Here the notation (Pa)(Db) implies 'Parent wave' with 'mode-a' and 'Daughter wave' with 'mode-b'.

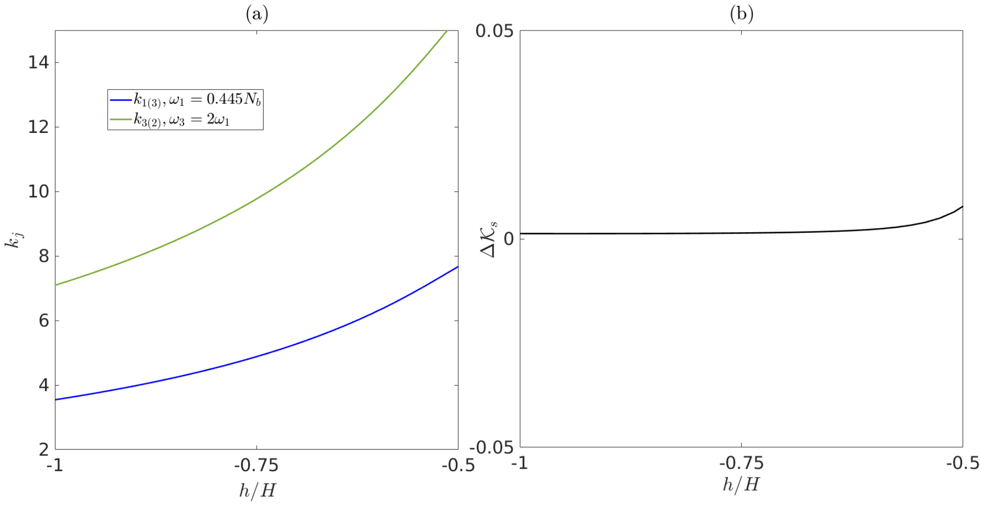

Figure 2.10: (a) Variations of $k_{3(2)}$ and $k_{1(3)}$ with h/H for the stratification profile $N^{(6)}$. (b) Variation of detuning ($\Delta\mathcal{K}_s$) with h/H for the same case.

are the $n-$th modes of their respective frequencies. Class-1 interactions, may undergo detuning with the variation in h, irrespective of the frequency. However, interestingly, certain Class-1 self-interactions do not undergo detuning as h is varied inside a certain range. For both triads and self-interactions, Class-2 interactions can only exist for $f \ll \omega_j \ll N(z)$, and does not get detuned as h is varied.

2.6 Variation of growth rates and nonlinear coupling coefficients with depth for non-uniform stratification

In this section, we focus on the effects of domain height variation on the growth rate (σ) of triads, and the nonlinear coupling coefficient $\mathcal{N}_3$, which provides a measure of the growth of the daughter wave in a self-interaction. The non-uniform stratification profile (2.60) will be used in this section.

2.6.1 Variation of growth rates with domain height for triads

Triad interactions are important for the decay of internal waves near the 28.9° latitude (MacKinnon & Winters, 2005; MacKinnon *et al.*, 2013), specifically the mode-1 wave, which is the most energy containing mode (Vic *et al.*, 2019). Here we study this phenomenon in the high latitude region ($f/\omega_3 \geq 0.3$) for varying $N(z)$ and h. The mode-1 wave (which, being the parent wave, is wave-3) can decay forming various triad combinations; we restrict the subharmonic daughter waves (wave-1 and wave-2) up to mode-50. Moreover, for studying growth rates in the presence of varying h, the triads are identified separately at different h/H. This is because a triad combination at a particular h/H value may not satisfy the horizontal wavenumber condition at a different h/H (as explained in §2.5). Three main branches of triads are considered here for the mode-1 internal wave:

$$\underbrace{\mathcal{K}_3 = \mathcal{K}_2 - \mathcal{K}_1}_{\text{Branch-1}} \quad \text{or} \quad \underbrace{\mathcal{K}_3 = \mathcal{K}_1 - \mathcal{K}_2}_{\text{Branch-2}} \quad \text{or} \quad \underbrace{\mathcal{K}_3 \approx \mathcal{K}_1 + \mathcal{K}_2}_{\text{Branch-3}}. \tag{2.67}$$

For Branch-1(2) triads, wavenumber of wave-2(1) is larger in magnitude than that of wave-1(2). The only possible Branch-3 interaction is a Class-2 interaction, where both the daughter waves are also mode-1 of their respective frequencies. However this interaction, like the Class-2 self-interaction, also undergoes heavy detuning for high f values. Therefore Branch-3 being an inefficient energy transfer pathway, we restrict our focus to Branch-1 and Branch-2. Triads are studied for $f/\omega_3 = (0.3, 0.4, 0.45)$ in the presence of various stratification profiles. The triads are computed for $\alpha \in [0.31, 0.5]$, $\alpha \in [0.41, 0.5]$ and $\alpha \in [0.455, 0.5]$ for $f/\omega_3 = 0.3, 0.4$ and 0.45 respectively (see §2.5.1 for the definition of α).

Figure 2.11 shows the non-dimensionalised growth rate contour for a mode-1 wave. All growth rates σ are non-dimensionalised with a reference growth rate value σ_{ref}, where the

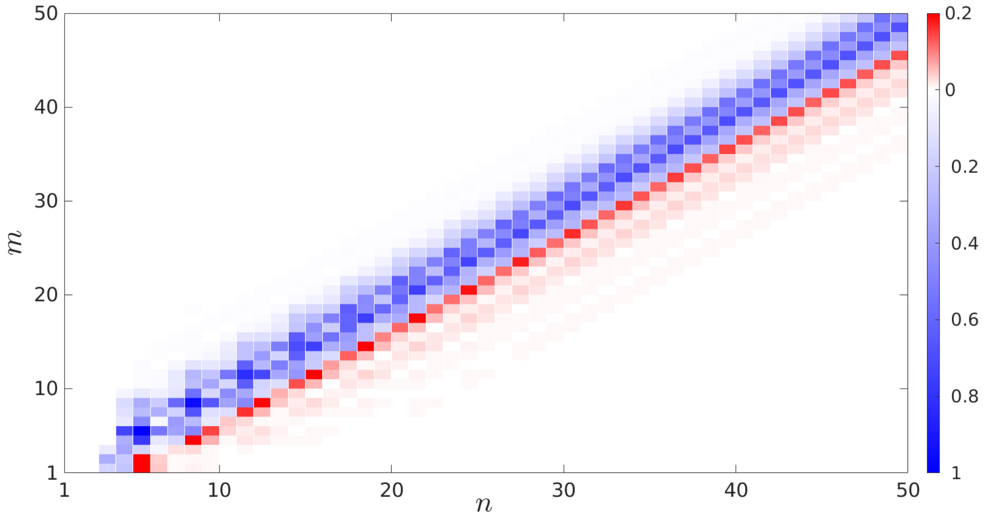

Figure 2.11: Contours of non-dimensional growth rate ($\sigma/\sigma_{\text{ref}}$) of triads formed between mode-n, mode-m, and mode-1 (i.e., wave-3). Blue and red colors respectively represent Branch-1 and Branch-2 triads, and both colors represent positive values. For Branch-1 triads, mode-$m(n)$ is wave-1(2), while for Branch-2 triads, mode-$n(m)$ is wave-1(2).

latter denotes the maximum growth rate for all Branch-1 triads at $h = -H$ (hence the value of A_3 does not impact the results shown). The frequency of the mode-1 wave is $\omega_3/N_b = 0.2$, while $f/\omega_3 = 0.4$ is taken. The stratification profile is given by

- $N^{(8)}$: $N_{\text{max}} = 10N_b$, $W_p = H/50$, $z_c = H/20$.

Branch-1(2) triads have the higher(lower) frequency daughter wave propagating in the same direction as the parent wave. Figure 2.11 reveals that from both branches, the highest growth rates are centered around $n \approx m$. However, majority of the white region contains resonant triads, but their growth rates are significantly lower in comparison to that clustered around $n \approx m$. Note that the central region is asymmetric between Branch-1 and Branch-2 triads, and this is purely a consequence of internal wave's dispersion relation. When the lower frequency daughter wave (wave-1) travels in the same direction as the parent wave (i.e. Branch-2), wave-1's modenumber (n) should always be higher than wave-2's modenumber (m) for the triad condition to be satisfied. However for Branch-1, where wave-2 travels in the same direction as the parent wave, the modenumber of wave-2 (n) need not be higher than wave-1's modenumber (m).

The clustering around $n \approx m$ is consistently observed for any setting or stratification profile considered in this study. As a result instead of focusing on all possible triads, we choose specific lines of interaction near the central region and plot the growth rate along

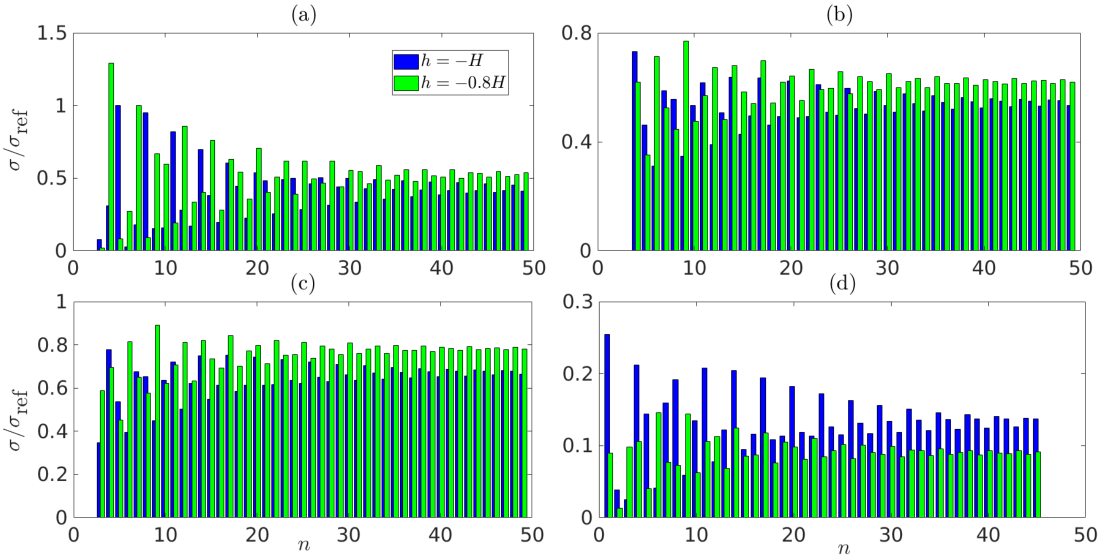

Figure 2.12: Plots of non-dimensional growth rates of mode-1 triads for profile $N^{(8)}$ with $f/\omega_3 = 0.4$ and $\omega_3/N_b = 0.2$. (a) Line (n, n) of Branch-1, (b) line $(n+1, n)$ of Branch-1, (c) line $(n, n+1)$ of Branch-1, and (d) line $(n+4, n)$ of Branch-2.

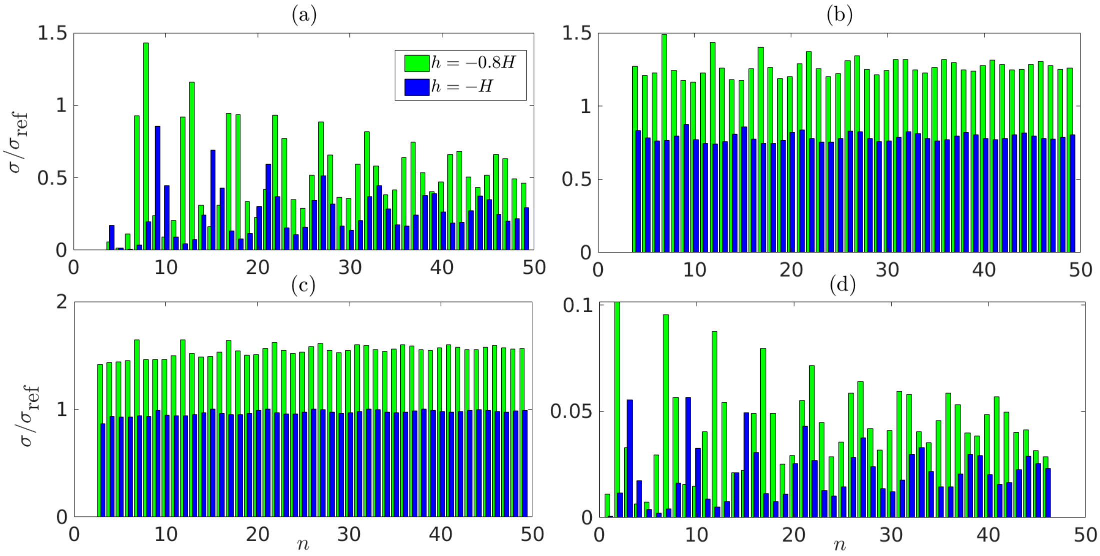

Figure 2.13: Plots of non-dimensional growth rates of mode-1 triads for profile $N^{(9)}$ with $f/\omega_3 = 0.4$ and $\omega_3/N_b = 0.2$. (a) Line (n, n) of Branch-1, (b) line $(n+1, n)$ of Branch-1, (c) line $(n, n+1)$ of Branch-1, and (d) line $(n+6, n)$ of Branch-2.

that line of interaction. For example, the interaction lines (n,n), ($n+1$,n) and (n,$n+1$) are plotted for $n \in (1, 50)$ in figures 2.12(a)–2.12(c) for Branch-1 triads, and ($n+4$,n) in figure 2.12(d) for Branch-2 triads. The notation (a,b) means wave-1(2) is mode-a(b). The notation is same for both branches. The dominant nature of the interaction lines (n,n), (n,$n+1$), ($n+1$,n) has also been observed in Young *et al.* (2008) while studying the stability of mode-1 internal wave in the presence of near inertial daughter waves (with frequency f). Furthermore, figure 2.12 also reveals that the different lines are sensitive to h. For completeness, we explore another stratification profile given by:

- $N^{(9)}$: $N_{\text{max}} = 10N_b$, $W_p = H/50$, $z_c = H/80$,

and the corresponding plots are in figure 2.13. Both figures 2.12 and 2.13 show that the growth rates along different lines of interaction have a significant oscillatory nature with n. In general, line (n, n) has the largest amplitude of oscillations. More importantly, the growth rate of a modal combination can significantly change as h changes. For example, figure 2.12(a) shows that the most unstable modal combination at $h = -H$ is (5,5). However, for $h = -0.8H$, the most unstable triad is the modal combination (4,4). Moreover, the combination (5,5) has approximately 0.25 times of (4,4) growth rate at $h = -0.8H$. This behavior can be seen for the line (n, n) in both figures 2.12 and 2.13. This effectively means that the growth rate of certain daughter wave combinations can be sensitive to changes in h (especially the combinations which involve lower modes). Such combinations may not be effective in a region of varying h because of the significant drop in the growth rates. However, sensitivity to h is slowly reduced as the modenumber is increased for both the branches. Even though Branch-2 triads have considerably less growth rates for the profiles $N^{(8)}$ and $N^{(9)}$, for different profiles (not displayed here) Branch-2 can have σ comparable to that of the Branch-1 triads. Growth rate of some particular modal combinations rapidly changes in certain scenarios as the depth is varied. This is due to a combination of factors such as the change in wavenumber, wave's $z-$direction mode shape (ϕ_j) etc. The change in mode shape, which in turn effects the nonlinear coefficients (Γ's), can especially make the growth rates sensitive to changes in h. Note that nonlinear coefficients are terms that arise from projecting the nonlinear terms on to a wave's $z-$direction modal shape.

A particular example is given to highlight the change in nonlinear coefficients. The interaction $\mathcal{K}_{3(1)}, \mathcal{K}_{1(5)}, \mathcal{K}_{2(5)}$ at $h = -H$ and $h = -0.8H$ is studied, and the background stratification profile $N^{(8)}$ is taken. The growth rate at $h/H = -1$ is ten times more than

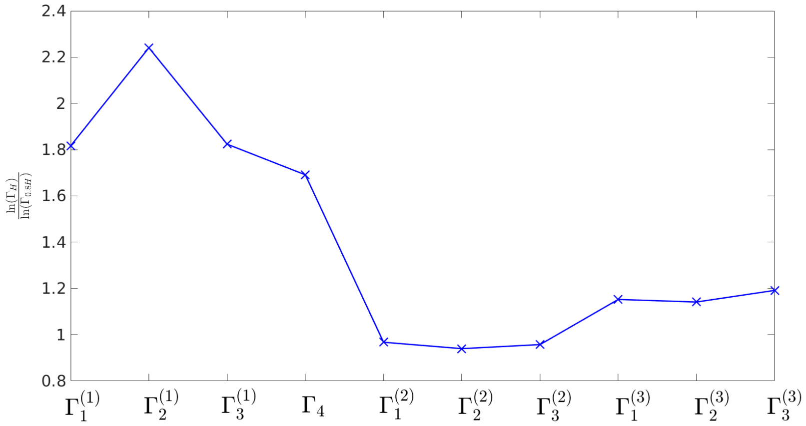

Figure 2.14: Variation of Γ as h/H is varied. Note that the y-axis is given in logarithmic scale.

$h = -0.8H$. A comparison between the nonlinear coefficients (Γ) at $h = -H$ and $h = -0.8H$ is plotted in figure 2.14. It can be seen that some of them vary by a factor of ≈ 9 due to the change in depth.

2.6.1.1 Effect of variation of f/ω_3 and ω_3/N_b on different Branches.

For both stratification profiles used in §2.6.1, $f/\omega_3 = (0.3, 0.45)$ for $\omega_3/N_b = (0.2, 0.7)$ is explored (hence total of 4 different combinations). For $N^{(8)}$, in all 4 cases, the qualitative behaviour of all Branch-1 lines are similar to figure 2.12. However, the maximum growth rate has a significant increase from $h = -H$ to $h = -0.8H$ for $\omega_3/N_b = 0.7$. Moreover, Branch-2 triads' maximum growth rate significantly increases in 2 cases of $f/\omega_3 = 0.3$ in comparison to $f/\omega_3 = 0.4$. For $N^{(9)}$, the qualitative behaviour of line (n, n) is similar to what was observed in $f/\omega_3 = 0.4$. In general, the maximum growth rate is the (n, n) modal combination. Interestingly, it is found that the maximum growth rate among all triads increased nearly twice from $h = -H$ to $h = -0.8H$ for $(f/\omega_3 = 0.45, \omega_3/N_b = 0.7)$. Significant increase in maximum growth rate is also found for $\omega_3/N_b = 0.2$ for the same f. For $(f/\omega_3 = 0.3, \omega_3/N_b = 0.7)$ the behaviour of line $(n+1, n)$ has a significant oscillation with n, similar to line (n, n). Note that this is different from the line $(n+1, n)$ shown in figure 2.13. In general, it is also observed that reducing the fluid depth increases the maximum growth rate of all possible triads even without considering the β term of the parent wave amplitude.

2.6.2 Variation of nonlinear coupling coefficient with domain height for self-interaction process

Here we restrict to self-interaction of internal gravity waves that do not experience significant detuning $\Delta\mathcal{K}$ with changes in h. In this subsection, we mainly focus on the superharmonic wave's nonlinear coupling coefficient $\mathcal{N}_3$ given in (2.51b).

2.6.2.1 Class-1 interactions

As previously mentioned in §2.5.2, some Class-1 self-interactions can have negligible detuning even for a finite range of h/H. We study the variation of $\tilde{\mathcal{N}}_3$ under such circumstances; the different interactions considered (denoted by $\mathcal{I}_p$) are given below:

$\mathcal{I}_1$ - $[P3, D2]$	$\mathcal{I}_2$ - $[P4, D2]$	$\mathcal{I}_3$ - $[P4, D3]$	$\mathcal{I}_4$ - $[P5, D3]$	$\mathcal{I}_5$ - $[P5, D4]$
$\mathcal{I}_6$ - $[P6, D3]$	$\mathcal{I}_7$ - $[P6, D4]$	$\mathcal{I}_8$ - $[P6, D5]$	$\mathcal{I}_9$ - $[P7, D4]$	$\mathcal{I}_{10}$ - $[P7, D5]$

Here the notation $[Pm, Dn]$ denotes that the parent wave is the $m-$th mode and daughter (superharmonic) wave is the $n-$th mode.

The stratification profiles are chosen such that $N_{\text{max}} = (2N_b, 5N_b, 10N_b)$, $W_p = (H/200, H/100, H/5$ and $z_c = (H/40, H/20, H/10)$. For the profiles considered, we study variations of $\tilde{\mathcal{N}}_3$ for interactions that strictly satisfy $|\Delta\mathcal{K}_s| < 0.01$ for $h/H \in [-1, -0.8]$. Figure 2.15 shows variations of $\tilde{\mathcal{N}}_3 \equiv |\mathcal{N}_3|/\text{max}(|\mathcal{N}_3|)$ for two Class-1 self-interactions. Figure 2.15 reveals that interactions can have a non-monotonic variation of $\tilde{\mathcal{N}}_3$ with h/H. Moreover, the figure reveals that even relatively small changes in h/H can lead to significant variations in $\tilde{\mathcal{N}}_3$. For all interactions considered in table 2.2, small changes in h/H can cause significant change in $\tilde{\mathcal{N}}_3$. Some generic features are summarised below. Sensitivity of $\tilde{\mathcal{N}}_3$ to h/H increases as z_c is increased for a given W_p, N_{max} [1]. Moreover, increasing W_p also increases the sensitivity of $\tilde{\mathcal{N}}_3$ to changes in h/H. Increasing N_{max} for a given (z_c, W_p) also increases the sensitivity of $\tilde{\mathcal{N}}_3$ to h/H.

---

[1] For every interaction, there are specific combinations of W_p, N_{max} where this behaviour is not exhibited.

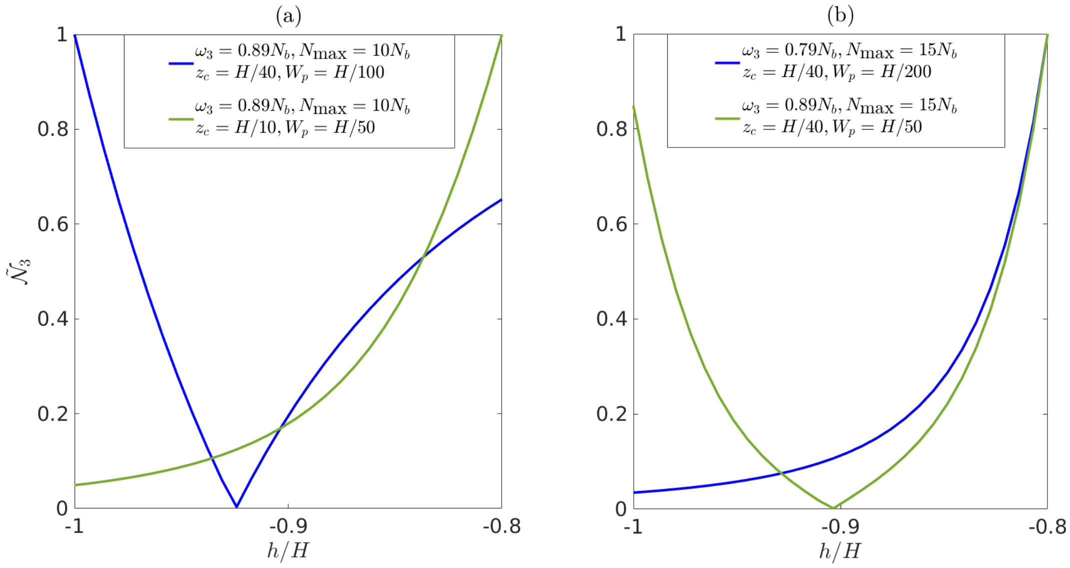

Figure 2.15: Variation of $\tilde{\mathcal{N}}_3$ with h for Class-1 self-interactions (a) $\mathcal{I}_1$ and (b) $\mathcal{I}_{10}$. Each sub-figure is plotted for two different stratification profiles (for details see legend).

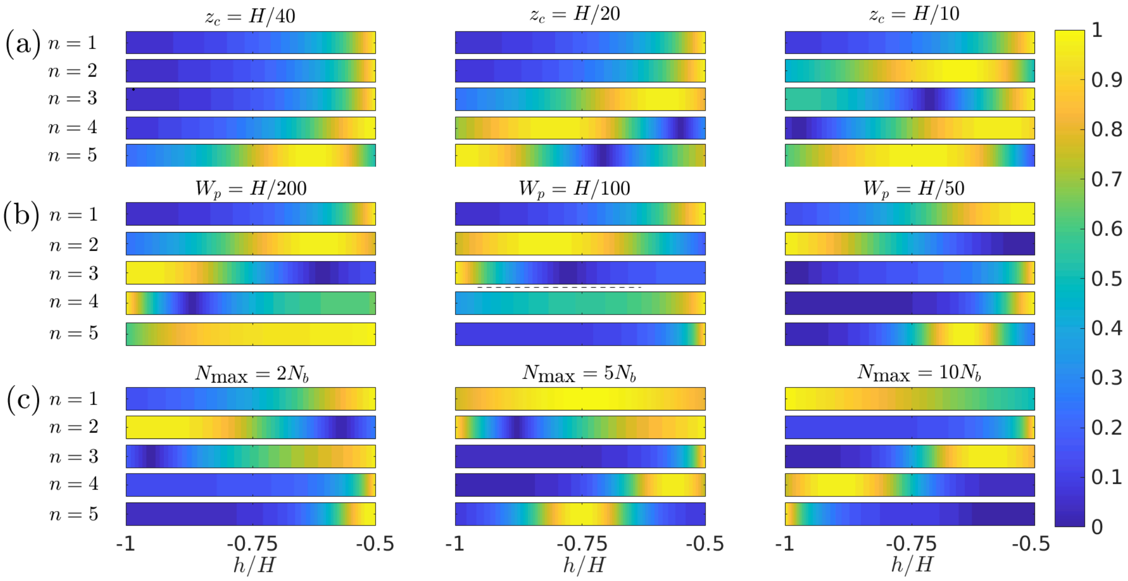

Figure 2.16: The variation of non-dimensionalised nonlinear coupling coefficient ($\tilde{\mathcal{N}}_3$) of wave-3 (the superharmonic wave) as h is varied. Altogether there are 9 blocks, each consisting of 5 units, and each unit represents the modenumber (given by n). For each block, $(N_{\max}, W_p, z_c)$ is fixed. The figure is further subdivided into three horizontal panels (each panel consisting of three blocks): (a) $N_{\max} = 2N_b$, $W_p = H/200$, and z_c is varied, (b) $N_{\max} = 5N_b$, $z_c = H/20$ and W_p is varied, and (c) $z_c = H/10$, $W_p = H/50$ and $N_{\max}$ is varied.

2.6.2.2 Class-2 interactions

We initially study the variation of $\mathcal{N}_3$ with h for Class-2 self interactions. To this end, we consider $\mathcal{N}_3$ of the first 5 modes for 27 different stratification profiles. Similar to the case of Class-1 self-interactions in §2.6.2.1, the stratification profiles are chosen such that $N_{\text{max}} = (2N_b, 5N_b, 10N_b)$, $W_p = (H/200, H/100, H/50)$, and $z_c = (H/40, H/20, H/10)$, where all possible (3^3) combinations are considered. Out of the $3^3 = 27$ combinations, 9 profiles are chosen for plotting figure 2.16 and thereby elucidating the effect of each individual parameter in the stratification profile. For all cases, $\omega_3 = 0.1N_b$ and $f = 0$. For some higher modes, the nonlinear coupling coefficient has a band like structure; there exists some range of h/H where $\tilde{\mathcal{N}_3}$ is significantly higher in magnitude than that corresponding to other values of h/H. For example, the mode $n = 5$ corresponding to $N_{\text{max}} = 5N_b$ in figure 2.16(c) reveals a large increase in $\tilde{\mathcal{N}_3}$ near $h/H \approx -0.75$, while it is much lower at either ends. Wunsch (2017) also observed such banded structure in the self-interaction of different modes as the stratification profile was changed. The reason behind the direct analogy between the observations in this chapter and that of Wunsch (2017) is as straightforward – when an internal wave travels to a different domain height, it essentially travels to a different stratification profile.

For mode-1, when z_c, W_p, N_{max} are all on the lower side, we observe that $\tilde{\mathcal{N}_3} \propto 1/h^4$. For higher N_{max}, even lower values of z_c and W_p do not have the property of $\tilde{\mathcal{N}_3} \propto 1/h^4$. In general for modes > 1, proportionality to $1/h^4$ is lost faster as z_c, W_p, N_{max} is increased. In several profiles, $\tilde{\mathcal{N}_3}$ of higher modes is also more sensitive to changes in h than $\tilde{\mathcal{N}_3} \propto 1/h^4$.

2.7 Higher order self-interactions in the presence of a small amplitude monochromatic topography

The focus of this section is on higher order self-interactions between a parent wave of frequency ω_1 and a superharmonic daughter wave of frequency $\omega_3 = 2\omega_1$ in the presence of a small amplitude monochromatic topography. In such kind of scenarios, the topography can act as a 'zero frequency wave', which can lead to resonant higher order interactions, and is similar to the Class-2 studied in Alam *et al.* (2009) for surface gravity waves. The pathways by which a parent wave provides its energy to a daughter wave through higher order self interaction is given in figure 2.17. Such kind of higher order self-interactions

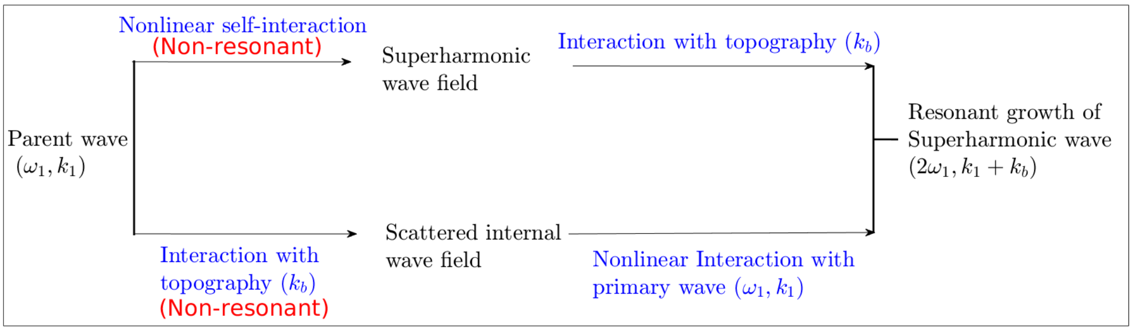

Figure 2.17: Schematic of a higher order self interaction.

might be important for mode-1 internal waves propagating in regions where $f > \omega_d/2$ (ω_d is the semidiurnal frequency), since triad interactions involving two (subharmonic) daughter waves is not possible. Moreover, resonant self-interaction for mode-1 internal wave of frequency ω_d is also not possible when $f > \omega_d/2$ for any stratification profile as a consequence of its dispersion relation (Wunsch, 2017). This arises from the fact that a mode-1 parent wave with frequency ω_d and a superharmonic daughter wave with frequency $2\omega_d$ fail to satisfy the horizontal wavenumber condition for a self-interaction process. Moreover, it is believed that the result is applicable for any stratification profile. This is a consequence of the dispersion relation being influenced by the $(\omega^2 - f^2)$ term in the denominator as shown below:

$$\frac{d^2\phi}{dz^2} + k^2\frac{N^2 - \omega^2}{\omega^2 - f^2}\phi = 0 \tag{2.68}$$

The $(\omega^2 - f^2)$ in the denominator provides a lower bound for detuning which will make the interaction detuned for any N profile. If $\omega \ll N$, then the above equation can be written as,

$$\frac{d^2\phi}{dz^2} + \hat{k}^2(N^2)\phi = 0 \tag{2.69}$$

where $\hat{k} = k^2/(\omega^2 - f^2)$. Note that for a particular N^2, eigenvalue spectrum $(\hat{k}^2)$ is fixed. For resonance, (ω, k) and $(2\omega, 2k)$ must satisfy the dispersion relation. In other words,

$$\frac{k^2}{(\omega^2 - f^2)} = \hat{k}_n \qquad \text{and} \qquad \frac{4k^2}{(4\omega^2 - f^2)} = \hat{k}_n \tag{2.70}$$

should be satisfied. $\hat{k}_n$ is the $n-$th eigenvalue of equation (2.69). This will not be possible as $f \to \omega$ for any $\hat{k}_n$ and hence N profile.

Higher order interactions are different from Bragg resonance focused in Buhler & Holmes-Cerfon (2011), which is also a mechanism via which a parent mode–1 wave can decay by transferring its energy to the higher modes. In a standard Bragg resonance, resonant wave-topography interaction occurs if the bottom topography has a wavenumber k_b such that $(\omega_1, k_b \pm k_1)$ satisfies the dispersion relation. More details on Bragg resonance are given in Chapter 4.

To study higher order self-interactions, we follow the streamfunction ansatz used in Couston *et al.* (2017) for studying internal wave Bragg resonance, and in Lahaye & Smith (2020) for studying internal wave scattering due to interaction with a large amplitude topography. This ansatz for the streamfunction of the $j-$th wave is as follows:

$$\Psi_j = \mathcal{A}_j(x)\phi_j(\eta; x)\mathrm{e}^{-\mathrm{i}\omega_j t} + \text{c.c.}. \tag{2.71}$$

The corresponding buoyancy frequency and meridional velocity is given by

$$\mathbb{B}_j = \frac{\mathrm{i}N^2}{\omega_j}\frac{\partial \mathcal{A}_j}{\partial x}\phi_j \mathrm{e}^{-\mathrm{i}\omega_j t} + \text{c.c.}., \tag{2.72}$$

$$\mathbb{V}_j = \frac{\mathrm{i}f}{\omega_j}\frac{\mathcal{A}_j}{h}\frac{\partial \phi_j}{\partial \eta}\mathrm{e}^{-\mathrm{i}\omega_j t} + \text{c.c.}. \tag{2.73}$$

The above-mentioned ansatz can also be used to study systems where the detuning $\Delta\mathcal{K}_s \sim \mathcal{O}(1)$ in the presence of a flat or slowly varying bathymetry. The functions ϕ_j are same as the functions used in §2 and are given by solving (2.27b). Here only small amplitude topography whose wavenumber is comparable to the parent wave is considered ($\epsilon_h \ll \mathcal{O}(1)$ and $\epsilon_k \sim \mathcal{O}(1)$).

To study higher order interactions of a parent wave propagating in the presence of a small amplitude topography, we also consider the linear scattering of the parent wave. Note that the linear scattering of the parent wave on its own is not resonant (resonant Bragg scattering is not allowed) and hence over a long distance has a negligible effect on the parent wave's amplitude. Note that resonant Bragg scattering is a more dominant decay mechanism than the higher order self interaction. To illustrate higher order self interaction, we needed to select cases where resonant Bragg scattering is negligible. However, even the non-resonant linear interaction of the parent wave with the topography, which leads to higher modes with ω_1 frequency, can significantly impact the growth of the superharmonic wave. To derive the linear scattering of the parent wave as it moves through a topography, we assume the streamfunction of the waves to be:

$$\Psi_1 = \sum_{n=1}^{n=M_n} \mathcal{A}_{(1,n)}(x)\phi_{(1,n)}(\eta;x)\mathrm{e}^{-\mathrm{i}\omega_1 t} + \text{c.c..} \tag{2.74}$$

where M_n is the maximum mode number after which the series is truncated, and $\phi_{(1,n)}$ is the $n-$th eigenfunction of ω_1 frequency. The streamfunction ansatz (2.74) is substituted in (2.18), and similar to §2.3, the linear terms of (2.18) is multiplied by $\phi_{(1,n)}$ and integrated in the η direction. This leads to M_n ordinary differential equations, where the $n-$th differential equation is given by:

$$\begin{aligned}\gamma_n^{(3)}\left[\frac{\partial^2\mathcal{A}_{(1,n)}}{\partial x^2}+\mathcal{K}^2_{(1,n)}\frac{\mathcal{A}_{(1,n)}}{h^2}\right] = &-\sum_{m=1}^{m=M_n}\left[\frac{2\gamma^{(5)}_{(m,n)}+\gamma^{(6)}_{(m,n)}}{h^2}\left(\frac{\partial h}{\partial x}\right)^2-\frac{2\gamma^{(7)}_{(m,n)}}{h}\frac{\partial h}{\partial x}\right]\mathcal{A}_{(1,m)}\\ &-\sum_{m=1}^{m=M_n}\left[\gamma^{(8)}_{(m,n)}-\frac{\gamma^{(5)}_{(m,n)}}{h}\left(\frac{\partial^2 h}{\partial x^2}\right)\right]\mathcal{A}_{(1,m)}\\ &-\sum_{m=1}^{m=M_n}2\left[\gamma^{(4)}_{(m,n)}-\frac{\gamma^{(5)}_{(m,n)}}{h}\frac{\partial h}{\partial x}\right]\frac{\partial\mathcal{A}_{(1,m)}}{\partial x},\end{aligned} \tag{2.75}$$

where $\mathcal{K}_{(1,n)}$ is the corresponding eigenvalue of $\phi_{(1,n)}$. Moreover $\gamma^{(*)}_{(m,n)}$ are evaluated using the expressions given in section 2.3.2.1. The above set of equations are similar to the equations derived in Lahaye & Smith (2020), except that we do not consider waves that travel in the direction opposite to the parent wave since they are assumed to be negligible. Now that we have the full wave spectrum with ω_1 frequency by solving (2.75), we model the evolution of the superharmonic wave. For simplicity, the feedback to the parent wave is neglected, which is analogous to the pump-wave approximation used in §2.3.

The streamfunction of the superharmonic wave Ψ_3 is substituted in (2.18), and the linear terms are multiplied by ϕ_3 and integrated in the η direction. This leads to:

$$\begin{aligned}\text{LIN}_3 \equiv &\left[\left(\gamma_3^{(3)}\frac{\partial^2\mathcal{A}_3}{\partial x^2}\right)+\mathcal{K}_3^2\left(\frac{\mathcal{A}_3}{h^2}\gamma_3^{(3)}\right)\right]\mathrm{e}^{-\mathrm{i}\omega_3 t}+2\left[\frac{\gamma_3^{(5)}}{h^2}\left(\frac{\partial h}{\partial x}\right)^2-\frac{\gamma_3^{(7)}}{h}\frac{\partial h}{\partial x}\right]\mathcal{A}_3\mathrm{e}^{-\mathrm{i}\omega_3 t}\\ &+\left[\frac{\gamma_3^{(6)}}{h^2}\left(\frac{\partial h}{\partial x}\right)^2-\frac{\gamma_3^{(5)}}{h}\left(\frac{\partial^2 h}{\partial x^2}\right)+\gamma_3^{(8)}\right]\mathcal{A}_3\mathrm{e}^{-\mathrm{i}\omega_3 t}+2\left(\gamma_3^{(4)}-\frac{\gamma_3^{(5)}}{h}\frac{\partial h}{\partial x}\right)\frac{\partial\mathcal{A}_3}{\partial x}\mathrm{e}^{-\mathrm{i}\omega_3 t},\end{aligned} \tag{2.76}$$

LIN_3 only contains linear terms, and models the propagation of superharmonic wave in the presence of a topography. Note that superharmonic wave cannot exchange energy with higher modes of ω_3. Now we move on to deriving the nonlinear terms which force the superharmonic wave. Since we are focusing on higher order interactions, all nonlinear terms (including terms containing $x-$direction derivatives of ϕ and h), which have the same angular frequency as the superharmonic wave, are retained. In the terrain following coordinates, this would however lead to a large number of terms that need to be evaluated. This issue can be circumvented following the procedure outlined below. The nonlinear terms in the terrain following coordinates are given by right hand side of (2.18).

We assume that the superharmonic wave is forced nonlinearly by the ω_1 spectrum. To model this, we substitute $\Psi_1, \mathbb{B}_1, \mathbb{V}_1$ into the nonlinear terms of (2.18). Note that we can obtain $\mathbb{B}_1$ and $\mathbb{V}_1$ from (2.72) and (2.73) respectively.

After the substitution, similar to the linear terms of wave-3, the nonlinear terms are multiplied by ϕ_3 and integrated in η direction within the domain limits. The resultant expression obtained is as follows:

$$\mathrm{NonL}_3 = \int_{-1}^{0} \phi_3 \left[\mathrm{i}\omega_3 \mathcal{J}\{(L_{xx} + L_{\eta\eta})\Psi_1, \Psi_1\} + L_x \left(\mathcal{J}\{\mathbb{B}_1, \Psi_1\}\right) - f L_\eta \left(\mathcal{J}\{\mathbb{V}_1, \Psi_1\}\right)\right] d\eta. \tag{2.77}$$

Therefore the final superharmonic wave equation can be written in a compact form:

$$\mathrm{LIN}_3 = \mathrm{NonL}_3. \tag{2.78}$$

In equations (2.76) and (2.77), instead of splitting $\mathcal{A}_j$ into a product of slowly varying amplitude and rapidly varying phase part, we simply solve the equations numerically by retaining $\mathcal{A}_j$ as it is. This is mainly because, as mentioned above, the number of nonlinear terms would be significantly high in terrain following coordinates. For high ratios of f/ω_1 (for example, north of critical latitude), the parent wave cannot resonantly self interact with the superharmonic wave in the presence of a flat bottom. However, a resonant higher order self-interaction can occur provided the topography has a wavenumber k_b such that:

$$k_b = k_3 - 2k_1, \tag{2.79}$$

where k_3 is the wavenumber of the superharmonic wave and the k_1 is the wavenumber of the parent wave. In such scenarios, the daughter wave's amplitude will consistently grow. However this being a higher order interaction, the growth rate of daughter wave (consequently, the decay of the parent wave) can be expected to be slower than a resonant self interaction. The choice of k_b is indeed special here, however, the system is similar to Bragg resonance focused in Refs. Couston *et al.* (2017); Buhler & Holmes-Cerfon (2011)

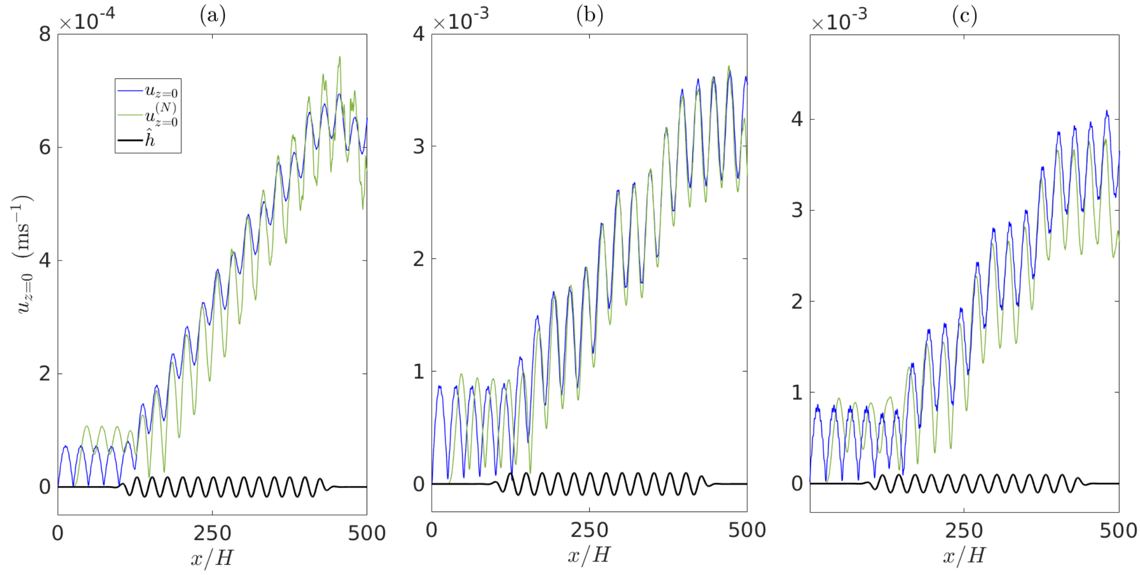

Figure 2.18: Higher order self-interaction of mode-1 internal wave in the presence of a monochromatic bathymetry for three different cases: (a) Case-1, (b) Case-2, and (c) Case-3. $u_{z=0}$ and $u^{(N)}_{z=0}$ denote the results obtained from the reduced order model and the 2D Boussinesq equations, respectively. The topography profile (not to scale) is shown for all three cases.

where resonance occurs only for a specific set of k_b. Moreover, under small amplitude topography assumption, the 'non-resonant' wavenumbers in the bathymetry cannot influence the growth due to resonant wavenumbers if they are present. Even if a spectrum of wavenumbers are present, as long as a specific wavenumber is resonant, then resonant interactions will occur. This is a consequence of the small amplitude bottom boundary condition.

To elucidate and validate the higher order self interaction process, we perform numerical simulations by solving the complete 2D Boussinesq equations and comparing the output with the results of the reduced order model derived in this section. We run three simulations where the parent and daughter waves' frequencies are held fixed. They are denoted by Case-1, Case-2, and Case-3. For all the simulations, the parent wave frequency is $\omega_1/N_b = 0.2$, where ω_1 is the semi-diurnal frequency, i.e. $\omega_1 = 1.4 \times 10^{-4}\text{s}^{-1}$. Both the parent and daughter waves are mode-1 of their respective frequencies (ω_1 and $2\omega_1$). These parameters would result in a significant detuning between the two waves at high f values. The bathymetry profile is given by:

$$h = -H + [\epsilon_h H \sin\left(k_b(x - \text{Len}_x/2)\right)] \times \frac{1}{(1 + (x - \text{Len}_x/2)^{32}/W_T^{32})}, \qquad (2.80)$$

	W_p/H	z_c/H	$N_{\max}/N_b$	f/ω_d	$u_{\max}(\mathrm{ms}^{-1})$	W_T/Len_x
Case-1	1/16	1.5/1000	4.5	0.58	0.0120	0.30
Case-2	29.5/400	1.5/1000	7	0.64	0.0227	0.30
Case-3	1/20	1.5/1000	10	0.60	0.0232	0.31

Table 2.1: The stratification profile parameters, Coriolis frequency, W_T, and the velocity amplitude of the three waves for Case-1, Case-2, and Case-3.

where $\epsilon_h = 0.01$, $H = 3000\mathrm{m}$, and domain length $\mathrm{Len}_x = 540H$ are held fixed across all three simulations. The stratification profile parameters, f value, incoming maximum velocity of the parent mode ($u_{\max}$), and W_T for the three simulations are given in table 2.1. The results after solving the reduced order model and 2D Boussinesq equations for the above mentioned parameters are shown in figure 2.18. The 2D Boussinesq equations are solved using Dedalus. More details on the simulations are given in the end of §2.8. In all three sub-figures, the amplitude of the daughter wave is observed to be slowly increasing due to the higher order self-interaction. Moreover, the daughter wave's amplitude also rapidly oscillates because of the non-resonant standard self-interaction process between the parent wave and the daughter wave. In the absence of a varying bathymetry, only the rapid non-resonant interaction would be present without any consistent growth in the daughter wave's amplitude. The rapid oscillations that are much faster than the steady linear growth can be visualised in figure 2.17 for all the cases. Therefore we have shown that for scenarios where Bragg resonances are not resonant, higher order interaction might be a possible mechanism that can scatter the energy of the mode–1 internal wave.

2.8 Numerical Validation

In this section, numerical validations are provided for the reduced–order equations derived in section 2.3. We solve the 2D Boussinesq equations in terrain-following coordinates using an open–source, pseudo–spectral code Dedalus (Burns *et al.*, 2020), and compare the results with output of the reduced order models. Class-1 triad interactions and self-interactions are validated, and we begin with the Class-1 triad interactions.

2.8.1 Class-1 triad interactions

The 2D Boussinesq equations in primitive variables and in terrain following coordinates with diffusion/dissipation terms are given below:

$$\frac{\partial \mathbb{U}}{\partial t} + L_x(\mathbb{P}) + \mathbb{U}L_x(\mathbb{U}) + \mathbb{W}L_\eta(\mathbb{U}) - f\mathbb{V} = \text{Dif}(\mathbb{U}), \tag{2.81a}$$

$$\frac{\partial \mathbb{V}}{\partial t} + \mathbb{U}L_x(\mathbb{V}) + \mathbb{W}L_\eta(\mathbb{V}) + f\mathbb{U} = \text{Dif}(\mathbb{V}), \tag{2.81b}$$

$$\frac{\partial \mathbb{W}}{\partial t} + L_\eta(\mathbb{P}) + \mathbb{U}L_x(\mathbb{W}) + \mathbb{W}L_\eta(\mathbb{W}) = \text{Dif}(\mathbb{W}) + \mathbb{B}, \tag{2.81c}$$

$$\frac{\partial \mathbb{B}}{\partial t} + N^2\mathbb{W} + \mathbb{U}L_x(\mathbb{B}) + \mathbb{W}L_\eta(\mathbb{B}) = \text{Dif}(\mathbb{B}), \tag{2.81d}$$

$$L_x(\mathbb{U}) + L_\eta(\mathbb{W}) = 0. \tag{2.81e}$$

Here $(\mathbb{U}, \mathbb{W}) = (L_\eta(\Psi), -L_x(\Psi))$, which are the equivalent velocity field defined in x–η instead of x–z coordinates. The operator Dif() is used for dissipation and diffusing small scale waves. It is defined as

$$\text{Dif}() \equiv \nu L_{\eta\eta}() + \left(\nu\frac{\partial^2}{\partial x^2}() + \nu_{12x}\frac{\partial^{12}}{\partial x^{12}}()\right) \tag{2.82}$$

where $\nu \sim 10^{-5}\text{m}^2\text{s}^{-1}$ and $\nu_{12x} \sim 10^{25}\text{m}^{12}\text{s}^{-1}$ are used for all simulations. For the time-stepping, modified Crank-Nicholson method is always used, and 500 time steps are used per one time period of the parent wave. The vertical direction is resolved using Chebyshev polynomials, where 128 or 160 grid points/polynomials are used. The horizontal direction is resolved using 768 or 862 Fourier modes. The reduced order equations (2.45a)–(2.45c) are solved using RK4 method for time-stepping and second order accurate discretization scheme for the term $\partial a_j/\partial x$, where the scheme is forward or backward depending on the group speed direction of the particular wave.

In this subsection, 3 pairs of Class-1 triad simulations are run, and for each pair, one is for varying fluid depth (denoted by Case-j) while the other is for flat topography (denoted by Case-(j+3)), where $j = 1, 2, 3$. The bathymetry profile ($h(x)$) is the same for Cases-1, -2, and -3, and is given by

$$h(x) = -H + 0.2H \exp\left[-(x - \text{Len}_x/2)^2/(0.15\text{Len}_x)^2\right]. \tag{2.83}$$

Here $H = 3000$m, and $\text{Len}_x = 1000H$. For flat topography, $h(x) = -H$ is taken consistently. Note that the topography used is a Gaussian shaped topography. For shapes

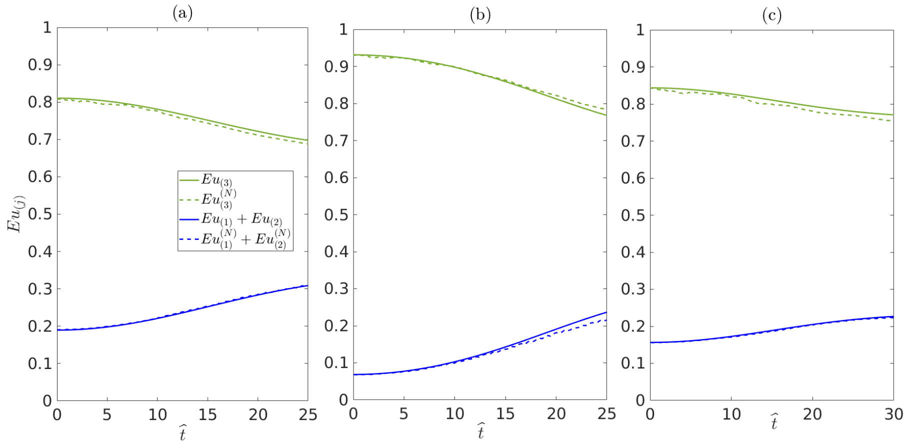

Figure 2.19: Class-1 interactions in the presence of a topography. (a) Case-1, (b) Case-2, and (c) Case-3. $\hat{t} \equiv \omega_3 t/2\pi$. Superscript '$(N)'$ denotes results from 2D Boussinesq equations.

that are very close to the Gaussian shape, internal wave mode-mode coupling may not be present at all (Maas, 2011). Hence the results can be sensitive to the topography shape as well.

The stratification profile (2.60) is used again, and N_{max}, W_p, and z_c used in the three pairs of simulations are given in table 2.2.

At $t = 0$, the wave packets in Case-j and Case-(j+3) (for $j = 1, 2, 3$) have the same energy in the presence of the same background stratification profile. In this way, the energy transfer between wave packets having same initial energy, modenumber, and frequency are compared in the presence of a flat and a non-flat topography. Non-zero Coriolis frequency is considered for all the simulations, and it is varied across the three pairs of simulations (see table 2.2). In all cases, the results obtained from the reduced order model with the results obtained from solving the full 2D Boussinesq equations are plotted.

For all simulations, $\omega_3/N_b = 0.2$ is taken with $N_b = 10^{-3}\text{s}^{-1}$, and (ω_3, k_3) is the parent wave (which is always mode-1). Moreover, modenumber, and the frequency of the waves are also given in table 2.2.

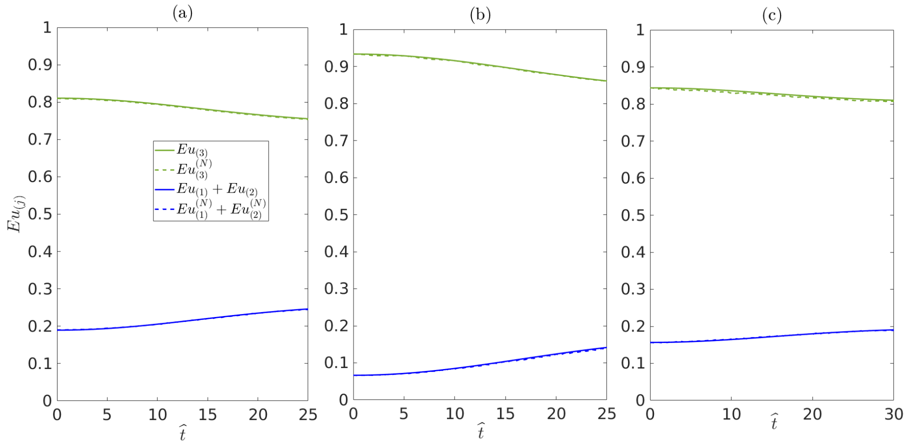

Figure 2.20: Class-1 interactions in a flat domain, with the wave-packets having the same energy as the packets in the presence of a topography. (a) Case-4, (b) Case-5, and (c) Case-6.

	W_p/H	z_c/H	N_{max}/N_b	f/ω_3	α	Waves-involved
Case-1&4	3/100	1/100	10	0.30	0.414	$(-\mathcal{K}_{1(3)}, \mathcal{K}_{2(4)}, \mathcal{K}_{3(1)})$
Case-2&5	2/100	1/100	8	0.20	0.432	$(-\mathcal{K}_{1(4)}, \mathcal{K}_{2(5)}, \mathcal{K}_{3(1)})$
Case-3&6	3/100	1/100	14	0.35	0.446	$(-\mathcal{K}_{1(5)}, \mathcal{K}_{2(6)}, \mathcal{K}_{3(1)})$

Table 2.2: Stratification profile parameters, Coriolis frequency, and the modal numbers of the three waves for Case-1&4, Case-2&5, and Case-3&6 are given.

The initial conditions used in the reduced order model are provided below. The wave-packet envelope of the streamfunction (a_j) for the three waves at $t = 0$ is given by:

$$a_j(x,0) = u_{(\text{max},j)} F(x) \left[\text{max} \left(2 \frac{F(x)}{h\beta_j} \frac{\partial \phi}{\partial \eta} \right) \Bigg|_{\eta=0} \right]^{-1},$$

$$F(x) = \left[\frac{1}{[1 + (x - \text{Len}_x/2)^8/(0.3\text{Len}_x)^8]} \exp\left(-(x - \text{Len}_x/2)^2/(0.3\text{Len}_x)^2\right) \right] \quad (2.84)$$

Because of the normalising constant, $u_{(\text{max},j)}$ would simply give the maximum u-velocity of the wave in the entire domain. $u_{(\text{max},j)}$ for the three waves in the three simulations with a varying h are given below:

- Case-1: $u_{(\text{max},1)} = 0.02\text{ms}^{-1}$, $u_{(\text{max},2)} = 0.00\text{ms}^{-1}$, $u_{(\text{max},3)} = 0.08\text{ms}^{-1}$.
- Case-2: $u_{(\text{max},1)} = 0.02\text{ms}^{-1}$, $u_{(\text{max},2)} = 0.00\text{ms}^{-1}$, $u_{(\text{max},3)} = 0.08\text{ms}^{-1}$.
- Case-3: $u_{(\text{max},1)} = 0.015\text{ms}^{-1}$, $u_{(\text{max},2)} = 0.00\text{ms}^{-1}$, $u_{(\text{max},3)} = 0.08\text{ms}^{-1}$.

Note that packets are on top of the topography at $t = 0$ for all three simulations with a varying h so that they can interact in a region of varying h. The evolution of the three waves' energy (Eu_j) obtained from theory and simulations is shown in figure 2.19 for all three cases with a varying h. The definition of Eu_j is given by:

$$Eu_j \equiv \frac{\int_{A^{(R)}} u_j^2 \, dA^{(R)}}{\int_{A^{(R)}} (u_1^2 + u_2^2 + u_3^2)|_{t=0} \, dA^{(R)}} \tag{2.85}$$

where the operator $\int_{A^{(R)}} dA^{(R)}$ denotes the quantity is integrated throughout the simulation domain. Note that using horizontal velocity field (u_j) alone is enough because in the simulations it was observed that $\int_{A^{(R)}} u_j^2 \, dA^{(R)} \approx \int_{A^{(R)}} (u_j^2 + w_j^2) \, dA^{(R)}$.

In the 2D Boussinesq simulations, the daughter waves' energy is isolated from the parent wave's energy by using the orthogonality property of the eigenfunction in the $z-$direction. The energy exchange between wave packets in a flat domain is given in figure 2.20. By comparing figures 2.19 and 2.20, it can be seen that the energy exchanged is different, which means that the energy transfer rate is different. Energy contained in each wave is found by using the orthogonality property of the functions $d\phi_j/dz$. Note that the orthogonality property is strictly valid only for waves with the same frequency as previously shown. However, for waves with $\omega_j \ll N$, the property can still be used with high accuracy.

Daughter waves at the end of Case-1 have 6.4% more energy than Case-4. Moreover, daughter waves at the end of Case-2 have 7.7% more energy than Case-5. Furthermore, daughter waves at the end of Case-3 have 3.4% more energy than Case-6. For the same energies at $t = 0$, the energy exchanged among the packets is higher in the presence of the topography considered, implying that the growth rates are also higher in comparison to the flat topography situation.

2.8.2 Self-interactions

The 2D Boussinesq equations used in this sub-section to validate self interactions are given by

$$\frac{\partial \mathbb{U}}{\partial t} + L_x(\mathbb{P}) + \mathbb{U}L_x(\mathbb{U}) + \mathbb{W}L_\eta(\mathbb{U}) = \nu L_{\eta\eta}(\mathbb{U}) + \left(\frac{\nu_{6z}}{H^6}\frac{\partial^6 \mathbb{U}}{\partial \eta^6} + \nu_{6x}\frac{\partial^6 \mathbb{U}}{\partial x^6}\right), \tag{2.86a}$$

$$\frac{\partial \mathbb{V}}{\partial t} + \mathbb{U}L_x(\mathbb{V}) + \mathbb{W}L_\eta(\mathbb{V}) = \nu L_{\eta\eta}(\mathbb{W}) + \mathbb{B}, \tag{2.86b}$$

$$\frac{\partial \mathbb{W}}{\partial t} + L_\eta(\mathbb{P}) + \mathbb{U}L_x(\mathbb{W}) + \mathbb{W}L_\eta(\mathbb{W}) = \nu L_{\eta\eta}(\mathbb{B}) + \left(\frac{\nu_{6z}}{H^6}\frac{\partial^6 \mathbb{B}}{\partial \eta^6} + \nu_{6x}\frac{\partial^6 \mathbb{B}}{\partial x^6}\right), \tag{2.86c}$$

$$L_x(\mathbb{U}) + L_\eta(\mathbb{W}) = 0. \tag{2.86d}$$

where $\nu = 10^{-5}\mathrm{m}^2\mathrm{s}^{-1}$, $\nu_{6x} = 10^8\mathrm{m}^6\mathrm{s}^{-1}$ and $\nu_{6z} = 81\mathrm{m}^6\mathrm{s}^{-1}$ is used consistently. For the time-stepping, modified Crank-Nicholson method is once again used for all simulations, and 1000 time steps are used per one time period of the parent wave. We estimate the validity of the reduced order equations (2.50a)–(2.50b) for two different cases. All the hyperviscous terms perform the same function: they damp the small scale waves which cannot be resolved without a tremendous increase in computational power. However, over the course of the study, we realised that some hyperviscous terms (numerically) are simply more efficient than the other terms. As a result, hyperviscous terms were changed in §2.8.1 and §2.8.2. We do not expect results to change with respect to the hyperviscous terms.

For Case 1, self interaction of a plane wave in the presence of a constant h is simulated. The parameters of the simulation are as follows: $H = 3000\mathrm{m}$ and $N_b = 10^{-3}\mathrm{s}^{-1}$. The frequency of the parent wave is taken as $\omega_1/N_b = 0.447$, while $f = 0$ is chosen. The stratification profile (2.60) is considered and the parameters used are:

- $N^{(13)}$: $N_{\mathrm{max}} = 3N_b$, $W_p = 3H/100$, $z_c = H/10$.

Mode-3 of parent wave frequency (ω_1) in this scenario resonantly self interacts with mode-2 of $2\omega_1$ (Varma & Mathur, 2017). The parent wave streamfunction input (initial condition) to the full numerical simulation is given by:

$$\Psi = A_1\phi_1 \sin(k_1 x)\exp(-(x - x_{\mathrm{PCK}})^2/W_{\mathrm{PCK}}^2), \tag{2.87}$$

where $|A_1| = 0.06$, $W_{\mathrm{PCK}} \to \infty$ is chosen (note that x_{PCK} can be any value since $W_{\mathrm{PCK}} \to \infty$). Ψ is used to obtain all the other fields. The numerical code is also initialised with the

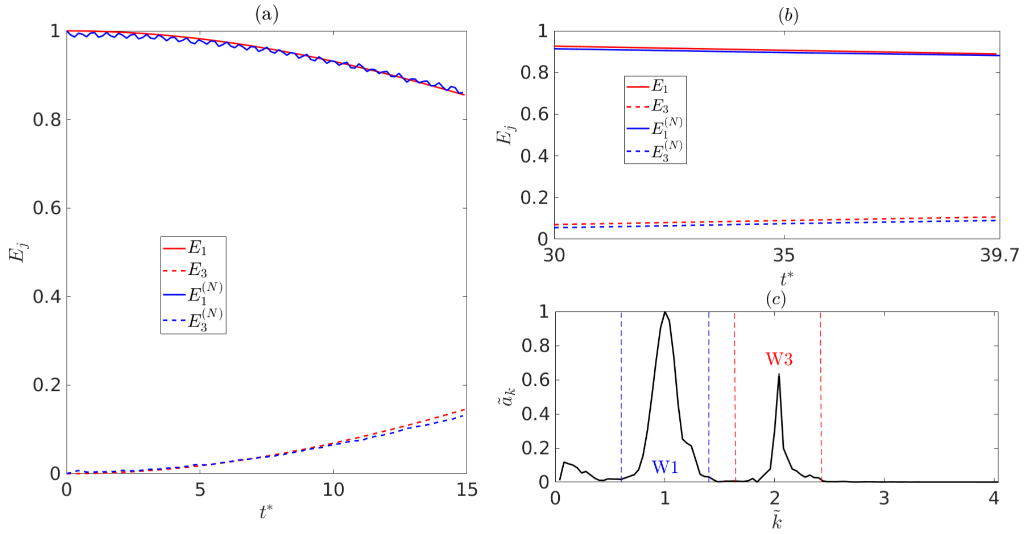

Figure 2.21: (a) The energy evolution of waves for Case-1 from reduced–order equations and numerical simulations. The superscript (N) denotes the results from numerical simulation of 2D Boussinesq equations. (b) The energy evolution of waves for Case-2 from reduced–order equations and numerical simulations in the time span $t^* = 30$ to $t^* \approx 40$, where $t^* \equiv \omega_1 t/2\pi$. (c) Fourier transform of $\mathbb{B}$ at $\eta = -0.42$ and $t^* = 40$.

corresponding buoyancy frequency for the streamfunction given in (2.87). The vertical (horizontal) direction is resolved using 192 Chebyshev (Fourier) modes.

For estimating the energy of parent and daughter waves from the numerical simulations, only the potential energy of the waves is considered. This is valid because when $f = 0$, energy is equally partitioned between potential energy and kinetic energy. For evaluating the potential energy of the two waves, we take the Fourier transform of $\mathbb{B}$ in the $x-$direction. Then by simply isolating the k_3 and k_1 wavenumbers, the respective fields due to wave-3 and wave-1 can be obtained for all time. The resulting energy evolution of the waves for Case 1 is shown in figure 2.21(a). At the end of the simulation, the parent wave energy was observed to be 86% of the total energy in the Boussinesq equations simulation, while the reduced order model predicted that 85.5% of the total energy will be contained in the parent wave at the specified time interval. Moreover, at the end of the simulation, the daughter wave's energy in Boussinesq equations simulation and the reduced order model are 13.0% and 14.4% respectively.

In Case 2, we consider the self interaction of a parent wave packet travelling in the presence of a slowly varying bathymetry. The parameters considered are as follows: $H = 3000$m and $N_b = 2.5 \times 10^{-3}\text{s}^{-1}$. The following stratification profile is used:

- $N^{(14)}$: $N_{\text{max}} = 5N_b$, $W_p = 3H/100$, $z_c = H/10$.

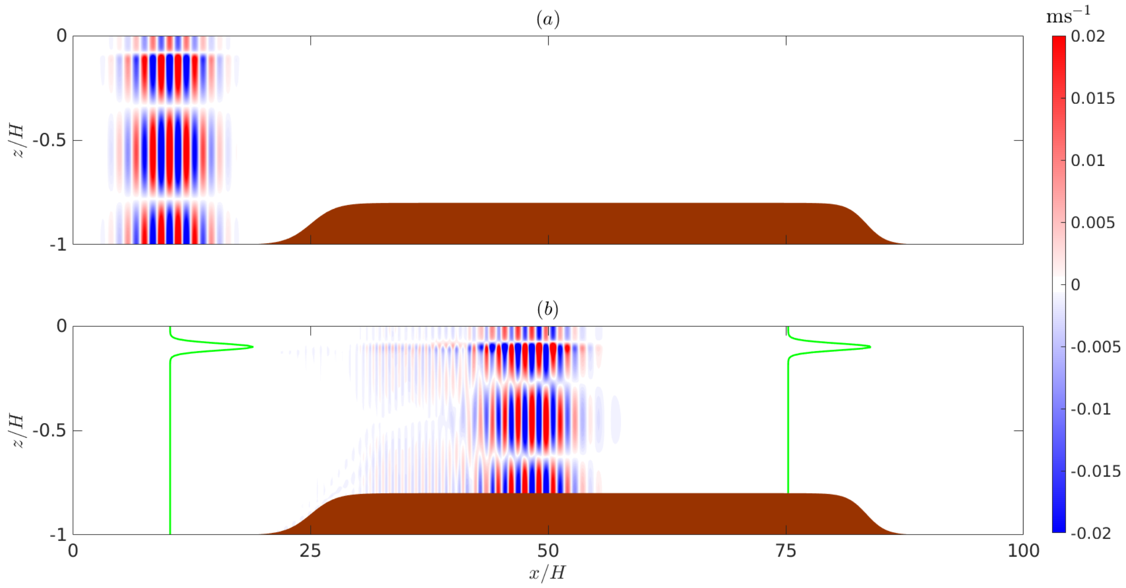

Figure 2.22: Horizontal velocity plot (u) from Case-2 simulation at (a) $t^* = 0$ and (b) $t^* = 30$. The stratification profile shape used is also shown for visual purposes. A faint but clear mode-2 trail left by the mode-3 parent wave can be seen at (b). The shape of the stratification profile used in Case-2 is given by green curves in (b).

$\omega_1/N_b = 0.447$ with $f = 0$ is chosen. Mode-3 of ω_1 resonantly self interacts with mode-2 of $2\omega_1$ for $h/H \in [-1, -0.8]$. The bathymetry is given by:

$$h = -H + 0.1H\left[\tanh((x - 25H)/2.7H) + \tanh((83H - x)/3.5H)\right], \tag{2.88}$$

and $\mathrm{Len}_x = 100H$ is taken. The bathymetry shape can be visualised in figure 2.22.

The parent wave streamfunction of the form (2.87) is used with $|A_1| = 0.022$, $W_{\mathrm{PCK}} = 3.57H$ and $x_{\mathrm{PCK}} = 10.2H$ is chosen. Here k_1 is evaluated at $h = -H$ for the initial conditions. The x_{PCK} value is chosen such that the wave packet is just at the bottom of the ‘plateau-like’ topography at $t = 0$ (as shown in figure 2.22(a)). The bathymetry is considered to be slowly varying so that the wave packet scattering by the bathymetry is negligible. For this simulation, the vertical direction is resolved using 144 Chebyshev polynomials, while the horizontal direction is resolved 576 Fourier modes.

The same procedure of energy evaluation as Case 1 is followed, except the energy is evaluated from $t^* = 30$, when the entire energy of both wave packets is almost confined to the top of the plateau region (where $h = -0.8H$). This makes the energy evaluation straightforward. We only consider $\mathbb{B}$ in the range $x/H \in [33, 68]$ (where most of the energy is contained), and then again perform Fourier transform to separate the energy of the daughter and parent wave packets.

In Case-2, since wave packets are considered, the Fourier transform of B would not have a sharp peak at k_1 and k_3. Instead, a smoother peak in k–space would be produced as shown in figure 2.21(c). We define a nondimensional wavenumber $\tilde{k}$ as $\tilde{k} \equiv k/k_1$. For evaluating the energy of both wave packets, amplitude ($|a_{\tilde{k}}|$) in a finite range of $\tilde{k}$ is considered. The energy contained in ($\tilde{k} \in [0.6, 1.4]$) is considered as the energy of the parent wave packet, while the energy in ($\tilde{k} \in [1.6, 2.4]$) is considered as the daughter wave's energy. For example, the $\tilde{k}$ range considered for the parent and daughter waves are highlighted in figure 2.21(c) using colored dotted lines for a specific η and t^*. For the parent wave, $|a_{\tilde{k}}|$ between the blue dotted lines is considered. Similarly for evaluating the energy of the daughter wave packet, we consider the amplitude ($|a_{\tilde{k}}|$) between the red dotted lines. The energy evolution of the wave packets are shown in 2.21(b). The Parent wave packet energy in Boussinesq equations simulation and the reduced order model was observed to be 88.1% and 88.9% respectively at the end of the simulations. At the same time, the daughter wave's energy in Boussinesq equations simulation and the reduced order model are 8.95% and 10.6% respectively.

We now briefly mention the method used to obtain the numerical results of higher order self interactions given in figure 2.18. Equations (2.81a)–(2.81e) were solved with $\nu_{12x} = 1.4 \times 10^{25}\text{m}^{12}\text{s}^{-1}$. The kinematic viscosity was chosen to be $\nu = 10^{-3}\text{m}^2\text{s}^{-1}$. The primary wave was forced by using a forcing function in the zonal momentum equation, which sends a constant amplitude mode-1 wave train onto the small amplitude topography.

2.9 Summary and Conclusion

Weakly nonlinear wave-wave interactions is one of the mechanisms through which internal gravity waves' energy cascade from large length scales (hundreds of kilometers) to small scales (centimeters to meters). At small length scales, internal waves can give rise to convective or shear instabilities (Koudella & Staquet, 2006) and cause mixing, thus resulting in increased diffusion in oceans. The 2D Boussinesq equations are written in terrain following coordinates (x–η). Using multiple-scale analysis, we derive the amplitude evolution equations for internal gravity waves undergoing weakly nonlinear wave-wave interactions in the presence of varying density stratification (resembling that of actual oceanic scenarios) as well as mild slope bathymetry in a vertically bounded domain. If the stratification varies with z in the x–z coordinates, then it becomes a function of both x and

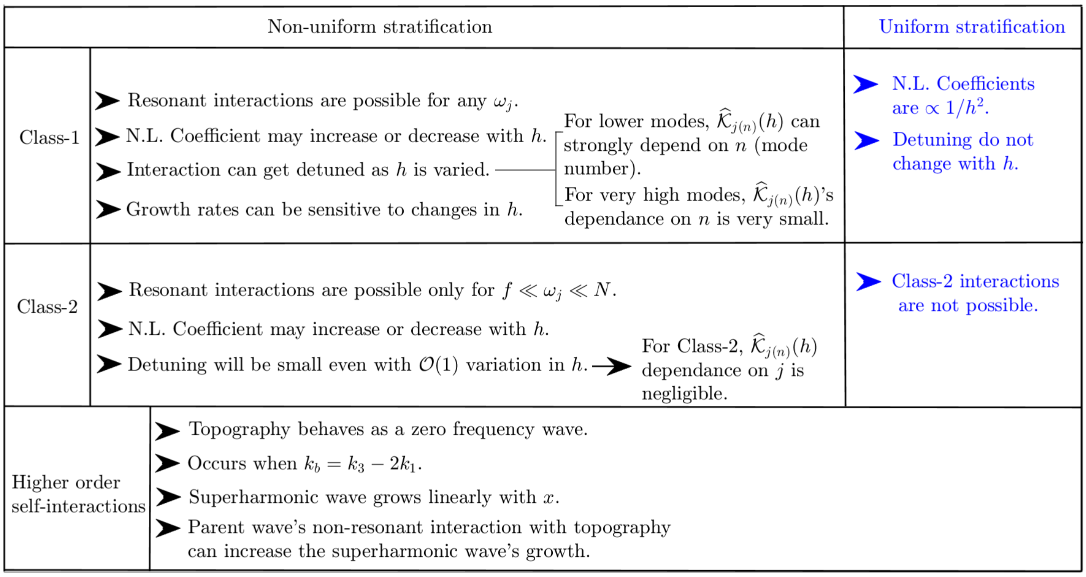

	Non-uniform stratification	Uniform stratification
Class-1	➤ Resonant interactions are possible for any ω_j. ➤ N.L. Coefficient may increase or decrease with h. ➤ Interaction can get detuned as h is varied. ➤ Growth rates can be sensitive to changes in h. For lower modes, $\widehat{\mathcal{K}}_{j(n)}(h)$ can strongly depend on n (mode number). For very high modes, $\widehat{\mathcal{K}}_{j(n)}(h)$'s dependance on n is very small.	➤ N.L. Coefficients are $\propto 1/h^2$. ➤ Detuning do not change with h.
Class-2	➤ Resonant interactions are possible only for $f \ll \omega_j \ll N$. ➤ N.L. Coefficient may increase or decrease with h. ➤ Detuning will be small even with $\mathcal{O}(1)$ variation in h. ➤ For Class-2, $\widehat{\mathcal{K}}_{j(n)}(h)$ dependance on j is negligible.	➤ Class-2 interactions are not possible.
Higher order self-interactions	➤ Topography behaves as a zero frequency wave. ➤ Occurs when $k_b = k_3 - 2k_1$. ➤ Superharmonic wave grows linearly with x. ➤ Parent wave's non-resonant interaction with topography can increase the superharmonic wave's growth.	

Figure 2.23: A summary diagram shows how different factors such as detuning, nonlinear coefficients can vary for different classes of interaction in the presence of non-uniform stratification. It also provides a brief picture of the higher order self interaction studied in §2.7.

η in the x–η coordinates when bathymetry, h, varies with x. In other words, the effective stratification profile varies with the ocean depth. Both triads and self-interactions are studied, and both pure resonant conditions as well as systems with wavenumber detuning are analyzed.

In the presence of uniform stratification, we show that the horizontal wavenumber triad condition, given by $k_{(1,a)} + k_{(2,b)} + k_{(3,c)} = 0$, is not violated due to changes in h. Here (a, b, c) are the modenumbers of waves 1, 2, and 3 respectively. Moreover, in the presence of uniform stratification, the nonlinear coupling coefficients are inversely proportional to the square of the fluid depth ($\propto 1/h^2$).

For non-uniform stratifications, we define two classes of interaction for both triads and self-interactions. Class-1 involves weakly nonlinear interactions of waves that do not have the same mode number. Class-2 is a special situation that involves interactions of waves with the same modenumber, i.e. $a = b = c$. Note that $a = b = c$ violates the vertical wavenumber condition in the presence of a uniform stratification. However, in the presence of non-uniform stratification, the vertical wavenumber is replaced by a non-orthogonality condition (Varma & Mathur 2017). This condition is not as stringent as the vertical wavenumber condition. Hence, there is no violation of the triad conditions. Class-2 triad interactions can exist only in the parameter regime of $f \ll \omega_j \ll N$. Moreover, in the same parameter regime, near-resonant Class-2 self-interactions can exist with very low detuning even as h is varied. This is because the wavenumbers involved in a self-interaction, change in the same way as h changes. For Class-1 interactions, detuning may be induced in triads and self-interactions if the waves interact in a region of varying h. This is because in a vertically bounded domain, the horizontal wavenumbers are not only a function of h but is also a function of the modenumber. Moreover, the functional dependence of the wavenumber on h may change as the modenumber changes. Therefore, in a weakly nonlinear interaction where different modenumbers are involved, there is no constraint for the wavenumbers to satisfy the triad condition in a given range of h.

The variation of the growth rate of the daughter waves in both triadic- and self-interactions is studied when h is varied. For both Class-1 and Class-2 self-interactions, it is observed that small changes in h may result in large changes in the growth rate of the daughter waves. This characteristic is especially observed for Class-1 self-interactions. Variation of growth rates with h is studied for triads of a mode-1 parent wave in the presence of non-uniform stratification. Triads were identified such that the daughter waves can be up to mode-50. For relatively small changes in h, the growth rates can vary significantly for triads that involve only lower modes. Moreover, the most unstable daughter wave combination for the same parent wave can also change for relatively small changes in h. Unlike uniform stratification, in non-uniform stratification, the growth rates do not have a monotonic behavior with h. This was observed for both triadic- and self-interactions.

Reduced-order equations for higher-order self-interactions of an internal wave in the presence of a small amplitude, monochromatic topography is also derived. In the higher-order self-interaction process, the small amplitude topography behaves as a zero frequency wave. It is shown that such higher-order interactions can cause resonant growth of the superharmonic wave. Such higher-order interactions can play a crucial role in the decay of the mode-1 internal wave at latitudes greater than $28.9°$. This is because sum-type triad interactions are not possible (Olbers *et al.*, 2020) and a mode-1 internal wave cannot resonantly self-interact for high values of f (Wunsch, 2017).

Chapter 3

5 wave interactions in internal gravity waves

3.1 Introduction

In the last chapter, the main focus was on the stability of a single internal wave mode in a vertically bounded domain. However, in the ocean, apart from low mode internal waves, vertically propagating internal waves (plane waves) are abundant as well. In this chapter, we study the stability of two weakly nonlinear plane parent waves that coexist in a region. The motivation for this study is parent internal waves generated in different locations meet/overlap in the oceans often. For example, tide-topography interactions result in the generation of internal waves that propagate in horizontally opposite directions, and these waves overlap and coexist above the topography. This is shown in figure 3.1. When two energetic parent waves meet in a region, they can resonantly interact with each other. Internal wave beam collision is an example of such direct interaction between the parent waves, and it has been studied extensively over the last few decades (Tabaei *et al.*, 2005; Jiang & Marcus, 2009; Akylas & Karimi, 2012). Parent waves, however, do not always resonantly interact with each other and form a triad. In the absence of direct interaction, each parent wave would still be susceptible to triad interactions leading to the growth of daughter waves, and this is the setting explored in this paper. Specifically, we focus on the 5-wave system instability. In this instability, five waves (two parent waves and three daughter waves) are involved, and two distinct triads are formed between the five waves. Note that this implies one daughter wave is forced by both parent waves and is a part of two different triads. Some examples of parent waves overlapping (that commonly occurs in the topographic generation of internal waves) are given in figures 3.2(a)–3.2(b). In both figures, the region enclosed inside the green box would be a potential location for a 5-wave system. The wavevector and frequency condition satisfied in a 5-wave system is given in figure 3.2(c). Note that the study in this chapter 3 focuses only on plane waves. The study can be extended to wave beams in the future, and the results would be applicable in cases where multiple internal wave beams meet (often occurs near topographies). A finite-width beam of a given frequency contains a spectrum of internal waves with different wavevectors. Interaction of involving beams means an interaction between two different spectrums of waves, and this is a much more complicated scenario than the one we have considered in the thesis. For simplicity, we chose to begin with plane waves. For two parent plane waves, there are only two wavevectors and as a result, the problem can be explored in depth for a wide parameter space. Note that the results should be applicable for wide internal wave beams since wide beams essentially behave like plane waves.

In the context of internal gravity waves, 5-wave systems have been studied recently (Pan *et al.*, 2021*a*,*b*). Pan *et al.* (2021*a*) focus on 5-wave systems where the same parent wave generates four different daughter waves, which is not the focus of this paper. Pan *et al.* (2021*b*) explore 5-wave interactions that consist of two parent waves and three daughter waves, but their focus is on rogue wave generation. They study the 5-wave systems in a 2D setting without the rotational effects. Moreover, no detailed study was conducted on the growth rates. In this paper, we consider a 3D setting with rotational effects, which is observed to be important in our case. The primary focus is on the growth rates of the daughter waves and to understand scenarios in which the 5-wave system instability is faster than the 3-wave system instability (standard triads). In our study, the frequencies of the two parent waves are always assumed to be the same, and this assumption can be important in an oceanographic context. This is because different internal waves generated by the same tide have the same frequency.

The remaining sections are organised as follows. In §3.2, we use multiple scale analysis to simplify the 3D, Boussinesq, Navier-Stokes equations in the $f-$plane and derive the wave amplitude equations. Expressions for growth rates are provided. In §3.3, theoretical comparisons between 3-wave systems' growth rates and 5-wave systems' growth rates for different combinations of parent waves are conducted. In §3.4, numerical validation is provided for the 5-wave system. The chapter is summarized in §3.5.

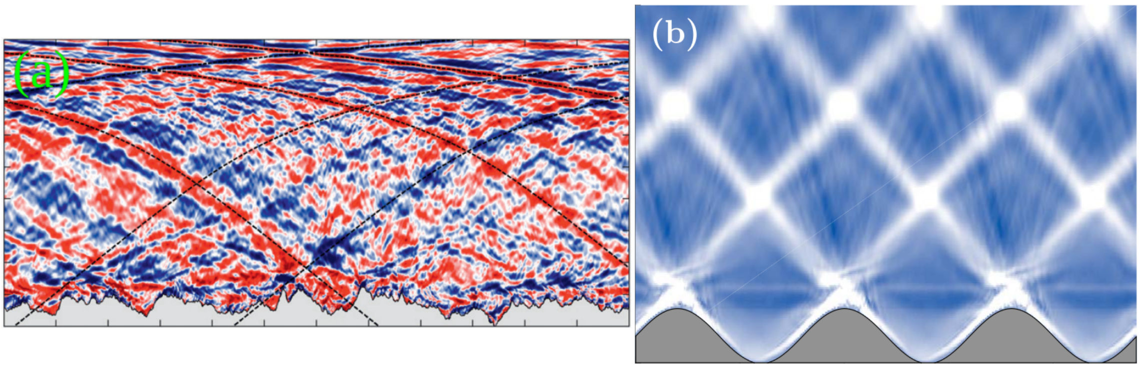

Figure 3.1: Simulations in (a) (Nikurashin & Legg, 2011) and (b) Richet *et al.* (2018) showing the parent wave intersections. The black dotted lines in (a) show the trajectory of the internal wave beam.

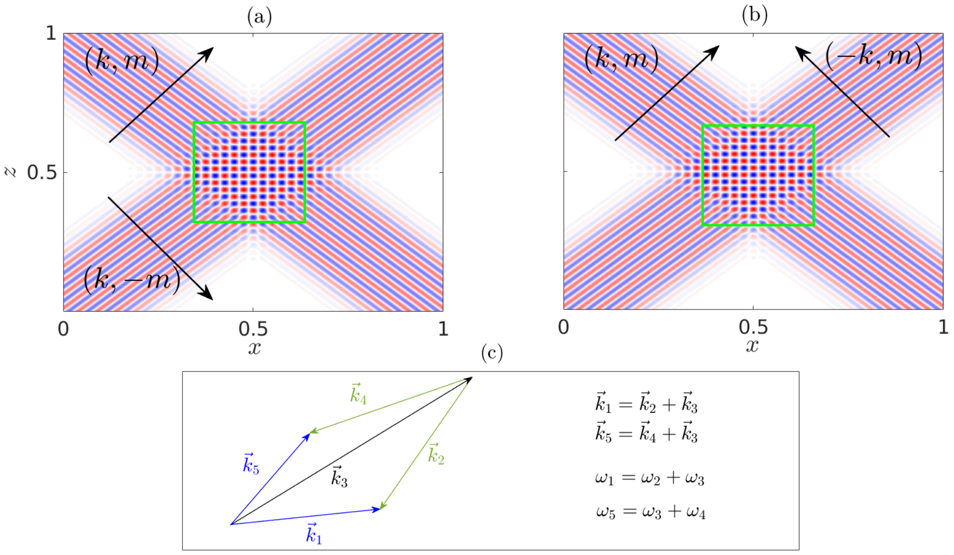

Figure 3.2: Examples of different orientations of propagating parent waves: in (a) vertically and (b) horizontally opposite directions, with the intersection region marked in green. (c) Frequency and wavevector triad conditions that are satisfied between the 5 waves that are involved in the interaction region. Waves 1 and 5 are parent waves, while waves 2,3, and 4 are daughter waves, with wave-3 being the common daughter wave.

3.2 Governing Equations and Multiple Scale Analysis

In this section, the 3D, incompressible, Boussinesq, Navier-Stokes equations in the $f-$plane and the advection-diffusion for the buoyancy in three dimensions is considered. The equations are given in Chapter 1, see (1.7)–(1.10) along with (1.13). Similar to the previous chapter, a multiple scale analysis approach is used to estimate the growth rate of the daughter waves. It is convenient to derive the reduced order equations by combining the above set of governing equations into a single equation. Following Neef (2004), the operation

$\partial/\partial t$(1.10) $-g/\rho_0$(1.13) is first performed which leads to:

$$\frac{\partial^2 w}{\partial t^2} + \frac{\partial}{\partial t}\left(\mathbf{u}.\nabla w\right) + N^2 w + \mathbf{u}.\nabla b = \frac{\partial}{\partial t}\left(-\frac{1}{\rho_0}\frac{\partial p'}{\partial z} + \nu\Delta w\right) + \kappa\Delta\left(b - \frac{g\rho_{\text{base}}}{\rho_0}\right) \tag{3.1}$$

where $\mathbf{u} = (u, v, w)$ is the velocity vector. Now to cancel the pressure term, ∇_h^2(3.1) $-$ $\partial/\partial t(\partial/\partial x(\partial/\partial z$(1.8)))$-\partial/\partial t(\partial/\partial y(\partial/\partial z$(1.9))) is conducted. This leads to (after some simplification),

$$\begin{align}
\frac{\partial^2(\nabla_h^2 w)}{\partial t^2} + \frac{\partial}{\partial t}\nabla_h^2\left(\mathbf{u}.\nabla w\right) + N^2(\nabla_h^2 w) \quad &= \quad \nu\frac{\partial}{\partial t}\left(\Delta^2 w\right) + \nabla_h^2(\kappa\Delta b) \nonumber\\
+ \nabla_h^2(\mathbf{u}.\nabla b) - \frac{\partial^3(\mathbf{u}.\nabla u)}{\partial x\partial z\partial t} - \frac{\partial^3(\mathbf{u}.\nabla v)}{\partial y\partial z\partial t} \quad & \quad - f\frac{\partial^3 v}{\partial x\partial z\partial t} + f\frac{\partial^3 u}{\partial y\partial z\partial t} \tag{3.2}
\end{align}$$

where $\nabla_h^2 \equiv \partial^2/\partial x^2 + \partial^2/\partial y^2$. Using (1.8) and (1.9), the term $f\partial^3 u/\partial y\partial z\partial t - f\partial^3 v/\partial x\partial z\partial t$ can be re-written as,

$$\begin{align}
f\frac{\partial^3 u}{\partial y\partial z\partial t} - f\frac{\partial^3 v}{\partial x\partial z\partial t} = &- \frac{\partial^2(\mathbf{u}.\nabla u)}{\partial y\partial z} + \frac{\partial^2(\mathbf{u}.\nabla v)}{\partial x\partial z} + f^2\frac{\partial^2 u}{\partial x\partial z} + f^2\frac{\partial^2 v}{\partial y\partial z} \nonumber\\
&+ f\nu\frac{\partial^2(\Delta u)}{\partial y\partial z} - f\nu\frac{\partial^2(\Delta v)}{\partial x\partial z} \tag{3.3}
\end{align}$$

Using $\nabla.\mathbf{u} = 0$ and (3.3), (3.2) can be further simplified to,

$$\frac{\partial^2(\Delta w)}{\partial t^2} + N^2(\nabla_h^2 w) + f^2\frac{\partial^2 w}{\partial z^2} + \text{NLT} \quad = \quad \text{VT} \tag{3.4}$$

where NLT denotes all the nonlinear terms, and is given by,

$$\begin{align}
\text{NLT} = \nabla_h^2\frac{\partial(\mathbf{u}.\nabla w)}{\partial t} + \nabla_h^2(\mathbf{u}.\nabla b) - \frac{\partial^3(\mathbf{u}.\nabla u)}{\partial x\partial z\partial t} \tag{3.5}\\
+ f\frac{\partial^2(\mathbf{u}.\nabla u)}{\partial y\partial z} - f\frac{\partial^2(\mathbf{u}.\nabla v)}{\partial x\partial z} - \frac{\partial^3(\mathbf{u}.\nabla v)}{\partial y\partial z\partial t} \tag{3.6}
\end{align}$$

Moreover, VT denotes all the viscous terms and is given by,

$$\text{VT} = \nu\frac{\partial}{\partial t}\left(\Delta^2 w\right) + \nabla_h^2(\kappa\Delta b) + f\nu\frac{\partial^2(\Delta u)}{\partial y\partial z} - f\nu\frac{\partial^2(\Delta v)}{\partial x\partial z} \tag{3.7}$$

For simplicity, $\kappa = 0$ is assumed hereafter. Furthermore, the primary focus is on plane waves. Similar to the procedure used in Bourget *et al.* (2013), the vertical velocity of the $j-$th wave $(j = 1, 2, \ldots, 5)$ is assumed to be a product of a rapidly varying phase and an amplitude that slowly varies in time. Mathematically this can be written as

$$w_j(x, y, z, t) = a_j(\epsilon_t t) \exp\left[\mathrm{i}(k_j x + l_j y + m_j z - \omega_j t)\right] + \text{c.c.}, \tag{3.8}$$

where k_j, l_j, m_j, and ω_j are respectively the zonal wavenumber, meridional wavenumber, vertical wavenumber, and frequency of the $j-$internal wave. The amplitude is assumed to evolve on a slow time scale $\epsilon_t t$, where ϵ_t is a small parameter. Moreover, a_j itself is $\mathcal{O}(\epsilon_a)$, where $\epsilon_a \ll 1$. Basically ϵ_a is chosen such that waves have small steepness, and this is the condition needed for the resonant wave-wave interaction instability to occur (Koudella & Staquet, 2006). Note that the amplitude only varies in time unlike the previous chapter. This is because the primary focus is here on growth rates, and the temporal variation alone is sufficient for that. Significant focus is not given to the finite width effects that can arise when the amplitude is also a function of space. On substituting (3.8) in (3.4), at the leading order ($\mathcal{O}(\epsilon_a)$) we obtain the dispersion relation in 3D:

$$\omega_j^2 = \frac{N^2(k_j^2 + l_j^2) + f^2 m_j^2}{k_j^2 + l_j^2 + m_j^2}. \tag{3.9}$$

All 5 waves involved in the interaction must satisfy this dispersion relation. Energy transfer between the waves due to weakly nonlinear wave-wave interactions occurs at $\mathcal{O}(\epsilon_a^2)$. For the j-th wave, the amplitude evolution equation reads

$$\mathcal{D}_j^{(3)} \frac{\partial a_j}{\partial t} = -\mathrm{NLT}_j + \mathrm{VT}_j, \tag{3.10}$$

where $\mathcal{D}_j^{(3)} \equiv 2\mathrm{i}\omega_j(k_j^2 + l_j^2 + m_j^2)$ is defined for convenience. NLT_j and VT_j represent all the nonlinear and viscous terms with the phase of the $j-$th wave, respectively. The expression for VT_j is given by

$$\mathrm{VT}_j = -\mathcal{D}_j^{(3)} \nu/2 \left(\frac{f^2 m_j^2}{\omega_j^2} + m_j^2 + l_j^2 + k_j^2 \right). \tag{3.11}$$

NLT_j is obtained by substituting the fields (u_j, v_j, w_j, b_j) in NLT, and by retaining all the nonlinear terms that have the same phase as the $j-$th wave. Nonlinear terms that do not have the phase of any of the five waves are the ‘non-resonant terms’ and are neglected.

From w_j, we can obtain u_j, v_j, and b_j by using the polarisation relations:

$$\begin{bmatrix} u_j \\ v_j \\ b_j \\ p_j \end{bmatrix} = \begin{bmatrix} \mathscr{U}_j \\ \mathscr{V}_j \\ \mathscr{B}_j \\ \mathscr{P}_j \end{bmatrix} w_j = \begin{bmatrix} -m_j(\omega_j k_j + \mathrm{i} l_j f_j)/[\omega_j(k_j^2 + l_j^2)] \\ -m_j(\omega_j l_j - \mathrm{i} k_j f_j)/[\omega_j(k_j^2 + l_j^2)] \\ -\mathrm{i}N^2/\omega_j \\ (\omega_j^2 - N^2)/\omega_j m_j \end{bmatrix} w_j. \tag{3.12}$$

Polarisation expressions are also used to evaluate NLT_j, and the expressions for NLT_j are provided in section 3.2.1 given below.

3.2.1 Wave-amplitude equations and growth rates

The amplitude evolution of each of the 5 waves can be obtained from (3.10):

$$\frac{da_1}{dt} = \mathcal{S}_1 a_2 a_3 - \mathcal{V}_1 a_1, \qquad \frac{da_2}{dt} = \mathcal{S}_2 a_1 \bar{a}_3 - \mathcal{V}_2 a_2 \tag{3.13}$$

$$\frac{da_5}{dt} = \mathcal{E}_5 a_4 a_3 - \mathcal{V}_5 a_5 \qquad \frac{da_4}{dt} = \mathcal{E}_4 a_5 \bar{a}_3 - \mathcal{V}_4 a_4 \tag{3.14}$$

$$\frac{da_3}{dt} = \mathcal{S}_3 a_1 \bar{a}_2 + \mathcal{E}_3 a_5 \bar{a}_4 - \mathcal{V}_3 a_3 \tag{3.15}$$

where $\mathcal{V}_j = -\mathrm{VT}_j/\mathcal{D}_j^{(3)}$. As depicted in figure 3.2(c), wave-1,-2, and -3 form a triad, whose nonlinear coefficients are given by $\mathcal{S}_j$. Likewise, wave-3, -4, and -5 also form a triad, whose nonlinear coefficients are given by $\mathcal{E}_j$. Expressions for $\mathcal{S}_j$ and $\mathcal{E}_j$ are given below. Two quantities $\mathfrak{C}_{(j,p,d)}$ and $\mathfrak{O}_{(j,b,c)}$ are defined so that the nonlinear coefficients can be written in a compact form.

$$\begin{aligned}
\mathfrak{E}_{(j,p,d)} =& -(\omega_p-\omega_d)k_j m_j \left[\left(\mathscr{U}_p\bar{\mathscr{U}}_d(k_j)+\mathscr{U}_p\bar{\mathscr{V}}_d l_p-\mathscr{V}_p\bar{\mathscr{U}}_d l_d+\mathscr{U}_p m_p-m_d\bar{\mathscr{U}}_d\right)\right]\\
&-(\omega_p-\omega_d)l_j m_j \left[\left(\mathscr{V}_p\bar{\mathscr{V}}_d(l_j)-\mathscr{U}_p\bar{\mathscr{V}}_d k_d+\mathscr{V}_p\bar{\mathscr{U}}_d k_p+\mathscr{V}_p m_p-m_d\bar{\mathscr{V}}_d\right)\right]\\
&+(\omega_p-\omega_d)(l_j^2+k_j^2)\left[\bar{\mathscr{V}}_d l_p-l_d\mathscr{V}_p+m_j+k_p\bar{\mathscr{U}}_d-\mathscr{U}_p k_d\right]\\
&+\mathrm{i}(l_j^2+k_j^2)\left[\bar{\mathscr{U}}_d\mathscr{B}_p k_p-\mathscr{U}_p\bar{\mathscr{B}}_d k_d+\bar{\mathscr{V}}_d\mathscr{B}_p l_p-\mathscr{V}_p\bar{\mathscr{B}}_d l_d+\mathscr{B}_p m_p-\bar{\mathscr{B}}_d m_d\right]\\
&+\mathrm{i}f l_j m_j\left[\left(\mathscr{U}_p\bar{\mathscr{U}}_d(k_j)+\mathscr{U}_p\bar{\mathscr{V}}_d l_p-\mathscr{V}_p\bar{\mathscr{U}}_d l_d+\mathscr{U}_p m_p-m_d\bar{\mathscr{U}}_d\right)\right]\\
&-\mathrm{i}f k_j m_j\left[\left(\mathscr{V}_p\bar{\mathscr{V}}_d(l_j)-\mathscr{U}_p\bar{\mathscr{V}}_d k_d+\mathscr{V}_p\bar{\mathscr{U}}_d k_p+\mathscr{V}_p m_p-m_d\bar{\mathscr{V}}_d\right)\right] \qquad (3.16)
\end{aligned}$$

$$\begin{aligned}
\mathfrak{O}_{(j,b,c)} =& -(\omega_b+\omega_c)k_j m_j\left[(\mathscr{U}_b\mathscr{U}_c(k_j)+\mathscr{U}_b\mathscr{V}_c l_b+\mathscr{V}_b\mathscr{U}_c l_c+\mathscr{U}_b m_b+\mathscr{U}_c m_c)\right]\\
&-(\omega_b+\omega_c)l_j m_j\left[(\mathscr{V}_b\mathscr{V}_c l_j+\mathscr{U}_b\mathscr{V}_c k_c+\mathscr{V}_b\mathscr{U}_c k_b+\mathscr{V}_b m_b+m_c\mathscr{V}_c)\right]\\
&+(\omega_b+\omega_c)(l_j^2+k_j^2)\left[\mathscr{V}_c l_b+l_c\mathscr{V}_b+m_j+k_b\mathscr{U}_c+\mathscr{U}_b k_c\right]\\
&+\mathrm{i}(l_j^2+k_j^2)\left[\mathscr{U}_c\mathscr{B}_b k_b+\mathscr{U}_b\mathscr{B}_c k_c+\mathscr{V}_c\mathscr{B}_b l_b+\mathscr{V}_b\mathscr{B}_c l_c+\mathscr{B}_b m_b+\mathscr{B}_c m_c\right]\\
&+\mathrm{i}f l_j m_j\left[(\mathscr{U}_b\mathscr{U}_c k_j+\mathscr{U}_b\mathscr{V}_c l_b+\mathscr{V}_b\mathscr{U}_c l_c+\mathscr{U}_b m_b+m_c\mathscr{U}_c)\right]\\
&-\mathrm{i}f k_j m_j\left[(\mathscr{V}_b\mathscr{V}_c l_j+\mathscr{U}_b\mathscr{V}_c k_c+\mathscr{V}_b\mathscr{U}_c k_b+\mathscr{V}_b m_b+m_c\mathscr{V}_c)\right] \qquad (3.17)
\end{aligned}$$

where the indices (j,p,d,b,c) are used to denote waves. Using equations (3.16) and (3.17), the nonlinear terms and coefficients can be written in a compact form as given below

$$\mathcal{S}_1=\frac{\mathfrak{O}_{(1,2,3)}}{\mathcal{D}_1^{(3)}},\quad \mathcal{S}_2=\frac{\mathfrak{E}_{(2,1,3)}}{\mathcal{D}_2^{(3)}},\quad \mathcal{S}_3=\frac{\mathfrak{E}_{(3,1,2)}}{\mathcal{D}_3^{(3)}}, \qquad (3.18)$$

$$\mathcal{E}_5=\frac{\mathfrak{O}_{(5,3,4)}}{\mathcal{D}_5^{(3)}},\quad \mathcal{E}_4=\frac{\mathfrak{E}_{(4,5,3)}}{\mathcal{D}_4^{(3)}},\quad \mathcal{E}_3=\frac{\mathfrak{E}_{(3,5,4)}}{\mathcal{D}_3^{(3)}}, \qquad (3.19)$$

$$\mathrm{NLT}_4=\mathcal{E}_4\mathcal{D}_4^{(3)}a_5\bar{a}_3,\quad \mathrm{NLT}_3=\mathcal{E}_3\mathcal{D}_3^{(3)}a_5\bar{a}_4+\mathcal{S}_3\mathcal{D}_3^{(3)}a_1\bar{a}_2,\quad \mathrm{NLT}_2=\mathcal{S}_2\mathcal{D}_2^{(3)}a_1\bar{a}_3.$$

$$\mathrm{NLT}_1=\mathcal{S}_1\mathcal{D}_1^{(3)}a_2a_3,\quad \mathrm{NLT}_5=\mathcal{E}_5\mathcal{D}_5^{(3)}a_3a_4, \qquad (3.20)$$

Using pump wave approximation (McEwan & Plumb, 1977; Young *et al.*, 2008), (3.13)–(3.15) can be simplified to a set of linear differential equations which are given below in a compact form:

$$\begin{bmatrix} \dfrac{d\bar{a}_2}{dt} \\ \\ \dfrac{d\bar{a}_4}{dt} \\ \\ \dfrac{da_3}{dt} \end{bmatrix} = \begin{bmatrix} -\mathcal{V}_2 & 0 & \bar{\mathcal{S}}_2\bar{A}_1 \\ \\ 0 & -\mathcal{V}_4 & \bar{\mathcal{E}}_4\bar{A}_5 \\ \\ \mathcal{S}_3A_1 & \mathcal{E}_3A_5 & -\mathcal{V}_3 \end{bmatrix} \begin{bmatrix} \bar{a}_2 \\ \\ \bar{a}_4 \\ \\ a_3 \end{bmatrix}. \tag{3.21}$$

Note that $a_1(a_5)$ has been changed to $A_1(A_5)$ to denote the fact that they are now constants. By assuming $da_j/dt = \sigma a_j$, we arrive at the equation

$$(\sigma + \mathcal{V}_2)(\sigma + \mathcal{V}_3)(\sigma + \mathcal{V}_4) - \bar{\mathcal{E}}_4\mathcal{E}_3|A_5|^2(\sigma + \mathcal{V}_2) - \bar{\mathcal{S}}_2\mathcal{S}_3|A_1|^2(\sigma + \mathcal{V}_4) = 0, \tag{3.22}$$

where σ is the growth rate of the system of equations given in (3.21). A real, positive σ implies the daughter waves can extract energy from the parent wave. For $\nu = 0$ (inviscid flow), the growth rate has a simple expression given by

$$\sigma = \sqrt{\bar{\mathcal{S}}_2\mathcal{S}_3|A_1|^2 + \bar{\mathcal{E}}_4\mathcal{E}_3|A_5|^2}. \tag{3.23}$$

Note that by setting either $A_1 = 0$ or $A_5 = 0$, we arrive at the standard growth expression for triads (3-wave systems). Moreover, we can also obtain the condition

$$\sqrt{\bar{\mathcal{S}}_2\mathcal{S}_3|A_1|^2 + \bar{\mathcal{E}}_4\mathcal{E}_3|A_5|^2} \leq \sqrt{2}\widehat{\sigma}_1 \quad \text{or} \quad \sqrt{\bar{\mathcal{S}}_2\mathcal{S}_3|A_1|^2 + \bar{\mathcal{E}}_4\mathcal{E}_3|A_5|^2} \leq \sqrt{2}\widehat{\sigma}_5 \tag{3.24}$$

where $\widehat{\sigma}_1(\widehat{\sigma}_5)$ is the maximum growth rate of all 3-wave systems of parent wave-1(5). If both the parent waves have the same amplitude ($A_1 = A_5$), frequency, and wavevector norm, then $\widehat{\sigma}_1 = \widehat{\sigma}_5$. In such cases, (3.24) implies that any 5-wave system's growth rate could, in principle, be higher (maximum being $\sqrt{2}$ times) than the maximum growth rate of all 3-wave systems. For all the parent wave combinations considered in this paper, $A_1 = A_5$ is consistently taken to study the growth rates. Note that a 5-wave interaction can be faster than a 3-wave interaction because in a 5-wave interaction the daughter waves are being forced by two different parent waves. As a result, the small amplitude perturbations grow using two different reservoirs of energy.

3.2.1.1 5-wave system identification method

For a resonant 5-wave system, all three daughter waves should satisfy the dispersion relation. This leads to 3 constraints, which are given below:

$$\omega_3^2 = \frac{N^2(k_3^2 + l_3^2) + f^2 m_3^2}{k_3^2 + l_3^2 + m_3^2}, \tag{3.25a}$$

$$\omega_2^2 = \frac{N^2(k_2^2 + l_2^2) + f^2 m_2^2}{k_2^2 + l_2^2 + m_2^2}, \tag{3.25b}$$

$$\omega_4^2 = \frac{N^2(k_4^2 + l_4^2) + f^2 m_4^2}{k_4^2 + l_4^2 + m_4^2}. \tag{3.25c}$$

The following triad conditions also add additional constraints:

$$\omega_2 = \omega_1 - \omega_3, \quad \mathbf{k}_2 = \mathbf{k}_1 - \mathbf{k}_3, \tag{3.26a}$$

$$\omega_4 = \omega_5 - \omega_3, \quad \mathbf{k}_4 = \mathbf{k}_5 - \mathbf{k}_3, \tag{3.26b}$$

where $\mathbf{k}_j = (k_j, l_j, m_j)$ is the wavevector of the $j-$wave. Substitution of (3.26a) in (3.25b), and (3.26b) in (3.25c) lead to

$$\omega_3^2 = \frac{N^2(k_3^2 + l_3^2) + f^2 m_3^2}{k_3^2 + l_3^2 + m_3^2}, \tag{3.27a}$$

$$(\omega_1 - \omega_3)^2 = \frac{N^2((k_1 - k_3)^2 + (l_1 - l_3)^2) + f^2(m_1 - m_3)^2}{(k_1 - k_3)^2 + (l_1 - l_3)^2 + (m_1 - m_3)^2}, \tag{3.27b}$$

$$(\omega_5 - \omega_3)^2 = \frac{N^2((k_5 - k_3)^2 + (l_5 - l_3)^2) + f^2(m_5 - m_3)^2}{(k_5 - k_3)^2 + (l_5 - l_3)^2 + (m_5 - m_3)^2}. \tag{3.27c}$$

Solutions for (3.27a)-(3.27c) would provide resonant 5-wave systems, and they are found by varying $(\omega_3, k_3, l_3, m_3)$. Hereafter we always assume $|\mathbf{k}_1| = |\mathbf{k}_5|$, however, $\mathbf{k}_1 \neq \mathbf{k}_5$, and $\omega_1 = \omega_5 = 0.1N$. Such small frequency values appear in many other studies, for example, Mathur *et al.* (2014); Nikurashin & Legg (2011).

3.3 Results from the reduced–order model

3.3.1 Parent waves in the same vertical plane

3.3.1.1 $\mathbf{k}_1 = (k_1, 0, m_1)$ and $\mathbf{k}_5 = (k_1, 0, -m_1)$

We first consider the scenario where the two parent waves have the same horizontal wavevector (k, l) but travel in vertically opposite directions, see figure 3.2(a). For simplicity, the meridional wavenumbers of the parent waves (l_1 and l_5) are assumed to be 0. Internal waves propagating in vertically opposite directions can arise in many different circumstances. For example, internal wave beams getting reflected from the bottom surface of the ocean, or from the air-water interface, or even from the pycnocline, will result in scenarios where parent waves travelling in vertically opposite directions meet.

For the given set of parent waves, a resonant 5-wave system is possible only when $\omega_3 \approxeq \omega_1 - f$. No other resonant 5-wave systems were found for $0 < f/\omega_1 < 0.5$. Equations (3.27a)–(3.27c) were solved numerically for many $f-$ values and the solution for ω_3 was $\omega_3 = \omega_1 - f$. Specifically, for $f/\omega_1 = (0.05, 0.1, 0.2, 0.4)$, no resonant 5-wave systems were found for $\omega_3 \in (f+\delta\omega, \omega_1 - f - \delta\omega)$, where $\delta\omega = 0.01\omega_1$. Hence, the 5-wave system always consists of (a) two parent waves, each with frequency ω_1 (as per our assumption), (b) a common daughter wave with frequency $\omega_1 - f$, and (c) two inertial (frequency f) daughter waves, which also propagate in vertically opposite directions.

Next we study the growth rates of the 5-wave system. First, we decide on the viscosity values in a non-dimensionalised form. In this regard we choose $|A_1|/k_1\nu = 10^4$ and $|A_1|/k_1\nu = 10^7$, which are used throughout the chapter. At $|A_1|/k_1\nu = 10^7$, viscous effects are usually negligible, hence $|A_1|/k_1\nu = 10^4$ is also considered to see what 5-wave systems are affected by the viscosity. We note in passing that $|A_1|/k_1\nu \approx 3 \times 10^6$ was used by Bourget *et al.* (2013) to study triads with realistic oceanic parameters. Figure 3.3(a) shows how the maximum growth rate of the 5-wave system and 3-wave systems vary with f/ω_1 for different ν. The growth rates are evaluated by fixing k_1 and A_1 as f is varied. Figures 3.3(b)–3.3(c) respectively show the horizontal and the vertical wavenumbers of the daughter waves involved in the 5-wave interaction. Note that the common daughter wave's horizontal wavevector $(k_1, 0)$ is always the same as that of the parent waves. This is expected since the other two daughter waves are near-inertial waves. Moreover, the common daughter wave can have a positive or negative vertical wavenumber, and both cases have the same growth rate. In a 5-wave interaction (or a 3-wave interaction), the length scale of the near-inertial daughter waves generated strictly depends on the length scale of the parent waves and also on the depth of the domain. For low f values, the 3-wave system has a higher growth rate, hence it is the dominant instability. This is because the two 3-wave systems that combine to form the 5-wave system always contain inertial daughter waves. Moreover, the growth rate of 3-wave systems containing near-inertial waves is much smaller than the maximum possible growth rate (Richet *et al.*, 2018, figure 8). As a result, the resonant 5-wave system is of little significance at low latitudes. An important point to realise is that triads with the highest growth rates need not necessarily combine to form 5-wave systems because the conditions required for a resonant 5-wave system (equations (3.27a)–(3.27c)) are more stringent.

As f is increased, the 5-wave system's growth rate becomes higher than the maximum growth rate of all 3-wave systems. The transition occurs near $f/\omega_1 \approx 0.3$, see figure 3.3(a). For high values of f/ω_1, 5-wave systems may be faster in locations where an internal wave beam gets reflected from a flat bottom surface or from a nearly flat air-water surface. However, for inclined reflecting surfaces, the results presented here (which are based on the assumption that the two parent waves have the same wavevector norm) may not be valid since inclination results in a significant change in wavevector norm (Phillips, 1977).

Finally, we note that two parent waves with equal amplitude travelling in vertically opposite directions in a constant N produce a field that resembles an internal wave mode in a vertically bounded domain (Johnston & Merrifield, 2003). Hence, the predictions made in this section should also hold for modes in a bounded domain. However, in a vertically bounded domain, only a discrete set of vertical wavenumbers are allowed for a particular frequency. As a result, for a resonant 5-wave system to exist, the vertical wavenumbers of the daughter waves should be a part of the discrete vertical wavenumber spectrum. Note that this means considering only three waves (as we have done in the chapter 2) may under-predict the growth rates at certain latitudes.

3.3.1.2 $\mathbf{k}_1 = (k_1, 0, m_1)$ and $\mathbf{k}_5 = (-k_1, 0, m_1)$

Here we focus on the scenario where the two parent waves have the same vertical wavenumber but travel in horizontally opposite directions, as given in figure 3.2(b). Moreover, $l_1 = l_5 = 0$ is again assumed. For this particular combination of parent wavevectors,

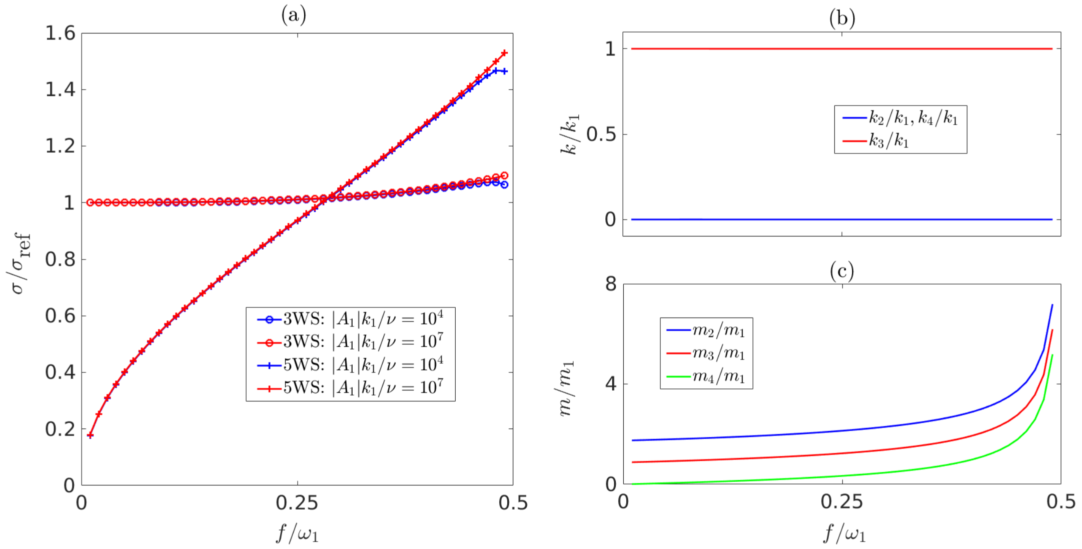

Figure 3.3: (a) Variation of 5-wave system's growth rate(denoted by 5WS in the legend) and the maximum growth rate of all 3-wave systems (denoted by 3WS) with f for $\mathbf{k}_1 = (k_1, 0, m_1)$ and $\mathbf{k}_5 = (k_1, 0, -m_1)$. Two different viscosity values are used. The horizontal wavenumber and vertical wavenumber of the daughter waves in the 5-wave system are shown in (b) and (c), respectively.

resonant 5-wave systems are possible for $\omega_3 \in (f, 0.53\omega_1)$. For $f/\omega_1 = 0.01$, resonant 5-wave systems exist up to $\omega_3 \approx 0.53\omega_1$. As f increases, the maximum possible value of ω_3 slowly reduces to $0.5\omega_1$. We define two branches: 5-wave systems where the common daughter wave has a positive (negative) vertical wave number is defined as Branch-1(2). Figures 3.4(a)–3.4(b) show how the maximum growth rate for each of these two branches varies with f for two different viscosity values. The maximum growth rate of 3-wave systems is once again plotted so as to provide a clear comparison between 5-wave and 3-wave systems. For lower f values, resonant 5-wave systems have a lesser maximum growth rate than the maximum growth rate of 3-wave systems ($\sigma/\sigma_{\text{ref}} < 1$). However, the 5-wave instability is faster than the 3-wave instability for the higher f values. The transition once again occurs near $f \approx 0.3\omega_1$. All these observations are similar to that in figure 3.3(a). Viscosity has a non-negligible effect only when $f \approx \omega_1/2$, where the daughter waves have a high vertical wavenumber.

Figures 3.5(a)–3.5(c) show how the growth rate of both the branches vary with ω_3/ω_1 for three different f/ω_1 values that are greater than 0.3. Figure 3.5 reveals that growth rates always decrease as ω_3 is increased, indicating the maximum growth rate is at $\omega_3 = f$. For $f/\omega_1 > 0.3$, the common daughter wave is always an inertial wave in the most unstable 5-wave system. For high f values, the maximum growth rate of both branches is almost the

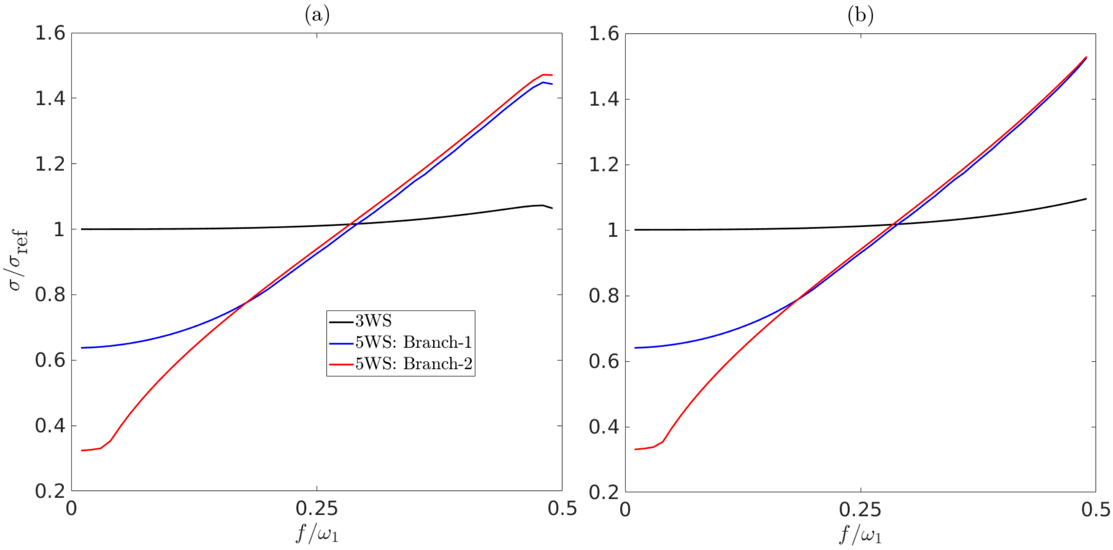

Figure 3.4: Comparison of maximum growth rates of 5-wave systems and 3-wave systems for $\mathbf{k}_1 = (k_1, 0, m_1)$ and $\mathbf{k}_5 = (-k_1, 0, m_1)$. (a) $|A_1|/k_1\nu = 10^4$, and (b) $|A_1|/k_1\nu = 10^7$.

same. The viscous effect is more apparent for $|A_1|/k_1\nu = 10^4$, and Branch-1 is affected by viscous effects more than Branch-2. Interestingly, as ω_3 is increased from f, the meridional wavenumber of the common daughter wave increases, hence making the instability 3D. Moreover, for the three f values analysed in figure 3.5, the zonal wavenumber of the common daughter wave (k_3) is nearly zero for all the 5-wave systems. Note that the maximum growth rate occurs at $\omega_3 \approx f$ where $(k_3, l_3) \to 0$. As a result, the system's most unstable mode can be studied/simulated by considering a 2D system.

For high f values, near-inertial waves have been observed to be the daughter waves of a parent internal wave with semidiurnal frequency, see Yi *et al.* (2017); Richet *et al.* (2017, 2018); Chen *et al.* (2019). In topographic generation of internal waves, internal wave beams intersecting each other is quite common. The locations where internal wave beams intersect can serve as spots where a single inertial wave can extract energy from two different internal wave beams.

3.3.2 Oblique parent waves

In the oceans, parent waves that are not on the same vertical plane can also propagate amidst each other. Here we study the maximum growth rate for 5-wave systems where the parent waves have a non-zero meridional wavenumber. The parent wavevectors are given

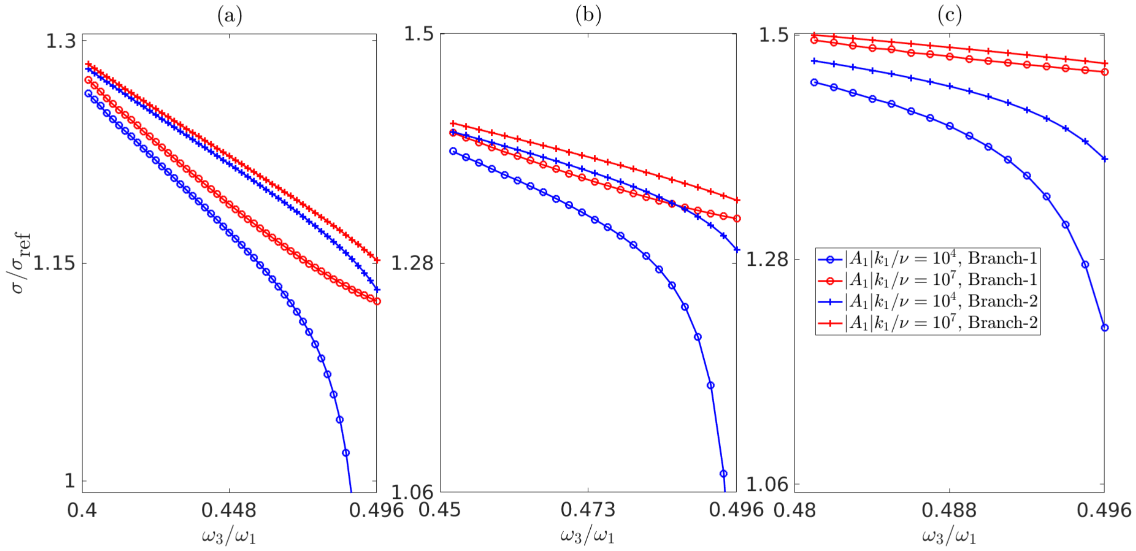

Figure 3.5: Growth rate variation with ω_3/ω_1 for Branch-1 and 2 for (a) $f/\omega_1 = 0.40$, (b) $f/\omega_1 = 0.45$, and (c) $f/\omega_1 = 0.48$.

by

$$\mathbf{k}_1 = (k_1 \sin(\theta/2), k_1 \cos(\theta/2), m_1), \qquad \mathbf{k}_5 = (-k_1 \sin(\theta/2), k_1 \cos(\theta/2), m_1), \tag{3.28}$$

where the parameter θ is used to vary the angle between the two parent wavevectors in the (k, l) plane. Note that $\theta = \pi$ leads to the wavevector combination $\mathbf{k}_1 = (k_1, 0, m_1)$ and $\mathbf{k}_5 = (-k_1, 0, m_1)$ considered in §3.3.1.2. Following (3.28), the condition $|\mathbf{k}_1| = |\mathbf{k}_5|$ will be automatically satisfied. The direction of the parent wavevectors can be changed by varying θ, and how that impacts the growth rates of 5-wave systems will be explored and analysed. Figures 3.6(a)–3.6(c) show the variation of the maximum growth rate of 3-wave systems and 5-wave systems with f respectively for three different θ values: $\pi/4$, $\pi/2$, and $3\pi/4$. Increasing θ results in 5-wave systems being less effective than 3-wave systems in the lower latitudes. For $\theta = \pi/4$, the 5-wave system is the dominant instability regardless of the latitude. A similar result is observed for $\theta = \pi/2$, however, the difference between the 5-wave and 3-wave systems is clearly reduced compared to $\theta = \pi/4$. For $\theta = 3\pi/4$, the 5-wave system is the dominant instability only for $f/\omega_1 \gtrapprox 0.25$. Note that regardless of the θ value, 5-wave instability is expected to be faster than the 3-wave instability when $f/\omega_1 \gtrapprox 0.3$ considering the results from §3.3.1.2. For $\theta = \pi$ and $f/\omega_1 \gtrapprox 0.3$, the maximum growth rate for 5-wave systems occurs when $\omega_3 = f$. However, for $\theta = \pi/4$ and $\pi/2$, in the most unstable 5-wave system, wave-3 is not an inertial wave even for $f/\omega_1 = 0.45$. Hence, as θ is reduced, it is not necessary that the most unstable 5-wave

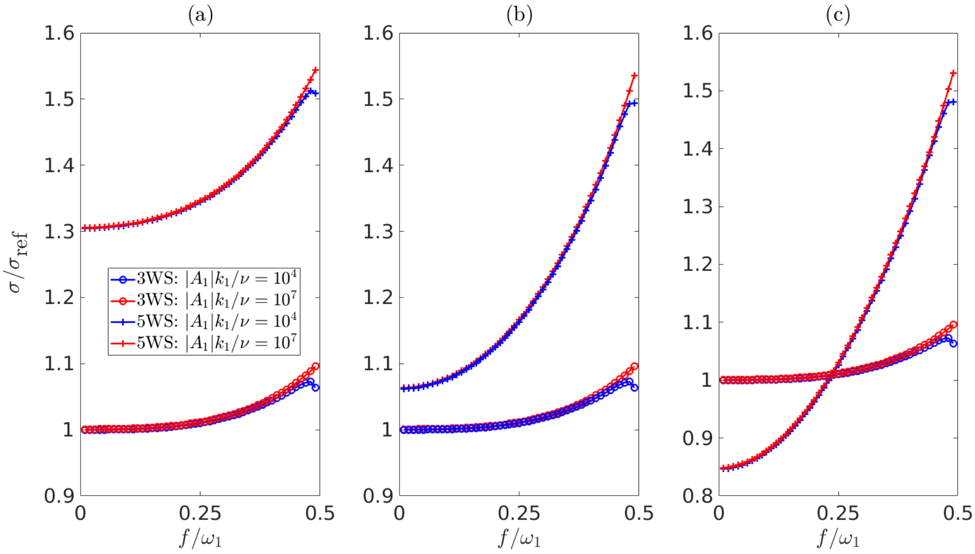

Figure 3.6: Variation of maximum growth rate with f for 5-wave systems and 3-wave systems for a oblique set of parent waves. (a) $\theta = \pi/4$, (b) $\theta = \pi/2$, and (c) $\theta = 3\pi/4$.

system contains near-inertial waves. Note that the predictions for the 5-wave system will fail as $\theta \to 0$ since both parent waves will have the same wavevector.

3.4 Numerical simulations

Here we present results from numerical simulations conducted to validate the predictions from reduced-order analysis presented in §3.3, with the primary focus being on §3.3.1.1 and §3.3.1.2. Equations (1.7)–(1.10) along with equation (1.13) are solved with Dedalus. For numerical validations, we only consider 2D situations, i.e. $\partial/\partial y = 0$, implying $l = 0$. The details of the simulations are as follows: we fix the parent waves' horizontal wavenumber at $k_1 = 1/H$, where $H = 500$m. We consistently use $N = 10^{-3}$s^{-1} and $\omega_1/N = 0.1$. However f/ω_1 is varied, and hence the vertical wavenumber of the parent waves (m_1) is a function of f/ω_1. The amplitude of the parent waves is chosen such that the maximum zonal velocity (u) is always 0.001ms^{-1}. Computational time is variable and depends on the simulation in question. For all simulations, 4-th order Runge-Kutta method is used as the time-stepping scheme with a time step size of $(2\pi/\omega_1)/800$ (i.e. 800 steps for one time period of the parent wave). All the fields are expressed as Fourier modes in the horizontal direction, and either 64 or 128 grid points/modes are used per one horizontal wavelength of the parent wave. Moreover, the vertical direction is resolved using Chebyshev polynomials or Fourier modes, and the vertical resolution is varied from a minimum of 96 to a maximum of 512 grid points per one vertical wavelength of the parent wave. All simulations are initialised with a small amplitude noise, the spectrum of which is given by

$$\mathcal{R}_{\text{noise}}(x,z) = \int_{0}^{k_{\text{noise}}} \int_{m_{\text{lowest}}}^{m_{\text{noise}}} A_{\text{noise}} \sin(kx + mz + \text{Phase}_{\text{noise}}(k,m))dmdk, \tag{3.29}$$

where $\text{Phase}_{\text{noise}}(k,m) \in [0, 2\pi]$ is the random phase part, which is generated using the 'rand' function in Matlab for each (k, m). Unless otherwise specified, $k_{\text{noise}} = 48k_1$ and $m_{\text{noise}} = 48m_1$. Moreover, $m_{\text{lowest}} = 2\pi/\text{Len}_z$, where Len_z is the length of the domain in the z-direction. Equation (3.29) is added to the b or v field. The noise amplitude A_{noise} is at least 10^{-3} times smaller than the primary waves' corresponding amplitude. The simulations are initialised with small amplitude noise so that the growth of daughter waves is completed in a shorter time. As a result, to consume fewer computer resources and run more simulations more efficiently, we initialise simulations with the small amplitude noise. If there is no small amplitude noise, the daughter waves will take much longer time to completely extract the parent wave's energy as the daughter wave's amplitude will be very low (depending on the number of decimal places the computer uses/resolves the numbers with) at the beginning of the simulation. Unless otherwise mentioned, $\nu = 10^{-6}\text{m}^2\text{s}^{-1}$ is taken.

3.4.1 $\mathbf{k}_1 = (k_1, 0, m_1)$ and $\mathbf{k}_5 = (k_1, 0, -m_1)$

We first focus on the parent wavevector combination $\mathbf{k}_1 = (k_1, 0, m_1)$ and $\mathbf{k}_5 = (k_1, 0, -m_1)$. As mentioned previously, the combination of wavevectors $\mathbf{k}_1 = (k_1, 0, m_1)$ and $\mathbf{k}_5 = (k_1, 0, -m_1)$ leads to fields that are very similar to an internal wave mode in a vertically bounded domain. As a result, we also simulate low modes (modes-1 and 2) in a vertically bounded domain to observe whether there is an emergence of the '5-wave instability'. The decay of the parent waves are simulated at specific latitudes where the daughter waves' vertical wavenumbers in the resonant 5-wave system are multiples of $m_1/3$ or $m_1/2$. The reason for this selection is as follows. For example, when the vertical wavenumbers are chosen to be multiples of $m_1/2$ so that the domain height can be chosen as twice the vertical wavelength of the parent wave. Any vertical wavenumber that is a multiple of $m_1/2$ is a possible solution of the dispersion relation where the domain height $H = 4\pi/m_1$. This reduces the computational resources required for the simulations because of the shorter computational domain. Note that if the vertical wavenumbers are chosen such that they are multiples of $m_1/3$, then the domain height has to be at least $H = 6\pi/m_1$. Hence, the number of grid points per $2\pi/m_1$ decreases in the simulations. This choice helps in reducing the computational resources required for the simulations. To estimate the energy (per unit length in the $y-$ direction) in different wavevectors, we simply use the Fast Fourier Transform (FFT) for both x and z directions in simulations where the parent waves are plane waves. In a vertically bounded domain, FFT is used only in the x direction, while for the $z-$direction, the orthogonal nature of the modes is exploited. As a measure of the energy (per unit length in the $y-$ direction) contained in a wavevector, a non-dimensionalised energy $\widehat{E}$ is introduced:

$$\widehat{E}(k,0,m,t) = \frac{|\hat{u}_{\text{FR}}(k,0,m,t)|^2 + |\hat{w}_{\text{FR}}(k,0,m,t)|^2 + |\hat{v}_{\text{FR}}(k,0,m,t)|^2 + |\hat{b}_{\text{FR}}(k,0,m,t)|^2/N^2}{E_{\text{ref}}} \tag{3.30}$$

where the hat variables $(\hat{u}_{\text{FR}}, \hat{w}_{\text{FR}}, \hat{v}_{\text{FR}}, \hat{b}_{\text{FR}})$ respectively denote the Fourier amplitudes of (u, w, v, b). E_{ref} serves as the measure of parent waves' energy per unit length in the $y-$ direction at $t = 0$ and is defined as

$$E_{\text{ref}} = \left(|\hat{u}_{\text{FR}}(k_1,0,m_1)|^2 + |\hat{w}_{\text{FR}}(k_1,0,m_1)|^2 + |\hat{v}_{\text{FR}}(k_1,0,m_1)|^2 + |\hat{b}_{\text{FR}}(k_1,0,m_1)|^2/N^2\right)\Bigg|_{t=0} \tag{3.31}$$

We simulate a total of 6 cases: 2 cases for parent waves in an unbounded domain (plane waves), and 2 cases each for mode-1 and mode-2 waves in a vertically bounded domain. For mode-1, $m_{\text{noise}} = 96m_1$ is chosen. For every simulation, a different f value is used, and hence the resonant 5-wave system is different in each case. Figure 3.7 shows the exponential growth of daughter waves at 6 different latitudes due to 5-wave interactions. Figures 3.7(a)–3.7(e) plot four different wavevectors. The wavevector $(|k_1|, 0, |m_1|)$ contains the energy of both parent waves, while the other three wavevectors indicate the daughter waves. All three daughter waves grow exponentially, which provides clear evidence that this is a 5-wave system. In 3.7(f), two different 5-wave systems emerge and both of them are plotted. In triad interactions, the transfer of energy is cyclical in nature: the daughter waves extract the energy from the parent and after some time, they can give back that energy. However, if the daughter waves have very small length scales, they can act as parent waves and give their energy to daughter waves of their own. In this process, the energy will cascade to small length scales and eventually causes turbulence and mixing. This is what happens in figure 3.7(f). As the f value increases, the daughter waves' vertical wavenumber also increases in the simulations (see the legend) which is in line with the theoretical predictions given in figure 3.3(c). In all six simulations, near-inertial waves are present ($k = 0$). The growth rate of the daughter waves is calculated by estimating

$d\ln(\widehat{E})/dt$. The comparison of growth rates from simulations and theory is presented in figure 3.8, which shows a reasonably good agreement. For all the cases, the average of the three daughter waves' growth rate in a particular 5-wave system is taken. Moreover, figure 3.8 reveals that the growth rates are well above the maximum growth rate of all 3-wave systems. Note that the 5-wave interactions can happen for standing modes only at specific latitudes because the vertical wavenumbers are discrete, not continuous. However, for plane waves, there is no such constraint. As per the predictions in §3.3, 5-wave interactions should be faster than the 3-wave interactions provided $f/\omega_1 \gtrapprox 0.3$. Considering the results (for modes) we have seen in this chapter, the triad interaction equations given in chapter 2 may under-predict the growth rates of daughter waves at very specific latitudes since only 3 waves are considered. Resonant 5-wave interactions require near-inertial waves to be a part of the interaction which inherently means it also requires a wave with frequency $\omega_1 - f$. As a result, for modes, at latitudes where k_1 is an eigenvalue of frequency $\omega_1 - f$, resonant 5-wave interactions are possible. In chapter 2, we saw how the stratification profile can play a major role in deciding the wavenumber spectrum for a given frequency. Hence, the latitudes where the 5-wave interaction can occur will also depend on the stratification profile.

It was observed that as $f/\omega_1 \to 0.5$, multiple daughter wave combinations grow as a result of the subharmonic instability and extract a considerable amount of energy from the parent waves. This can even be seen in figure 3.7(f), where two different 5-wave systems emerge and extract a significant amount of energy. As $f/\omega_1 \to 0.5$, multiple 5-wave systems can become coupled and grow at a rate which is faster than any single 5-wave system (discussed in detail in §3.4.2). Hence, the growth rates predicted from a single 5-wave interaction will not be accurate when $f \approx \omega_1/2$. The growth rate for a mode-1 wave as $f \to \omega_1/2$ will approach $2\sigma_{\text{cl}}$ instead of $\sqrt{2}\sigma_{\text{cl}}$, where σ_{cl} is the maximum growth rate for a plane wave with zonal velocity amplitude 0.001ms^{-1} at the critical latitude (Young *et al.*, 2008). We realise that in Young *et al.* (2008), the mode-1 wave was considered in the presence of a non-constant N. However, their prediction is still expected to hold in the present scenario (constant N). Our numerical simulations (results not shown here) also show the growth rates of the daughter waves being well above $\sqrt{2}\sigma_{\text{cl}}$ for $f \approx \omega_1/2$. Note that considering just three waves near the critical latitude may be an oversimplification, hence care should be taken while using wave amplitude equations given in chapter 2 for $f \approx \omega_1/2$.

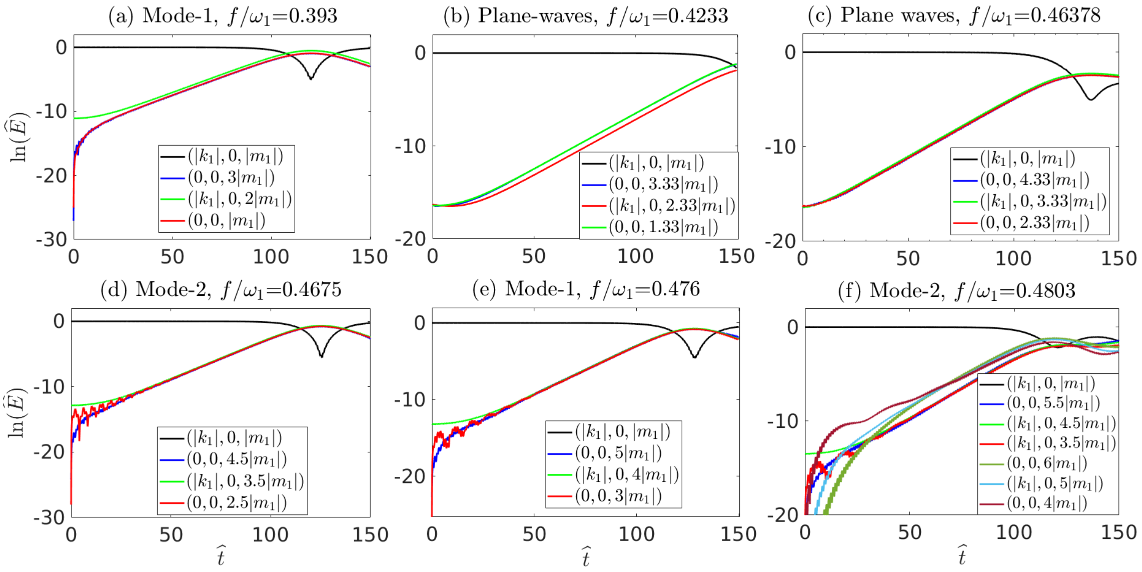

Figure 3.7: 5-wave interactions for plane waves, mode-1, and mode-2 different f values (i.e. latitudes), plotted in ascending order. $\hat{t} \equiv t\omega_1/2\pi$.

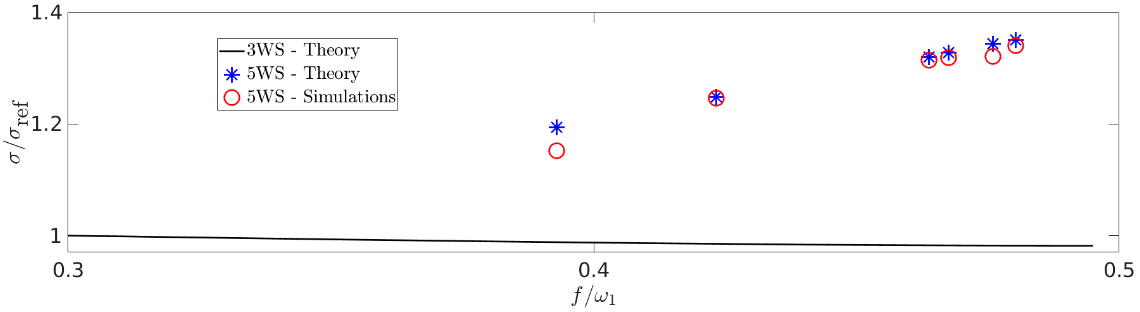

Figure 3.8: Comparison between theoretical growth rates and growth rates obtained from the simulations for $\mathbf{k}_1 = (k_1, 0, m_1)$ and $\mathbf{k}_5 = (k_1, 0, -m_1)$. Red (blue) markers indicate results from the simulations (theory), see legend. The black curve plots the variation of maximum growth rate of 3-wave systems with f.

3.4.2 $\mathbf{k}_1 = (k_1, 0, m_1)$ and $\mathbf{k}_5 = (-k_1, 0, m_1)$

We now validate 5-wave interactions for parent waves propagating in horizontally opposite directions. In this regard, we focus on latitudes where the daughter waves' vertical wavenumbers are multiples of $m_1/2$. Figure 3.9 shows the growth of daughter waves for four different f/ω_1 values. Figures 3.9(a)–3.9(b) show energy in three wavevectors growing exponentially. The three wavevectors encompass both branch-1 and branch-2 daughter waves' wavevectors, and the simulation results are in line with theoretical predictions. The green curve (the wave with non-zero horizontal wavenumber) contains the energy of both leftward and rightward propagating waves. The growth rates estimated from the simulations are much higher than what is expected for a 3-wave interaction. For

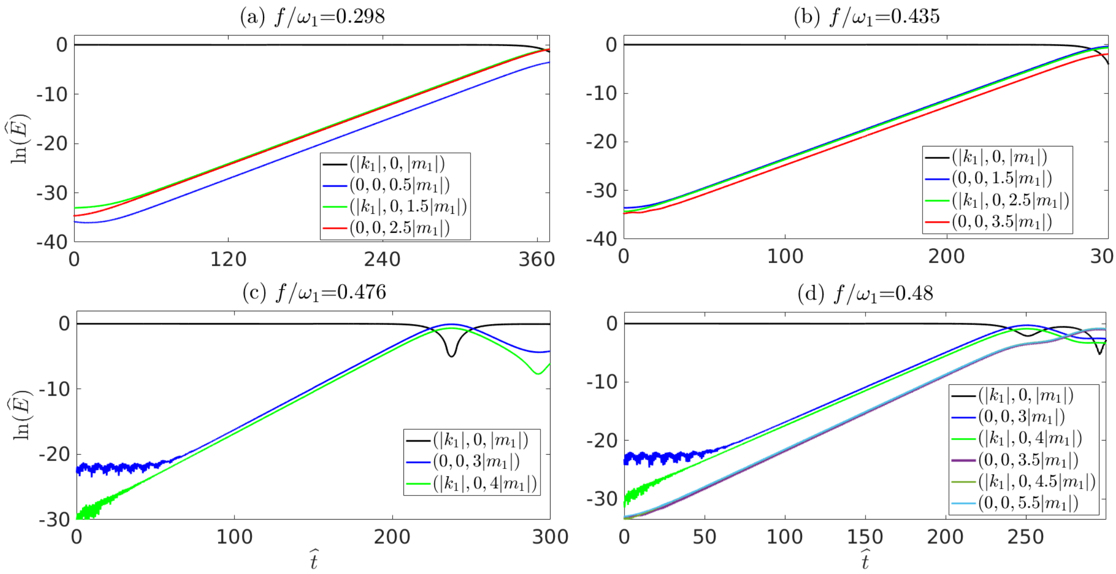

Figure 3.9: Four different 5-wave interactions for parent waves with wavevectors $\mathbf{k}_1 = (k_1, 0, m_1)$ and $\mathbf{k}_5 = (-k_1, 0, m_1)$.

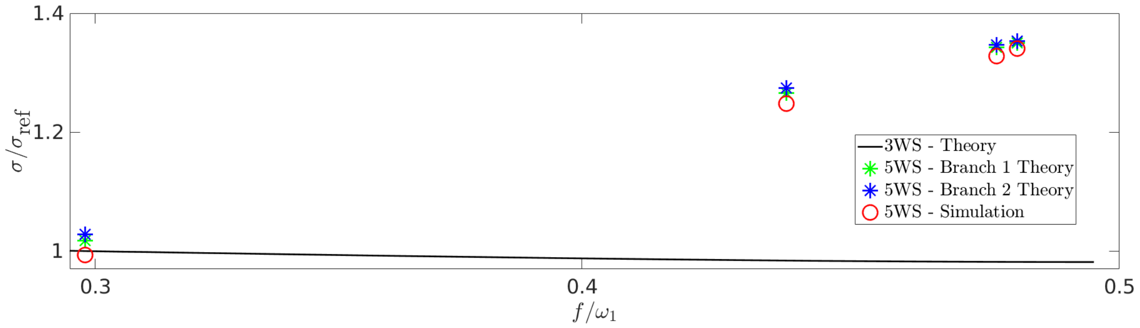

Figure 3.10: Comparison between theoretical growth rates and growth rates obtained from the simulations for $\mathbf{k}_1 = (k_1, 0, m_1)$ and $\mathbf{k}_5 = (-k_1, 0, m_1)$. Red markers indicate results from the simulations. Blue and green markers are predictions from the reduced order model. The black curve plots the variation of maximum growth rate of all 3-wave systems with f.

example, at $f = 0.298\omega_1$, the growth rate of the daughter waves is $\approx$ 30% more than the growth rate of the individual 3-wave interactions that combine to form the 5-wave interaction. Figure 3.9(c) shows only two daughter waves, which are part of the Branch-2 5-wave system. In this case, Branch-1 did not have a growth comparable to Branch-2. Finally, 3.9(d) has three distinct 5-wave systems

- System-1 (daughter waves): $(k_1, 0, 4m_1)$, $(-k_1, 0, 4m_1)$, $(0, 0, -3m_1)$,
- System-2 (daughter waves): $(k_1, 0, 4.5m_1)$, $(-k_1, 0, 4.5m_1)$, $(0, 0, -3.5m_1)$,
- System-3 (daughter waves): $(k_1, 0, -4.5m_1)$, $(-k_1, 0, -4.5m_1)$, $(0, 0, 5.5m_1)$.

System-1 is also present for $f/\omega_1 = 0.476$. This 5-wave system is present in both $f/\omega_1 = 0.476$ and 0.48 because the change in f is not that significant and hence the specific interaction is not expected to be detuned significantly. As a result, the system has an exponential growth. Even though the growth rates of System-2 and System-3 are observed to be higher than the growth rate of System-1, System-1 drains the largest amount of energy from the parent waves because the daughter waves in this system have a slightly higher energy at $t = 0$. Growth rates obtained from the reduced order models are once again compared with the growth rates obtained from the numerical simulations, see figure 3.10. When there are multiple branches growing, the average growth rate of the (two) branches is taken since both branches have nearly the same growth rate. For $f/\omega_1 = 0.48$ in figure 3.9(d), the average of system-2 and system-3's growth rates is compared with the theoretical growth rate since these are the two resonant Branch-1 and Branch-2 systems at $f/\omega_1 = 0.48$. It can be seen that theoretical predictions match reasonably well with the simulations. Moreover, similar to §3.4.1, the growth rates of 5-wave systems are well above the maximum growth of 3-wave systems (shown by the black curve in figure 3.10) for $f/\omega_1 > 0.4$.

3.4.3 Simulations and analysis for $f \approx \omega_1/2$

In §3.4.1, we saw that the theoretical growth rates of 5-wave systems are not accurate for $f \approx \omega_1/2$. To test whether the 5-wave systems' growth rate holds near the critical latitude for $\mathbf{k}_1 = (k_1, 0, m_1)$ and $\mathbf{k}_5 = (-k_1, 0, m_1)$, we ran simulations for three different f/ω_1 values: $f/\omega_1 = 0.496, 0.498$ and 0.499. Moreover, for each f, we ran three simulations: one with $\nu = 10^{-6}\mathrm{m}^2\mathrm{s}^{-1}$, one with $\nu = 0.25 \times 10^{-6}\mathrm{m}^2\mathrm{s}^{-1}$, and finally one simulation with hyperviscous terms instead of viscous terms (i.e. by setting $\nu = 0$). The hyperviscous operator $-\nu_H \Delta^4()$ is added to right hand side of (1.8)–(1.10) and (1.13) with $\nu_H = 0.25 \times 10^{-6}\mathrm{m}^8\mathrm{s}^{-1}$. Hyperviscous terms are intended to make the simulation nearly inviscid, and they have been used previously to study PSI (Hazewinkel & Winters, 2011). All simulations are run for 150 time periods of the parent wave. The simulations are stopped before the small-scale daughter waves attain energy comparable to the parent waves. The small-scale waves will break in such cases, and the ensuing turbulence is not resolved and is also not the focus of this study. We are only interested in the growth rate of the daughter waves.

Figure 3.11 shows the non-dimensionalised growth rates ($\sigma/\sigma_{\mathrm{cl}}$) of the daughter waves for all nine cases. In figure 3.11, each row is for a different f value. Moreover, for each column, ν or ν_H is held constant. For the hyperviscous simulations and simulations with the lower viscosity, it can be seen that the non-dimensionalised growth rates are well above $\sqrt{2}$ for all three f-values (second and third column of figure 3.11). Daughter waves with $m = 20 - 40m_1$ have $\sigma/\sigma_{\mathrm{cl}} \approx 1.85$ in the simulations with hyperviscous terms. For each f, simulations with $\nu = 10^{-6}\mathrm{m}^2\mathrm{s}^{-1}$ have considerably lower growth rates (especially for higher wavenumbers) compared to the other simulations because of the viscous effects.

We provide the reason for $\sigma/\sigma_{\mathrm{cl}}$ being well above $\sqrt{2}$ using the reduced order model. The dispersion relation for the daughter waves can be rewritten as

$$(f + \delta\omega)^2 = \frac{N^2(nk_1)^2 + f^2m^2}{(nk_1)^2 + m^2}, \tag{3.32}$$

where $\delta\omega$ is the difference between the wave's frequency $(f + \delta\omega)$ and the inertial frequency (f), and n is some constant (but for our purposes, will primarily be an integer). Note that k_1 is the zonal wavenumber of the parent waves, but m is *not* the vertical wavenumber of parent waves. Near the critical latitude, in a wave-wave interaction, any daughter wave's frequency would be approximately equal to the inertial frequency, implying $\delta\omega \ll f$. Hence (3.32) leads to

$$\frac{\delta\omega}{f} \approx \frac{(N^2 - f^2)(nk_1)^2}{2f^2[(nk_1)^2 + m^2]} \ll 1. \tag{3.33}$$

In scenarios where $N^2 \gg f^2$, this yields

$$m^2 \gg \frac{N^2(nk_1)^2}{2f^2}. \tag{3.34}$$

Near the critical latitude, $2f \approx \omega_1$. As a result, the sum of two daughter waves' frequencies would be $\approx\omega_1$ provided their wavenumbers satisfy (3.34). As a consequence of this special scenario, a chain of coupled triads is possible as shown in figure 3.12. Every box contains the wavevector of a daughter wave. The absolute value of the horizontal wavenumber is lowest at the center of the chain, and it increases in either direction. However, the vertical wavenumber takes only two values. Note that n would be an integer considering how the absolute value of the horizontal wavenumber increases in either direction of the central box $(0, 0, m)$. Any two boxes that are connected by the same blue line add up to give a parent wave's wavevector. For example, $(2k_1, 0, m) + (-k_1, 0, m_1 - m)$ gives $(k_1, 0, m_1)$, which is the wavevector of one of the parent waves. Moreover, $(-k_1, 0, m_1 -$

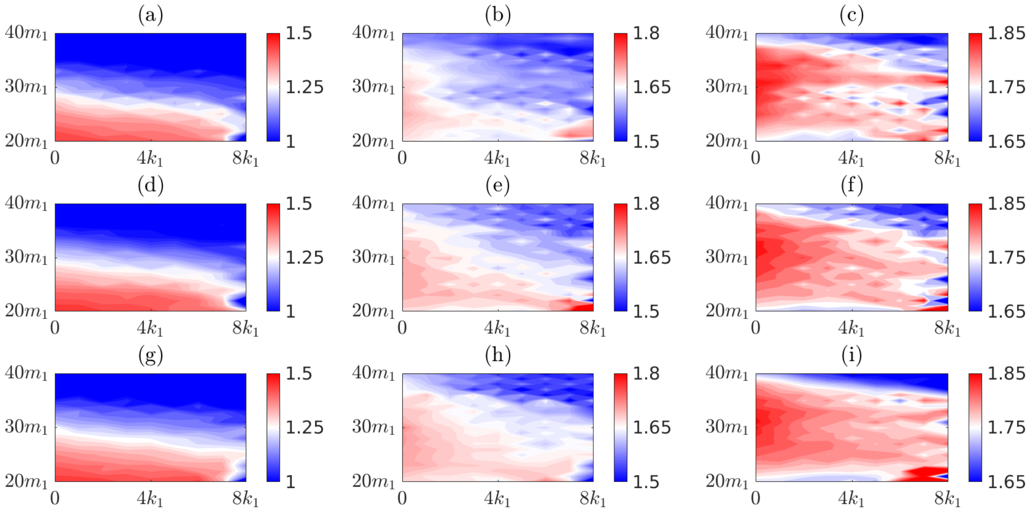

Figure 3.11: Growth rate contours ($\sigma/\sigma_{\rm cl}$) for the parent waves with wavevectors $\mathbf{k}_1 = (k_1, 0, m_1)$ and $\mathbf{k}_5 = (-k_1, 0, m_1)$ near the critical latitude ($f/\omega_1 \approx 0.5$). $f/\omega_1 = 0.496$ for Row-1 ((a), (b) and (c)), $f/\omega_1 = 0.498$ for Row-2 ((d), (e) and (f)), and $f/\omega_1 = 0.499$ for Row-3 ((g), (h) and (i)). Viscosity/hyperviscosity values used are as follows: $\nu = 10^{-6}\mathrm{m}^2\mathrm{s}^{-1}$ for Column-1 ((a), (d) and (g)), $\nu = 0.25 \times 10^{-6}\mathrm{m}^2\mathrm{s}^{-1}$ for Column-2 ((b), (e) and (h)), and $\nu_H = 0.25 \times 10^{-6}\mathrm{m}^8\mathrm{s}^{-1}$ for Column-3 ((c), (f) and (i)).

$m) + (0, 0, m)$ gives $(-k_1, 0, m_1)$, which is the other parent wave's wavevector. Except for the daughter waves at the ends of the chain, every daughter wave would be forced by both parent waves. Assuming the wavenumbers of the daughter waves in the chain satisfy (3.34), the sum of any two waves' frequencies would be $\approx \omega_1$, thus satisfying all the required triad conditions. For a fixed m, $\delta\omega$ would increase as n is increased, which is evident from (3.32). Hence for very large n, the daughter wave's frequency ($f + \delta\omega$) cannot be approximated by f and the sum of two daughter waves' frequencies cannot be approximated by ω_1 simply because $\delta\omega$ would be large. As a result, the triad conditions would not be satisfied for very large n. Assuming $\delta\omega$ is negligible up to some n, the wave amplitude equations for the $2n + 1$ daughter waves shown in figure 3.12 can be written in a compact way as follows:

$$\frac{d\mathbf{a}}{dt} = \mathcal{Q}\bar{\mathbf{a}} \tag{3.35}$$

$$\mathbf{a} = [a_{-n}\ a_{1-n}\ \dots\ a_{n-1}\ a_n]^T \tag{3.36}$$

$$\mathcal{Q} = \begin{bmatrix} -\mathcal{V}_{-n} & \mathcal{E}_{(-n,1-n)}A_5 & 0 & 0 & 0 \\ \mathcal{E}_{(1-n,-n)}A_5 & -\mathcal{V}_{1-n} & \mathcal{S}_{(1-n,2-n)}A_1 & 0 & 0 \\ \vdots & \ddots & \ddots & \ddots & \vdots \\ 0 & 0 & \mathcal{E}_{(n-1,n-2)}A_5 & -\mathcal{V}_{n-1} & \mathcal{S}_{(n-1,n)}A_1 \\ 0 & 0 & 0 & \mathcal{S}_{(n,n-1)}A_1 & -\mathcal{V}_n \end{bmatrix} \tag{3.37}$$

where the coefficients $\mathcal{E}_{(i,j)}$ and $\mathcal{S}_{(i,j)}$ are given by

$$\mathcal{E}_{(i,j)} = \frac{\mathfrak{C}_{(i,5,j)}}{\mathcal{D}_i^{(3)}}, \qquad \mathcal{S}_{(i,j)} = \frac{\mathfrak{C}_{(i,1,j)}}{\mathcal{D}_i^{(3)}}. \tag{3.38}$$

The expression for $\mathfrak{C}_{(i,*,j)}$ is given in section 3.2. Equation (3.35) is an extension of the system given in (3.21) to an arbitrary number of daughter waves. Note that using $n = 1$ in (3.35) would result in equation (3.21). The growth rate for the system given in (3.35) can be found by calculating the eigenvalues of $\mathcal{Q}$. In addition to the $\mathbf{k}_1 = (k_1, 0, m_1)$ and $\mathbf{k}_5 = (-k_1, 0, m_1)$ case, we also analyze the theoretical growth rates for oblique parent waves near the critical latitude using (3.35). To this end, we consider four θ values: $\theta = \pi/4$, $\pi/2$, $3\pi/4$, and π (see (3.28) for the definition of θ). For $\theta \neq \pi$, the parent waves have a non-zero meridional wavenumber (l_1). In such cases, the meridional wavenumber of all the daughter waves in the chain is simply assumed to be $l_1/2$. For all four θ values, figure 3.13 shows the gradual increase of the growth rate as n increases for two different m values. The vertical wavenumbers are chosen to be a large value so that they satisfy (3.34) up to $n = 7$. For all the θ values, $\sigma/\sigma_{\text{cl}} \approx 2$ for the higher n values, which is what we observed in the simulation results shown in figure 3.11. Moreover, for $n = 1$, $\sigma/\sigma_{\text{cl}} \approx \sqrt{2}$ which is what we would expect for a 5-wave system with three daughter waves. Interestingly, for an oblique set of parent waves, the results are similar to the 2D case. Hence, 5-wave system growth rates do not apply near the critical latitude for an oblique set of parent waves as well. Note that even though high values of m are used in the reduced order model, simulations show that the resonance can occur even at $m = 20 - 40m_1$. Note that by resonance, here we mean the exponential growth of the daughter waves. The exponential growth is what we observed for resonant 5-wave systems earlier as well. As a result, near the critical latitude, regardless of the θ value, two parent waves force daughter waves as

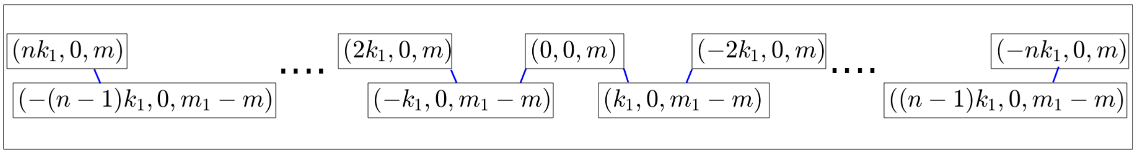

Figure 3.12: A simplified schematic showing how different daughter waves are coupled. Any two wavevectors (boxes) connected by the same blue line can act as a daughter wave combination for the wavevector $\mathbf{k}_1 = (k_1, 0, m_1)$ or $\mathbf{k}_5 = (-k_1, 0, m_1)$.

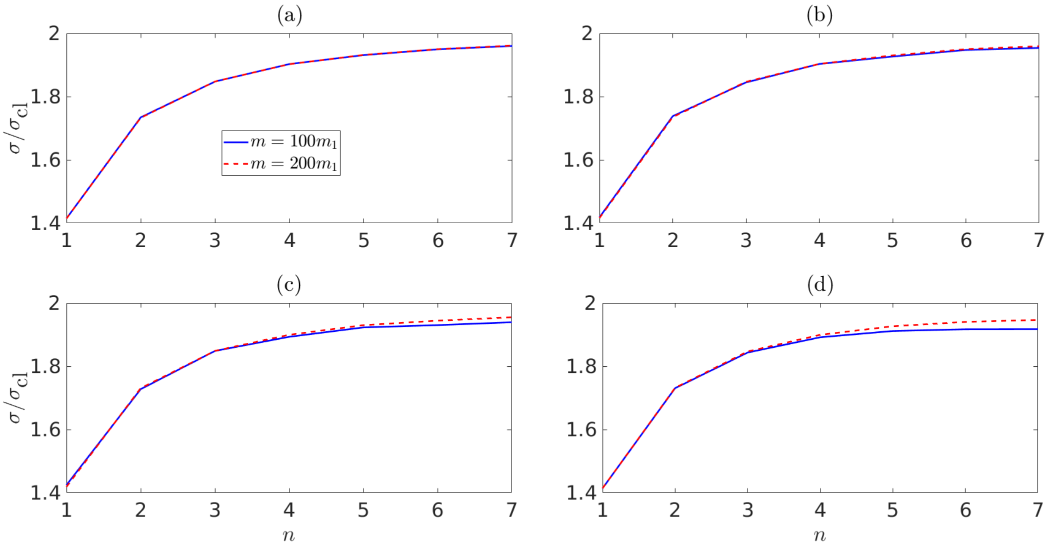

Figure 3.13: Variation of maximum growth rate with n for triad chains near the critical latitude. (a) $\theta = \pi/4$, (b) $\theta = \pi/2$, (c) $\theta = 3\pi/4$, and (d) $\theta = \pi$. Two different m values are shown for each θ.

if they are a single wave with approximately twice the amplitude.

3.5 Conclusions

Wave-wave interactions play a major role in the energy cascade of internal gravity waves. In this paper, we use multiple scale analysis to study wave-wave interactions of two plane parent waves co-existing in a region. The main instability mechanism that is focused on is the 5-wave system instability that involves two parent waves and three daughter waves. The 5-wave system is composed of two different triads (3-wave systems) with one daughter wave being a part of both triads (see figure 3.2(c)). For parent waves with wavevectors $(k_1, 0, m_1)$ and $(k_1, 0, -m_1)$, the 5-wave system is only possible when the common daughter wave's frequency is almost equal to $\omega_1 - f$ (where ω_1 is the parent wave's frequency). The other two daughter waves are near-inertial waves that always propagate in vertically opposite directions. The growth rate of the above-mentioned 5-wave system is higher than the maximum growth rate of 3-wave systems for $f/\omega_1 \gtrapprox 0.3$. For parent waves with wavevectors $(k_1, 0, m_1)$ and $(-k_1, 0, m_1)$ (parent waves that propagate in horizontally opposite directions), similar to the previous parent wave combination, the maximum growth rate of 5-wave systems is higher than the maximum growth rate of 3-wave systems for $f/\omega_1 \gtrapprox 0.3$. For $f/\omega_1 \gtrapprox 0.3$, the common daughter wave's frequency is nearly equal to f in the most unstable 5-wave system. Moreover, as the common daughter wave's frequency is increased from f, the meridional wavenumber increases significantly while the zonal wavenumber of the common daughter wave stays negligible.

We also study 5-wave systems for cases where the two parent waves are not confined to the same vertical plane. In such scenarios, the dominance of the 5-wave systems increase as the angle between the horizontal wavevectors of the parent waves (denoted by θ) is decreased. Moreover, for any θ, the 5-wave system's instability is more dominant than the 3-wave system's instability for $f \gtrapprox 0.3\omega_1$. Numerical simulations are conducted to test the theoretical predictions, and the theoretical growth rate of the 5-wave systems matches reasonably well with the results of the numerical simulations for a wide range of $f-$values. However, for all the 2D parent wave combinations considered, the growth rates from the simulations do not match the theoretical 5-wave systems' growth rate near the critical latitude where $f \approx \omega_1/2$. Near the critical latitude, more than two triads become coupled, hence a chain of daughter waves is forced by the two parent waves. By modifying the reduced order model to account for a chain of daughter waves, the maximum growth rate is shown to be twice the maximum growth rate of all 3-wave systems. Moreover, the reduced order model showed similar results for parent waves that are not on the same vertical plane. Hence, near the critical latitude, the 5-wave systems' prediction is not expected to hold for oblique parent waves as well.

Note that the study was conducted only for plane waves. The study can be extended to wave beams in future, and the results would be applicable in cases where multiple internal wave beams meet (often occurs near topographies). A finite width beam of a given frequency contains a spectrum of internal waves with different wavevectors. Interaction of involving beams means an interaction between two different spectrum of waves, and this is much more complicated scenario than the one we have considered in the thesis. For simplicity, we chose to begin with plane waves. For two parent plane waves, there are only two wavevectors and as a result the problem can be explored in depth for a wide parameter space. Note that the results should be applicable for wide internal wave beams since wide beams essentially behave like plane waves.

Chapter 4

Topographic scattering of internal waves in the presence of a steady surface current

4.1 Introduction

In chapter 2, we saw that topography influences mode-1 internal wave in multiple ways. It can alter the properties of the internal waves without directly inducing an energy cascade. As a result of the change in properties, wave-wave interactions are modified in the presence of topography. Moreover, we also saw how topography can behave as a zero-frequency wave and facilitate some higher-order interactions which otherwise would not be possible. Hence, even for modelling wave-wave interactions properly, topographies are important. In this chapter, wave-topography interactions are considered where the topography plays a more direct role in causing the energy cascade.

Internal wave-topography interactions is one of the primary mechanisms through which the low-mode internal wave energy cascades to small length scales (de Lavergne *et al.*, 2019, 2020). Figure 4.1 shows what basically happens in an internal wave (mode-1)-topography interaction. An internal wave (mode-1) encounters a topography and three main things occur: (1) Some amount of energy is transmitted past the topography in the form of mode-1, (2) some amount of energy is reflected by the topography in the form of mode-1, and (3) some amount of energy is 'scattered' into higher modes. Note that the higher modes can be transmitted, reflected, or both. The 'scattering' process, where the

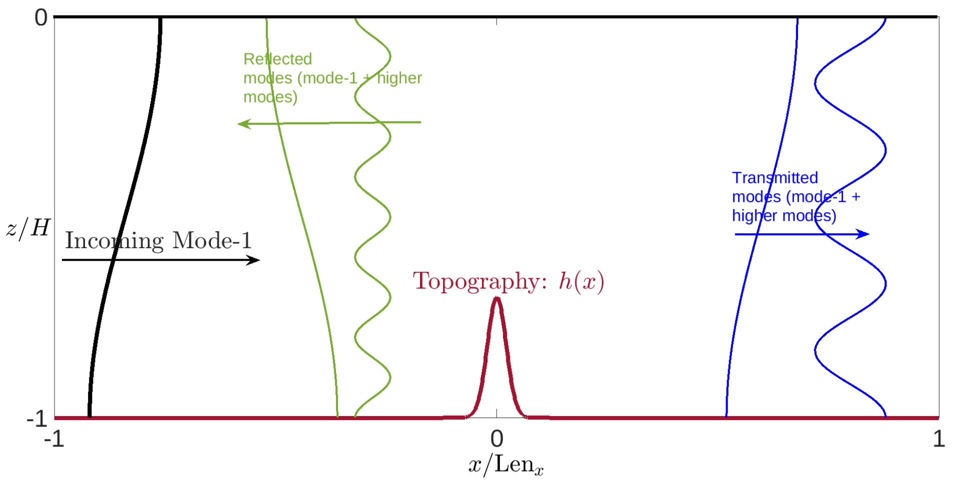

Figure 4.1: Basics of an internal wave-topography interaction. An incoming mode-1 wave impacts the topography resulting in energy getting transmitted, reflected and scattered.

energy in a mode-1 wave is transferred to modes higher than 1, is why wave-topography interactions are primarily studied. The word scattering is used to denote the generation of waves with higher wavenumbers at the cost of the incoming mode-1. The energy transfer among the modes can occur only in the regions where $dh/dx \neq 0$. Note that interaction of surface barotropic tide with the topography generates also multiple internal waves/modes. The scattering process can be similar: a barotropic surface tide can be thought of a mode-0 wave generating modes > 0, where as an internal wave mode-1 interacting with a topography generates modes $>= 1$ by scattering. Interestingly, the interaction of a stratified tide and the topography can also create small scale bottom intensified residual currents that has lower frequency compared to the tidal frequency (Maas & Zimmerman, 1989).

Internal wave-topography interactions have been extensively studied over the last few decades. A low mode internal wave can interact with isolated large amplitude topographies (Müller & Liu, 2000; Johnston & Merrifield, 2003; Klymak *et al.*, 2013; Legg, 2014; Mathur *et al.*, 2014), as well as continental shelf like structures (Hall *et al.*, 2013; Legg & Adcroft, 2003; Klymak *et al.*, 2011; Nazarian & Legg, 2017*a*,*b*). A low mode internal wave can also resonantly interact with small amplitude, sinusoidal topographies (Buhler & Holmes-Cerfon, 2011; Li & Mei, 2014; Couston *et al.*, 2017). Assuming the incoming mode-1 wave's amplitude is low, interactions involving small amplitude and large amplitude topography have been studied extensively using analytical techniques such as ray tracing, asymptotic methods, and Green's functions. Shape, criticality, and height of the topography are the important factors in internal wave scattering (Müller & Liu, 2000). Criticality (Υ) is the ratio of the maximum slope of the topography to the slope of the

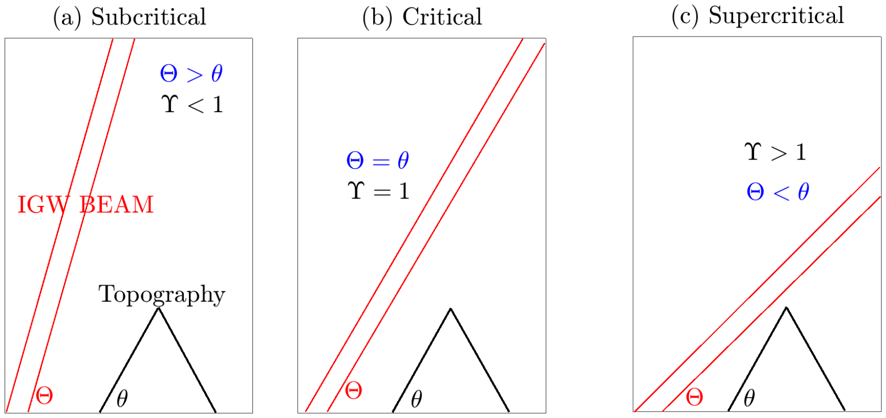

Figure 4.2: Subplots (a), (b), (c) show subcritical, critical, and supercritical topographies, respectively. The red parallel lines represent an internal wave beam with a slope $\tan\Theta$, while the black triangle at the base is assumed to be a model topography with a slope $\tan\theta$.

internal wave:

$$\Upsilon \equiv \max\left(\frac{1}{\tan\Theta}\frac{dh}{dx}\right) \tag{4.1}$$

where $h(x)$ is the topography function, and $\tan^2\Theta \equiv \omega^2/(N^2-\omega^2)$ is the slope of internal wave when $f = 0$. Here ω is the frequency of the incoming wave, and N is the local Brunt-Vaisala frequency as always. Topographies with $\Upsilon > 1$ are referred to as supercritical topographies, while $\Upsilon < 1$ are known as subcritical topographies. A simple schematic of this classification is given in figure 4.2. Transmission of the incoming internal wave energy is much higher for subcritical topographies than supercritical topographies (Müller & Liu, 2000; Johnston & Merrifield, 2003; Mathur *et al.*, 2014). Large amplitude topographies with $\Upsilon > 1$ have more reflection than transmission. However, even small amplitude supercritical topographies can have high transmission and can scatter nearly $20-40\%$ of the incoming mode-1 wave's energy (Mathur *et al.*, 2014). In general, scattering is lesser for subcritical topographies compared to supercritical topographies when the incoming mode-1 wave has a very low amplitude (linear limit). For $\Upsilon < 1$, small amplitude topographies may cause more scattering than large amplitude topographies. Large amplitude, critical topographies cause the highest scattering (Mathur *et al.*, 2014). A mode-1 internal wave interacting with a critical topography can result in a significant generation of waves with high wavenumbers.

Interaction with small amplitude, sinusoidal topographies can also result in a significant cascade of mode-1 internal wave's energy. If the topography has 'resonant' wavenumbers, then there can be a continuous cascade of energy from the incoming low mode to higher modes. For a 2D setting ($x - z$), Buhler & Holmes-Cerfon (2011) showed that the decay of mode-1's flux is exponential in nature due to scattering by the sinusoidal topography. The decay rate increased with the topography's amplitude and was found to be independent of (ω, f, N). Note that the patch of topography has to be long enough to cause a non-negligible energy cascade. Scattering by a small amplitude, subcritical, random topography (the topography was assumed to be a stationary Gaussian process) was also studied, and the decay of the mode-1 internal wave flux was observed to be exponential in nature again. Using multiple scale analysis, Li & Mei (2014) studied scattering due to small amplitude random topographies that vary in both zonal and meridional directions (2D topography). In the absence of rotation, an isotropic random 2D topography was found to be less proficient in scattering the mode-1 compared to a 1D topography. The decay rate of mode-1 increased with f/ω for an isotropic 2D topography. Couston *et al.* (2017) studied mode-1 internal wave scattering due to small amplitude resonant subcritical topographies and focused on the effects of detuning and oblique incidence. Oblique incidence leads to detuning and the explanation is as follows. For a chain resonance, the topography's wavenumber k_b should be equal to k_1 (incoming wave's wavenumber). With this specific choice of k_b, a chain resonance can occur, where the energy goes from k_1 to $2k_1$ and then to $3k_1$ and so on. The chain resonance can only occur with waves whose wavenumber is a integer multiple of the parent wave's horizontal wavenumber. This is because the $2k_1$, $3k_1$ (up to nk_1) all satisfy the dispersion relation. For an oblique incidence of the internal wave, the wave also has a meridional component (l_1). Because of the meridional wavenumber (l_1), the energy cannot go from (k_1, l_1) to $(2k_1, l_1)$ and then to $(3k_1, l_1)$ because $(3k_1, l_1)$ simply does not satisfy the internal wave dispersion relation. As a result, the resonance is cut off. As the detuning was increased, the scattering of the mode-1 wave was significantly reduced. Oblique incidence of the mode-1 wave can introduce a detuning that significantly reduces the continuous energy cascade to higher modes. Detuning can also affect the Bragg-resonance interactions. For Bragg-resonance, the wavenumber of the topography should be an integer multiple of the incoming mode-1 wave for the continuous cascade of the internal waves' energy in the presence of uniform stratification. If the 'integer-multiple' condition is not satisfied, then the detuning will affect the energy transfer.

Nonlinearity cannot be ignored if the incoming wave has a large amplitude. Legg (2014) showed that even for small amplitude $\Upsilon < 1$ topographies, rate of kinetic energy dissipation can be non-negligible when the incoming wave's Froude number is large. One of the mechanisms by which wave breaking can occur is when the wave's Froude number increases significantly due to shoaling and reaches a critical value. Results show that if a wave's Froude number is in the range $(0.3 - 1)$, then the internal mode-1 wave will break. Even topographies with low Υ can lead to significant dissipation provided it has a large amplitude, and the incoming wave's Froude number is large enough. Under linear limit, scattering is quite low ($< 10\%$) for the same topographies (Mathur *et al.*, 2014), hence amplitude of the waves can play a major role in scattering. For critical topographies, it was observed that dissipation increases linearly with height of the topography, and it is nearly independent of the incoming wave's Froude number (Legg, 2014). For $\Upsilon = 1$, dissipation was not negligible even for small amplitude topographies. Legg & Adcroft (2003) studied the interaction of finite amplitude internal wave with different shapes (convex, concave and linear) of topographies, and observed mixing regardless of the shape of the topography. This is because the interaction caused the generation of very small length scale waves in locations where the topography slope was almost equal to the internal wave slope. Nonlinear features such as internal bores were observed for different shapes of topography.

Waves getting reflected from a topography increase as Υ increases even for high amplitude incoming mode-1 waves (Hall *et al.*, 2013; Klymak *et al.*, 2013). A significant portion of the reflected energy is in the form of lower modes for tall supercritical topographies,. For supercritical topographies with very high criticality (also known as knife-edge topographies), very tall ridges dissipate less energy locally than relatively shorter ridges if the incoming wave is mode-1 (Klymak *et al.*, 2013). For a supercritical topography, the percentage of incoming mode-1's energy dissipated increases monotonically with the incident wave's amplitude regardless of the topography's height. Interestingly, it was concluded that knife-edge topographies with high criticality were not that efficient in scattering/dissipating the incoming internal waves (Klymak *et al.*, 2013). A similar result was also observed in Hall *et al.* (2013) for different non-uniform stratification profiles.

Understanding internal wave scattering and dissipation occurring in the presence of non-uniform stratification is also vital. Internal waves' dissipation in the presence of non-uniform stratification can be qualitatively similar to the constant N case when WKB scaled vertical coordinate is used to rescale the topography's height (Hall *et al.*, 2013; Legg, 2014). The WKB scaled vertical coordinate (Hall *et al.*, 2013) is given by:

$$z_{WKB} = \int_{z}^{0} \frac{N(z')}{N_{\text{mean}}} dz' \tag{4.2}$$

where N_{mean} is the average/mean value of $N(z)$. As long as the assumptions underlying WKB still hold, scattering in $(x - z_{WKB})$ in the presence of constant N_{mean} is similar to scattering in $(x - z)$ in the presence of varying $N(z)$. The above theory can even hold for wave-breaking scenarios as shown by the results in (Legg, 2014). Strong stratification near the surface enhances transmission of the internal wave energy (Hall *et al.*, 2013; Mathur *et al.*, 2014). Interestingly, for a large amplitude continental shaped topography, it was observed that the amount of energy reflected depended only on Υ even for different non-uniform stratification profiles (Hall *et al.*, 2013).

Until now, studies have primarily focused on internal wave scattering in a quiescent fluid which may have constant or varying stratification. In this chapter, the scattering of a mode-1 wave in the presence of a steady surface current is studied. The current is assumed to vary only in the vertical direction, and is not susceptible to shear instabilities. Surface currents are ubiquitous in nature (for example, the north equatorial countercurrent), and internal waves may propagate in the presence of a surface current. Internal wave generation due to tide-topography interaction in the presence of a surface current has been recently studied (Lamb & Dunphy, 2018) as well. Hence, understanding internal wave topography interactions when the mode-1 wave propagates in the presence of a surface current may help in developing better parametrisations, especially near the equator where strong currents such as Equatorial counter current exist.

The remaining sections are organised as follows. Section 4.2 outlines the derivation of the governing equations, which will be solved numerically. In section 4.3, we focus on the simulations run, results, and analysis. Section 4.4 provides a summary of the chapter. The numerical methods and validation processes are given in detail in Appendix B.

4.2 Governing equations

The incompressible, 2D (in $x - z$ plane) Navier-Stokes equations under the Boussinesq approximation, the continuity equation, along with the advection-diffusion equation for density are the governing equations considered in this study. Rotational effects are not considered for this study. Moreover, we assume the horizontal velocity u_{total} of the fluid to be the sum of a steady surface current $u_{\text{base}}(z)$ varying in the vertical direction, and a perturbation quantity $u(x, z, t)$:

$$u_{\text{total}} = u_{\text{base}}(z) + u(x, z, t). \tag{4.3}$$

Considering (4.3), the complete set of governing equations are as follows:

$$\frac{Du}{Dt} + w\frac{du_{\text{base}}}{dz} = -u\frac{\partial u}{\partial x} - w\frac{\partial u}{\partial z} - \frac{1}{\rho_0}\frac{\partial p}{\partial x} + \nu\Delta_{2D}u - \text{SP}(x)u + \mathcal{F}_u + \mathcal{H}(u), \tag{4.4}$$

$$\frac{Dw}{Dt} - b = -u\frac{\partial w}{\partial x} - w\frac{\partial w}{\partial z} - \frac{1}{\rho_0}\frac{\partial p}{\partial z} + \nu\Delta_{2D}w - \text{SP}(x)w + \mathcal{F}_w + \mathcal{H}(w), \tag{4.5}$$

$$\frac{Db}{Dt} + N^2 w = -u\frac{\partial b}{\partial x} - w\frac{\partial b}{\partial z} + \kappa\Delta_{2D}b - \text{SP}(x)b + \mathcal{F}_b + \mathcal{H}(b), \tag{4.6}$$

$$\frac{\partial u}{\partial x} + \frac{\partial w}{\partial z} = 0, \tag{4.7}$$

where $D/Dt \equiv \partial/\partial t + u_{\text{base}}\partial/\partial x$ is the linearised material derivative, $\Delta_{2D} \equiv \partial^2/\partial x^2 + \partial^2/\partial z^2$, ρ_0 is the reference density, ν and κ are respectively the kinematic viscosity and diffusivity of the stratifying agent. Throughout this study, we consider a constant stratification of $N = 10^{-3}\text{s}^{-1}$. The terms $\text{SP}(x)(u, w, b)$ are the Rayleigh sponge terms, the functional form of $\text{SP}(x)$ being

$$\text{SP}(x) = \vartheta_S\left[1 + \tanh\left(\frac{-x + x_{s1}}{W_s}\right)\right] + \vartheta_S\left[1 + \tanh\left(\frac{x - x_{s2}}{W_s}\right)\right]. \tag{4.8}$$

The values of x_{s1}, x_{s2}, W_s, and ϑ_S are varied according to the requirements of the simulation in question. The Rayleigh sponge terms are used to dampen the internal waves that propagate away from the topography. Without the damping, the waves would eventually reach the horizontal limits of the computational domain and then come back into the topography. While ϑ_S decides the strength of the sponge layer, x_{s1}, x_{s2}, and W_s are chosen such that $\text{SP}(x)$ is zero around the region of interest (here, the region where wave-topography interaction takes place), and non-zero near the horizontal limits of the computational domain, so as to absorb the waves scattered by the topography. The sponge terms, however, do not affect or dampen the base flow $u_{\text{base}}(z)$. Furthermore, $\mathcal{F}_u, \mathcal{F}_w$, and $\mathcal{F}_b$ are the wave generator functions, respectively given in (4.14)–(4.16), which send a constant amplitude mode-1 internal gravity wave towards the topography. $\mathcal{H}_u, \mathcal{H}_w$, and $\mathcal{H}_b$ are the hyperviscous terms used for numerical stability, details about which are given in Appendix B.

We use impenetrability condition at the bottom surface, while rigid lid approximation is used at the top surface. Mathematically, these respectively result in

$$w = (u_{\text{base}}(z) + u)dh/dx \quad \text{at} \quad z = h(x), \tag{4.9}$$

$$w = 0, \quad \text{at} \quad z = 0 \tag{4.10}$$

where $h(x)$ is the bottom topography profile. Moreover, we also assume free slip boundary conditions at both the bottom and top surfaces. The surface current profile is chosen such that $du_{\text{base}}/dz \approx 0$ at $z = 0$ and $z = h(x)$; in addition, $u_{\text{base}} \approx 0$ at $z = h(x)$. We use $\nu = \kappa$ consistently for simplicity. Note that we have not included the term $\nu d^2 u_{\text{base}}/dz^2$ in the equation (4.4), the reason for this approximation is provided in Appendix B. The governing equations (4.4)–(4.7) are solved numerically using Dedalus. Details about the simulations such as time-stepping scheme, grid size used along with validation of the code are provided in Appendix B. A simplified schematic of the simulation setup is given in figure 4.3. The topography is always taken to be an idealised Gaussian function, given by

$$h(x) = H\left[-1 + \frac{h_T}{H} \exp\left\{ -\frac{(x - x_T)^2}{W_T^2} \right\}\right], \tag{4.11}$$

where H ($=$ 5000m throughout the chapter) is the mean depth of the ocean, h_T/H is the non-dimensionalised topography height, and x_T decides the horizontal location of the topography. Furthermore, h_T/H and W_T together decides the criticality(Υ) of the topography. Internal waves or modes' properties in the presence of a shear flow and a constant buoyancy frequency can be obtained by solving the Taylor-Goldstein equation (Drazin & Reid, 2004). Solutions from the Taylor Goldstein equation are used in the forcing functions $\mathcal{F}_u, \mathcal{F}_w$, and $\mathcal{F}_b$. Moreover, the solutions are also needed/used to understand the modal composition of the wave field that ensues from the scattering of a mode-1 wave.

4.2.1 Taylor-Goldstein equation

The waves' modal shape in the $z-$direction, and the corresponding horizontal wavenumbers, can be obtained by solving the Taylor-Goldstein equation, given by:

$$\frac{d^2\Phi}{dz^2} + k^2 \left(\frac{N^2}{(u_{\text{base}}k - \omega_d)^2} - \frac{1}{k(u_{\text{base}}k - \omega_d)} \frac{d^2 u_{\text{base}}}{dz^2} - 1 \right) \Phi = 0, \tag{4.12}$$

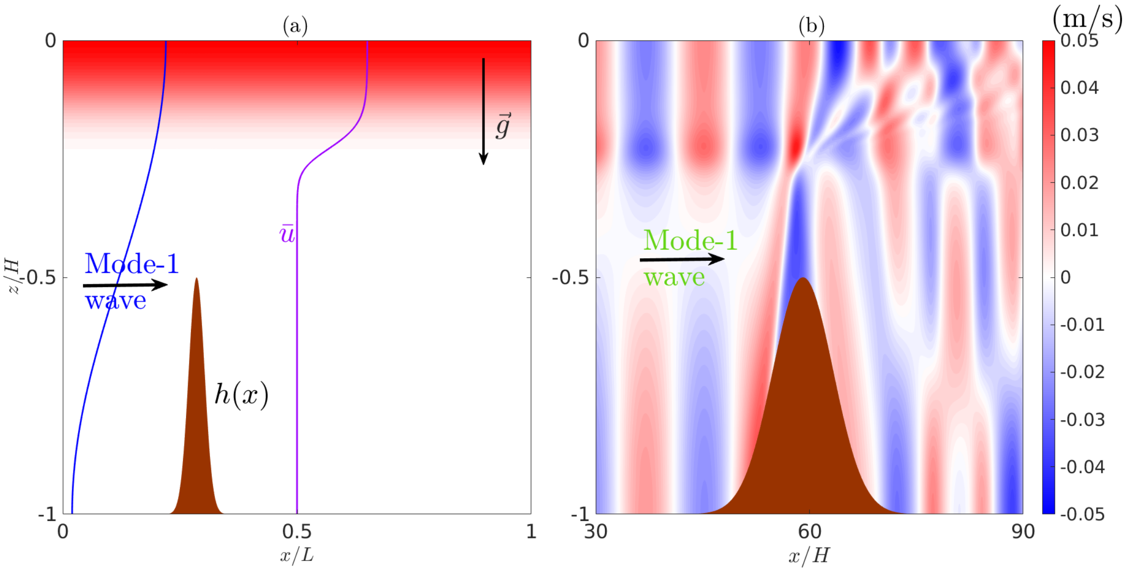

Figure 4.3: Schematic of the numerical setup. A mode-1 internal wave is generated by the forcing functions $(\mathcal{F}_u, \mathcal{F}_w, \mathcal{F}_b)$, and the wave propagates toward the topography in the presence of a steady surface current. (b) u-velocity plot for a model simulation.

where $\Phi(z)$ is the streamfunction eigenfunction in the $z-$direction. k is the horizontal wavenumber. The boundary conditions used are $\Phi = 0$ at $z = 0$ and $z = -H$. In this study, we only assume surface current profiles yielding stable configurations, that is $Ri \equiv N^2/(du_{\text{base}}/dz)^2 > 1/4$ for all z values. The frequency of the mode-1 wave is chosen to be the semi-diurnal frequency $\omega_d = 1.4 \times 10^{-4}\text{s}^{-1}$. The surface current profile is given by:

$$u_{\text{base}}(z) = \frac{U_c}{4}\left[1 + \tanh\left(\frac{z - z_{\text{crt}}}{W_{\text{crt}}}\right)\right]^2, \tag{4.13}$$

where the maximum surface current strength $U_c > 0$ is measured in terms of the velocity scale NH. We fix $W_{\text{crt}} = -0.06H$, and $z_{\text{crt}} = -0.25H$ for all the simulations, and only vary U_c. Similar surface current profile has been used in Lamb & Dunphy (2018). In the presence of a surface current profile, the wavenumbers k are not symmetric around 0, implying that if k_n is a solution, then $-k_n$ may not be a solution in general (Lamb & Dunphy, 2018). From here on, we follow the notation that the least positive wavenumber is denoted by k_1 and the subsequent positive eigenvalues are denoted by k_2, k_3, etc. In a similar way, k_{-n} denotes the negative wavenumbers where k_{-1} denotes the least absolute value of the negative wavenumbers. This study only focuses on the scattering of mode-1 internal waves. Mode-1 wave propagating with the current (wave with positive phase speed since the current itself travels along the positive $x-$direction) is denoted by M1W, while that propagating counter to the current (wave with negative phase speed) is denoted by M1C. $d\Phi/dz$ for some modes are shown in figure 4.4, and the modes are obtained by

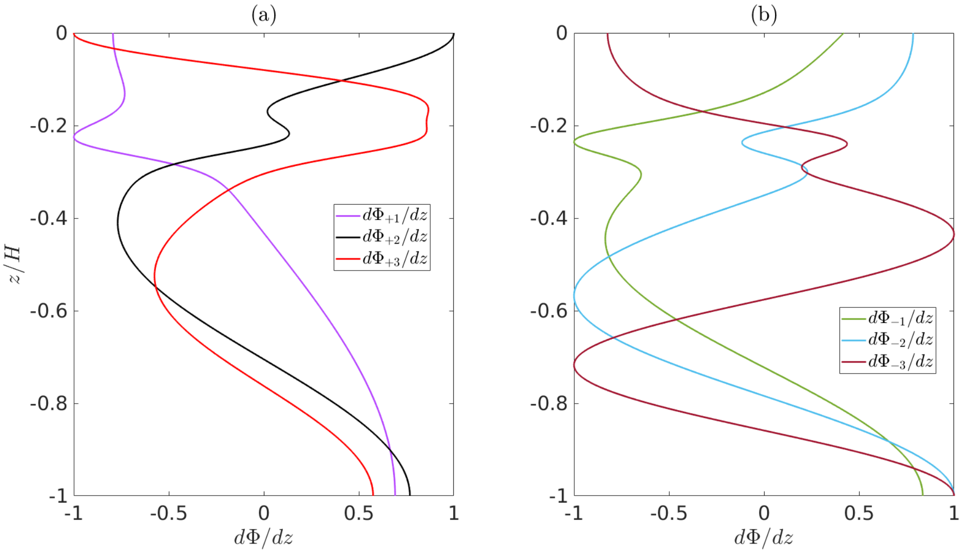

Figure 4.4: $d\Phi/dz$ for modes 1,2 and 3. (a) modes travelling with the current, and (b) modes travelling against the current. The legend provides the mode number.

solving the Taylor-Goldstein equation with $U_c = 0.10NH$.

The functions ($\mathcal{F}_u, \mathcal{F}_w$, and $\mathcal{F}_b$) are responsible for generating the mode-1 wave in the domain, and are given by:

$$\mathcal{F}_w = \vartheta_F \exp\left(-(x-x_F)^2/W_F^2\right) k_j \Phi_j \sin\left(k_j(x-x_F)\right) \tag{4.14}$$

$$\mathcal{F}_b = -\vartheta_F \exp\left(-(x-x_F)^2/W_F^2\right) k_j \Phi_j \sin\left(k_j(x-x_F)\right) \frac{N^2 k_j}{(\omega_d - u_{\text{base}} k_j)^2} \tag{4.15}$$

$$\mathcal{F}_u = \vartheta_F \exp\left(-(x-x_F)^2/W_F^2\right) k_j \frac{d\Phi_j}{dz} \cos\left(k_j(x-x_F)\right) \tag{4.16}$$

where $j = (1, -1)$ implies M1W (M1C). The values of (x_F, W_F, and ϑ_F) are varied according to the requirements of the simulation. While ϑ_F decides the amplitude of the incoming wave, x_F and W_F respectively decide the horizontal location and the width of the forcing function.

4.2.2 Energy equation

The total energy equation, obtained from the incompressible, 2D Navier-Stokes equations under the Boussinesq approximation, can be written in a compact form as follows:

$$\frac{d(E_{ke}+E_{pe})}{dt} + \nabla.((E_{ke}+E_{pe}+p)\mathbf{u}_{\text{total}}) = E^{(\text{vis})} + E_H^{(\text{vis})}, \tag{4.17}$$

where,

$$
\begin{aligned}
E_{ke} &= \frac{1}{2}\left(u_{\text{base}}^2 + 2u_{\text{base}}u + u^2 + w^2\right), \qquad E_{pe} = \frac{1}{2}\left(\frac{b^2}{N^2}\right), \\
E^{(\text{vis})} &= \nu(u_{\text{total}}\Delta u + w\Delta w) + \frac{\kappa}{N^2}b\Delta b, \qquad E_H^{(\text{vis})} = u_{\text{total}}\mathcal{H}(u) + \frac{b}{N^2}\mathcal{H}(b) + w\mathcal{H}(w).
\end{aligned}
\tag{4.18}
$$

Here E_{ke} is the total kinetic energy possessed by a fluid parcel, and E_{pe} is its potential energy. $E^{(\text{vis})}$ represents the energy dissipation and diffusion due to viscosity and molecular diffusion, while $E_H^{(\text{vis})}$ indicates the hyperviscous terms. $\mathbf{u}_{\text{total}} = (u_{\text{base}} + u, w)$ is the total velocity vector. Note that the sponge terms and the forcing (wave-generator terms) are not present in the above equation since we only use the energy equation in regions or control areas where these terms are negligible. Integration of (4.17) inside a control area whose vertical bounds are at $z = h(x)$ and $z = 0$ would lead to:

$$
\frac{d(\tilde{E}_{ke} + \tilde{E}_{pe})}{dt} + \text{TF}\bigg|_{x_R} - \text{TF}\bigg|_{x_L} = \tilde{E^{(\text{vis})}} + \tilde{E^{(\text{vis})}}_H. \tag{4.19}
$$

Here x_L and x_R respectively represent the left and right ends of the control area in question. All tilde quantities denote the area integral:

$$
\tilde{J} = \int_{A^{(R)}} J \; dA^{(R)}, \tag{4.20}
$$

where $A^{(R)}$ denotes the control area chosen. TF, i.e. total flux across a vertical section, is mathematically defined as

$$
\begin{aligned}
\text{TF} &= \int_h^0 [u_{\text{total}}((E_{ke} + E_{pe}) + p)]dz \\
&= \int_h^0 \left[(u_{\text{base}} + u)\left(\frac{1}{2}\left(u_{\text{base}}^2 + 2u_{\text{base}}u + u^2 + w^2\right) + E_{pe} + p\right)\right]dz \\
&= \underbrace{\int_h^0 \frac{1}{2}u_{\text{base}}\left(u_{\text{base}}^2 + 3u_{\text{base}}u + 3u^2\right) + \frac{1}{2}u\left(u^2\right)dz}_{\text{Advection of horizontal kinetic energy}} \\
&+ \underbrace{\int_h^0 p(u_{\text{base}} + u)dz}_{\text{Pressure Work}} + \underbrace{\int_h^0 \frac{1}{2}(u_{\text{base}} + u)\left(w^2\right)dz}_{\text{Advection of vertical kinetic energy}} \\
&+ \underbrace{\int_h^0 \frac{1}{2}(u_{\text{base}} + u)\left(E_{pe}\right)dz}_{\text{Advection of potential energy}}
\end{aligned}
\tag{4.21}
$$

Note that the kinetic and potential energy can be advected by the surface current u_{base}, and also the perturbation velocity u. Equation (4.19) implies that the energy inside a control area varies because of the flux, viscous and the hyperviscous terms. Diffusion at the horizontal limits of the control area is usually negligible for the parameter regime considered in this study. The rate of kinetic energy dissipation inside the control domain is given by

$$\tilde{K}_D = -\nu \int_{A^{(R)}} \left[\left(\frac{\partial u}{\partial x}\right)^2 + \left(\frac{\partial w}{\partial x}\right)^2 + \left(\frac{\partial u}{\partial z}\right)^2 + \left(\frac{\partial w}{\partial z}\right)^2 + \left(\frac{\partial u}{\partial z}\frac{\partial u_{\text{base}}}{\partial z}\right) \right] dA^{(R)}. \tag{4.22}$$

Note that the integral of the viscous term ($E^{(\text{vis})}$) would include both viscous diffusion and viscous dissipation. We only require rate of kinetic energy dissipation, which is the measure of how much kinetic energy is destroyed in the control volume per unit time. Note that kinetic energy diffusion does not destroy the energy. It simply moves the kinetic energy outside the control volume/area. The final term in (4.22) is a consequence of the assumption that the base flow is non-dissipative. We mainly focus on the modal composition of the scattered field which has the same frequency as the incoming mode-1 wave (ω_d). To measure how much energy resides in a particular mode, we concentrate on the 'linear' flux terms of equation (4.21) (Lamb & Dunphy, 2018). By linear flux terms, we refer to the terms that can have a non-zero contribution (in a time averaged sense) when only a linear wave is considered. These terms are given by,

$$\mathcal{T} = \int_h^0 pu + \frac{u_{\text{base}}}{2}\left(3u^2 + w^2 + \frac{b^2}{N^2}\right) dz. \tag{4.23}$$

Note that terms like pu_{base} and $3u_{\text{base}}^2 u/2$, which arise in (4.21), can have a non-negligible contribution, in a time-averaged sense, only when the nonlinear terms in the Navier-Stokes equations are considered. Because of nonlinearity, p and u contain time-invariant mean fields (Lamb & Dunphy, 2018). However, these flux terms do not provide any extra information on the amplitude, or the energy, residing in a particular mode after scattering. As a result, these terms are not taken into consideration. The linear fluxes we are focusing on is expected to be nearly same with or without the nonlinear terms (Lamb & Dunphy, 2018) because the incoming wave amplitude is chosen such that the scattering process is nearly at a linear regime. The simulations are still run with the nonlinear terms because we also want to study superharmonic generation due to internal wave scattering. Defining

$$\langle ... \rangle \equiv \int_0^{2\pi/\omega_d} ... \; dt,$$

the normalised, time-integrated, total linear flux due to $j-$th internal wave mode with frequency ω_d is given by

$$\langle \mathcal{T}_j \rangle = \frac{1}{\langle \mathcal{T}_{inc} \rangle} \int_0^{2\pi/\omega_d} \int_h^0 p_j u_j + \frac{u_{\text{base}}}{2} \left(3u_j^2 + w_j^2 + \frac{b_j^2}{N^2} \right) dz dt \tag{4.24}$$

where

$$\langle \mathcal{T}_{inc} \rangle = \int_0^{2\pi/\omega_d} \int_h^0 p_{inc} u_{inc} + \frac{u_{\text{base}}}{2} \left(3u_{inc}^2 + w_{inc}^2 + \frac{b_{inc}^2}{N^2} \right) dz dt.$$

For all variables, the subscript 'inc' denotes the corresponding incoming mode-1's field.

4.2.3 Mode-isolation method

The subsection explains the method used to find the amplitude of a particular internal wave mode which oscillates in time with frequency ω_d. The amplitude of the mode can then be used to find the flux $\langle \mathcal{T}_j \rangle$. To this end, we focus on the perturbation horizontal velocity field. In the simulation data, the perturbation velocity contains multiple frequencies ($0, \omega_d, 2\omega_d, \ldots$) apart from the frequency (ω_d) we are interested in because of the nonlinear terms in the governing Navier-Stokes equations. We first obtain the ω_d component of the $u-$field (denoted by u_{ω_d} hereafter) using Fourier transforms. Note that u_{ω_d} is not the Fourier coefficient, rather the horizontal velocity field which oscillates in time only with frequency ω_d. Now, we assume that for every (x, t), u_{ω_d} can be written as a linear combination of discrete internal wave modes (Φ_n), where the latter is obtained by solving equation (4.12). Mathematically, this implies

$$u_{\omega_d} \approx u_R = \sum_{n=1}^{n=M_n} A_n(x,t) \frac{d\Phi_n}{dz} \tag{4.25}$$

where u_R denotes the reconstructed horizontal velocity field, M_n is the total number of modes considered, and $A_n(x, t)$ is the amplitude coefficient of $n-$th mode, which will be obtained using the simulation data. For a particular (x, t), A_n is obtained by solving the linear system of equations provided below in a compact form:

$$\begin{bmatrix} \int_{-H}^{0}\left(\frac{d\Phi_1}{dz}\right)^2 dz & \int_{-H}^{0}\left(\frac{d\Phi_1}{dz}\frac{d\Phi_2}{dz}\right) dz & \cdots \\ \vdots & \ddots & \\ \vdots & \ddots & \\ & & \int_{-H}^{0}\left(\frac{d\Phi_{Mn}}{dz}\right)^2 dz \end{bmatrix} \begin{bmatrix} A_1 \\ A_2 \\ \vdots \\ A_{M_n} \end{bmatrix} = \begin{bmatrix} \int_{-H}^{0} u_{\omega_d}\frac{d\Phi_1}{dz} dz \\ \int_{-H}^{0} u_{\omega_d}\frac{d\Phi_2}{dz} dz \\ \vdots \\ \int_{-H}^{0} u_{\omega_d}\frac{d\Phi_{Mn}}{dz} dz \end{bmatrix} \tag{4.26}$$

Without the current, the square matrix in the LHS of (4.26) will be a diagonal matrix. The presence of surface current renders the modes non-orthogonal, hence the non-diagonal entries are non-zero in general. Moreover, the modal coefficients (A_n) themselves can vary depending on the choice of M_n, which is not the case for the orthogonal modes. In spite of these, as explained below, we observe that the above method of mode isolation provides a reasonably accurate reconstruction of the fluxes. Moreover, we observe that the u_R obtained by our method matches exactly with the u_R obtained using Gram-Schmidt Orthonormalization.

In section 4.3, the above mentioned method is used to estimate the flux ($\langle \mathcal{T}_j \rangle$) for each mode after the scattering of the mode-1 wave. $\langle \mathcal{T}_j \rangle$ is calculated using the amplitude $A_n(x,t)$, and by assuming the waves nearly satisfy the normal mode form. Using the normal mode assumption, the amplitude of a particular mode's other fields ($w, b,$ and p) can be found using $A_n(x,t)$. To see whether u_R is a good approximation of u_{ω_d} and to verify the validity of the normal mode assumption, we compare the time and depth-integrated linear pressure work and linear horizontal kinetic energy flux of the reconstructed fields with the flux data obtained from simulations. We do not consider the linear vertical kinetic energy and potential energy flux because, for all the simulations, the sum of time and depth-integrated vertical kinetic energy and potential energy flux is less than 4% of sum of pressure work and linear horizontal kinetic energy flux. Mathematically,

$$\frac{\max\left|\langle \int_h^0 u_{\text{base}}/2\left(w_{\omega_d}^2 + b_{\omega_d}^2/N^2\right) dz\rangle\right|}{\max\left|\langle \int_h^0 p_{\omega_d} u_{\omega_d} + u_{\text{base}}/2\left(3u_{\omega_d}^2\right) dz\rangle\right|} < 0.04 \tag{4.27}$$

where $(p_{\omega_d}, w_{\omega_d}, b_{\omega_d})$ denote the pressure, vertical velocity, and buoyancy fields that oscillate in time with frequency ω_d, respectively. Hence, we only use the sum of pressure work and horizontal kinetic energy for validation. The sum of time and depth-integrated linear pressure work and horizontal kinetic energy flux for a range of x using p_{ω_d} and u_{ω_d} is first calculated. Mathematically the quantity is given by,

$$P_{f2}^{(N)} = \int_0^{2\pi/\omega_d} \int_{-H}^{0} \left(p_{\omega_d} u_{\omega_d} + \frac{3}{2} u_{\text{base}} \left(u_{\omega_d} \right)^2 \right) dz dt \tag{4.28}$$

Note that $P_{f2}^{(N)}$ is directly obtained from the simulation data without any mode separation. Now using u_R and p_R we once again evaluate the same flux quantity, where p_R denotes the reconstructed pressure field, and it can be found using u_R and the linearised $u-$momentum equation as given below

$$p_R = \sum_{n=1}^{n=M_n} \left[\left(\frac{\omega_d}{k_n} - u_{\text{base}} \right) \frac{d\Phi_n}{dz} + \frac{du_{\text{base}}}{dz} \Phi_n \right] A_n(x,t). \tag{4.29}$$

$dA_n/dx \approx \mathrm{i} k_n A_n$ is used to arrive at equation (4.29). The sum of time and depth-integrated linear pressure work and horizontal kinetic energy flux calculated using p_R and u_R is given by,

$$P_{f2} = \int_0^{2\pi/\omega_d} \int_{-H}^{0} \left(p_R u_R + \frac{3}{2} u_{\text{base}} \left(u_R \right)^2 \right) dz dt. \tag{4.30}$$

$P_{f2}^{(N)}$ and P_{f2} are functions of x only. For every simulation, we compare $P_{f2}^{(N)}$ and P_{f2} for a range of x to validate the method. Two quantities are defined to estimate the difference between $P_{f2}^{(N)}$ and P_{f2}:

$$\text{Er}_{\text{avg}} = \frac{1}{x_R - x_L} \int_{x_R}^{x_L} \left| \frac{P_{f2}^{(N)} - P_{f2}}{\langle \mathcal{T}_{inc} \rangle} \right| dx, \qquad \text{Er}_{\text{max}} = \max \left(\left| \frac{P_{f2}^{(N)} - P_{f2}}{\langle \mathcal{T}_{inc} \rangle} \right| \right) \tag{4.31}$$

Er_{avg} gives a measure of the average error induced in the reconstruction in a given range of x. Moreover, Er_{max} gives the maximum error in the reconstruction for the same range. For all the simulations, Er_{avg} is observed to be < 0.01. For all the simulations, including supercritical topographies, Er_{max} is observed to be < 0.03. Only 5 simulations have $\text{Er}_{\text{max}} > 0.015$, indicating that for majority of the simulations $\text{Er}_{\text{max}} < 0.015$. All simulations involving a subcritical topography have $\text{Er}_{\text{max}} < 0.015$. For supercritical topographies, we apply the mode-isolation method for both transmitted and reflected wave fields. As a result, for a single simulation, we use the method twice. Considering this, for supercritical topographies, 5 instances (out of 60) $\text{Er}_{\text{max}} > 0.015$ was observed, where

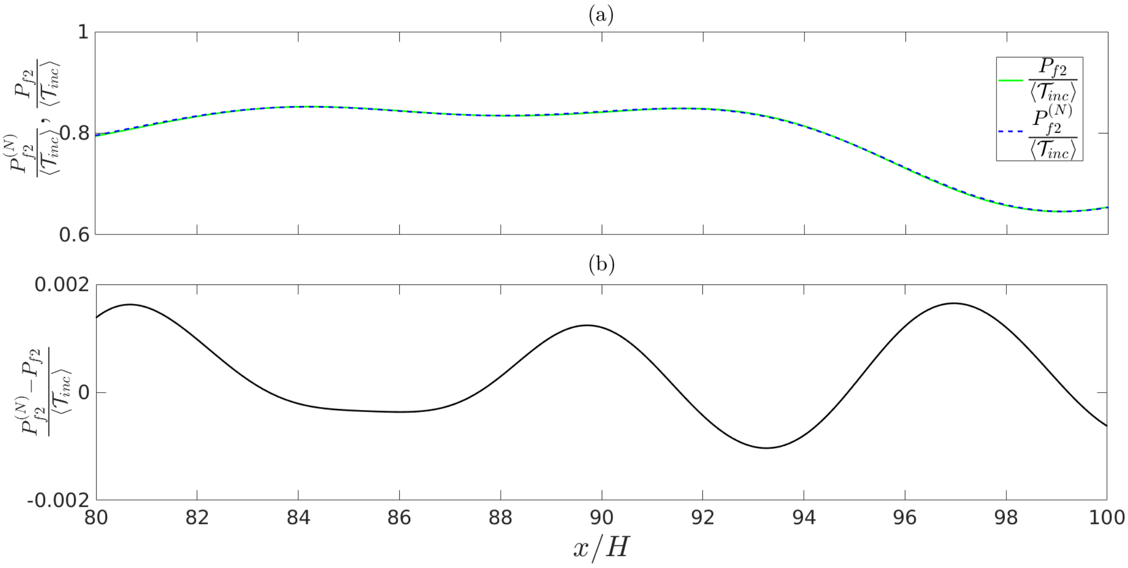

Figure 4.5: (a) compares normalized $P_{f2}^{(N)}$ and P_{f2} obtained after the scattering of M1W by a topography with parameters $\Upsilon = 0.5$ and $h_T/H = 0.5$. $U_c = 0.1NH$ is used. (b) shows the normalised difference between the two quantities plotted in (a).

the maximum $\mathrm{Er}_{\max}$ is ≈ 0.03. Figure 4.5 shows $P_{f2}^{(N)}$ and P_{f2} obtained from the simulation which models the scattering of M1W ($U_c = 0.10NH$) by a topography with $(\Upsilon, h_T/H) = (0.5, 0.5)$. The method is applied to a region where the scattered wave field is present. It can be seen that the reconstruction of the flux is within < 0.002, and the mode-1 loses around 50% of its energy due to the scattering in this particular case. For the same control area, figure 4.6 shows the reconstructed velocity field and the pressure field (15 modes are used), and p_{ω_d} and u_{ω_d} obtained from the simulation at a particular instance. In this particular case, it can be seen that the features in u_{ω_d} and p_{ω_d} have been reconstructed in u_R and p_R, respectively. Likewise, figure 4.7 shows a comparison between $(u_{\omega_d}, p_{\omega_d})$ and (u_R, p_R) from the simulation that models the scattering of M1C ($U_c = 0.10NH$) by a topography with $(\Upsilon, h_T/H) = (0.75, 0.35)$.

4.3 Results

4.3.1 Subcritical topographies

We first focus on subcritical ($\Upsilon < 1$) topographies. In this regard, we consider three different heights: $h_T/H = 0.2, 0.35$, and 0.5, and for each height, we vary Υ. For all topographies, scattering of both M1C and M1W is studied. All simulations are at least

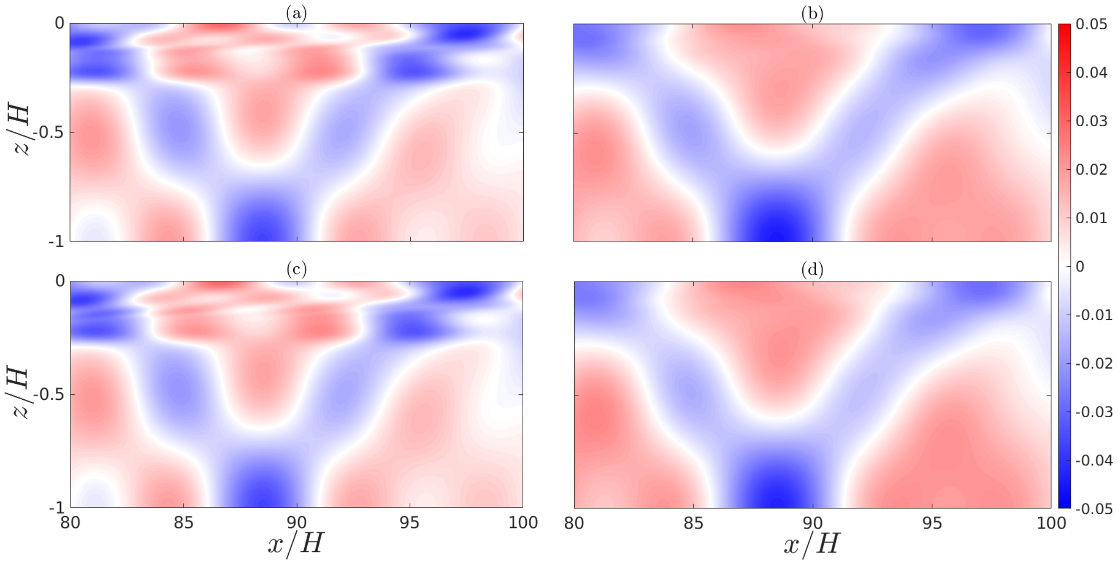

Figure 4.6: (a) and (b) show the reconstructed u-velocity field (u_R) and the pressure field (p_R) after the incoming M1W was scattered, respectively. (c) and (d) show the u-velocity field (with frequency ω_d) (u_{ω_d}) and the pressure field (p_{ω_d}) obtained from the simulation, respectively. Topography used in this simulation has parameters $\Upsilon = 0.5$ and $h_T/H = 0.5$. The values given in the colorbar applies for all the subplots with appropriate units.

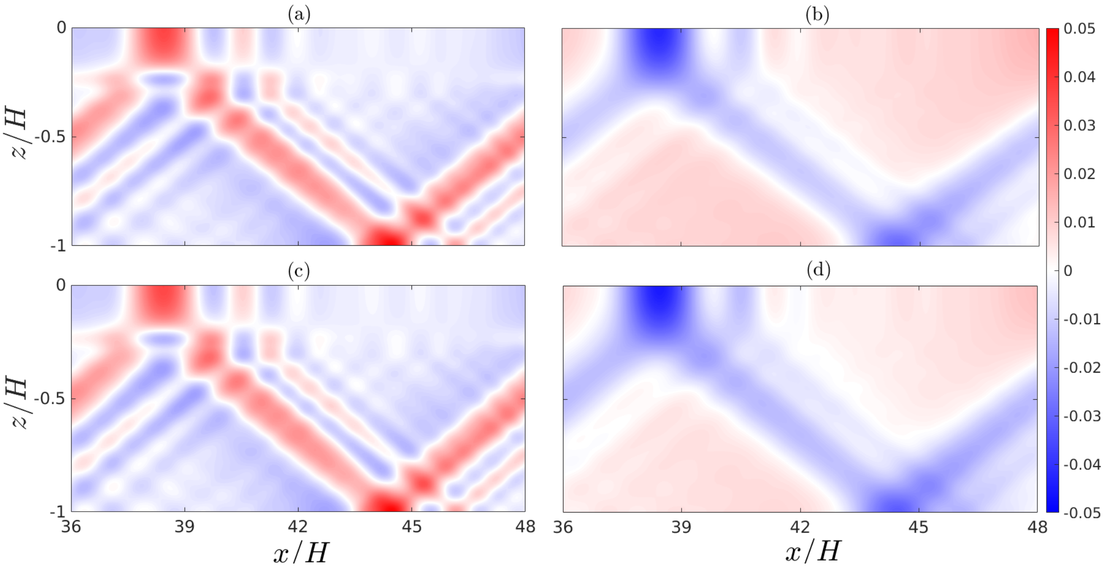

Figure 4.7: Caption same as figure 4.6 except the fields shown are from the simulation modeling the scattering of M1C by a topography with $\Upsilon = 0.75$ and $h_T/H = 0.35$.

run for 30 time periods of the parent wave. A complete list of simulations run for the subcritical topographies is given in table 4.1. The table provides the different values of current strength U_c used for each topography, along with the incoming mode-1 wave's amplitude and the kinematic viscosity value used. Note that a high value of viscosity is used. High values of viscosity has been used so that the small scale waves/features dissipate. Reducing viscosity effectively means that we are increasing Reynolds number, and as we increase Reynolds Number we need to increase the resolution of the simulations as well. However, it is very computationally expensive to match the exact Reynolds number observed in the ocean. As a result, we increase the viscosity value. High values of viscosity have been used previously in studies involving internal wave interactions with topographies (Nikurashin & Legg, 2011; Nazarian & Legg, 2017*b*).

h_T/H	Υ	max($d\Phi_{\text{inc}}/dz$) (ms^{-1})	ν (m$^2s^{-1}$)	U_c/NH for M1W and M1C
0.20	(0.1,0.2)	0.03	0.01	$(0, 0.1)$
”	(0.25,0.50,0.75)	”	”	$(0, 0.04, 0.07, 0.1)$
”	(0.40,0.60,0.90)	”	”	$(0, 0.04, 0.1)$
0.35	(0.10)	”	”	$(0, 0.1)$
”	(0.25,0.50)	”	”	$(0, 0.04, 0.07, 0.1)$
”	(0.40,0.60)	”	”	$(0, 0.04, 0.1)$
”	(0.75)	0.015	0.005	$(0, 0.04, 0.07, 0.1)$
”	(0.85)	”	”	$(0, 0.04, 0.1)$
0.5	(0.10)	0.03	0.01	$(0, 0.1)$
”	(0.25,0.50)	”	”	$(0, 0.04, 0.07, 0.1)$
”	(0.40,0.60)	”	”	$(0, 0.04, 0.1)$
”	(0.75)	0.015	0.005	$(0, 0.04, 0.07, 0.1)$
”	(0.85)	”	”	$(0, 0.04, 0.1)$

Table 4.1: List of simulations run for subcritical ($\Upsilon < 1$) topographies. The double quotation mark indicates that the value or array is the same as the one above it.

4.3.1.1 Scattering of M1W and M1C for $h_T/H = 0.2$.

We first focus on mode-1's interaction with small amplitude topographies for different Υ values with $h_T/H = 0.2$ held fixed. For both M1W and M1C, there is generally a consistent and gradual change in scattering behavior with the inclusion of a surface current, see figure 4.8. For any Υ, the maximum difference in scattering (difference in $\langle\mathcal{T}_1\rangle$) induced by the surface current is $\approx$ 7% for both M1W and M1C. For both M1W and M1C, the change in scattering introduced by the current has a complex behaviour as Υ is varied, and this is shown in figure 4.9 where $\Delta\langle\mathcal{T}_1\rangle$ – the difference between $\langle\mathcal{T}_1\rangle$ values computed

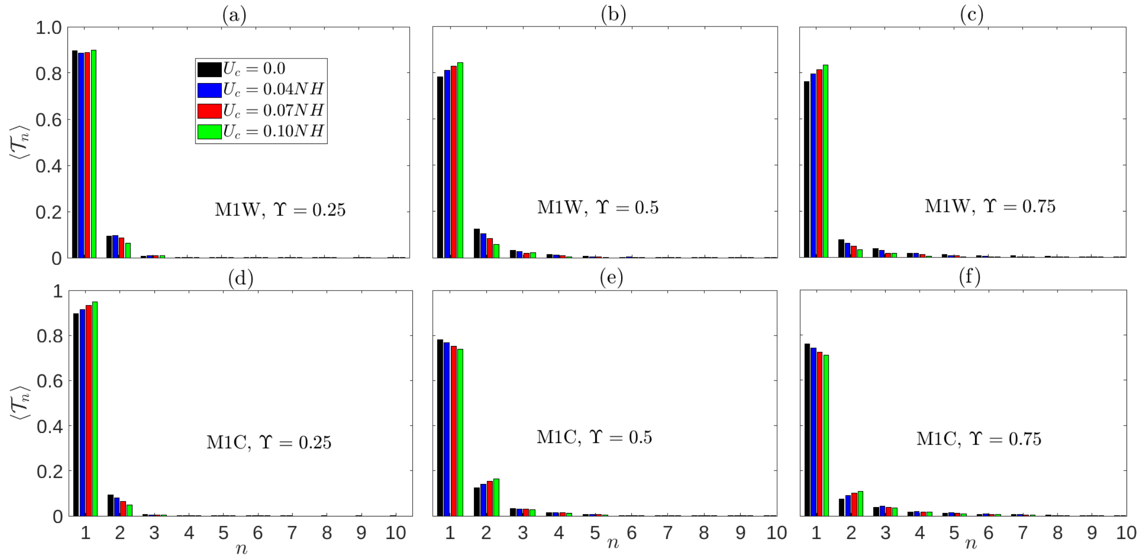

Figure 4.8: $\langle \mathcal{T}_n \rangle$ plots for the first 10 modes. Top row: M1W, bottom row: M1C. $\Upsilon = 0.25$ ((a) & (d)), $\Upsilon = 0.5$ ((b) & (e)), and $\Upsilon = 0.75$ ((c) & (f)). For all cases, $h_T/H = 0.2$. Colors correspond to various U_c values (see legend).

at $U_c = 0.10NH$ and at $U_c = 0$ is plotted. Note that a negative (positive) $\Delta\langle \mathcal{T}_1 \rangle$ implies the current increased (decreased) the scattering compared to the 'no-current' $U_c = 0$ case. For a very low Υ, the current has very little influence on the scattering: $\Delta\langle \mathcal{T}_1 \rangle$ is very low for $\Upsilon = 0.1$ for both M1W and M1C. As Υ is increased, $\Delta\langle \mathcal{T}_1 \rangle$ is positive (negative) for M1C (M1W) for a small range of Υ. However, as Υ is increased further, $\Delta\langle \mathcal{T}_1 \rangle$ changes to a negative (positive) quantity for M1C (M1W), which is the opposite of the behaviour seen previously. For $\Upsilon \gtrapprox 0.25$, the current strictly decreases the scattering of M1W compared to the $U_c = 0$ case, while for $\Upsilon \gtrapprox 0.40$ the current strictly increases the scattering for M1C. Note that $|\Delta\langle \mathcal{T}_1 \rangle|$ is similar for both M1W and M1C, however, there can still be $> 10\%$ difference in $\langle \mathcal{T}_1 \rangle$ between M1C and M1W because the current increases (decreases) the scattering for M1C (M1W) for the higher Υ values. Moreover, the difference between M1C and M1W's scattering is expected to increase if the wave is scattered by an array of small amplitude topographies instead of a single topography.

4.3.1.2 Scattering of M1W and M1C for $h_T/H = 0.35$.

For $h_T/H = 0.35$, figure 4.10 shows the modal composition of the transmitted wave field after the scattering. For both M1W and M1C, scattering changes gradually as U_c is varied, which is similar to what was observed for $h_T/H = 0.2$. However, the magnitude of the change in scattering introduced by the current is higher compared to $h_T/H = 0.2$.

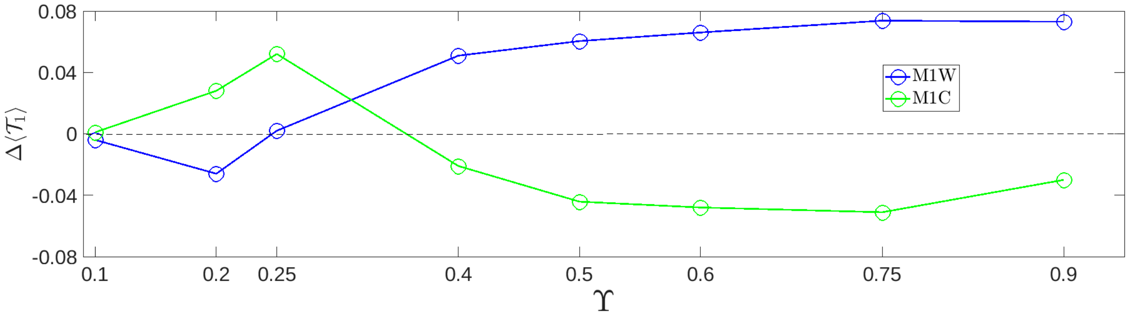

Figure 4.9: Difference between $\langle\mathcal{T}_1\rangle$ for $U_c = 0.10NH$ and $U_c = 0.0$ for various topographic configurations with $h_T/H = 0.2$. $\Delta\langle\mathcal{T}_1\rangle \equiv \langle\mathcal{T}_1\rangle(U_c = 0.10NH) - \langle\mathcal{T}_1\rangle(U_c = 0)$.

The maximum $|\Delta\langle\mathcal{T}_1\rangle|$ observed for M1W (M1C) is $\approx 0.11(0.17)$. Increasing the height of the topography does not necessarily mean the scattering also increases, and this can be seen by comparing the $\Upsilon = 0.25$ case for $h_T/H = 0.2$ and 0.35. For low Υ, small amplitude topographies can be more proficient in scattering the mode-1 wave (Mathur *et al.*, 2014, figure 4). As Υ is increased, scattering is higher for $h_T/H = 0.35$ compared to 0.2 regardless of the current strength.

Similar to $h_T/H = 0.2$, for both M1W and M1C, the current may increase or decrease the scattering compared to the $U_c = 0$ case depending on the Υ value, as shown in figure 4.11. The behaviour of $\Delta\langle\mathcal{T}_1\rangle$ is very similar to what was observed for the case of $h_T/H = 0.2$. For very low Υ values, the current does not create much of a difference and this can be seen for M1W when $\Upsilon = 0.1$, and for M1C when $\Upsilon \leq 0.25$. Moreover, as Υ is increased, the current increases (decreases) the scattering of M1W (M1C) for a finite range of Υ. Furthermore, beyond a certain Υ, the current decreases (increases) scattering for M1W and M1C. For M1W (M1C), $\Delta\langle\mathcal{T}_1\rangle$ changes from a negative (positive) to a positive (negative) quantity at $\Upsilon \approx 0.4$ (0.6). The transition is permanent (the sign of $\Delta\langle\mathcal{T}_1\rangle$ does not change again), and this will be evident in the section focusing on supercritical topographies. Note that for M1W (M1C), the transition occurred at $\Upsilon \approx 0.25(0.4)$ for $h_T/H = 0.2$. Hence, the Υ at which $\Delta\langle\mathcal{T}_1\rangle$ changes sign is observed to be a function of h_T/H.

4.3.1.3 Scattering of M1W and M1C for $h_T/H = 0.5$.

The results for $h_T/H = 0.5$ are shown in figure 4.12. For large amplitude topographies, the influence of the current on the scattering is much higher for M1W than what was observed for $h_T/H = 0.2$ and 0.35. Note that for M1W, even if the 'no-current' ($U_c =$

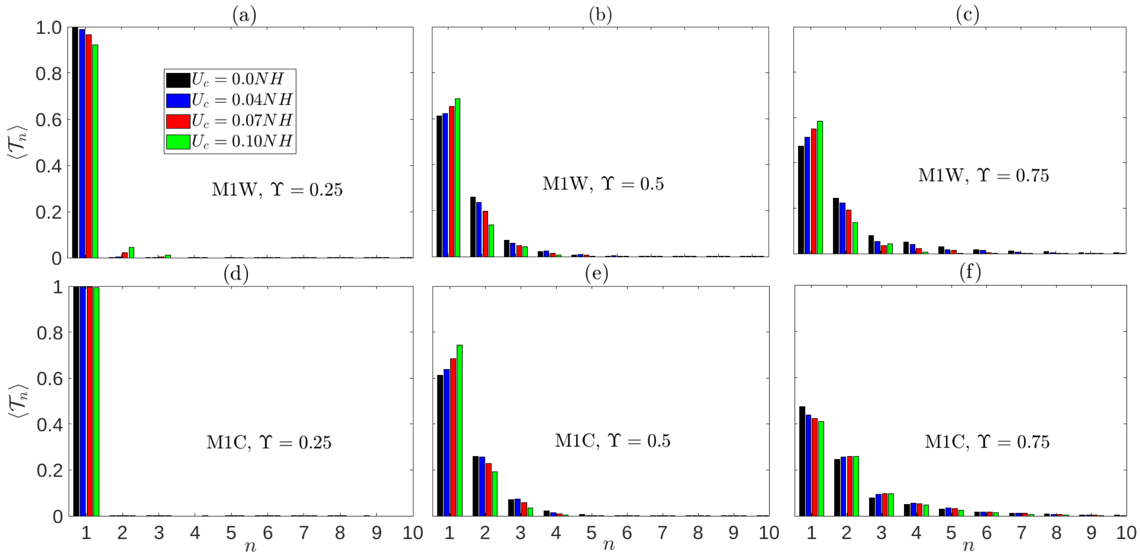

Figure 4.10: Caption same as figure 4.8 except $h_T/H = 0.35$.

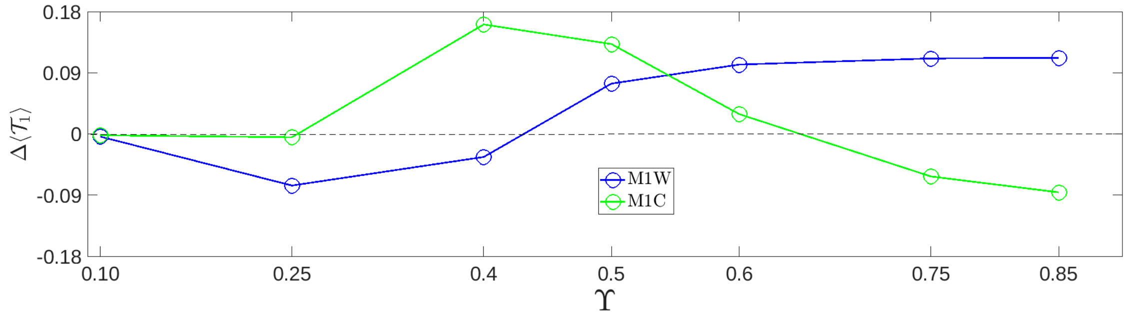

Figure 4.11: Caption same as figure 4.9 except $h_T/H = 0.35$.

0) case has negligible scattering for a particular topography, $U_c \neq 0$ cases can have a significant scattering. In contrast, for M1C, topographies which cause minimal scattering when $U_c = 0$ also cause very little scattering when $U_c \neq 0$. This can be seen for $\Upsilon \leq 0.5$ where there is very little scattering for $U_c = 0$, and there is not a significant change in the scattering behaviour as U_c is increased. Similar behaviour can also be seen in figure 4.10 for $h_T/H = 0.35$ when $\Upsilon \leq 0.25$. As a result, for M1C, the current will not cause a significant difference in scattering if the $U_c = 0$ case has very low scattering.

We can once again observe a similar pattern for $\Delta\langle \mathcal{T}_1 \rangle$ for both M1W and M1C, as shown in figure 4.13. For very low Υ, $\Delta\langle \mathcal{T}_1 \rangle$ is negligible. For M1W and for $0.1 \lessapprox \Upsilon \lessapprox 0.6$, $\Delta\langle \mathcal{T}_1 \rangle$ is a negative quantity, while for $\Upsilon \gtrapprox 0.6$, the current reduces scattering ($\Delta\langle \mathcal{T}_1 \rangle$ is positive). The value at which the transition occurs ($\Delta\langle \mathcal{T}_1 \rangle$ changing from a positive to a negative quantity) monotonically increases with the height of the topography. For M1C, the current has a stabilising effect for $0.5 \lessapprox \Upsilon \lessapprox 0.85$. Hence for large amplitude subcritical topographies adding a current reduces the scattering of M1C for a significant range of Υ. Note that for M1C, $\Delta\langle\mathcal{T}_1\rangle$ was observed to be a negative quantity after a certain Υ value, however, that is not apparent in figure 4.13. This is because the transition of $\Delta\langle\mathcal{T}_1\rangle$ from a positive to a negative quantity occurs at $\Upsilon \approx 0.85$. For $\Upsilon \geq 0.85$, $\Delta\langle\mathcal{T}_1\rangle$ is strictly a negative quantity as will be shown in the section focusing on supercritical topographies. Similar to M1W, the Υ at which $\Delta\langle\mathcal{T}_1\rangle$ changes sign monotonically increases with the height of the topography for M1C. The results for $\Delta\langle\mathcal{T}_1\rangle^{(4)} \equiv \langle\mathcal{T}_1\rangle(U_c = 0.04NH) - \langle\mathcal{T}_1\rangle(U_c = 0)$ is qualitatively very similar to $\Delta\langle\mathcal{T}_1\rangle$. The primary difference is in the magnitude: $|\Delta\langle\mathcal{T}_1\rangle^{(4)}|$ is in general lower than $|\Delta\langle\mathcal{T}_1\rangle|$. Moreover, the Υ at which $\Delta\langle\mathcal{T}_1\rangle$ and $\Delta\langle\mathcal{T}_1\rangle^{(4)}$ change sign is slightly different. For example, $\Delta\langle\mathcal{T}_1\rangle^{(4)}$ is a negative quantity at $\Upsilon = 0.75$ for M1C (see figure 4.12(f)) while $\Delta\langle\mathcal{T}_1\rangle$ switches from positive to negative only at $\Upsilon \approx 0.85$.

Note that subcritical topographies can also reflect internal waves. However, the quantity of energy reflected back is quite low compared to the energy that is transmitted. In our numerical simulations, we did find a small amount of waves moving in the opposite direction of the incoming mode-1 internal wave when it interacts with the subcritical topography. In general, as Υ is increased, the amount of energy reflected from the topography also increases.

In summary, for $h_T/H = 0.2$, the maximum change in the scattering introduced by the current is less than 7.5% of $\langle\mathcal{T}_{inc}\rangle$, however the difference in $\langle\mathcal{T}_1\rangle$ between M1C and M1W can be greater than $0.1\langle\mathcal{T}_{inc}\rangle$. The influence of the current on the scattering increases monotonically with the height. If the height of the topography and Υ are both high, then the inclusion of a current is expected to create a significant difference in scattering. For M1W and M1C, depending on the Υ value, the current can increase or decrease the scattering compared to the 'no-current' case.

4.3.2 Supercritical topographies

In this subsection, we focus on supercritical topographies ($\Upsilon > 1$). The list of simulations run are given in table 4.2. We consider $\Upsilon = 1.25, 1.5$ and 1.75 for $h_T/H = 0.2, 0.35$ and 0.5 leading to a total of 9 different combinations of h_T/H and Υ. For supercritical topographies, a significant portion of the incoming wave's energy can get reflected and travel in the opposite direction of the incoming mode-1. In this regard, we modify the

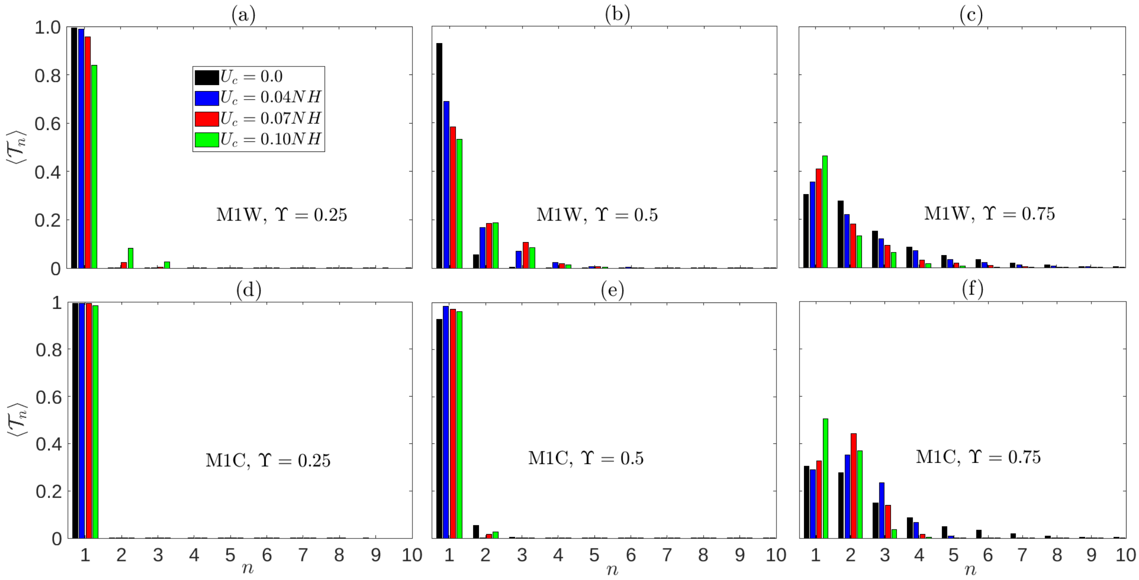

Figure 4.12: Caption same as figure 4.8 except $h_T/H = 0.5$.

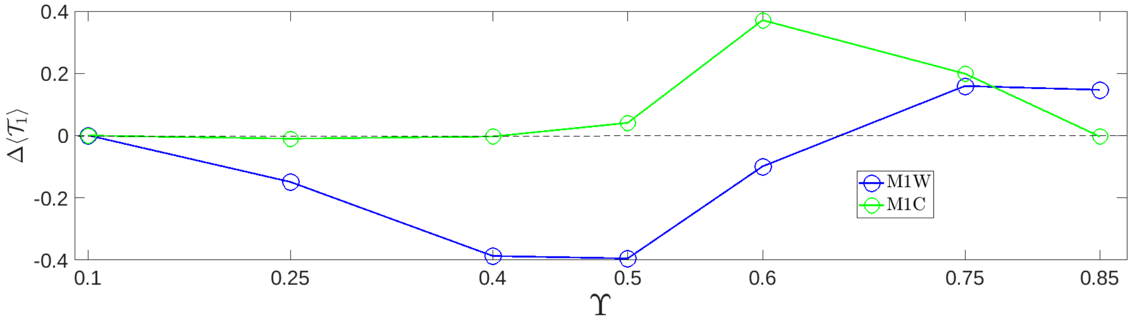

Figure 4.13: Caption same as figure 4.9 except $h_T/H = 0.5$.

mode-isolation method given in section 4.2.3 to also calculate the modal composition of the internal waves that propagate in the opposite direction of the incoming mode-1 wave.

h_T/H	Υ	max($d\Phi_{\text{inc}}/dz$) (ms^{-1})	ν (m$^2s^{-1}$)	U_c/NH for M1W and M1C
0.20	(1.25)	0.015	0.01	$(0, 0.1)$
0.20	(1.5,1.75)	”	”	$(0, 0.04, 0.1)$
0.35	(1.25)	”	0.005	$(0, 0.1)$
0.35	(1.5,1.75)	”	”	$(0, 0.04, 0.1)$
0.50	(1.25)	”	”	$(0, 0.1)$
0.50	(1.5,1.75)	”	”	$(0, 0.04, 0.1)$

Table 4.2: List of simulations run for supercritical ($\Upsilon > 1$) topographies.

4.3.2.1 Mode-isolation method for Reflected waves

For M1W (M1C), in the region left (right) of the supercritical topography, the wave field consists of an incoming mode-1 wave and reflected waves that propagate away from the topography. As a result, u_{ω_d} can be written as

$$u_{\omega_d} = u_{\text{ref}} + u_{\text{inc}}, \tag{4.32}$$

where u_{ref} denotes the $u-$velocity field of the waves that travel in the opposite direction (horizontally) of the incoming mode-1 wave. The method described in section 4.2.3 has to be applied to u_{ref} to find the modal composition of the reflected waves, however, u_{ref} cannot be directly obtained from the simulation data like u_{ω_d}. We need to first find u_{inc} and then use equation (4.32) to find u_{ref}. In the simulations, at any given time, u_{inc} is assumed to have a normal mode form as given below,

$$u_{\text{inc}} = A_{\text{inc}} \frac{d\Phi_{\mp 1}}{dz} \sin\left(k_{\mp 1} x - \omega_d t + \text{Ang}_{\text{inc}}\right) \tag{4.33}$$

To determine u_{inc}, amplitude (A_{inc}) and the phase (Ang_{inc}) of the wave have to be determined. To this end, we run a separate low-resolution simulation without the topography while other parameters are kept constant. Using the low-resolution simulation, the incoming mode-1's amplitude and phase are determined. Now u_{ref} can be found by using equation (4.32). After obtaining u_{ref}, the isolation method given in section 4.2.3 can be used straightforwardly to express u_{ref} as a sum of Taylor-Goldstein normal modes. Note that the waves that travel in the opposite direction of the incoming mode-1 wave have to be used. Finally, the reconstructed $u-$velocity can be compactly written as,

$$u_{\omega_d} \approx u_R = \left[\sum_{n=1}^{n=M_n} A_{\pm n}(x,t) \frac{d\Phi_{\pm n}}{dz} \right] + A_{\text{inc}} \frac{d\Phi_{\mp 1}}{dz} \sin\left(k_{\mp 1} x - \omega_d t + \text{Ang}_{\text{inc}}\right). \tag{4.34}$$

4.3.2.2 Scattering of M1W and M1C for $h_T/H = 0.35$

We begin our analysis with $h_T/H = 0.35$. Results for $h_T/H = 0.2$ are qualitatively similar to $h_T/H = 0.35$. Hence to avoid repetitiveness, we do not plot the results for $h_T/H = 0.2$, however they will be discussed in the analysis. The modal composition of the transmitted and reflected waves for $h_T/H = 0.35$ is shown for $\Upsilon = 1.5$ and 1.75 in figure 4.14. The reflected waves' amplitude is less compared to the transmitted waves' amplitude because the height of the topography is not very large (Mathur *et al.*, 2014), and adding a current does not massively change this fact. From figures 4.14(a) and (b), a clear pattern can be seen: for M1W, increasing U_c increases transmitted $\langle \mathcal{T}_1 \rangle$ compared to $U_c = 0$. For M1C, increasing the current strength decreases transmitted $\langle \mathcal{T}_1 \rangle$ compared to the $U_c = 0$ case. A monotonic increase in $\langle \mathcal{T}_1 \rangle$ is observed starting from M1C-$U_c = 0.1NH$ to M1W-$U_c = 0.1NH$. Moving on to the reflected wave field, we observe that increasing the current strength slightly increases (decreases) the reflected $\langle \mathcal{T}_1 \rangle$ for M1C (M1W) as shown in figures 4.14(c) and (d). Note that reflected $\langle \mathcal{T}_1 \rangle$ decreases from M1C-$U_c = 0.1NH$ to M1W-$U_c = 0.1NH$ (this trend is observed for both Υ values), which is the exact opposite of $\langle \mathcal{T}_1 \rangle$'s behaviour in the transmitted wave field. The same patterns were also observed for $h_T/H = 0.2$ (results not shown). However, for $h_T/H = 0.2$, the reflected waves' amplitudes are significantly lesser compared to $h_T/H = 0.35$. Flux of mode-1 wave after the scattering (considering both reflected and transmitted mode-1) monotonically decreases from M1W with $U_c = 0.10NH$ to M1C with $U_c = 0.10NH$, see figure 4.15. This is in line with the results observed for subcritical topographies with high Υ where increasing U_c reduces (increases) scattering for M1W (M1C). A similar pattern was also observed for $h_T/H = 0.2$. Finally, the discussion until now has been only for $\Upsilon = 1.5$ and 1.75. The results for $\Upsilon = 1.25$ were qualitatively very similar to the two Υ values discussed above (results not shown).

4.3.2.3 **Scattering of** M1W **and** M1C **for** $h_T/H = 0.50$

The results for $h_T/H = 0.50$ are shown in figure 4.16. For large amplitude supercritical topographies, reflected waves have a higher amplitude than the transmitted waves for $U_c = 0$. Adding a current does not change this fact for both M1W and M1C even for high U_c. We once again observe the same pattern for $h_T/H = 0.5$ that was observed for $h_T/H = 0.35$: increasing U_c increases (decreases) the transmission of M1W (M1C) compared to $U_c = 0$. Moreover, increasing U_c increases (decreases) the reflection of M1C (M1W) compared to $U_c = 0$. Now we move on to the discussion of scattering for $h_T/H = 0.5$. Similar to $h_T/H = 0.35$, for M1C (M1W), the scattering increases (decreases) as U_c is increased. This is shown in figure 4.17. Once again, the results for $\Upsilon = 1.25$ were qualitatively very similar to the two Υ values discussed. Interestingly, the difference between M1W and M1C is more pronounced in $h_T/H = 0.35$ than $h_T/H = 0.5$. However, as $h_T/H \to 0$, the difference is also expected to be shrink. The scattering properties and the reflection-transmission properties do not change significantly from $\Upsilon = 1.5$ to $\Upsilon = 1.75$ for all the

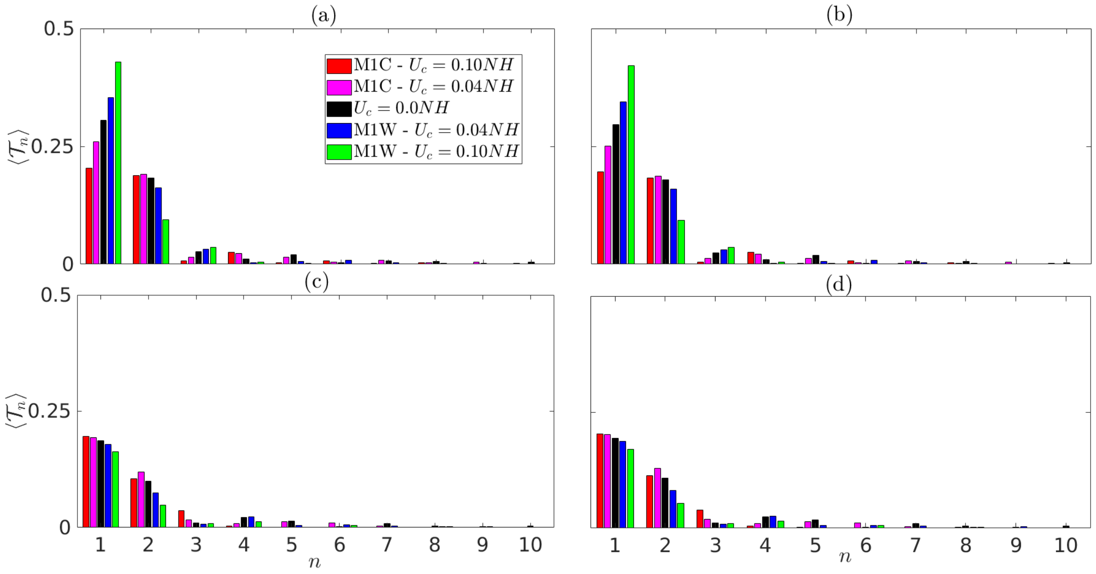

Figure 4.14: $\langle \mathcal{T}_n \rangle$ for $\Upsilon = 1.5$ and 1.75 where $h_T/H = 0.35$ is held fixed. The first column (consisting (a) and (c)) show results for $\Upsilon = 1.5$, and the second column (consisting (b) and (d)) show results for $\Upsilon = 1.75$. (a) and (b) show $\langle \mathcal{T}_n \rangle$ for transmitted wave field, while (c) and (d) show $\langle \mathcal{T}_n \rangle$ for reflected wave field.

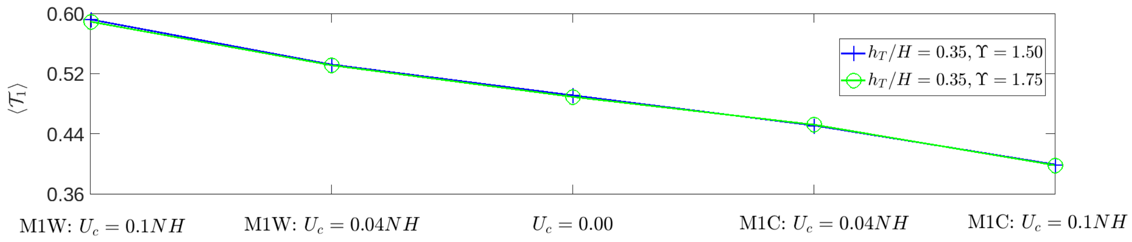

Figure 4.15: Sum of reflected and transmitted $\langle \mathcal{T}_1 \rangle$ for supercritical topographies with $h_T/H = 0.35$. The horizontal axis shows the current strength and the type of mode-1 wave (M1W or M1C) studied.

heights. For uniform stratification, scattering does not vary significantly as Υ is increased beyond a certain value (Mathur *et al.*, 2014). Introducing a current does not seem to change this fact significantly. Hence, for $\Upsilon > 1.75$ similar results to the simulations presented in this section can be expected.

Using results from subcritical and supercritical topographies, we summarise the conclusions. For M1C, the current does not have any influence on scattering when Υ is very low. Then for a range of Υ, scattering is lower for $U_c \neq 0$ compared to the 'no-current' $U_c = 0$ case. Moreover, increasing the Υ further results in the scattering of M1C being more for $U_c \neq 0$ cases compared to $U_c = 0$. The transition is observed to be permanent regardless of the U_c or h_T/H value as shown in this subsection. For M1W, the current has a negligible influence on scattering when Υ is very low. As Υ is increased, scattering is

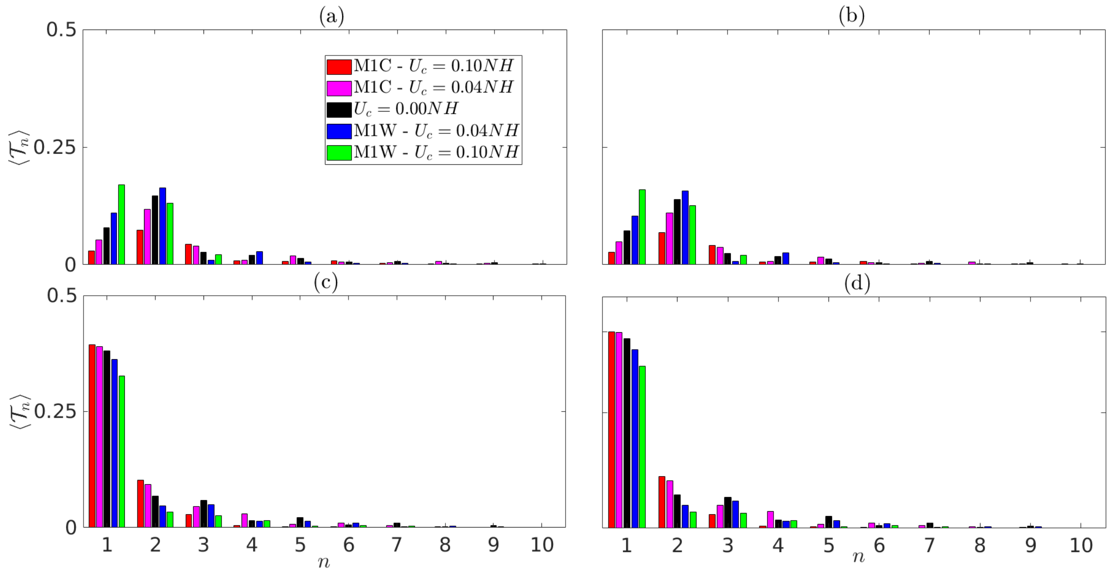

Figure 4.16: Caption same as figure 4.14 except $h_T/H = 0.5$.

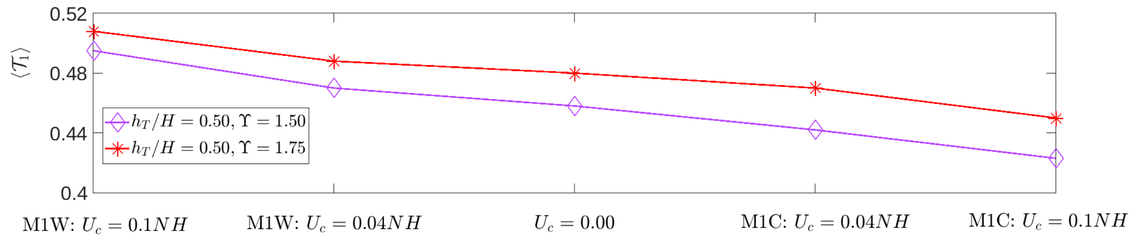

Figure 4.17: Caption same as figure 4.15 except $h_T/H = 0.5$.

higher for $U_c \neq 0$ compared to $U_c = 0$. By increasing the Υ further, we see that the scattering of M1W is lesser for $U_c \neq 0$ cases compared to $U_c = 0$. Once again the transition is observed to be permanent for all the U_c or h_T/H values studied.

4.3.3 Flux of modes higher than 3

In the oceans, higher modes do not travel as far as the mode-1 wave because of their lower group speed and they get attenuated by wave-wave interactions at a faster rate compared to a mode-1 wave (de Lavergne *et al.*, 2019; Olbers *et al.*, 2020). As a result, higher modes get dissipated very close to the place of their origin. For calculating near field dissipation, Vic *et al.* (2019) assumes that the modes higher than 3 (mode-3 not included) get dissipated at or very close near to their place of generation. To this end, it would be useful to see how much energy resides in modes higher than 3 after the scattering of mode-1 wave. For the three heights, figure 4.18 plots $\langle \mathcal{T}_{4-\infty} \rangle \equiv \sum_{n=4}^{n=\infty} \langle \mathcal{T}_n \rangle$ for M1W and M1C

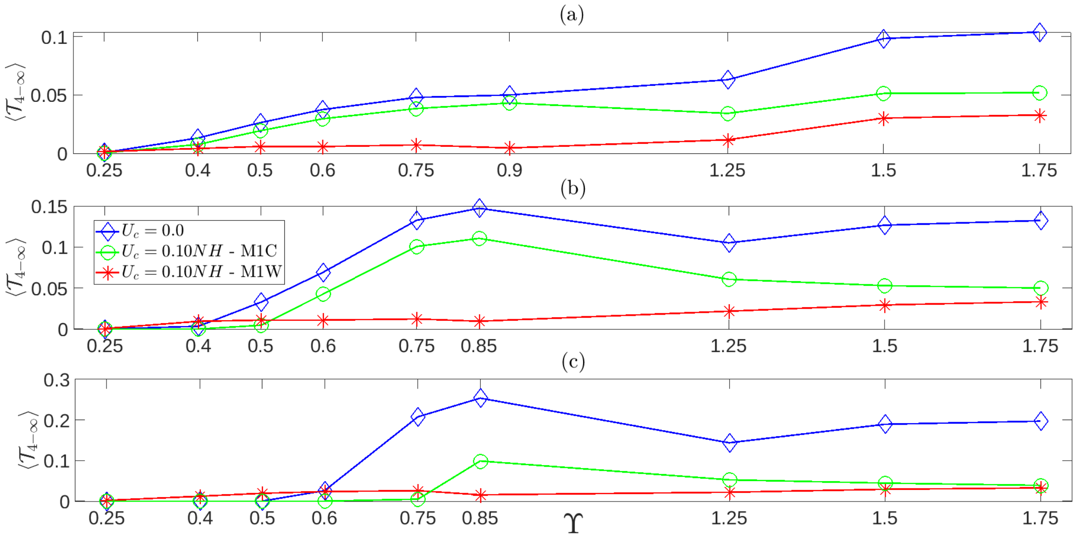

Figure 4.18: $\langle \mathcal{T}_{4-\infty} \rangle$ for M1C and M1W with $U_c = 0.10NH$ is shown along with the $U_c = 0$ case for the three heights. (a) $h_T/H = 0.2$, (b) $h_T/H = 0.35$, and (c) $h_T/H = 0.5$.

for $U_c = 0.10NH$. $\langle \mathcal{T}_{4-\infty} \rangle$ is also plotted for the $U_c = 0$ case. Interestingly, for all three heights, M1W and M1C have lesser energy residing in the higher modes for $U_c = 0.10NH$ compared to the $U_c = 0$ case. M1W especially has very low energy residing in the higher modes, and the difference between M1W and the no-current case is especially large for $h_T/H = 0.5$ and $\Upsilon > 0.75$. Energy in the higher modes is higher for M1C and than M1W except at the low Υ values for $h_T/H = 0.35$ and 0.5. This is line with the observation that at low Υ values the current increases scattering for M1W for large amplitude topographies.

4.3.4 Generation of $2\omega_d$ superharmonics

In the process of low mode scattering, internal wave beams can be produced (for example, Johnston & Merrifield (2003)). Moreover, superharmonic waves (with frequency $2\omega_d$) can be generated by nonlinear interactions that ensues from the reflection of an internal wave beam from a rigid surface (Lamb, 2004; Tabaei *et al.*, 2005). As a result, internal wave beams with frequency ω_d (hereafter referred as primary wave beam) generated due to scattering of the low mode can force superharmonic internal wave beams as they get reflected from the air-water interface in the ocean, or from bottom surface (bottom topography). Note that the surface current can also reflect internal wave beams. In this sub-section, we focus on the influence of the current on the generation of superharmonic waves that ensues from the scattering of a mode-1 internal wave with frequency ω_d.

We first focus on subcritical topographies with $\Upsilon \geq 0.75$ where clear beams are observed after the scattering of the incoming mode-1 wave. To this end, we first focus on the topography with parameters $(h_T/H = 0.5, \Upsilon = 0.85)$, and then generalise the results observed for all other topographies. Figure 4.19 shows u_{ω_d} and $u_{2\omega_d}$ fields after the scattering of M1C and M1W, and the figure shows simulations that use $U_c = 0.10NH$. For M1C, the primary internal wave beam gets reflected after it impacts the current near $x/H \approx 62$, see figure 4.19(a). As a result, the incident and the reflected primary wave beam nonlinearly interact and generate superharmonic wave beams. A notable superharmonic wave field can be noticed on the top of the topography in figure 4.19(b). Superharmonic beams are also generated due to the reflection of the primary internal wave beam from the bottom surface in the lee of the topography near $x/H \approx 57$. In contrast, for M1W, the primary beam loses its coherence on its impact with the current and does not have a strong reflected beam, see near $x/H \approx 60$ in figure 4.19(c). Hence, the generated superharmonic wave field is weak compared to what was observed in the case of M1C. To quantify the superharmonic wave field, we measure the energy flux of the superharmonic wave fields. For M1C, the superharmonic flux is approximately 3.3% of $\langle \mathcal{T}_{inc} \rangle$ for $U_c = 0.10NH$. However, for M1W, the superharmonic flux is approximately 0.068% of $\langle \mathcal{T}_{inc} \rangle$. In the presence of a strong current, similar contrast between M1W and M1C was observed for all subcritical topographies with $\Upsilon \geq 0.75$. Note that even without the current, the primary beam can get reflected from the top surface. As a result, even for $U_c = 0$, a notable superharmonic wave field was observed. It was only in the case of M1W, the superharmonic wave fields were very weak. For topographies with $\Upsilon < 0.6$, a consistent pattern between M1C and M1W was not observed for all the heights.

For supercritical topographies, the superharmonic waves' energy flux is lesser ($\lessapprox 0.01\langle \mathcal{T}_{inc} \rangle$) than the maximum flux that was observed for subcritical topographies with high Υ. This is because in supercritical topographies, considerable portion of the incoming mode-1's energy is reflected by the topography. Since the energy is split between a reflected and transmitted primary wave beam, the respective amplitudes of the primary beams will be lower compared to the case of subcritical topography where most of the energy would reside in the transmitted primary beam. As a consequence of the lesser amplitude, the nonlinear interaction is also weaker thus resulting in weaker superharmonics.

We now focus on the supercritical topography with parameters $(h_T/H = 0.5, \Upsilon = 1.75)$. Other supercritical topographies are qualitatively similar to the case focused here. For M1W, in the transmitted wave field, the results are similar to what was observed for the subcritical topographies, see figure 4.20(d). The primary beam loses coherence near the

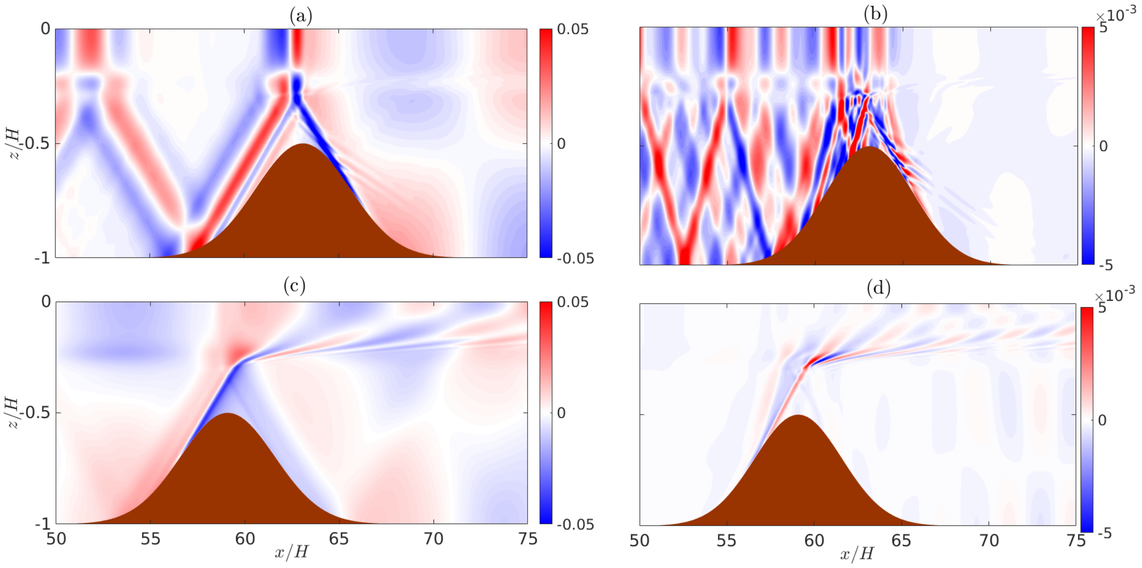

Figure 4.19: u_{ω_d} and $u_{2\omega_d}$ field that ensues from the interaction of M1C and M1W with a subcritical topography ($\Upsilon = 0.85$ and $h_T/H = 0.5$). (a) and (c) show u_{ω_d} due to the scattering of M1C and M1W, respectively. (b) and (d) show $u_{2\omega_d}$ due to the scattering of M1C and M1W, respectively. The unit of the colorbar values is ms^{-1}.

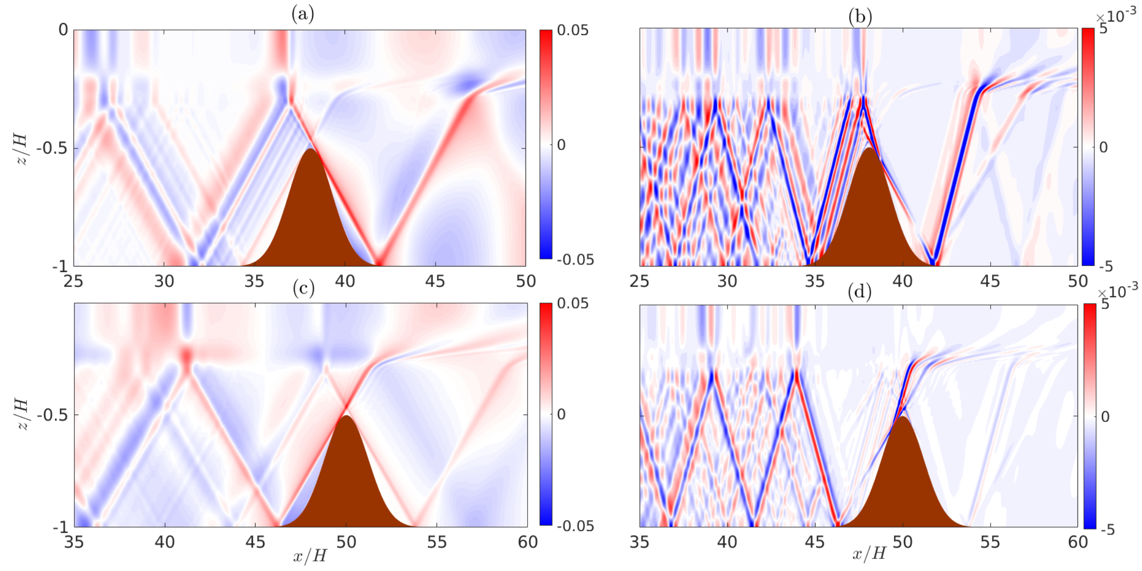

Figure 4.20: Caption same as figure 4.19 except $\Upsilon = 1.75$.

current hence no notable superharmonic waves are found after $x/H \geq 55$. For supercritical topographies, internal wave beams with frequency ω_d are created on either side of the topography after the scattering. For M1W, the beam which propagates in the opposite direction of the incoming mode does not lose coherence on its impact with the current. Note that there is a stronger superharmonic wave field (in the form of an internal wave beam) which propagates against the incoming mode-1 wave. The superharmonic beam originates near $x/H \approx 46$ where the primary wave beam gets reflected from the bottom surface.

For M1C, the beam composed of reflected waves travels in the same direction as the current, as shown in figure 4.20(a). As a result, the beam will lose its coherence as soon as it impacts the current, which can be seen near $x/H \approx 47$. However, unlike the beam composed of the transmitted waves, the beam composed of the reflected waves travels towards the bottom surface first, and as a result of this bottom reflection, a superharmonic wave beam can be generated. This can be seen in figure 4.20(b) near $x/H \approx 42$. Note that the superharmonic and primary wave beam lose their coherence once they reach the current , and the superharmonic flux is observed to be very small compared to subcritical topographies.

In Figure 4.20(b), an interesting non-resonant signal is found: A superharmonic wave beam has the same inclination as the parent wave beam. As a result, the superharmonic wave beam cannot satisfy the dispersion relation. Usually a parent internal wave beam does not self interact in an unbounded domain under inviscid conditions. However, we believe the viscous and the boundedness of the domain cause a non-resonant interaction in the primary internal wave beam which produces this specific superharmonic internal wave beam. We note that the daughter waves stay on top of the parent internal wave beam, and this may give the daughter wave ample time to extract considerable energy. Non-resonant interactions usually do not cause the parent wave to lose significant amount of energy. For example, many studies show that as the detuning (which is a measure of non-resonance) is increased, the energy transfer from the parent wave to the daughter waves is reduced. Even in our case, the simulation was run for a sufficiently long time to generate Figure 4.20(b), however, the non-resonant signal is still weak. We note that the points we made may not be applicable in this case and hence to conclusively show that non-resonant interactions are not as effective as resonant interactions more studies have to be undertaken.

4.3.5 Rate of Kinetic energy dissipation

Rate of kinetic energy dissipation is one of the key quantities that is used in parameterising ocean mixing (for example, Nikurashin & Legg (2011)). In this subsection, we focus on rate of kinetic energy dissipation normalised by the incoming mode-1 wave's linear flux. Mathematically, the above-mentioned quantity is given by $\langle \tilde{K}_D \rangle / \langle \mathcal{T}_{inc} \rangle$. Topographies with high Υ ($\Upsilon \geq 0.85$) are focused. To evaluate the rate of dissipation, we choose a control area that encloses the full topography. In the horizontal direction, the length of the control area is $5W_T$, where W_T is the standard deviation for a particular topographic configuration (see equation 4.11). The center of the control area in the horizontal direction coincides with the location where the topography height is maximum. In the vertical direction, the control area spans from $z = -h$ at the bottom to $z = 0$ at the top. Figure 4.21 shows $\langle \tilde{K}_D \rangle / \langle \mathcal{T}_{inc} \rangle$ for six different topography configurations with $\Upsilon \geq 0.85$. The configurations are given in the legend of the figure. For each topography, dissipation that ensues from the scattering of M1C and M1W for different U_c values is shown. Note that the horizontal axis of figure 4.21 provides information on the type of mode-1 and the current strength. In general, we can see a monotonic behaviour: $\langle \tilde{K}_D \rangle / \langle \mathcal{T}_{inc} \rangle$ is consistently higher for modes that travel against the current compared to modes that travel with the current. Similar contrast between M1C and M1W was also observed for $h_T/H = 0.2$, and for all the heights with $\Upsilon = 1.25$ (results not shown in figure). For the smaller Υ values, a consistent pattern was not observed. Near $\Upsilon = 1$, the slope of the internal waves match with the slope of the topography. As a result, the reflected internal waves are focused indefinitely and this results in a very large increase in the wavenumber of the reflected waves. As a consequence of the increase in wavenumbers, rate of kinetic energy dissipation also increases. Note that we only focus on the scattering of small amplitude mode-1 internal wave. Strong nonlinear phenomena such as wave breaking or internal wave bores are not present because of the incoming mode-1's low amplitude. As a result, dissipation is a measure of small scale waves generated due to the scattering of the mode-1 wave. Higher amount of small scale waves are generated by the scattering of M1C compared to M1W for $\Upsilon \geq 0.85$.

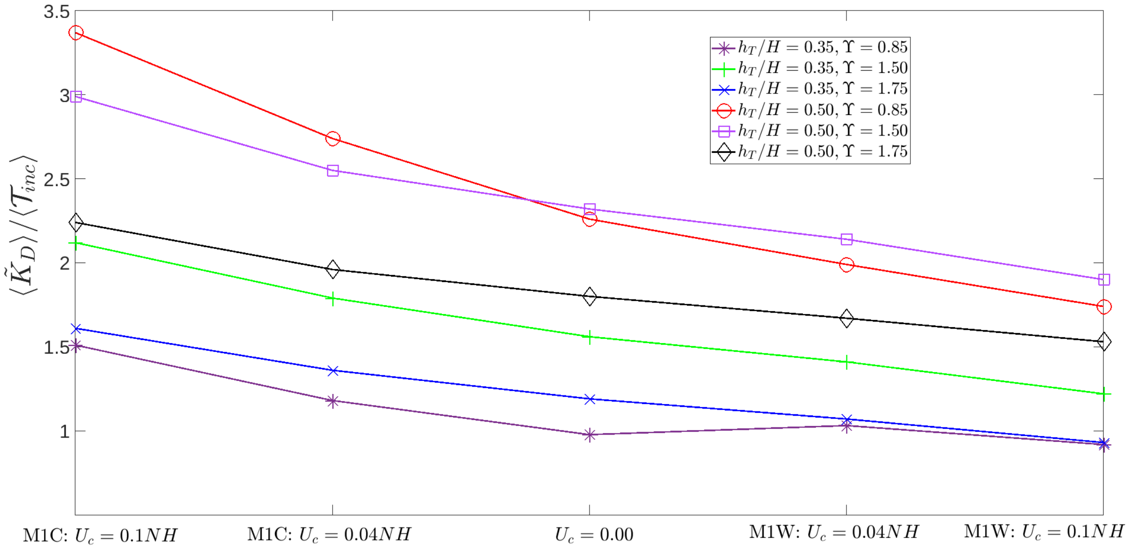

Figure 4.21: The figure shows the normalised kinetic dissipation for different topographic configurations, and for different current strengths for both M1C and M1W.

4.4 Summary and Conclusion

Internal wave topography interaction can facilitate energy cascade in large length scale mode-1 waves. Using numerical simulations, we study a mode-1 internal wave's interaction with topography in the presence of a steady, stable, surface-confined current. The mode-1's amplitude is assumed to be small so that the physics is almost in a linear regime. A mode-1 wave travelling with the current (denoted by M1W) can have different properties compared to a mode-1 wave that travels against the current (denoted by M1C). Scattering of both M1W and M1C is studied. The current's depth and the shear layer thickness are fixed, while the amplitude of the current (U_c) is varied ($U_c = 0$ simply implies that there is no current). The topography is modeled by the Gaussian function, and the height and the criticality of the topography are varied. Some of the main results of this chapter are given succinctly in figure 4.22.

For small amplitude, subcritical ($\Upsilon < 1$) topographies, the inclusion of a current does not induce a very significant change in the scattering of mode-1 compared to the $U_c = 0$ case. In general, there is approximately a 10% difference between M1W and M1C's flux after the scattering. This is observed for a wide range of criticality. Increasing the height of the topography results in the current having a more pronounced effect on the scattering for both M1W and M1C. For some large amplitude topographies, the inclusion of the current has increased or decreased the scattering by 40% compared to the $U_c = 0$ case.

Definitions:

- M1W: Mode that travels with the current
- M1C: Mode that travels against the current
- Υ : Criticality of the topography
- U_c : Amplitude of the current

- The maximum influence of the current on scattering increases monotonically with the height of the topography.
- Fixing the height and increasing Υ results in the current first increasing (decreasing) the scattering of M1W (M1C). Then eventually, beyond a certain Υ, the current reduces the scattering of M1W (M1C), as shown in the figure.
- For any supercritical topography, the scattering of M1W is always lesser than M1C

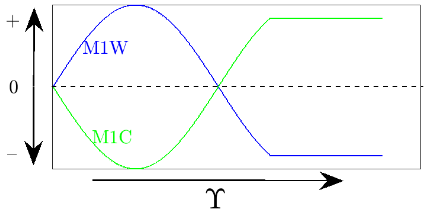

(+,0,–) respectively indicate increased, decreased, and the same scattering as the 'no-current' case

- Generation of superharmonics is very low for M1W
- Kinetic energy dissipation is lower in cases of M1W compared to M1C for $\Upsilon \geq 0.85$
- For $\Upsilon > 0.6$, flux in higher modes (mode>3) is less for both M1W and M1C ($U_c = 0.10NH$) compared to the $U_c = 0$ case.

Figure 4.22: A summary of the main (but not exhaustive) results of this chapter.

For M1C, if the scattering is low for $U_c = 0$, then increasing U_c does not create much of a difference. However, for M1W, the scattering properties may significantly change as the current amplitude is increased even if scattering is very low for $U_c = 0$. For all the heights considered, the current does *not* have a singular effect: it can reduce or increase scattering depending on the criticality value. This is observed for both M1W and M1C. For M1W, the current has a very low effect on the scattering for very low Υ values. However, as Υ is increased, the current increases the scattering compared to the $U_c = 0$ case. Moreover, as Υ is increased further, the scattering is always lower for $U_c \neq 0$ in comparison to $U_c = 0$. Thus the effect of the current changes after a certain Υ. The above-mentioned transition was observed for all the heights. For $\Upsilon > 1$, current always reduces scattering for M1W. Interestingly, for M1C, the exact opposite effect is observed. Up to a certain Υ value, the current has no effect on the scattering. Then as Υ is increased further, the current reduces the scattering of the mode-1. As Υ is increased furthermore, the current increases the scattering compared to the $U_c = 0$ case. For $\Upsilon > 1$, current always increases the scattering of M1C compared to the 'no-current' case. Increasing the amplitude of the current almost always increases the influence of the current on the scattering process.

Scattering by a supercritical topography produces a constant pattern: energy leaving in the form of a mode-1 wave is always higher in the case of M1W compared to the case of M1C. As a result, a supercritical topography is more efficient in scattering a mode-1 wave that travels against the current compared to a mode that travels with the current.

Superharmonic wave generation ensuing from the scattering of M1C and M1W is studied for topographies with high Υ. For subcritical topographies with high Υ ($\Upsilon = 0.75, 0.85$), the scattering of M1C consistently produces a stronger superharmonic beam compared to M1W. In the case of M1C, the primary beam (beam with frequency ω_d) generated by the scattering process does not lose coherence when it impacts the surface current. As a result, the incident and the reflected (by reflected, we mean the beam that is reflected by the current) wave beam interact to generate a superharmonic wave beam. In the case of M1W, the primary beam loses coherence when it impacts the current. Thus without a strong reflected beam, superharmonic field generation is weaker compared to results observed for M1C. Rate of kinetic energy dissipation is studied for topographies with high Υ. It is observed that normalised dissipation is always higher for M1C than M1W. As a result, for high Υ, the scattering of M1C results in a higher amount of energy cascading to small length scales in comparison to M1W.

Chapter 5

Summary of the thesis

5.1 Thesis overall summary

Internal waves influence the Earth's climate by mixing waters of different densities (diapycnal mixing) in the bulk of the ocean. The mixing plays a vital role in sustaining the overturning circulation, and alters the temperature and salinity (and hence the stratification) in the ocean. To model the Earth's climate properly, we need to include the effects of mixing. However, mixing occurs at very small length scales (centimeters to meters), whereas the ocean we are trying to model spans thousands of kilometers. Because of the massive scale separation, we cannot simply resolve all the vital processes in the ocean. To circumvent this issue, the flow is compartmentalised into multiple manageable subdivisions. The mixing and the processes that cause it are studied in idealised settings, and then the effects of the mixing are parameterised and provided as an input to the Ocean general circulation models. This thesis is dedicated to understanding the mechanisms that cause the energy in an internal wave to cascade to small length scales. With a better understanding of the mechanisms, the locations in the oceans where internal waves cause mixing can be predicted reliably. To this end, the thesis is dedicated to understanding wave-wave interactions and wave-topography interactions, which are the two of the most dominant mechanisms that reduce the length scales of the internal waves (de Lavergne *et al.*, 2019, 2020).

Estimating diffusivity in oceans requires detailed individual studies of wave-topography interactions and wave-wave interaction under numerous realistic scenarios. In the past

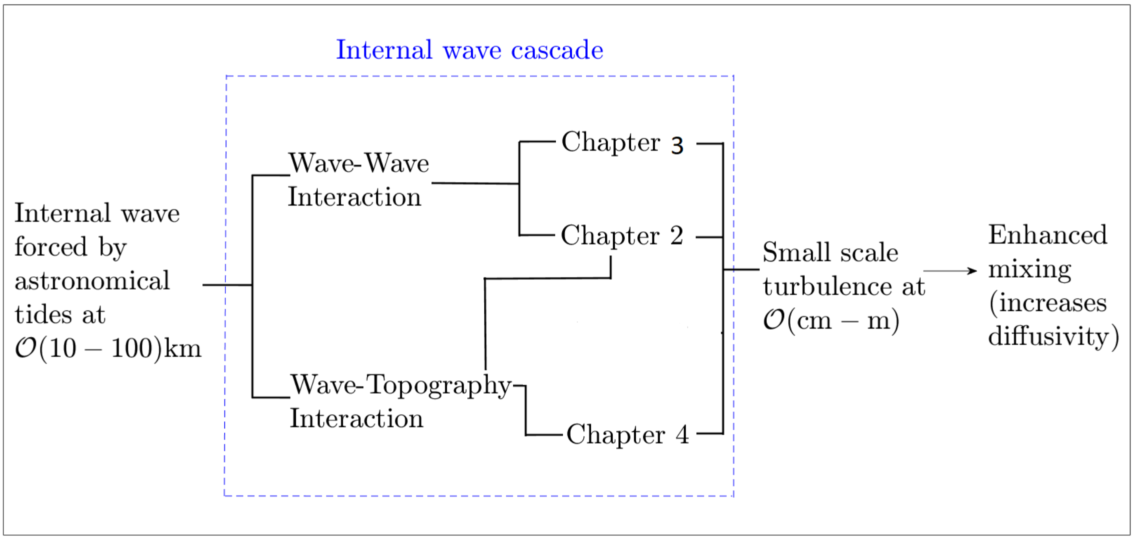

Figure 5.1: The focus of the thesis.

two decades, wave-wave interactions and wave-topography interactions have been studied extensively. However, there are still certain underlying physics that have remained unclear. The objective/overall aim of the thesis is to improve/add to the current theories and reduced-order models that are used to model IGW cascade (and dissipation) due to wave-topography interactions and wave-wave interactions in the ocean. The results will aid in the estimation of the decay of an IGW as it propagates through the ocean under circumstances which mimic realistic ocean scenarios. Such compartmentalised studies of different physics, such as wave-topography interaction and wave-wave interaction, are required because IGWs can break through either mechanism. Moreover, the rate and quantity of IGW cascade (and dissipation) significantly vary according to the mechanism, and the conditions in which the mechanism itself takes place (for example: amplitude of the wave, topography, Brunt-Väisälä frequency). The thesis is dedicated to understanding the IGW energy cascade (and dissipation) through both wave-topography interaction and wave-wave interaction. In this thesis, 3 processes of wave-wave interactions and wave-topography interactions, under conditions that are relevant to oceanic scenarios are studied. Each individual chapter of the thesis is dedicated to understanding a particular scenario of wave-wave interaction and/or wave-topography interaction, which paves the way for a better diffusivity parameterization. Figure 5.1 shows the overall outline of the thesis; it shows how each chapter is dedicated to a specific mechanism behind IGWs' energy cascade, as well as the connection between the chapters.

The specific focus of the thesis has been on the effects of the topography on the internal wave energy cascade. We have shown that topography plays different kinds of roles in the cascade of internal waves' energy. Topography, smooth or rough, has to be taken when estimating the internal wave's decay. Although smooth topographies do not cause direct internal wave cascade, they can change the dispersion relation of the internal waves and thus influence wave-wave interactions. The energy transfer rate can rapidly vary as the fluid depth varies. We also saw that topographies can cause wave-wave interactions (Higher order interactions) which otherwise would not be possible. These higher order interactions can cause an energy cascade of semidiurnal internal tides even for $f > 7 \times 10^{-5}\text{s}^{-1}$ thus the topographies play a major role here as well. The studies in the thesis also showed inertial waves can play a very important role in the energy cascade of internal waves when there are multiple parent waves present in the same region. In oceans, multiple energetic internal gravity waves often co-exist in a region, for example, leftward and rightward propagating internal waves generated by tide-topography interactions overlap in the vicinity of the topography. Moreover, multiple internal waves with different wavevectors are often generated even when an internal wave mode-1 gets scattered by the topography. When multiple small amplitude parent waves are present in a region, we observe that the standard triad interactions (3-wave systems) may not be the most dominant instability. Specifically, for two co-existing plane internal gravity waves with the same frequencies (ω_1) and wavevector norms, we observe that 5-wave interactions are the most dominant instability for a wide range of latitudes. The results in the thesis also show that internal wave-topography interactions traveling in the presence of the current can be quite different compared to the 'no-current' scenario. As a result, internal wave scattering by topographies in the equatorial regions, where strong surface currents such as the North equatorial counter current and equatorial counter current are present, can be quite different from other regions where there are no currents present.

We now present a short summary of the main results/conclusions from chapters 2,3 and 4.

5.2 Summary for chapters 2,3 and 4

Low mode internal waves often travel long distances, and they carry a significant amount of energy. Mapping their decay across the ocean is vital for mixing parameterisations. Although, the depth of the fluid (from the free-surface to the seafloor) may not be constant as they propagate in the ocean. Considering this, in chapter 2, weakly nonlinear interactions of low mode internal waves that occur in the presence of a varying bathymetry is studied. Oceans typically have a non-uniform density stratification profile as well. Under these conditions and assuming mild-slope bathymetry, multiple-scale analysis is used to derive wave amplitude equations for weakly nonlinear wave-wave interactions. The waves are assumed to have a slowly (rapidly) varying amplitude (phase) in space and time. The horizontal wavenumber (k) condition for waves (1,2,3) is given by,

$$k_{(1,a)} + k_{(2,b)} + k_{(3,c)} = \Delta k \tag{5.1}$$

where (a, b, c) denote the modenumber, and Δk is the detuning. For uniform stratification (constant N), regardless of the mode number of the waves involved in the interaction, detuning does not vary with h. As a result, if the waves are resonant for any single value of h, then they are resonant for all values of h. Moreover, the nonlinear coupling coefficients (NLC) are proportional to $1/h^2$, implying that the waves grow faster as the fluid depth decreases. The physics becomes more interesting for non-uniform stratifications. For non-uniform stratifications, triads that do not satisfy the condition $a = b = c$ may not satisfy the horizontal wavenumber condition as h is varied. This is because the horizontal wavenumbers' (eigenvalues of a Sturm-Liouville problem) variation with h depends on the mode number of the wave. The same applies to self-interactions. For self-interactions where the parent wave and the daughter wave are of the same mode number, change in h does not increase detuning. These kinds of self-interactions can dominant triads when $f \approx 0$ as shown in Sutherland (2016) and Sutherland & Dhaliwal (2022). For triads, the nonlinear coupling coefficients may not decrease (increase) monotonically with increasing (decreasing) h. Nonlinear coupling coefficients, and hence wave growth rates for weakly nonlinear wave-wave interactions, can also vary rapidly with h. The most unstable daughter wave combination of a triad with a mode-1 parent wave can also change for relatively small changes in h. Higher-order self-interactions in the presence of a monochromatic, small amplitude topography are studied; here the topography behaves as a zero frequency wave. In summary, chapter 2 shows that the topography can significantly influence wave-wave interactions as well.

Apart from low mode internal waves, internal waves generated by rough topographies can dissipate in the vicinity of the topography itself. Moreover, in such cases, multiple parent waves often co-exist in the presence of each other. In chapter 3, we analyse the stability of two parent waves co-existing in a region. Specifically, we use multiple scale analysis to study a 5-wave system (5WS) composed of two different internal gravity wave triads. Each of these triads consists of a parent wave and two daughter waves, with one daughter wave common between the two triads. The parent waves are assumed to have the same frequency and wavevector norm co-existing in a region of constant background stratification. We consider two cases where the parent waves are confined to the same vertical plane: Case 1(2) has parent waves with the same horizontal (vertical) wavenumber but with different vertical (horizontal) wavenumber. Note that parent waves need not have the same frequency and wavevector norm for resonant 5-wave interactions to occur. The cases we have studied falls under the mentioned assumption, and the assumption is mainly made for simplicity. We believe 5-wave interactions can also occur when these conditions are not satisfied. For both cases, the 5-wave system instability is more dominant than triads for $f/\omega_1 \gtrapprox 0.3$, where ω_1 and f are the parent wave and the local Coriolis frequency, respectively. For $f/\omega_1 \gtrapprox 0.3$, the common daughter wave's frequency is $\approx \omega_1 - f$ and f for case 1 and 2, respectively. For oblique parent waves, 5-wave system instability become more dominant as the angle between the horizontal wavevectors of the parent waves (denoted by θ) is decreased. Moreover, for any θ, 5-wave system instabilities are more dominant than triads for $f/\omega_1 \gtrapprox 0.3$. Numerical simulations match the theoretical growth rates of 5-wave system instabilities for a wide range of latitude except when $f/\omega_1 \approx 0.5$ (critical latitude). More than three daughter waves are forced by the two parent waves when $f/\omega_1 \approx 0.5$. Using the reduced order model, for any θ, the maximum growth rate near the critical latitude is shown to be approximately twice the maximum growth rate of all triads. Numerical simulations showed that 5-wave interactions can also occur for vertically bounded modes. Hence, the wave amplitude equations given in chapter 2 (which only takes three waves into account) may under-predict the growth rates at certain latitudes. Moreover, the latitude where the 5-wave interactions can occur will also change with the stratification profile itself.

In chapter 2, the topography played a passive but significant role in wave-wave interactions. By altering the fluid depth, the topography changed the properties of the internal waves. This caused the wave-wave interactions to be impacted as well. In chapter 4, we study wave-topography interactions where the topography plays a more direct role and causes the energy to cascade. In chapter 4, the interaction of a mode-1 internal wave with topography in the presence of a steady surface current is studied. The mode-1 wave that travels with the current (denoted by M1W) has different properties compared to the mode-1 wave that travels against the current (denoted by M1C), and we study the scattering of both M1W and M1C. The influence of the surface current on the scattering increases as the height of the topography is increased. Moreover, in general, the influence of the current increases as the amplitude of the current is increased. For M1W, for the low criticality values, either the current has negligible impact or increases the scattering compared to the no-current case. However, the current reduces the scattering of M1W for high criticality. For supercritical topographies ($\Upsilon > 1$), the current always decreases the scattering of M1W compared to the no-current case. For M1C, an opposite effect seems to occur. For the low criticality values, the current has negligible influence or decreases the scattering compared to the no-current case. Moreover, for high Υ values, the current always increases the scattering of M1C. For supercritical topographies, the current always increases the scattering of M1C compared to the no-current case. For most of the topographies, the flux in modes higher than 3 after the scattering is lower if a current is present. Higher modes' flux is especially low for M1W for almost all the topographies. We also studied the generation of superharmonics due to the scattering of the mode-1. Superharmonics generated in the case of M1W scattering are low compared to what is observed for M1C. Rate of kinetic energy dissipation is always higher for M1C compared to M1W for topographies with $\Upsilon \geq 0.85$.

5.3 Future work

The studies presented in this thesis can be easily extended for a better understanding of the fate of internal waves in the ocean. In this section, a brief outline of the most valuable avenues where the studies can be improved is provided.

5.3.1 Chapter 2

The stability of a mode-1 wave to small amplitude perturbations in the presence of varying depth was studied in detail. To understand the decay rate of a mode-1 wave in the ocean, its interactions with a wave field that follows the Garrett-Munk spectrum in a region of varying fluid depth should be studied. Moreover, time-invariant mean flows (balanced flows) are ubiquitous in the ocean and a significant portion of the internal wave low modes have to propagate through the balanced flows. There is increasing evidence (from both observations and models) that wave-wave interactions are influenced/modified by mean flows (for example, see Richet *et al.* (2017); Fan & Akylas (2019); Xu *et al.* (2022)). Understanding how the decay of a low mode by wave-wave interactions is impacted by the presence of mesoscale eddies is necessary and a vital step in quantifying their decay. Interestingly, in the fully nonlinear simulations conducted by Savva *et al.* (2021), there is no evidence of wave-wave interactions even at the critical latitude as the low mode is getting scattered by baroclinic geostrophic flows. Our study also mostly focuses on mode-1 internal wave. However, the fate of mode-2 and mode-3 waves are important to track as well.

5.3.2 Chapter 3

For Chapter 3, analyses were conducted for plane waves, and briefly for internal wave modes. However, the stability of overlapping internal wave beams should be studied to understand the near field dissipation of the small amplitude rough topographies. Internal wave beams often intersect other beams when tides interact with the rough seafloor or a large seamount. Note that we can see internal wave beams collision even when a mode-1 wave gets scattered in chapter 4. 5-wave interactions for internal wave beams can be quite interesting since the three daughter waves have to be confined to the region where the beams collide. This may pose a more stringent condition on the daughter waves' group speed. 5-wave interactions were studied for parent waves whose wave vector magnitudes were equal. However, in the ocean, waves often propagate in the presence of other waves with higher or lower wavevector magnitude. For example, mode-1 and mode-2 often travel together for hundreds of kilometers. Understanding the 5-wave interactions (or triad chains) in such scenarios can be central to tracking the decay of the internal wave modes. The current study also assumes the frequency of the parent waves to be the same. The underlying reason for that assumption was the waves generated by a particular tide have the same frequency. However, in the oceans, internal waves can be generated by different tidal constituents, for example, M_2, K_2, K_1. Hence, considering the geophysical significance, 5-wave interactions that consist parent waves with different frequencies should also be studied.

5.3.3 Chapter 4

All the simulations presented in Chapter 4 model the scattering by isolated large amplitude topographies. However, a major portion of the ocean's seafloor can be essentially modeled as a continuous, small amplitude, polychromatic deviation from a mean depth.

Mathematically, the topographies are usually expressed as

$$h(x) = -H\left(1 + \epsilon_h \int_{-\infty}^{\infty} \mathrm{AS}_k \sin(kx + \mathcal{Z}_k)dk\right) \tag{5.2}$$

where ϵ_h is used to denote the small amplitude nature (with respect to the mean depth H) of the corrugations. AS_k and $\mathcal{Z}_k$ denote the amplitude and phase of a particular wavenumber k, respectively. It is important to know how the scattering of internal wave modes by the small amplitude corrugations with a realistic wavenumber spectrum (for example, see Goff & Jordan (1989)) changes in the presence of a surface current. Moreover, extending the theory provided by Li & Mei (2014) for a randomly rough seabed to the setting considered here may also be needed. Interactions of the mode-1 with a continental shelf in the presence of a steady surface current may also be important, since a major portion of low mode internal waves are estimated to reach the continental shelves (Waterhouse *et al.*, 2014; Buijsman *et al.*, 2016).

For all the simulations in this thesis, the incoming mode-1 wave has a very low amplitude. This results in the physics being almost linear. The scattering of large amplitude mode-1 waves and the ensuing nonlinear physics are vital for quantifying the energy dissipation near a topography. Legg (2014) showed that shoaling of an internal wave causes wave breaking even for subcritical topographies with very low criticality provided the wave reaches a large enough amplitude/Froude number. Note that this may seem contradictory with the assumptions we have made in chapter 2. However, if the amplitude of the parent wave is low, then shoaling does not increase the energy density significantly. As a result, weakly nonlinear wave-wave interactions will still occur. Shoaling in the presence of a surface current is an important topic that should be explored. Similar to chapter 2, the study exclusively focuses on mode-1 internal wave. The scattering properties of mode-2 and mode-3 wave is necessary to understand as well.

Appendix A

Scaling analysis for finding the relation between the small parameters in Chapter 2

Here we perform a scaling analysis for all the terms appearing in (2.35). Equation (2.35) is chosen here so that scaling analysis can be also done for the different terms that compose the β_j function (2.37). Integrals (γ_j) in (2.35) (γ_j expressions are given in (2.36)) cannot be analytically simplified for non-uniform stratification profiles. Hence, we adopt a numerical approach where we study how different integrals scale in an ensemble of stratification profiles that resemble the profiles used throughout the paper. Using this information, we scale the different terms. To this end, the stratification profiles are chosen such that $N_{\text{max}} = (5N_b, 10N_b, 15N_b)$, $W_p = (H/100, 2H/100, 3H/100)$, and $z_c = (H/80, H/40, H/20, H/10)$; and we consider all possible (36) combinations.

The analysis provides a relation between the time scale of the amplitude's temporal evolution ($\epsilon_t t$), length scale of the amplitude function ($\epsilon_x x$), and the magnitude of the waves' amplitude ($\epsilon_a a_j$). Small parameters (ϵ_h, ϵ_k) represent the bathymetry and they also influence the wave amplitude evolution. Equation (2.35), after some simplifications to the nonlinear term, is given below:

$$\frac{\partial a_j}{\partial t} + \frac{1}{\mathfrak{D}_j}\left[2\mathrm{i}\gamma_j^{(3)}\left(\frac{\mathcal{K}_j}{h}\frac{\partial a_j}{\partial x}\right) + \frac{\gamma_j^{(6)}}{h^2}\left(\frac{dh}{dx}\right)^2 a_j\right]$$
$$+\frac{1}{\mathfrak{D}_j}\left[\frac{2\mathcal{K}_j}{h}\gamma_j^{(4)} + \gamma_j^{(3)}\frac{\partial}{\partial x}\left(\frac{\mathcal{K}_j}{h}\right) - \gamma_j^{(5)}\frac{2}{h}\frac{\partial h}{\partial x}\left(\frac{\mathcal{K}_j}{h}\right) - \frac{\gamma_j^{(3)}}{\beta_j}\frac{2\mathcal{K}_j}{h}\frac{d(\beta_j)}{dx}\right] a_j = \widehat{\mathfrak{N}}_j a^2, \tag{A.1}$$

where $\widehat{\mathfrak{N}}_j$ is defined as:

$$\widehat{\mathfrak{N}}_j = \frac{1}{\mathfrak{D}_j}\left[\mathrm{NL}_{(\mathbb{V},j)} + \mathrm{NL}_{(\mathbb{B},j)} + \mathrm{NL}_{(\Psi,j)}\right]. \tag{A.2}$$

The analysis is similar for all three waves, hence from here on all subscripts j (denoting the $j-$th wave) are dropped for convenience. Moreover, a term containing $\gamma^{(6)}$ is also included in the above equation. It will be proved in this section that this term is an order of magnitude smaller than the other terms for the parameter regime we consider.

The time scale of wave amplitude's evolution is assumed to be at least an order of magnitude larger than the time period of the wave. Therefore $\partial a/\partial t$ will approximately scale as: $\partial a/\partial t \sim \epsilon_t\epsilon_a\omega$. The amplitude's length scale is assumed to be much larger than the wavelength of the wave. Hence $\partial a/\partial x$ will scale as $\partial a/\partial x \sim \epsilon_x\epsilon_a\mathcal{K}/h$. Using the above scaling, the $\partial a/\partial x$ term in (A.1) (including its coefficients) will scale as:

$$2\frac{\gamma^{(3)}}{\mathfrak{D}}\left(\frac{\mathcal{K}}{h}\frac{\partial a}{\partial x}\right) \sim \frac{1}{\omega}\frac{\gamma^{(3)}\mathcal{K}^2}{\gamma^{(1)}\mathcal{K}^2 - \gamma^{(2)}}\epsilon_x\epsilon_a \sim (\widehat{c}_g\epsilon_x)\omega\epsilon_a, \tag{A.3}$$

where $\widehat{c}_g$ represents the scale of group speed term for the packet, and is given by:

$$\widehat{c}_g \equiv \frac{(\omega^2 - f^2)}{\omega^2}\left[\frac{\gamma^{(3)}}{(\omega^2 - f^2)\gamma^{(1)} + \gamma^{(3)}}\right]. \tag{A.4}$$

It can be noticed that as ϵ_x is reduced, the effect of group speed diminishes as expected since a decrease in ϵ_x means the length scale of the packet is increased. Here we also emphasize that for $\omega \approx N$: $\gamma^{(3)} \ll \omega^2\gamma^{(1)}$. In such kind of parameter regime, $\widehat{c}_g \ll 1$, hence $\partial a/\partial x$ term will have a reduced effect on the amplitude evolution. Moreover, for $\omega \approx f$, similar behavior is observed since $\widehat{c}_g \ll 1$.

Now we focus on the term containing $\gamma^{(6)}$ in (A.1), which is given below (after some simplification):

$$\left(\frac{dh}{dx}\right)^2 \frac{\mathcal{W}}{\mathcal{K}^2}\frac{\omega a}{2}, \tag{A.5}$$

where $\mathcal{W}$ is a non-dimensional quantity defined as:

$$\mathcal{W} = \frac{\omega^2 - f^2}{\omega^2}\frac{\gamma^{(6)}}{(\omega^2 - f^2)\gamma^{(1)} + \gamma^{(3)}}. \tag{A.6}$$

The integral $\gamma^{(6)}$ is evaluated numerically to study its scaling. For uniform stratification, $\mathcal{W}$ can be evaluated analytically, which is given below:

$$\mathcal{W}_u = -\mathcal{M}^2\left[\frac{\omega^2 - f^2}{\omega^2}\frac{N_b^2 - \omega^2}{N_b^2 - f^2}\right]\left(\frac{1}{3} - \frac{1}{2\mathcal{M}^2}\right) \tag{A.7}$$

where $\mathcal{W}_u$ is used to denote $\mathcal{W}$ in constant stratification N_b, and $\mathcal{M} = n\pi$ is the non-dimensionalised vertical wavenumber of the wave. Moreover, using $(dh/dx)^2 \sim (\epsilon_h\epsilon_k)^2\mathcal{K}^2$, the term given in equation (A.5) will scale as

$$\left(\frac{(\epsilon_h\epsilon_k)^2}{2}\mathcal{W}\right)\omega\epsilon_a. \tag{A.8}$$

Hence for the multiple-scale analysis to be consistent, $\mathcal{W}((\epsilon_h\epsilon_k)^2/2)$ has to be a small quantity. $\mathcal{W}$ is plotted in figure A.1 for nine stratification profiles, where $f = 0$ and $\omega/N_b = 0.4$ were used. In all subfigures, $\mathcal{W}_u$ is also plotted for reference, where $\mathcal{W}_u$ is evaluated with constant stratification N_b (hence $\mathcal{W}_u$ in all subfigures is same). From figure A.1, it can be seen that in general for any stratification profile, $\mathcal{W}$ is almost proportional to the square of the modenumber n, similar to $\mathcal{W}_u$. Hence the bathymetry has to be more slowly varying (ϵ_k has to be smaller) as the modenumber increases. Other pycnocline depths ($z_c = H/20, H/40, H/80$) were also tested for different combinations of W_p, $N_{\max}$ used in figure A.1 that provided similar results.

The term which contains the $\gamma^{(5)}$ integral is now analysed. For all non-uniform stratification profiles used in this appendix, it was observed that

$$\gamma^{(5)} \lesssim \frac{1}{2}\gamma^{(3)}. \tag{A.9}$$

Using (A.9), the term containing $\gamma^{(5)}$ can be scaled to:

$$\frac{1}{\mathfrak{D}_j}\left[\gamma^{(5)}\frac{2}{h}\frac{\partial h}{\partial x}\left(\frac{\mathcal{K}}{h}\right)a\right] \sim \left(\frac{\widehat{c}_g}{2}\epsilon_h\epsilon_k\right)\omega\epsilon_a. \tag{A.10}$$

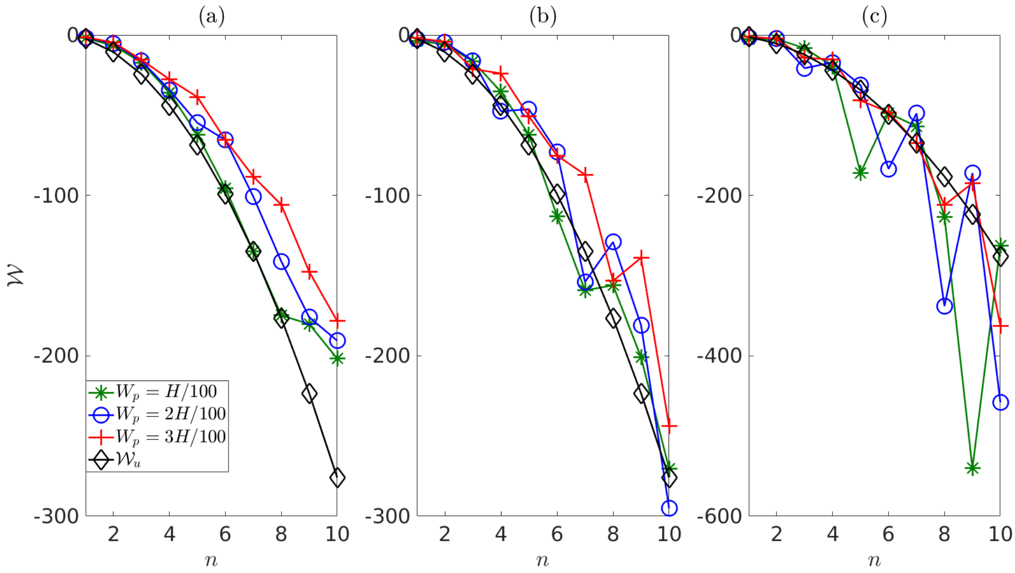

Figure A.1: The variation in $\mathcal{W}$ for modes 1–10 for different stratification profiles. (a) $N_{\text{max}} = 5N_b$ is used with $z_c = H/10$ and W_p is varied. (b) $N_{\text{max}} = 10N_b$ is used with $z_c = H/10$ and W_p is varied. (c) $N_{\text{max}} = 15N_b$ is used with $z_c = H/10$ and W_p is varied.

The changes in the wavenumber of a mode as h is varied is analysed. To this end, (2.27b), which provides the n-th eigenfunction, is differentiated in $x-$direction, yielding:

$$\left[\frac{\partial^2}{\partial \eta^2} + \mathcal{K}_n^2 \chi^2\right] \frac{\partial \phi_n}{\partial x} = -\mathcal{K}_n^2 \frac{\partial \chi^2}{\partial x} \phi_n - \frac{d\mathcal{K}_n^2}{dx} \chi^2 \phi_n, \tag{A.11}$$

where $\mathcal{K}_n = k_n h$. Equation (A.11) can have a non-trivial solution only when the RHS is orthogonal to the solution of the self adjoint operator in the LHS. Hence mutliplying RHS with ϕ_n, and then integrating in the η–direction between the domain limits would result in:

$$\frac{1}{k_n}\frac{dk_n}{dx} + \frac{1}{h}\frac{dh}{dx} = -\frac{1}{2\gamma_n^{(3)}} \int_{-1}^{0} \frac{\partial N^2}{\partial x} \phi_n^2 d\eta. \tag{A.12}$$

From (A.12), it can be noticed that the dimensional wavenumber k_n can change due to: (a) change in the domain height, and (b) change in the effective stratification profile. For uniform stratification, $d\mathcal{K}_n/dx = 0$. For the lower modes (1–10) in profiles considered in this appendix, it was observed that

$$\mathcal{O}\left(\frac{1}{k_n}\frac{dk_n}{dx}\right) \Big/ \mathcal{O}\left(\frac{1}{h}\frac{dh}{dx}\right) \sim \mathcal{O}(1). \tag{A.13}$$

Moreover, in general it was observed that as the modenumber increases, the term given in (A.13) increases. Using (A.13), the term containing the derivative of the wavenumber can be scaled as:

$$\frac{1}{\mathfrak{D}_j}\left[\gamma^{(3)}\frac{dk}{dx}a\right] \sim \left(\frac{\widehat{c}_g}{2}\epsilon_h\epsilon_k\right)\omega\epsilon_a. \tag{A.14}$$

We now evaluate $\gamma^{(4)}$ for the stratification profiles considered in this appendix. For modes 1–10, we find

$$\frac{\gamma^{(4)}}{\gamma^{(3)}} \sim \mathcal{O}\left(\frac{1}{h}\frac{dh}{dx}\right). \tag{A.15}$$

Using (A.15), the term containing $\gamma^{(4)}$ can be scaled to:

$$\frac{1}{\mathfrak{D}_j}\left[\frac{2\mathcal{K}}{h}\gamma^{(4)}a\right] \sim \left(\widehat{c}_g\epsilon_h\epsilon_k\right)\omega\epsilon_a. \tag{A.16}$$

Using (A.10), (A.14) and (A.16), we observe that for the lower modes, the three terms that compose the β function can scale to a maximum value which is of the same order of magnitude. Hence they are all retained and are used in evaluating the β function (2.37). Moreover, it can be seen that the topographic terms are all dependent on the magnitude of the group speed. This relation is naturally there because a wavepacket has to travel to different h fast enough to feel the effect of h variation. Scaling (A.16) also holds for uniform stratification, where ϕ still varies in the $x-$direction. This is because of the nature of the ϕ normalisation, i.e. (2.30), used in this paper.

The nonlinear coupling coefficient in the RHS cannot be further simplified, hence the nonlinear term scales as:

$$\text{RHS} \sim \widehat{\mathfrak{N}}\epsilon_a^2. \tag{A.17}$$

Hence the final scaling for (2.45a)–(2.45c), using all the scaling derived, and with the inclusion of the $\gamma^{(6)}$ term, is given below after some simplification:

$$\epsilon_t \sim \frac{\mathfrak{N}}{\omega}\epsilon_a - \widehat{c}_g\epsilon_x - \frac{(\epsilon_h\epsilon_k)^2}{2}\mathcal{W}. \tag{A.18}$$

Here an important point to remember is that the multiple-scale analysis was derived with the assumption that internal waves do not scatter/exchange energy to different modes of the same angular frequency. Therefore the reduced order equations provide the most accurate results when the internal waves do not scatter significant amount of its energy as it passes over a bathymetry. Moreover, even when $\mathcal{O}(\epsilon_h\epsilon_k) \ll \mathcal{O}(1)$ is satisfied, there could be special circumstances when waves may still get scattered significantly. An example of such a scenario is Bragg resonance of internal waves due to small amplitude, subcritical topographies (Buhler & Holmes-Cerfon, 2011; Li & Mei, 2014; Couston *et al.*, 2017). Scattering/energy exchange can also occur for large amplitude, slowly varying topographies. However, it was observed that modes 1–8 are scattered very little for large amplitude topographies ($\epsilon_h \approx 0.5$) with low criticality ($\lesssim 0.1$) in the presence of uniform stratification. Criticality is defined as the ratio of the maximum slope of the topography to the slope of the internal wave. Mode-8 has $\approx 8\%$ variation in its amplitude as it propagates through a Gaussian topography with $\epsilon_h = 0.5$ and criticality = 0.1. Low criticality topographies for mode n of any ω/N_b is obtained when the condition $n\epsilon_k \ll \mathcal{O}(1)$ is satisfied. Moreover for the condition $n\epsilon_k \ll \mathcal{O}(1)$, the last term in (A.18) becomes an ϵ_k^2 term even for large amplitude topographies. This can be seen by considering $\mathcal{W}_u$ (which can also be used as a reference for non-uniform stratifications) given in (A.7). Hence this term is neglected in the governing equations (2.45a)–(2.45c).

A.0.1 Scaling analysis for the governing equations in §2.7

The scaling analysis for the governing equation (2.78) derived in §2.7 is done with the help of results derived previously. The above-mentioned governing equations are given below:

$$\begin{aligned}&\left[\left(\gamma_j^{(3)}\frac{\partial^2\mathcal{A}_j}{\partial x^2}\right)+\mathcal{K}_j^2\left(\frac{\mathcal{A}_j}{h^2}\gamma_j^{(3)}\right)\right]\mathrm{e}^{-\mathrm{i}\omega_j t}+2\left(\gamma_j^{(4)}-\frac{\gamma_j^{(5)}}{h}\frac{\partial h}{\partial x}\right)\frac{\partial\mathcal{A}_j}{\partial x}\mathrm{e}^{-\mathrm{i}\omega_j t}+\gamma_j^{(8)}\mathcal{A}_j\mathrm{e}^{-\mathrm{i}\omega_j t}\\&+\left[\frac{\gamma_j^{(6)}}{h^2}\left(\frac{\partial h}{\partial x}\right)^2-\frac{\gamma_j^{(5)}}{h}\left(\frac{\partial^2 h}{\partial x^2}\right)+\frac{2\gamma_j^{(5)}}{h^2}\left(\frac{\partial h}{\partial x}\right)^2-2\frac{\gamma_j^{(7)}}{h}\frac{\partial h}{\partial x}\right]\mathcal{A}_j\mathrm{e}^{-\mathrm{i}\omega_j t}=\mathrm{NonL}_3.\end{aligned} \tag{A.19}$$

From here on the subscripts are omitted, since the analysis is similar for both the waves. The leading order terms scale as follows:

$$\left[\frac{\partial^2\mathcal{A}}{\partial x^2},\mathcal{K}^2\frac{\mathcal{A}}{h^2}\right]\sim\epsilon_a\frac{\mathcal{K}^2}{h^2}. \tag{A.20}$$

Using (2.22), the scalings derived in appendix A, and the small amplitude assumption for topography ($\epsilon_h \ll \mathcal{O}(1)$ and $\epsilon_k \sim \mathcal{O}(1)$), the following relations can be obtained:

$$\begin{aligned}&2\frac{\gamma^{(4)}}{\gamma^{(3)}}\frac{\partial\mathcal{A}}{\partial x}\sim 2\epsilon_h\epsilon_a\frac{\mathcal{K}^2}{h^2}, &&\frac{2}{h}\frac{\partial h}{\partial x}\frac{\gamma^{(5)}}{\gamma^{(3)}}\frac{\partial\mathcal{A}}{\partial x}\sim\epsilon_h\epsilon_a\frac{\mathcal{K}^2}{h^2},\\&\left(\frac{1}{h}\frac{\partial^2 h}{\partial x^2}\right)\frac{\gamma^{(5)}}{\gamma^{(3)}}\mathcal{A}\sim\frac{\epsilon_h}{2}\epsilon_a\frac{\mathcal{K}^2}{h^2}, &&2\left(\frac{1}{h}\frac{\partial h}{\partial x}\right)^2\frac{\gamma^{(5)}}{\gamma^{(3)}}\mathcal{A}\sim\epsilon_h^2\epsilon_a\frac{\mathcal{K}^2}{h^2}.\end{aligned} \tag{A.21}$$

For the profiles and the parameters used in appendix A, it is observed that $(\omega^2 - f^2)\gamma^{(1)} + \gamma^{(3)} \sim \gamma^{(3)}$. Hence the $\gamma^{(6)}$ term can be scaled as:

$$\frac{\gamma^{(6)}}{\gamma^{(3)}}\frac{1}{h^2}\left(\frac{\partial h}{\partial x}\right)^2 \mathcal{A} \sim \left(\mathcal{W}\epsilon_h^2\right)\epsilon_a \frac{\mathcal{K}^2}{h^2}, \tag{A.22}$$

where $\mathcal{W}$ is plotted in figure A.1 for various stratification profiles. Therefore similar to appendix A, the term $\mathcal{W}\epsilon_h^2$ has to be a small number for the multiple-scale analysis to be consistent. Furthermore, the $\gamma_j^{(7)}$ term was observed to scale as:

$$\left(\frac{2}{h}\frac{\partial h}{\partial x}\right)\frac{\gamma^{(7)}}{\gamma^{(3)}}\mathcal{A} \lesssim \frac{\mathcal{K}_n^2}{\mathcal{K}_1^2}\left(\frac{1}{h}\frac{\partial h}{\partial x}\right)^2 2\epsilon_a, \tag{A.23}$$

where $\mathcal{K}_n$ is the nondimensional wavenumber of wave-1 (or wave-3), and n gives the wave's modenumber. Note that this scaling has a similar behavior as $\mathcal{W}$, which is nearly proportional to n^2. The scaling of the integral $\gamma^{(8)}$ is focused upon:

$$\gamma^{(8)} = \left(\frac{dh}{dx}\right)^2 \int_{-1}^{0}(N^2 - \omega^2)\phi\frac{\partial^2\phi}{\partial h^2}d\eta + \frac{d^2h}{dx^2}\int_{-1}^{0}(N^2 - \omega^2)\phi\frac{\partial\phi}{\partial h}d\eta. \tag{A.24}$$

For a uniform stratification, $\partial^2\phi/\partial h^2 = 0$. Moreover, for the non-uniform stratification profiles used in appendix A, it was observed that:

$$\int_{-1}^{0}(N^2 - \omega^2)\phi\frac{\partial^2\phi}{\partial h^2}d\eta \lesssim \frac{\mathcal{K}_n^2}{\mathcal{K}_1^2}\frac{\gamma^{(3)}}{h^2}, \qquad \int_{-1}^{0}(N^2 - \omega^2)\phi\frac{\partial\phi}{\partial h}d\eta \sim \frac{\gamma^{(3)}}{h}. \tag{A.25}$$

Hence using (A.25), the scaling for $\gamma^{(8)}$ can be given in a simpler form which is as follows:

$$\gamma^{(8)} \sim \left[\frac{\mathcal{K}_n^2}{\mathcal{K}_1^2}\left(\frac{1}{h}\frac{dh}{dx}\right)^2 + \frac{1}{h}\frac{d^2h}{dx^2}\right]\gamma^{(3)}. \tag{A.26}$$

For low modes in the presence of small amplitude topographies, the second term in RHS of (A.26) would be significantly higher than the first term. For any mild-slope bathymetry, the nonlinear terms NonL$_3$ in (A.19) can be scaled using the relation $d^n\mathcal{A}/dx^n \approx (\mathcal{K}/h)^n\mathcal{A}$, where $n \in \mathbb{Z}^+$. Using this approximation, the nonlinear term can be scaled as:

$$\mathrm{NonL}_3 \sim \frac{1}{\gamma^{(3)}}\left[\mathrm{NL}_{(\mathbb{V},3)} + \mathrm{NL}_{(\mathbb{B},3)} + \mathrm{NL}_{(\Psi,3)}\right]\epsilon_a^2. \tag{A.27}$$

The nonlinear coupling coefficients cannot be simplified further. Moreover the nonlinear terms have to be at least one order of magnitude lesser than the leading order terms (given in (A.20)).

Appendix B

Numerical method used to solve the governing equations in Chapter 4

Dedalus is once again used to solve the governing equations. Equations (4.4)–(4.7) are first converted to terrain following coordinates. Corresponding to the change in coordinates, new variables for (u, w, b, p) in $x - \eta$ coordinates are introduced:

$$u(x, z, t) \Rightarrow \mathbb{U}(x, \eta, t), \qquad b(x, z, t) \Rightarrow \mathbb{B}(x, \eta, t), \tag{B.1}$$

$$w(x, z, t) \Rightarrow \mathbb{W}(x, \eta, t) \qquad p(x, z, t) \Rightarrow \mathbb{P}(x, \eta, t). \tag{B.2}$$

Note that the new variables are same as the previous definitions in the chapter 2, however, we are redefining this for the convenience of the reader. Then the governing equations (4.4)–(4.7) change to:

$$\frac{\widehat{D}\mathbb{U}}{\widehat{D}t} + \mathbb{W}L_\eta(u_{\text{base}}) + \frac{L_x(\mathbb{P})}{\rho_0} = -\mathbb{U}L_x(\mathbb{U}) - \mathbb{W}L_\eta(\mathbb{U}) + \nu\widehat{\Delta}_{2D}(\mathbb{U}) - \text{SP}(x)\mathbb{U} + \mathcal{F}_u + \widehat{\mathcal{H}}(\mathbb{U}) \tag{B.3}$$

$$\frac{\widehat{D}\mathbb{W}}{\widehat{D}t} - \mathbb{B} + \frac{L_\eta(\mathbb{P})}{\rho_0} = -\mathbb{U}L_x(\mathbb{W}) - \mathbb{W}L_\eta(\mathbb{W}) + \nu\widehat{\Delta}_{2D}(\mathbb{W}) - \text{SP}(x)\mathbb{W} + \mathcal{F}_w + \widehat{\mathcal{H}}(\mathbb{W}) \tag{B.4}$$

$$\frac{\widehat{D}\mathbb{B}}{\widehat{D}t} + N^2\mathbb{W} = -\mathbb{U}L_x(\mathbb{B}) - \mathbb{W}L_\eta(\mathbb{B}) + \kappa\widehat{\Delta}_{2D}(\mathbb{B}) - \text{SP}(x)\mathbb{B} + \mathcal{F}_b + \widehat{\mathcal{H}}(\mathbb{B}) \tag{B.5}$$

$$L_x(\mathbb{U}) + L_\eta(\mathbb{W}) = 0 \tag{B.6}$$

where the linearised material derivative in $(x-\eta)$ coordinates is defined as: $\widehat{D}/\widehat{D}t \equiv (\partial/\partial t + u_{\text{base}}L_x)$. Here $\widehat{\Delta}_{2D} \equiv (L_{xx}+L_{\eta\eta})$. The definitions of $L_x, L_\eta, L_{xx}, L_{\eta\eta}$ are given in chapter 2. The η direction is resolved using Chebyshev polynomials, while the $x-$direction is resolved using Cosine/Sine modes. The vertical resolution was chosen such that for all simulations with $\nu = 10^{-2}\text{m}^2\text{s}^{-1}$, 192 Chebyshev polynomials were used. For all simulations with $\nu = 0.5\times10^{-2}\text{m}^2\text{s}^{-1}$, 256 Chebyshev polynomials were used. In general, horizontal resolution was increased as Υ was increased. For simulations with $\Upsilon = 0.1$, there is not much scattering hence low horizontal resolution ($dx = 750$m) was used. For $\Upsilon = 0.4-0.9$, $dx \approx 260-340$m was used. For supercritical topographies, a resolution of $138-286$m was used, where in general resolution increased as the height increased. Second order IMEX (Implicit-Explicit) time stepping scheme given in equation (14) of Ascher *et al.* (1995) is used. For all simulations, 2000 time steps were taken for one time period of the wave ($2\pi/\omega_d$). Two types of hyperviscous operators are used and they are given by

$$\widehat{\mathcal{H}}_{12}() \equiv \nu_{12}\frac{\partial^{12}}{\partial x^{12}}(), \quad \widehat{\mathcal{H}}_{16}() \equiv \nu_{16}\frac{\partial^{16}}{\partial x^{16}}(), \tag{B.7}$$

where $\widehat{\mathcal{H}}_j$ is the equivalent operator of $\mathcal{H}_j$ in terrain following coordinates. ν_{12} and ν_{16} are constants. For a particular simulation, either $\widehat{\mathcal{H}}_{12}$ or $\widehat{\mathcal{H}}_{16}$ is used. It is ensured that the artificial hyperviscous term does not significantly affect the large scale physics. The above statement is verified by analysing the magnitude of $\widetilde{E^{(\text{vis})}}_H$ (in energy equation 4.19) which gives a measure of the effect of the hyper viscosity term. $\langle\widetilde{E^{(\text{vis})}}_H\rangle/\langle\mathcal{T}_{inc}\rangle$ was in the order of 10^{-4} (or lower) for any simulation with $\Upsilon \leq 0.75$. Moreover, for any simulation with $\Upsilon \geq 0.85$, $\langle\widetilde{E^{(\text{vis})}}_H\rangle/\langle\mathcal{T}_{inc}\rangle$ was in the order of 10^{-3} (or lower).

B.0.1 Validation of the numerical methods

To validate the code, following Lamb & Dunphy (2018), we estimate the residual in the energy equation (4.19). Mathematically the residual (denoted by Rsd) is given by:

$$\text{Rsd} \equiv \frac{d(\tilde{E}_{ke}+\tilde{E}_{pe})}{dt} + \text{TF}\Big|_{x_R} - \text{TF}\Big|_{x_L} - \widetilde{E^{(\text{vis})}} - \widetilde{E^{(\text{vis})}}_H \tag{B.8}$$

Here, we only focus on the residual in regions where the sponge and the forcing terms are negligible. Note that Rsd is a function of time only. Theoretically, Rsd $=0$ when the governing equations are solved perfectly. Due to a finite time step and grid size, computational errors will be introduced. We analyse Rsd for all the simulations. To this end, the control area is chosen such that its length is $5W_T$ in $x-$direction (W_T is the standard deviation of the topography), and in the η direction it spans from -1 to 0 thus enclosing the full fluid column. The horizontal center of the control area coincides with the top of the topography. For all simulations with $U_c \neq 0$, it was observed that Rsd is always less than 0.15% of the maximum value of the total flux of the incoming wave. Moreover, Rsd was observed to be less than 0.1% (hence $\mathcal{O}(10^{-4})$) for majority of the simulations ($> 80\%$). In this chapter, we consistently use time averaged/integrated quantities (for example, modes' flux and the rate of kinetic energy dissipation are all time averaged). As a result, we also estimate time integrated Rsd for all the simulations. For all the simulations that involves a surface current, $\langle \text{Rsd} \rangle / \langle \mathcal{T}_{inc} \rangle$ is observed to be $\mathcal{O}(10^{-4})$ or lesser.

For further validation, we compare the modal composition obtained in the $U_c = 0$ numerical simulations with results from analytical model of Lahaye & Smith (2020). We compare results for 6 simulations, and the comparison is given in figure B.1. The results from the simulations match reasonably well with the analytical model which validates the resolution we used. We further run simulations for 3 different topography configurations with $U_c = 0$ in the linear regime, and a comparison is made with results from Mathur *et al.* (2014). $\omega = \omega_d$ is used, however, $N^2 = 3 \times 10^{-5}\text{s}^{-2}$ is used which is the value used in Mathur *et al.* (2014). The results of Mathur *et al.* (2014) are obtained from figure 3 of their paper by an approximate manner. The topography configurations along with the results are all shown in table B.1. It can be seen that the values obtained from the simulations match reasonably close with the previous models/results. Note that since the results match with theoretical models, the sponges on the horizontal ends of the computational domain are also functioning as intended.

We also verify that the viscosity value used in the simulations for supercritical topographies does not significantly influence the modal composition of the transmitted and the reflected wave field. To this end, we run two simulations that model the scattering of M1C and M1W with a higher grid and with a lower viscosity. For both simulations, $U_c = 0.10NH$ and the topography with $\Upsilon = 1.5, h_T/H = 0.5$ is chosen. The results presented in section 4.3 for $\Upsilon = 1.5, h_T/H = 0.5$ were obtained from simulations that are run with 256×2592 grid (with $\nu = 0.5 \times 10^{-2}\text{m}^2\text{s}^{-1}$) while the higher resolution simulations use a 384×3840 grid with $\nu = 0.3 \times 10^{-2}\text{m}^2\text{s}^{-1}$. The comparison is shown in figure B.2. The figure shows both transmitted and reflected waves' modal composition. It can be seen that the difference in modal composition is not significant which validates the use of the current resolution which we employ.

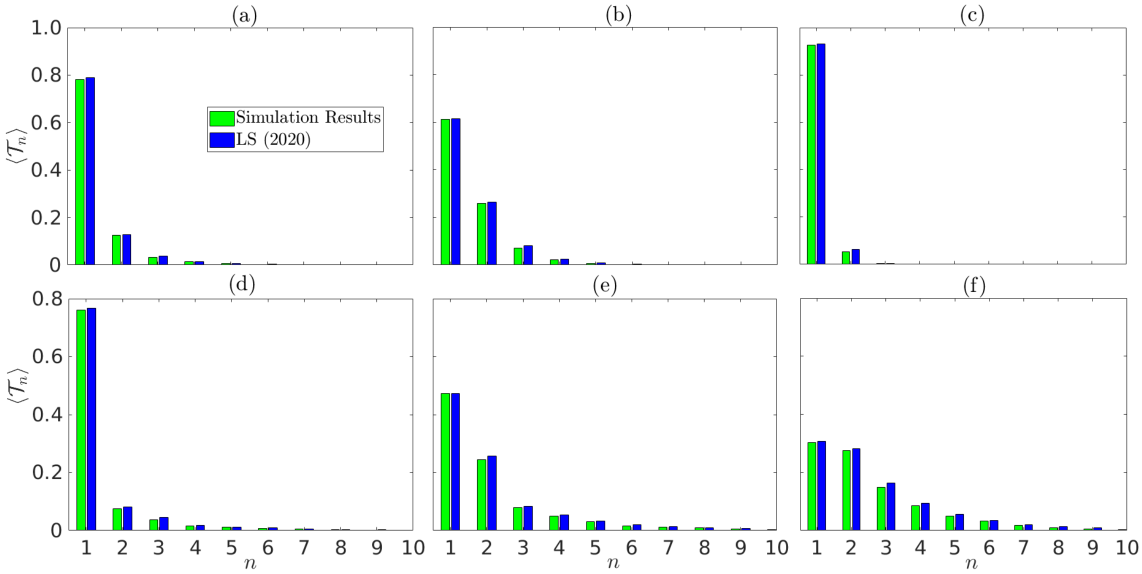

Figure B.1: $\langle \mathcal{T}_n \rangle$ obtained from simulations conducted for this chapter, and the results obtained from the analytical model provided in Lahaye & Smith (2020). Each subplot is for a different topography configuration which is as follows: (a) $\Upsilon = 0.5, h_T/H = 0.2$. (b) $\Upsilon = 0.5, h_T/H = 0.35$. (c) $\Upsilon = 0.5, h_T/H = 0.5$. (d) $\Upsilon = 0.75, h_T/H = 0.2$. (e) $\Upsilon = 0.75, h_T/H = 0.35$. (f) $\Upsilon = 0.75, h_T/H = 0.5$.

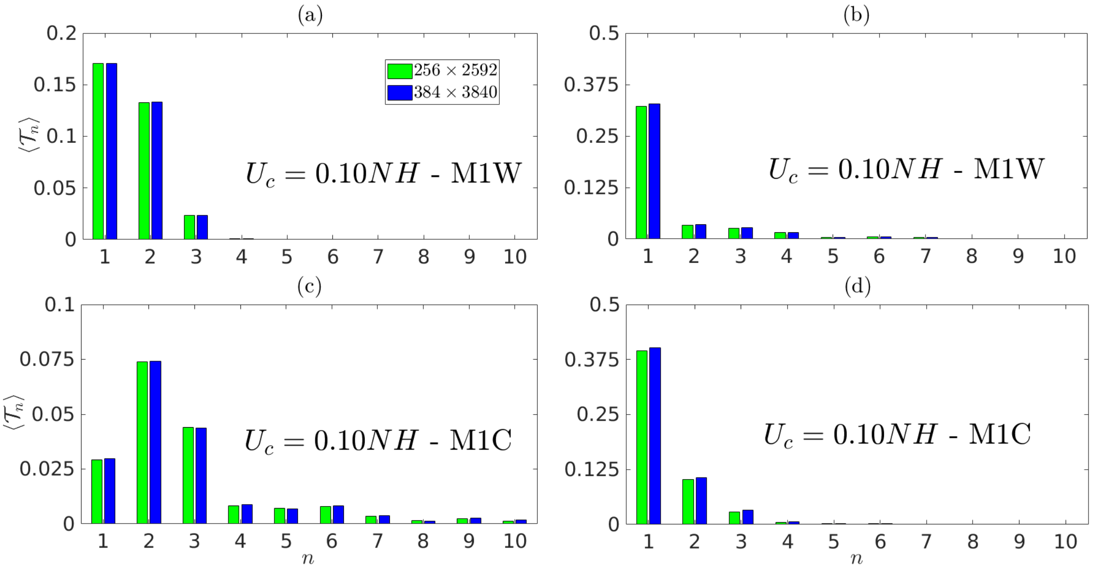

Figure B.2: $\langle \mathcal{T}_n \rangle$ obtained from simulations with grids 256×2592 and 384×3840. For the comparison between the grids, Scattering of M1C and M1W for $U_C = 0.10NH$ by a supercritical topography with $\Upsilon = 1.5$ and $h_T/H = 0.5$ is considered. (a) and (c) show the modal composition of the transmitted field while (b) and (d) show the modal composition of the reflected internal waves.

$(\Upsilon, h_T/H)$	Mode-1 (GG22,MM14)	Mode-2 (GG22,MM14)
(0.43,0.34)	(72.7,71.5)	(21.3,21.7)
(0.59,0.34)	(54.6,54.0)	(27.5,27.1)
(0.81,0.34)	(47.8,47.4)	(23.0,22.4)

Table B.1: Criticality and topography height is shown in column-1. Columns 2 and 3 show the normalised transmitted mode-1 and mode-2 pressure flux respectively obtained from our simulations (denoted by GG22) and Mathur *et al.* (2014) (denoted by MM14).

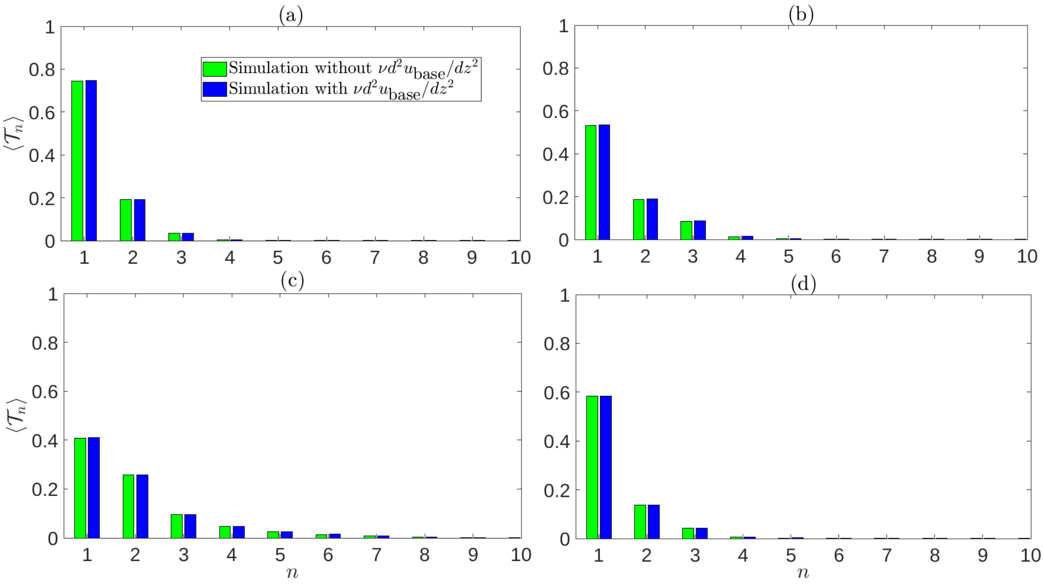

Figure B.3: Comparison of $\langle \mathcal{T}_n \rangle$ for simulations with and without the term $\nu d^2u_{\text{base}}/dz^2$ for four different topography configurations. The scattering of M1C for $(\Upsilon = 0.5, h_T/H = 0.35)$ and $(\Upsilon = 0.75, h_T/H = 0.35)$ are shown in (a) and (c), respectively. The scattering of M1W for $(\Upsilon = 0.5, h_T/H = 0.5)$ and $(\Upsilon = 0.75, h_T/H = 0.5)$ are shown in (b) and (d), respectively.

B.0.1.1 On base flow diffusion

We do not consider the term $\nu d^2u_{\text{base}}/dz^2$ because the simulations are run for a long time and the dissipation/diffusion term will change the base flow profile. The base flow diffusion term does not directly influence the scattering. However, the incoming wave and the other modes' modal shape in $z-$direction will slowly change with time because of the changes in the base flow, and the transient effect is undesired in this study. Running simulations without base flow diffusion is analogous to adding a "forcing" term in the $u-$momentum equation which counters the effect of $\nu d^2u_{\text{base}}/dz^2$, and makes u_{base} time invariant. Such forcing terms have been previously used in weakly nonlinear analysis in Cudby & Lefauve (2021), and in fully nonlinear direct numerical simulations in Howland *et al.* (2018). For 4 different topography configurations, we show that simulations with a higher viscosity and without $\nu d^2 u_{\text{base}}/dz^2$ term (results from section 4.3) provide nearly the same modal composition compared to simulations that are run with the term $\nu d^2 u_{\text{base}}/dz^2$ and with a lower ν. $\nu = 0.25 \times 10^{-2} \text{m}^2\text{s}^{-1}$ is taken consistently for simulations that are run with the term $\nu d^2 u_{\text{base}}/dz^2$, and the comparisons are shown in figure B.3. It can be seen that the results are nearly same, hence validating our current setup.

B.0.1.2 Rayleigh sponge to dampen the internal waves

The Rayleigh sponge terms are used to dampen the internal waves far away from the topography. The damping stops the wave from reflecting back from the horizontal limits of the computational domain. Rayleigh sponge terms are quite common and are used in open-source codes like MITgcm (MIT General Circulation Model). To calculate the efficiency we send a mode-1 internal wave into the sponge and measure how much the internal wave's flux changes. The measurement of the flux starts before the wave touches the sponge. If the sponge reflects significant energy, then the energy flux after the wave reaches the sponge will be quite different compared to the flux before the wave reaches the sponge. Figure B.4(a) shows an image of the horizontal velocity field before the wave reaches the sponge. The sponge region is marked for the convenience of the reader. We measure the energy flux of the wave near the region where the wave is forced ($x/L \approx 0.35$). We employ the same procedure for three different simulations: simulation (1) is for a mode that travels with the current (M1W with $U_C = 0.10NH$), simulation (2) is for a mode that travels against the current (M1C with $U_C = 0.10NH$), and simulation (3) is for a mode that travels without any current ($U_c = 0$). The flux data for all three simulations are shown in figure B.5. Note that the flux variation is less than $< 1\%$ for all three simulations. We started to take the measurement before the wave reaches the sponge. From the results, we can conclude that the sponge does not reflect a significant amount of energy.

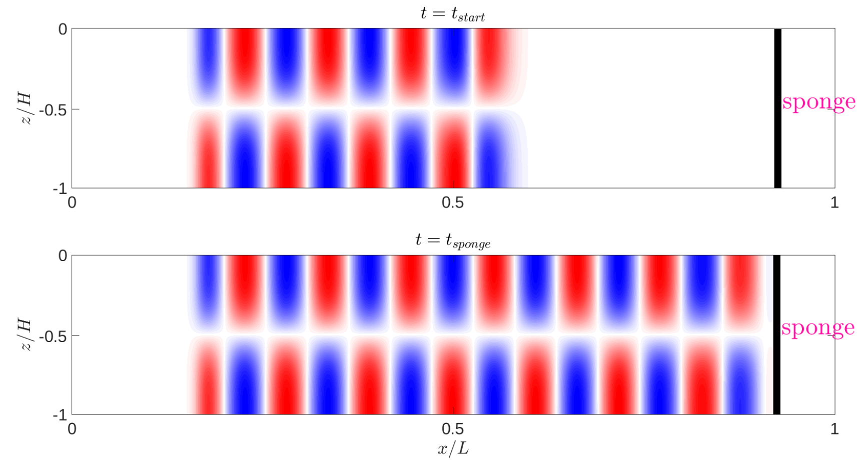

Figure B.4: (a) Horizontal velocity field when the flux is initially measured. (b) Horizontal velocity field when the wave touches the sponge. The sponge region is also shown for the convenience of the reader.

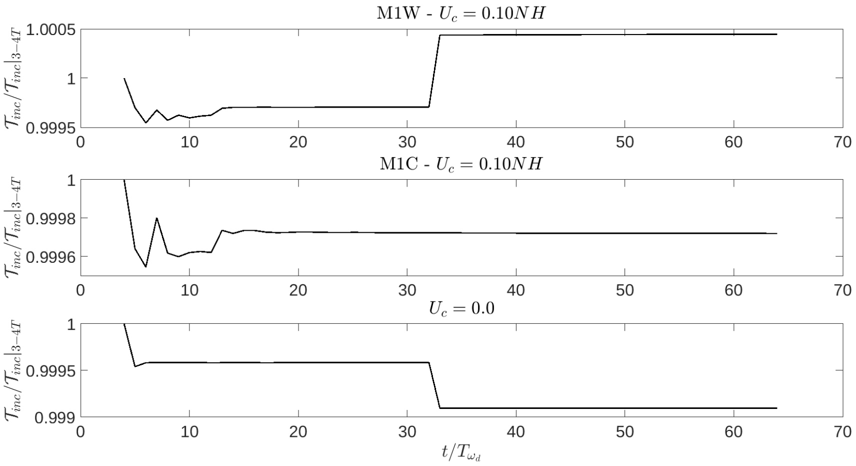

Figure B.5: Normalised flux data for three different simulations. The flux in all three simulations does not vary significantly as the wave impacts the sponge. $T_{\omega_d} \equiv 2\pi/\omega_d$.

Bibliography

Akylas, T. R. & Karimi, H. H. 2012 Oblique collisions of internal wave beams and associated resonances. *J. Fluid Mech.* **711**, 337–363.

Alam, M-R., Liu, Y. & Yue, D. K. P. 2009 Bragg resonance of waves in a two-layer fluid propagating over bottom ripples. Part I. Perturbation analysis. *J. Fluid Mech.* **624**, 191–224.

Alford, M. H., MacKinnon, J. A., Simmons, H. L. & Nash, J. D. 2016 Near-inertial internal gravity waves in the ocean. *Annu. Rev. Mar. Sci.* **8** (1), 95–123, pMID: 26331898.

Alford, M. H., MacKinnon, J. A., Zhao, Zhongxiang, Pinkel, Rob, Klymak, Jody & Peacock, Thomas 2007 Internal waves across the pacific. *Geophys. Res. Lett.* **34** (24).

Ascher, U. M., Ruuth, S. J. & Wetton, B. T. R. 1995 Implicit-explicit methods for time-dependent partial differential equations. *SINUM* **32** (3), 797–823.

Baines, P.G. 1973 The generation of internal tides by flat-bump topography. *Deep Sea Res. Part I Oceanogr. Res. Pap.* **20** (2), 179–205.

Baker, L. E. & Sutherland, B. R. 2020 The evolution of superharmonics excited by internal tides in non-uniform stratification. *J. Fluid Mech.* **891**, R1.

Balmforth, N. J., Ierley, G. R. & Young, W. R. 2002 Tidal conversion by subcritical topography. *J. Phys. Oceanogr.* **32** (10), 2900 – 2914.

Barkan, R., Srinivasan, K., Yang, L., McWilliams, J. C., Gula, J. & Vic, C. 2021 Oceanic mesoscale eddy depletion catalyzed by internal waves. *Geophys. Res. Lett.* **48** (18).

Bell Jr., T. H. 1975 Topographically generated internal waves in the open ocean. *J. Geophys. Res. (1896-1977)* **80** (3), 320–327.

Bourget, B., Dauxois, T., Joubaud, S. & Odier, P. 2013 Experimental study of parametric subharmonic instability for internal plane waves. *J. Fluid Mech.* **723**, 1–20.

Bourget, B., Scolan, H., Dauxois, T., Le Bars, M., Odier, P. & Joubaud, S. 2014 Finite-size effects in parametric subharmonic instability. *J. Fluid Mech.* **759**, 739–750.

Buhler, O. & Holmes-Cerfon, M. 2011 Decay of an internal tide due to random topography in the ocean. *J. Fluid Mech.* **678**, 271–293.

Buijsman, M. C., Ansong, J. K., Arbic, B. K., Richman, J. G., Shriver, J. F., Timko, P. G., Wallcraft, A. J., Whalen, C. B. & Zhao, Z. 2016 Impact of parameterized internal wave drag on the semidiurnal energy balance in a global ocean circulation model. *J. Phys. Oceanogr.* **46** (5), 1399 – 1419.

Burns, K. J., Vasil, G. M., Oishi, J. S., Lecoanet, D. & Brown, B. P. 2020 Dedalus: A flexible framework for numerical simulations with spectral methods. *Phys. Rev. Research* **2**, 023068.

Carr, M., Davies, P. A. & Hoebers, R. P. 2015 Experiments on the structure and stability of mode-2 internal solitary-like waves propagating on an offset pycnocline. *Physics of Fluids* **27** (4), 046602.

Chen, Z., Chen, S., Liu, Z., Xu, J., Xie, J., He, Y. & Cai, S. 2019 Can tidal forcing alone generate a GM-like internal wave spectrum? *Geophys. Res. Lett.* **46** (24), 14644–14652.

Couston, L-A., Liang, Y. & Alam, M-R. 2017 Oblique internal-wave chain resonance over seabed corrugations. *J. Fluid Mech.* **833**, 538–562.

Craik, A. D. D. 1971 Non-linear resonant instability in boundary layers. *J. Fluid Mech.* **50** (2), 393–413.

Craik, A. D. D., Adam, J. A. & Stewartson, K. 1978 Evolution in space and time of resonant wave triads - 1. the 'pump-wave approximation'. *Proc. Roy. Soc. A* **363** (1713), 243–255.

Cudby, J. & Lefauve, A. 2021 Weakly nonlinear holmboe waves. *Phys. Rev. Fluids* **6**, 024803.

Davis, R. E. & Acrivos, A. 1967 The stability of oscillatory internal waves. *J. Fluid Mech.* **30** (4), 723–736.

de Lavergne, C., Falahat, S., Madec, G., Roquet, F., Nycander, J. & Vic, C. 2019 Toward global maps of internal tide energy sinks. *Ocean Model.* **137**, 52 – 75.

de Lavergne, C., Vic, C., Madec, G., Roquet, F., Waterhouse, A. F., Whalen, C. B., Cuypers, Y., Bouruet-Aubertot, P., Ferron, B. & Hibiya, T. 2020 A parameterization of local and remote tidal mixing. *J. Adv. Model. Earth Syst.* **12** (5).

Diamessis, P.J., Wunsch, S., Delwiche, I. & Richter, M.P. 2014 Nonlinear generation of harmonics through the interaction of an internal wave beam with a model oceanic pycnocline. *Dynam. Atmos. Ocean* **66**, 110 – 137.

Dong, W., Bühler, O. & S., K. Shafer 2020 Frequency diffusion of waves by unsteady flows. *J. Fluid Mech.* **905**, R3.

Drazin, P. G. & Reid, W. H. 2004 *Hydrodynamic Stability*, 2nd edn. Cambridge University Press.

Duda, T.F., Lynch, J.F., Irish, J.D., Beardsley, R.C., Ramp, S.R., Chiu, Ching-Sang, Tang, Tswen Yung & Yang, Y.-J. 2004 Internal tide and nonlinear internal wave behavior at the continental slope in the northern south china sea. *IEEE Journal of Oceanic Engineering* **29** (4), 1105–1130.

Dunphy, M. & Lamb, K. G. 2014 Focusing and vertical mode scattering of the first mode internal tide by mesoscale eddy interaction. *J. Geophys. Res.* **119** (1), 523–536.

Dunphy, M., Ponte, A. L., Klein, P. & Gentil, S. L. 2017 Low-mode internal tide propagation in a turbulent eddy field. *J. Phys. Oceanogr.* **47** (3), 649 – 665.

Echeverri, P., Flynn, M. R., Winters, K. B. & Peacock, T. 2009 Low-mode internal tide generation by topography: an experimental and numerical investigation. *J. Fluid Mech.* **636**, 91–108.

Fan, B. & Akylas, T. R. 2019 Effect of background mean flow on PSI of internal wave beams. *J. Fluid. Mech.* **869**, R1.

Frajka-Williams, E., Ansorge, I. J., Baehr, J., Bryden, H. L., Chidichimo, M. P., Cunningham, S. A., Danabasoglu, G., Dong, S., Donohue, K. A., Elipot, S., Heimbach, P., Holliday, N. P., Hummels, R., Jackson, L. C., Karstensen, J., Lankhorst, M., Le Bras, I. A., Lozier, M. S., McDonagh, E. L., Meinen, C. S., Mercier, H., Moat, B. I., Perez, R. C., Piecuch, C. G., Rhein, M., Srokosz, M. A., Trenberth, E., Bacon, S., Forget, G., Goni, G., Kieke, D., Koelling, J., Lamont, T., McCarthy, G. D., Mertens, C., Send, U., Smeed, D. A., Speich, S., van den Berg, M., Volkov, D. & Wilson, C. 2019 Atlantic meridional overturning circulation: Observed transport and variability. *Front. Mar. Sci.* **6**.

Fructus, DORIAN, CARR, MAGDA, GRUE, JOHN, JENSEN, ATLE & DAVIES, PETER A. 2009 Shear-induced breaking of large internal solitary waves. *Journal of Fluid Mechanics* **620**, 1–29.

Gayen, B. & Sarkar, S. 2013 Degradation of an internal wave beam by parametric subharmonic instability in an upper ocean pycnocline. *J. Geophys. Res* **118** (9), 4689–4698.

Gayen, B. & Sarkar, S. 2014 PSI to turbulence during internal wave beam refraction through the upper ocean pycnocline. *Geophys. Res. Lett.* **41** (24), 8953–8960.

Gerkema, T. & J. Zimmerman, J. 2008 *An introduction to internal waves*.

Ghaemsaidi, S. J. & Mathur, M. 2019 Three-dimensional small-scale instabilities of plane internal gravity waves. *J. Fluid Mech.* **863**, 702–729.

Goff, John A. & Jordan, Thomas H. 1989 Stochastic modeling of seafloor morphology: A parameterized gaussian model. *Geophys. Res. Lett.* **16** (1), 45–48.

Gregory, J. M., Dixon, K. W., Stouffer, R. J., Weaver, A. J., Driesschaert, E., Eby, M., Fichefet, T., Hasumi, H., Hu, A., Jungclaus, J. H., Kamenkovich, I. V., Levermann, A., Montoya, M., Murakami, S., Nawrath, S., Oka, A., Sokolov, A. P. & Thorpe, R. B. 2005 A model intercomparison of changes in the atlantic thermohaline circulation in response to increasing atmospheric co2 concentration. *Geophys. Res. Lett.* **32** (12).

Grimshaw, R. 1988 Resonant wave interactions in a stratified shear flow. *J. Fluid Mech.* **190**, 357–374.

Grimshaw, R. 1994 Resonant wave interactions near a critical level in a stratified shear flow. *J. Fluid Mech.* **269**, 1–22.

Grisouard, N., Staquet, C. & Gerkema, T. 2011 Generation of internal solitary waves in a pycnocline by an internal wave beam: A numerical study. *J. Fluid Mech.* **676**, 491–513.

Gururaj, S. & Guha, A. 2020 Energy transfer in resonant and near-resonant internal wave triads for weakly non-uniform stratifications. Part 1. Unbounded domain. *J. Fluid Mech.* **899**, A6.

Gururaj, S. & Guha, A. 2022 Resonant and near-resonant internal wave triads for non-uniform stratifications. part 2. vertically bounded domain with mild-slope bathymetry. *J. Fluid Mech.* **943**, A33.

Hall, R. A., Huthnance, J. M. & Williams, R. G. 2013 Internal wave reflection on shelf slopes with depth-varying stratification. *J. Phys. Oceanogr.* **43** (2), 248 – 258.

Hasselmann, K. 1967 A criterion for nonlinear wave stability. *J. Fluid Mech.* **30** (4), 737–739.

Hazewinkel, J. & Winters, K. B. 2011 PSI of the internal tide on a β plane: Flux divergence and near-inertial wave propagation. *J. Phys. Oceanogr.* **41** (9), 1673 – 1682.

Hibiya, T., Niwa, Y. & Fujiwara, K. 1998 Numerical experiments of nonlinear energy transfer within the oceanic internal wave spectrum. *J. Geophys. Res. Oceans* **103** (C9), 18715–18722.

Hieronymus, M., Nycander, J., Nilsson, J., Döös, K. & Hallberg, R. 2019 Oceanic overturning and heat transport: The role of background diffusivity. *J. Clim.* **32** (3), 701 – 716.

Howland, C. J., Taylor, J. R. & Caulfield, C. P. 2018 Testing linear marginal stability in stratified shear layers. *J. Fluid. Mech.* **839**, R4.

Ince, E. L. 1956 *Ordinary differential equations*. New York, NY: Dover.

Jan, S., Lien, R.-C. & Ting, C.-H. 2008 Numerical study of baroclinic tides in luzon strait. *J. Oceanogr.* **64** (5), 789–802.

Jiang, C.-H. & Marcus, P. S. 2009 Selection rules for the nonlinear interaction of internal gravity waves. *Phys. Rev. Lett.* **102**, 124502.

Johns, W. E., Baringer, M. O., Beal, L. M., Cunningham, S. A., Kanzow, T., Bryden, H. L., Hirschi, J. J. M., Marotzke, J., Meinen, C. S., Shaw, B. & Curry, R. 2011 Continuous, array-based estimates of atlantic ocean heat transport at 26.5°n. *J. Clim.* **24** (10), 2429 – 2449.

Johnston, T. M. S. & Merrifield, M. A. 2003 Internal tide scattering at seamounts, ridges, and islands. *J. Geophys. Res. Oceans* **108** (C6).

Kafiabad, H. A., Savva, M. A. C. & Vanneste, J. 2019 Diffusion of inertia-gravity waves by geostrophic turbulence. *J. Fluid Mech.* **869**, R7.

Kelly, S. M. & Lermusiaux, P. F. J. 2016 Internal-tide interactions with the gulf stream and middle atlantic bight shelfbreak front. *J. Geophys. Res* **121** (8), 6271–6294.

Kirby, J. T. 1986 A general wave equation for waves over rippled beds. *J. Fluid Mech.* **162**, 171–186.

Klostermeyer, J. 1991 Two- and three-dimensional parametric instabilities in finite-amplitude internal gravity waves. *Geophys. Astrophys. Fluid Dyn.* **61** (1-4), 1–25.

Klymak, J. M., Alford, M. H., Pinkel, R., Lien, R.-C., Yang, Y. J. & Tang, T.-Y. 2011 The breaking and scattering of the internal tide on a continental slope. *J. Phys. Oceanogr.* **41** (5), 926 – 945.

Klymak, J. M., Buijsman, M., Legg, S. & Pinkel, R. 2013 Parameterizing surface and internal tide scattering and breaking on supercritical topography: The one- and two-ridge cases. *J. Phys. Oceanogr.* **43** (7), 1380 – 1397.

Klymak, J. M., Moum, J. N., Nash, J. D., Kunze, E., Girton, J. B., Carter, G. S., Lee, C. M., Sanford, T. B. & Gregg, M. C. 2006 An estimate of tidal energy lost to turbulence at the hawaiian ridge. *J. Phys. Oceanogr.* **36** (6), 1148 – 1164.

Koudella, C. R. & Staquet, C. 2006 Instability mechanisms of a two-dimensional progressive internal gravity wave. *J. Fluid Mech.* **548**, 165–196.

Kuhlbrodt, T., Griesel, A., Montoya, M., Levermann, A., Hofmann, M. & Rahmstorf, S. 2007 On the driving processes of the atlantic meridional overturning circulation. *Rev. Geophys.* **45** (2).

Kunze, E. 1985 Near-inertial wave propagation in geostrophic shear. *J. Phys. Oceanogr.* **15** (5), 544 – 565.

Lahaye, N. & Smith, S. G. Llewellyn 2020 Modal analysis of internal wave propagation and scattering over large-amplitude topography. *J. Phys. Oceanogr.* **50** (2), 305 – 321.

Lamb, K. G. 2004 Nonlinear interaction among internal wave beams generated by tidal flow over supercritical topography. *Geophys. Res. Lett.* **31** (9).

Lamb, K. G. & Dunphy, M. 2018 Internal wave generation by tidal flow over a two-dimensional ridge: energy flux asymmetries induced by a steady surface trapped current. *J. Fluid Mech.* **836**, 192–221.

LeBel, D. A., Smethie, W. M., Rhein, M., Kieke, D., Fine, R. A., Bullister, J. L., Min, D.-H., Roether, W., Weiss, R. F., Andrié, C., Smythe-Wright, D. & Peter Jones, E. 2008 The formation rate of north atlantic deep water and eighteen degree water calculated from cfc-11 inventories observed during woce. *Deep Sea Res. Part I Oceanogr. Res. Pap.* **55** (8), 891–910.

Legg, S. 2014 Scattering of low-mode internal waves at finite isolated topography. *J. Phys. Oceanogr.* **44** (1), 359 – 383.

Legg, S. & Adcroft, A. 2003 Internal wave breaking at concave and convex continental slopes. *J. Phys. Oceanogr.* **33** (11), 2224 – 2246.

Levermann, A., Griesel, A., Hofmann, M., Montoya, M. & Rahmstorf, S. 2005 Dynamic sea level changes following changes in the thermohaline circulation. *Clim. Dyn.* **24** (4), 347–354.

Li, Q., Mao, X., Huthnance, J., Cai, S. & Kelly, S. 2019 On internal waves propagating across a geostrophic front. *J. Phys. Oceanogr.* **49** (5), 1229 – 1248.

Li, Y. & Mei, C. C. 2014 Scattering of internal tides by irregular bathymetry of large extent. *J. Fluid Mech.* **747**, 481–505.

Liang, Y., Zareei, A. & Alam, M-R 2017 Inherently unstable internal gravity waves due to resonant harmonic generation. *J. Fluid Mech.* **811**, 400–420.

Liu, W., Fedorov, A. V., Xie, S.-P. & Hu, S. 2020 Climate impacts of a weakened atlantic meridional overturning circulation in a warming climate. *Sci. Adv.* **6** (26).

Llewellyn Smith, S. G. & Young, W. R. 2003 Tidal conversion at a very steep ridge. *J. Fluid. Mech.* **495**, 175–191.

Lombard, Peter N. & Riley, J. J. 1996 Instability and breakdown of internal gravity waves. I. linear stability analysis. *Phys. Fluids* **8** (12), 3271–3287.

Maas, Leo R. M. 2011 Topographies lacking tidal conversion. *Journal of Fluid Mechanics* **684**, 5–24.

Maas, L. R. M. & Zimmerman, J. T. F. 1989 Tide-topography interactions in a stratified shelf sea ii. bottom trapped internal tides and baroclinic residual currents. *Geophysical & Astrophysical Fluid Dynamics* **45** (1-2), 37–69.

MacKinnon, J. A., Alford, M. H., Sun, O., Pinkel, R., Zhao, Z. & Klymak, J. 2013 Parametric subharmonic instability of the internal tide at 29°N. *J. Phys. Oceanogr.* **43** (1), 17 – 28.

MacKinnon, J. A. & Winters, K. B. 2005 Subtropical catastrophe: Significant loss of low-mode tidal energy at 28.9°. *Geophys. Res. Lett.* **32** (15).

MacKinnon, J. A., Zhao, Z., Whalen, C. B., Waterhouse, A. F., Trossman, D. S., Sun, O. M., Laurent, L. C. St., Simmons, H. L., Polzin, K., Pinkel, R., Pickering, A., Norton, N. J., Nash, J. D., Musgrave, R., Merchant, L. M., Melet, A. V., Mater, B., Legg, S., Large, W. G., Kunze, E., Klymak, J. M., Jochum, M., Jayne, S. R., Hallberg, R. W., Griffies, S. M., Diggs, S., Danabasoglu, G., Chassignet, E. P., Buijsman, M. C., Bryan, F. O., Briegleb, B. P., Barna, A., Arbic, B. K., Ansong, J. K. & Alford, M. H. 2017 Climate process team on internal wave–driven ocean mixing. *Bull. Am. Meterol. Soc.* **98** (11), 2429 – 2454.

Mashayek, A., Ferrari, R., Nikurashin, M. & Peltier, W. R. 2015 Influence of enhanced abyssal diapycnal mixing on stratification and the ocean overturning circulation. *J. Phys. Oceanogr.* **45** (10), 2580 – 2597.

Mathur, M., Carter, G. S. & Peacock, T. 2014 Topographic scattering of the low-mode internal tide in the deep ocean. *J. Geophys. Res. Oceans* **119** (4), 2165–2182.

Mathur, M., Carter, G. S. & Peacock, T. 2016 Internal tide generation using green function analysis: To wkb or not to wkb? *J. Phys. Oceanogr.* **46** (7), 2157 – 2168.

Maugé, R. & Gerkema, T. 2008 Generation of weakly nonlinear nonhydrostatic internal tides over large topography: a multi-modal approach. *Nonlinear Process. Geophys.* **15** (2), 233–244.

Maurer, P., Joubaud, S. & Odier, P. 2016 Generation and stability of inertia–gravity waves. *J. Fluid Mech.* **808**, 539–561.

McEwan, A.D. & Plumb, R.A. 1977 Off-resonant amplification of finite internal wave packets. *Dynam. Atmos. Ocean* **2** (1), 83 – 105.

Melet, A., Hallberg, R., Legg, S. & Polzin, K. 2013 Sensitivity of the ocean state to the vertical distribution of internal-tide-driven mixing. *J. Phys. Oceanogr.* **43** (3), 602 – 615.

Melet, A., Legg, S. & Hallberg, R. 2016 Climatic impacts of parameterized local and remote tidal mixing. *J. Clim.* **29** (10), 3473 – 3500.

Mellor, G. L. & Ezer, T. 1995 Sea level variations induced by heating and cooling: An evaluation of the boussinesq approximation in ocean models. *J. Geophys. Res* **100** (C10), 20565–20577.

Meyer, R. E. 1979 Surface wave reflection by underwater ridges. *J. Phys. Oceanogr.* **9** (1), 150 – 157.

Munk, W. & Wunsch, C. 1998 Abyssal recipes II: energetics of tidal and wind mixing. *Deep Sea Res. Part I Oceanogr. Res. Pap.* **45** (12), 1977–2010.

Munk, W. H. 1966 Abyssal recipes. *Deep-Sea Res. Oceanogr. Abstr.* **13** (4), 707 – 730.

Müller, P. & Liu, X. 2000 Scattering of internal waves at finite topography in two dimensions. part i: Theory and case studies. *J. Phys. Oceanogr.* **30** (3), 532 – 549.

Nazarian, R. H. & Legg, S. 2017*a* Internal wave scattering in continental slope canyons, part 1: Theory and development of a ray tracing algorithm. *Ocean Model.* **118**, 1–15.

Nazarian, R. H. & Legg, S. 2017*b* Internal wave scattering in continental slope canyons, part 2: A comparison of ray tracing and numerical simulations. *Ocean Model.* **118**, 16–30.

Neef, L. 2004 Triad resonance as a mechanism for internal wave dissipation. *Online Document* pp. 164–180.

Nikurashin, M. & Legg, S. 2011 A mechanism for local dissipation of internal tides generated at rough topography. *J. Phys. Oceanogr.* **41** (2), 378 – 395.

Oka, A. & Niwa, Y. 2013 Pacific deep circulation and ventilation controlled by tidal mixing away from the sea bottom. *Nat. commun.* **4**, 2419.

Olbers, D., Pollmann, F. & Eden, C. 2020 On PSI interactions in internal gravity wave fields and the decay of baroclinic tides. *J. Phys. Oceanogr.* **50** (3), 751 – 771.

Onuki, Y. & Hibiya, T. 2018 Decay Rates of Internal Tides Estimated by an Improved Wave–Wave Interaction Analysis. *J. Phys. Oceanogr.* **48** (11), 2689–2701.

Palter, J. B. 2015 The role of the gulf stream in european climate. *Annu. Rev. Mar. Sci* **7**, 113–137.

Pan, Q., Peng, N. N., Chan, H. N. & Chow, K. W. 2021*a* Coupled triads in the dynamics of internal waves: Case study using a linearly stratified fluid. *Phys. Rev. Fluids* **6**, 024802.

Pan, Q., Yin, H.-M. & Chow, K. W. 2021*b* Triads and rogue events for internal waves in stratified fluids with a constant buoyancy frequency. *J. Mar. Sci. Eng.* **9** (6).

Paparella, F. & Young, W. R. 2002 Horizontal convection is non-turbulent. *J. Fluid Mech.* **466**, 205–214.

Perkins, H. 1976 Observed effect of an eddy on inertial oscillations. *Deep Sea Res. Part I Oceanogr. Res. Pap.* **23** (11), 1037–1042.

Phillips, O. M. 1977 The dynamics of the upper ocean. 2nd edition. *Cambridge University Press* .

Pingree, R.D. & New, A.L. 1995 Structure, seasonal development and sunglint spatial coherence of the internal tide on the celtic and armorican shelves and in the bay of biscay. *Deep Sea Res. Part I Oceanogr. Res. Pap.* **42** (2), 245–284.

Ray, R. D. & Mitchum, G. T. 1997 Surface manifestation of internal tides in the deep ocean: observations from altimetry and island gauges. *Prog. Oceanogr.* **40** (1), 135–162, Tidal Science In Honour of David E. Cartwright.

Richet, O., Chomaz, J.-M. & Muller, C. 2018 Internal tide dissipation at topography: Triadic resonant instability equatorward and evanescent waves poleward of the critical latitude. *J. Geophys. Res.* **123** (9), 6136–6155.

Richet, O., Muller, C. & Chomaz, J.-M. 2017 Impact of a mean current on the internal tide energy dissipation at the critical latitude. *J. Phys. Oceanogr.* **47** (6), 1457 – 1472.

Samelson, R. & Vallis, G. 1997 Large-scale circulation with small diapycnal diffusion: The two-thermocline limit. *J. Mar. Res.* **55**, 223–275.

Savva, M.A.C., Kafiabad, H.A. & Vanneste, J. 2021 Inertia-gravity-wave scattering by three-dimensional geostrophic turbulence. *J. Fluid Mech.* **916**, A6.

Savva, Miles A. C. & Vanneste, Jacques 2018 Scattering of internal tides by barotropic quasigeostrophic flows. *J. Fluid Mech.* **856**, 504–530.

Schmittner, A., Latif, M. & Schneider, B. 2005 Model projections of the north atlantic thermohaline circulation for the 21st century assessed by observations. *Geophys. Res. Lett.* **32** (23).

Smith, S. G. Llewellyn & Young, W. R. 2002 Conversion of the barotropic tide. *J. Phys. Oceanogr.* **32** (5), 1554 – 1566.

Sonmor, L. J. & Klaassen, G. P. 1997 Toward a unified theory of gravity wave stability. *J. Atmos. Sci.* **54** (22), 2655 – 2680.

St. Laurent, L. C., Simmons, H. L. & Jayne, S. R. 2002 Estimating tidally driven mixing in the deep ocean. *Geophys. Res. Lett.* **29** (23), 21–1–21–4.

Sutherland, B. R. 2010 *Internal Gravity Waves*. Cambridge University Press.

Sutherland, B. R. 2016 Excitation of superharmonics by internal modes in non-uniformly stratified fluid. *J. Fluid Mech.* **793**, 335–352.

Sutherland, B. R. & Dhaliwal, M. S. 2022 The nonlinear evolution of internal tides. part 1: the superharmonic cascade. *J. Fluid Mech.* **948**, A21.

Sutherland, B. R. & Jefferson, R. 2020 Triad resonant instability of horizontally periodic internal modes. *Phys. Rev. Fluids* **5**, 034801.

Tabaei, A. & Akylas, T. R. 2003 Nonlinear internal gravity wave beams. *J. Fluid Mech.* **482**, 141–161.

Tabaei, A., Akylas, T. R. & Lamb, K. G. 2005 Nonlinear effects in reflecting and colliding internal wave beams. *J. Fluid Mech.* **526**, 217–243.

Talley, Lynne D. 2013 Closure of the global overturning circulation through the indian, pacific, and southern oceans: Schematics and transports. *Oceanography* .

Thorpe, S. A. 1966 On wave interactions in a stratified fluid. *J. Fluid. Mech.* **24** (4), 737–751.

Vallis, G. K. 2017 *Atmospheric and Oceanic Fluid Dynamics: Fundamentals and Large-Scale Circulation*, 2nd edn. Cambridge University Press.

Van Gastel, Paul, Ivey, Gregory N., Meuleners, Michael J., Antenucci, Jason P. & Fringer, Oliver 2009 The variability of the large-amplitude internal wave field on the australian north west shelf. *Continental Shelf Research* **29** (11), 1373–1383.

Varma, D. & Mathur, M. 2017 Internal wave resonant triads in finite-depth non-uniform stratifications. *J. Fluid Mech.* **824**, 286–311.

Vellinga, M. & Wood, R. 2002 Global climatic impacts of a collapse of the atlantic thermohaline circulation. *Clim. Change* **54**, 251–267.

Vic, C., Garabato, A.C.N., Green, J.A.M., Waterhouse, A.F., Zhao, Z., Mélet, A., De Lavergne, C., Buijsman, M. C. & Stephenson, G. R. 2019 Deep-ocean mixing driven by small-scale internal tides. *Nat. Commun.* **10** (1), 1–9.

Voelker, G. S., Akylas, T. R. & Achatz, U. 2021 An application of WKBJ theory for triad interactions of internal gravity waves in varying background flows. *Q. J. R. Meteorol. Soc.* **147** (735), 1112–1134.

Wagner, G. L., Ferrando, G. & Young, W. R. 2017 An asymptotic model for the propagation of oceanic internal tides through quasi-geostrophic flow. *J. Fluid Mech.* **828**, 779–811.

Wang, W. & Huang, R. X. 2005 An experimental study on thermal circulation driven by horizontal differential heating. *J. Fluid Mech.* **540**, 49–73.

Waterhouse, A. F., MacKinnon, J. A., Nash, J. D., Alford, M. H., Kunze, E., Simmons, H. L., Polzin, K. L., Laurent, L. C. St., Sun, O. M., Pinkel, R., Talley, L. D., Whalen, Caitlin B., Huussen, T. N., Carter, G. S., Fer, I., Waterman, S., Garabato, A. C. N., Sanford, T. B. & Lee, C. M. 2014 Global patterns of diapycnal mixing from measurements of the turbulent dissipation rate. *J. Phys. Oceanogr.* **44** (7), 1854 – 1872.

Whalen, C. B, MacKinnon, J. A & Talley, L. D 2018 Large-scale impacts of the mesoscale environment on mixing from wind-driven internal waves. *Nat. Geosci.* **11** (11), 842–847.

Wunsch, C. & Ferrari, R. 2004 Vertical mixing, energy, and the general circulation of the oceans. *Annu. Rev. Fluid Mech.* **36** (1), 281–314.

Wunsch, S. 2017 Harmonic generation by nonlinear self-interaction of a single internal wave mode. *J. Fluid Mech.* **828**, 630–647.

Xu, H., Zhang, Z., Vetter, P. A., Xie, Q., Long, T. & Hong, B. 2022 Impact of anticyclonic eddy on nonlinear wave-wave interaction in the southern south china sea during late summer 2020. *Geophys. Res. Lett.* **49** (9).

Yi, Y. R., Legg, S. & Nazarian, R. H. 2017 The impact of topographic steepness on tidal dissipation at bumpy topography. *Fluids* **2** (4).

Young, W. R., Tsang, Y.-K. & Balmforth, N. J. 2008 Near-inertial parametric subharmonic instability. *J. Fluid Mech.* **607**, 25–49.

Zhao, Z., Alford, M. H., Girton, J. B., Rainville, L. & Simmons, H. L. 2016 Global Observations of Open-Ocean Mode-1 M2 Internal Tides. *J. Phys. Oceanogr.* **46** (6), 1657–1684.